Laser Deposition of Inconel 625/Tungsten Carbide Composite Coatings by Powder and Wire Feedstock

Taiwo Ebenezer Abioye, MSc BEng

Thesis submitted for the degree of Doctor of Philosophy

Department of Mechanical, Materials and Manufacturing Engineering

The University of Nottingham

February 2014

Preface

The thesis is submitted for the degree of Doctor of Philosophy at the University of Nottingham. The research was carried out under the supervision of Dr A.T. Clare and Professor D.G. McCartney in the department of Mechanical, Materials and Manufacturing Engineering.

The work presented in this thesis is original, and suitable references are made to any work from the literature or carried out elsewhere.

The list of Publications from the work presented in this thesis is listed below:

- T.E. Abioye, J. Folkes and A.T. Clare, *A parametric study of Inconel 625 wire laser deposition.* Journal of Materials Processing Technology, Vol 213 No12 (2013). Pp 2145-2151.
- T.E. Abioye, J. Folkes, A.T. Clare and D.G. McCartney, *Concurrent Inconel 625 wire and WC powder laser cladding: process stability and microstructural characterisation.* Journal of Surface Engineering, Vol 29 No 9 (2013). Pp. 647-653(7)
- T.E. Abioye, J. Folkes, A.T. Clare and D.G. McCartney, *Concurrent Inconel 625 wire and WC powder laser cladding on AISI 304L stainless steel,* in 37th International MATADOR conference, July 2012. Manchester, United Kingdom.
- T.E Abioye, A.T. Clare*, P.K. Farayibi and C. Li, *Direct laser metal deposition of Inconel 625 wire tracks: microstructural variation with processing parameters*, in 26th International conference on Surface Modification Technologies, June 20th – 22nd, 2012. Ecole Centrale de Lyon in Ecully, France.

Acknowledgements

If not for the grace of almighty God, I would never have been able to complete my PhD thesis. I sincerely thank the Nigerian government (Petroleum Technology Development Fund) for sponsoring my PhD program.

I would like to express my deepest gratitude to my supervisors, Dr Janet Folkes (late), Dr Adam Thomas Clare and Prof Graham McCartney for their guidance, patience and providing me an excellent atmosphere throughout my stay in United Kingdom. I also acknowledge the assistance rendered by Mr Stuart Branston, Mr Graham Malkinson, Mr Daine Mark, Dr Nigel Neate, Mr Thomas Buss and Mr Keith Dinsdale during my laboratory work.

I cannot but thank my colleagues, friends, and group members for their valuable advice. The memory of working with you will always be remembered. I appreciate my parents, brothers and sisters for always standing by me through the good and bad times.

Finally, my special thanks go to my wife (Arinola) and son (Richard). They are always supporting and encouraging me with their best wishes.

Abstract

There is an increasing global demand to extend the life span of down-hole drilling tools in order to improve operation effectiveness and efficiency of oil and gas production. Laser cladding of tungsten carbide/Ni-based alloy metal matrix composite (MMC) coatings is currently being utilised for this purpose. However, the effect of tungsten carbide dissolution on the corrosion performance of the MMC coatings has not been completely understood. In this work, a study was carried out in which laser cladding of a stainless steel substrate using (i) Inconel 625 wire and (ii) tungsten carbide powder (Spherotene)/Inconel 625 wire was undertaken. This work was performed using a fibre laser system and has examined the process characteristics, the microstructure and the corrosion performance of the clad layers. Process characteristics studies were carried out by visual observation of the cladding process within a process window (laser power: 1-1.8 kW, traverse speed: 100-300 mm min^{-1}, wire feed rate: 400-1000 mm min^{-1}, powder feed rate: 25 g min^{-1}). The microstructures were investigated using a combination of optical microscopy, scanning electron microscopy (with energy dispersive X-ray analysis) and X-ray diffraction. The volume fraction of tungsten carbide retained in the composite coatings was determined using image processing software. Corrosion performance was assessed using electrochemical corrosion testing in de-aerated 3.5 wt.% NaCl solution. Well bonded, minimally diluted, pore- and crack-free Inconel 625 wire and Spherotene (WC/W_2C) powder/Inconel 625 wire composite coatings were successfully deposited. Cladding process characteristics were categorised into wire dripping, smooth wire deposition and wire stubbing within the range of parameters used in this work. Process maps which predict the characteristic of Inconel 625 wire and Spherotene (WC/W_2C)/Inconel 625 wire fibre laser cladding at varying cladding conditions within the process window were developed. The volume fraction of tungsten carbide (WC/W_2C)

retained in the composite coatings was found to decrease with increasing laser power, traverse speed and wire feed rate. Tungsten carbide dissolution was found to result in the precipitation of intermetallic compounds including M_6C and $M_{23}C_6$ in the γ-Ni matrix, which is rich in W and C. The increase in tungsten carbide dissolution was also found to increase the propensity for corrosion in the MMC coatings compared to the Inconel 625 wire coatings. As a result, the corrosion performance of the tungsten carbide/Ni based alloy MMC coatings can be improved by reducing the level of tungsten carbide dissolution through process control.

List of symbols and abbreviations

A	Cross-sectional area of the wire (mm^2)
AISI	American Iron and Steel Institute
ANOVA	Analysis of variance
ASTM	American Society for Testing and Materials
BSE	Back scattered electrons
C	Carbon
MMC	Metal matrix composite
CNC	Computer Numerical Control
Cr	Chromium
D_{ratio}	Dissolution ratio
DOF	Degree of freedom
E_b	Breakdown potential (mV)
E_{corr}	Corrosion potential (mV)
E_L	Energy per unit length of track (J mm^{-1})
E_{oc}	Open circuit potential (mV)
EDM	Electrical-discharge machine
EDX	Energy Dispersive X-ray
FCC	Face-centred-cubic
Fe	Iron
G	Temperature gradient (K m^{-1})
H	height of the track (mm)
h	Melt depth into substrate (mm)
HAZ	Heat affected zone
HVOF	High velocity oxygen fuel
I_p	Passive current density (mA cm^{-2})
JCPDS	Joint Commission for Powder Diffraction Standards
LASER	Light amplification by stimulated emission of radiation
LENS	Laser engineering net shapping

Mo	Molybdenum
MS	Mean square
NaCl	Sodium Chloride
NbC	Niobium Carbide
Ni	Nickel
Nb	Niobium
θ	Theta (degrees)
P	Laser power (kW)
PFR	Powder feed rate (g min^{-1})
ρ	Density (g cm^{-3})
Ø	Diameter (mm)
R	Solidification growth rate
SE	Secondary electron
SEM	Scanning electron microscopy
SD	Standard deviation
SiC	Silicon carbide
SS	Sum of Squares
TEM	Transmission electron microscopy
TiC	Titanium carbide
V	Traverse speed (mm min^{-1})
W	Tungsten
WC	Tungsten carbide
WFR	Wire feed rate (mm min^{-1})
wrt	with respect to
W_{vol}	Wire deposition volume per unit length of track (mm^3 mm^{-1})
XRD	X-ray Diffraction
γ	Gamma
γ´	Gamma prime precipitate
γ´´	Gamma prime prime precipitate

Table of contents

1.0 Introduction

1.1 Background and problem definition

Surface modification of engineering components for protection against wear and corrosion is one of the growing fields of research in offshore industry. Among different coating methods for surface modification of ferrous metals, laser cladding offers advantages over thermal spraying and conventional arc welding. These include strong metallurgical bond at the coating-substrate interface [1, 2], minimal distortion of the substrate [3], low dilution [4], minimal porosity and controllable heat input often producing a small heat affected zone (HAZ) [5]. The use of lasers for cladding was first patented in 1976 by AVCO Everett research laboratory, USA [6]. In this method, laser acts as the heat source for creating a meltpool by simultaneously melting an additive material and a thin layer of a substrate. The relative movement of the laser beam and the substrate forms a track. The track is often referred to as a clad bead. The cladding can be carried out with wire or powder as the feedstock material. Overlapped tracks can be deposited for a complete coating of a component.

Laser cladding is commonly performed with CO_2 and various types of Nd:YAG lasers. Recently, fibre lasers are beginning to supplant the traditional lasers because of their better rewards in terms of cost, cladding efficiency and suitability to various working environments [7, 8]. Unlike CO_2 lasers, fibre lasers can deliver their energy through an integrated optical fibre, giving substantial flexibility in terms of how the cladding is implemented. Also the fibre laser beam gives excellent beam quality and can be focused to a very small spot [7].

Extensive research in laser cladding using metal alloy of superior properties has been undertaken for enhanced surface performance of engineering (metallic) components [9]. Consequently, a range of highly corrosion and wear resistant materials has been processed in this way [5, 10]. Due to the high corrosion and oxidation resistance properties of Inconel 625 alloy which contains Ni-Cr-Mo-Nb, Inconel 625 has always being a material of choice for coating components exposed to seawater for long-term protection [11, 12]. Consequently, engineering (metallic) components, particularly stainless steels, laser coated with Inconel-625 are common in the offshore industry [13]. To date, a number of studies have been reported on laser cladding of Inconel 625 using powder as the feedstock material. However, laser deposition using Inconel 625 wire as a feedstock material rather than powder has not been widely undertaken. Compared with powder feeding, laser cladding with wire has the potential to give cleaner process environment, higher deposition rate and improved surface quality. Also, the cost of producing wire is lower compared to the powder.

The application of laser cladding has also been extended to the deposition of metal matrix composite (MMC) coatings. This is currently being utilised in extending the life span of down-hole drilling tools in aggressive corrosive environment with the presence of suspended sand particles which contribute to overall abrasive wear of the component surface [14]. MMC coatings typically consist of at least two components. One is the matrix which is usually a metal alloy. The second is the reinforcement which is usually ceramic. The ceramics can be oxides or carbides or nitrides. Generally, there are wide combinations of ceramics and metal alloy materials, tungsten carbide (WC) embedded in a nickel-alloy (e.g. Inconel 625) matrix is mostly the material of choice for offshore applications. Ni-based self-fluxing alloys have been extensively used due to their high toughness and corrosion resistance [15]. Also, tungsten carbide is increasingly being used because it is known to be very hard (1.78×10^9 kg m^{-2}), possess a high melting point (2720^oC) and high density(15630 kg m^{-3}), and have a good

wettability with molten Ni alloys [11] [16]. The MMC coatings act as asphalt does on the roadway. The hard WC particles rub against the suspended soil therefore, protects the soft matrix from abrasive wear. The Inconel 625 alloy gives the coating a high resistance in the corrosive medium.

However, the major issues of concern about achieving optimal performance of WC/Inconel 625 composite coatings is the dissolution of reinforcing particles and substrate dilution [11, 17]. The WC dissolution is susceptible to the corrosion and wear performance while the substrate dilution is detrimental to the corrosion behaviour of the coating. The ability to minimise the WC dissolution and substrate dilution requires a proper control of the processing parameters. A control of the volume of tungsten carbide delivered into the meltpool is also required. Prior work has established that WC dissolution and substrate dilution increases with increasing the laser input [18-20]. Also, it has been reported that WC dissolution promotes microstructural in-homogeneity which results in galvanic corrosion in the MMC coatings [11]. However, it has not been established whether the corrosion damage increases with increasing the WC dissolution. Therefore, this work will involve the fibre laser cladding of tungsten carbide reinforced Inconel 625 composite coating within a process window with the aim of establishing suitable cladding parameters and controlling the tungsten carbide dissolution. Thereafter, the effect of increased tungsten carbide dissolution on the corrosion performance of the MMC coating will be investigated.

The amount of tungsten carbide fed into the molten Ni-matrix will be controlled by independently feeding the feedstock materials. Inconel 625 wire will be used because of its potential advantages over the powder. Also, special spherical cast tungsten carbide (commercially called Spherotene) will be used for this work. Spherotene is increasingly being used as hardfacing material in Ni alloy matrix because of its extremely high hardness (between 1800 and 3000 HV) and high density (16300 kg m-3) [21].

1.2 Overall objectives of the research work

This overall objective of this research can be broadly grouped into two areas. First, the fibre laser cladding of Inconel 625 wire will be investigated, within a window, for process stability, process characterisations, micro-hardness and corrosion behaviours. Secondly, concurrent fibre laser cladding of Spherotene-Inconel 625 composite will be studied, within the process window, with the aim of controlling the dissolution of Spherotene in the Inconel 625 alloy binder. The effect of Spherotene dissolution on the corrosion performance of the coating will be determined. The specific objectives of this research work are to:

1. Establish a process window within which continuous tracks of Inconel 625 wire fibre laser tracks can be deposited. A map which predicts Inconel 625 wire fibre laser deposition process characteristics at varying processing parameters will also be developed.

2. Investigate the effect of the processing parameters such as laser power, traverse speed and wire feed rate, within the established window, on the dilution ratio, process characteristics and microstructure of the Inconel 625 wire laser tracks. The microstructure of the tracks will be related their micro-hardness.

3. Deposit Inconel 625 powder laser tracks using similar process window. This is to compare laser cladding processes using wire and powder feeding system in terms of track qualities including degree of substrate (Fe) dilution ratio, microstructural evolution, micro-hardness and corrosion behaviours.

4. Deposit continuous, well bonded, crack-free and pore-free Spherotene (WC/W_2C) powder-Inconel 625 wire composite tracks via concurrent laser cladding.

5. Study the effects of Spherotene powder injection on the process characteristics and microstructures of Inconel 625 wire laser cladding.
6. Investigate the extent of Fe dilution and amount of Spherotene particle dissolution in the composite tracks as a function of the processing parameters. The results obtained from these will be related to the micro-hardness and corrosion performances of the coatings.
7. Identify the phases present and determine their effects on the micro-hardness and corrosion behaviour of the coatings.

1.3 Proposed methodology

The project methodology is sequentially described in Figure 1.1. Coating samples were produced by laser cladding of Inconel 625 using wire and powder feeding systems, and concurrent laser cladding of Inconel 625 wire and Spherotene (WC/W_2C) powder. 304L stainless steel was used as the substrate material throughout the experiments. The geometrical characterisation, dilution measurements, microstructural characterisation, hardness testing and corrosion testing were the main analysis performed on the samples. Hardness and corrosion testing of bulk 304L stainless steel were performed so as to provide reference data for comparison.

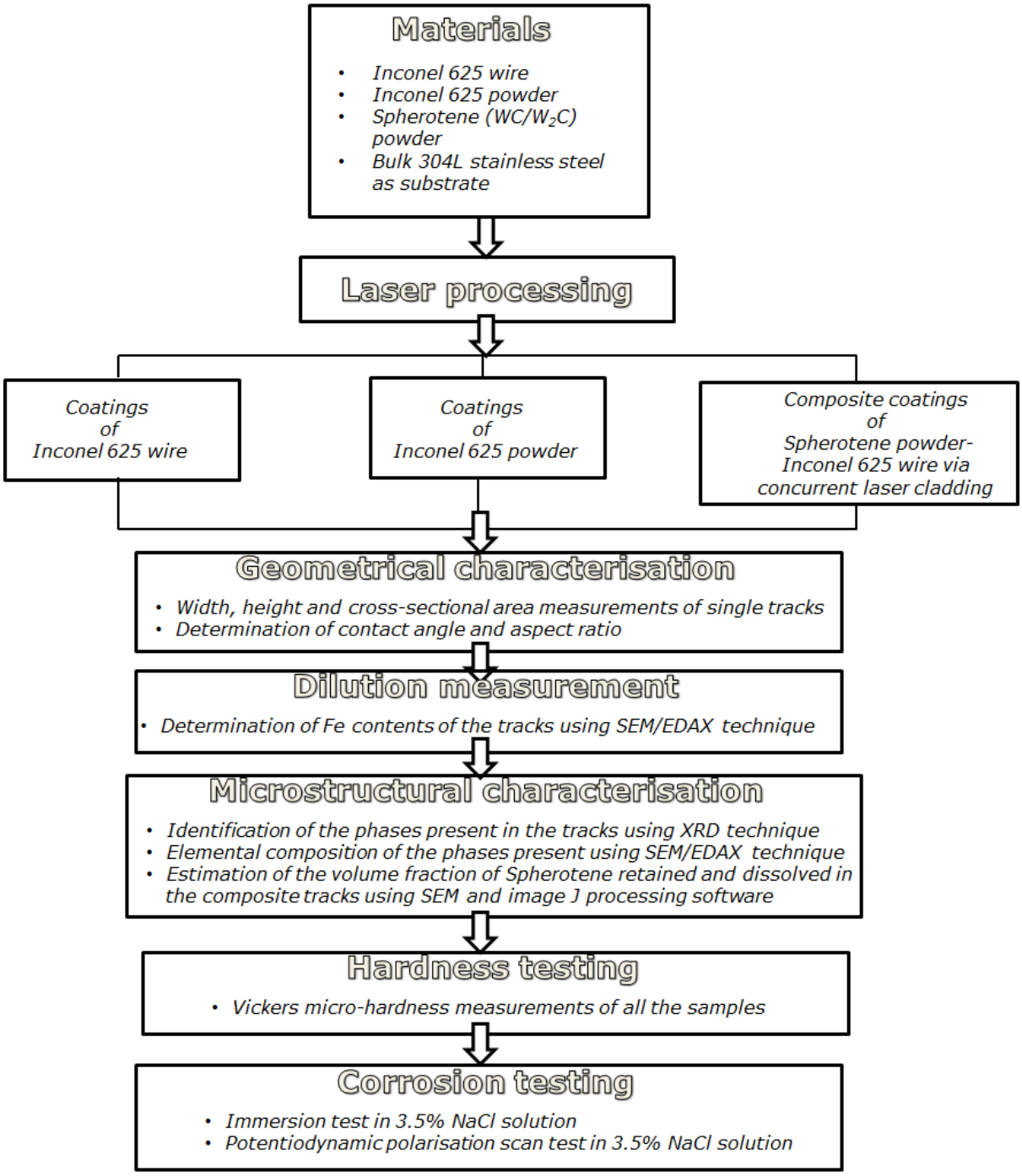

Figure1.1: Experiments carried out on the coating samples and 304 stainless steel substrate

1.4 Thesis structure

The thesis is organised into 7 chapters. Each chapter begins with the brief introduction of the contents and ends with the summary of the key findings. A list of references is provided at the end of the thesis. The 7 chapters are highlighted as follows.

- Chapter 1 provides the frame of reference for the reader.
- Chapter 2 presents a review of the existing literature about the research area. On the basis of the review, the research goals are defined after identifying the gaps in the literature.
- Chapter 3 contains the information about the materials, equipment, experiments and testing procedures utilised for carrying out the research work.
- Chapter 4-6 outline the results, each containing discussion of the relevant results.
- Chapter 4 presents the study of the geometrical and microstructural characterisation, process characterisation and the micro-hardness of the laser cladding of Inconel 625 by wire and powder feeding.
- Chapter 5 reports the process and microstructural characterisation as well as the micro-hardness of the Spherotene-Inconel 625 wire composite deposited via concurrent laser cladding.
- Chapter 6 presents the corrosion behaviour and microstructure before and after corrosion testing, of Inconel 625 laser coatings by wire and powder feeding, and concurrent laser deposited Spherotene-Inconel 625 wire composite at varying processing parameters
- Chapter 7 summarises the results and includes further discussions and conclusions. It also identifies some areas for future work.

2.0 Literature review

2.1 Introduction

This chapter presents a review of the literature about the research works reported in this thesis. The chapter is divided into various sections namely: lasers, materials, coatings technology, laser cladding, microstructure and corrosion measurement. Past work in these research areas is presented with respect to the overall objective of this thesis. The chapter ends with a separate section containing the summary of the literature review. The gaps in the literature are identified and the aims of this research work are defined and highlighted based on the gaps found in the literature.

Laser

2.2 Laser

"Laser" is an acronym for "Light Amplification by Stimulated Emission of Radiation". The name was coined by the laser pioneer Gordon Gould in 1957 [22]. This denotes its principle of operation and the term is now mostly used for devices generating light based on the laser principle. The term "optical MASER" (MASER = microwave amplification by stimulated emmision of radiation) was initially used and was later replaced with "laser*"*[22].

The following combination of characteristics distinguishes laser radiation from all other light sources:

- Highly monochromic – laser has narrow wavelength bandwidth which make gives it better materials process efficiency.
- Low divergence- laser is the only light that is almost parallel with the resonator axis (i.e. the principal axis). The parallel nature of a laser beam enables it to be focused to a very small radius.
- Highly coherent – Laser beam is said to be coherent because its waves are in phase. Two waves are said to be in phase if their crests and troughs meet at the same time whereas the waves are out of phase if the crests of one meet the troughs of another.

2.2.1 The basic laser principle

Figure 2.1 describes an excitation process of an atom. Laser operation involves the excitation of an atom from its ground state to a higher energy level. An atom at higher energy level is relatively unstable and wants to return to its ground state. When this happens, a photon is

released in form of light energy. In laser, the way the energised atoms release photons is controlled [23] and the details is given in the next paragraph.

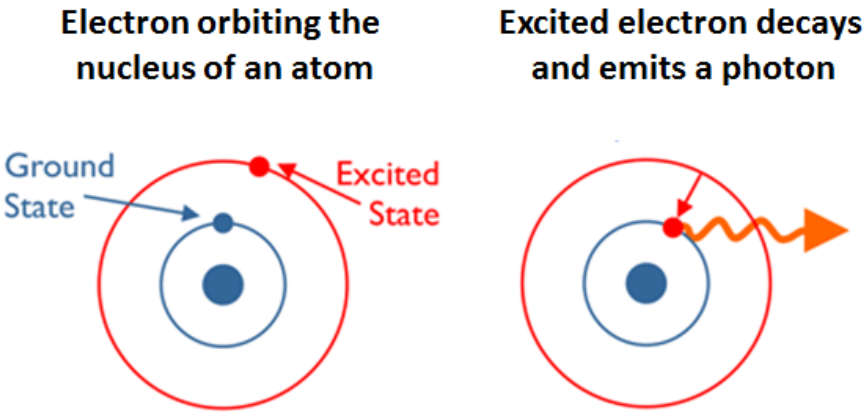

Figure 2.1: Excitation of an atom [23]

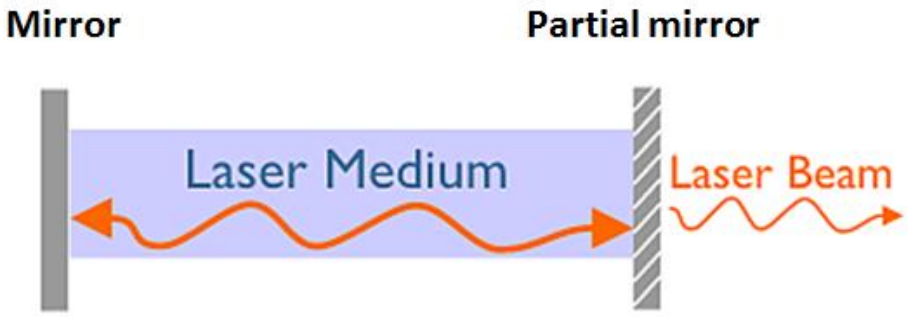

Figure 2.2: Laser gain medium [23]

As described in Figure 2.2, laser usually comprises of an optical resonator (laser resonator, laser cavity) in which light can oscillate (e.g. between two mirrors). Within this resonator is a gain medium (e.g. a laser crystal) which serves to amplify the light. The gain medium is pumped either by a very intense flashes of light or electrical discharges. Once the lasing (gain) medium is pumped, a collection of atoms with some electrons sitting in excited levels is built up. A large collection of highly excited atom is necessary for the laser to work

effectively. As the atoms return to their ground state after excitation, energy is released in the form of photons. The photon emitted by an atom has a very specific wavelength that is dependent on the energy difference between the excited state and the ground state of the atom [22-24]. Therefore, the photon emitted by the first excited atom has a particular wavelength.

In laser light production, subsequent photons are released by stimulated emission such that the first (stimulating) photon induces a new (emitted) photon from another atom that has its electron in the same excited state as the first atom. The stimulating and emitted photons are very identical and the waves associated with the two photons have the same energy, phase, wavelength, polarization and direction of travel. These photons, of the same waves' properties, travel back and forth within the laser resonator. In the process, they stimulate other electrons to make the downward energy jump and cause the emission of more identical photons of the same waves' properties. As the photons with same wavelength and phases build up and oscillate within the laser resonator, some photons in form of light make it through the partial mirror. The light that makes it through is emitted in a coherent beam of laser light [22-24].

2.2.2 Industrial Lasers

Common industrial lasers include fibre lasers, diode lasers, CO_2 lasers and Nd:YAG laser [25]. Fibre lasers are discussed in the next section however details of other industrial lasers are discussed by Rudiger [22]. A 2 kW IPG ytterbium doped fibre laser in the manufacturing laboratory of the University of Nottingham has a Gaussian beam delivery system.

2.2.3 The fibre laser

Fibre lasers are lasers with optical fibres as the gain media. Usually, the fibres are doped with rare earth ions such as erbium (Er^{3+}), neodymium (Nd^{3+}), ytterbium (Yb^{3+}), thulium (Tm^{3+}), or praseodymium (Pr^{3+}) [22, 26]. Among all the rare earth ions, ytterbium doped fibre lasers

are the most powerful. They can be pumped at 975nm and give a laser output of 1070-1080nm [26]. As shown in Figure 2.3, laser diodes are used for pumping the gain medium.

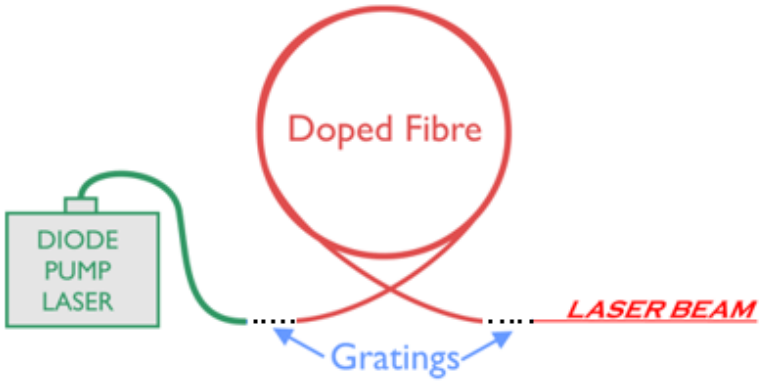

Figure 2.3: A fibre laser [23]

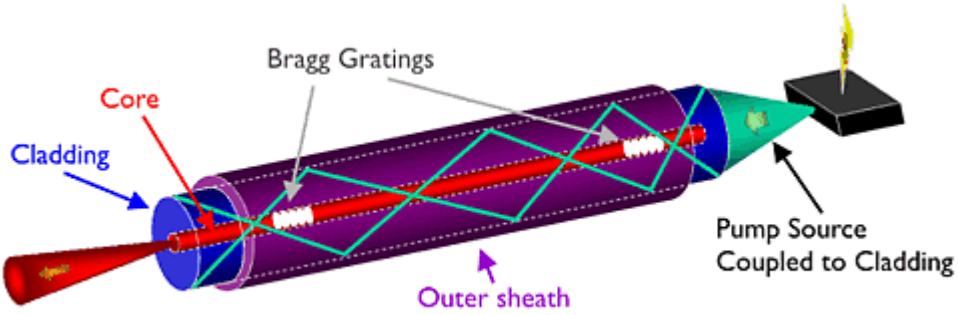

Figure 2.4: A fibre laser diagram showing the outer sheath containing the scattered diode laser [23]

Diode lasers produce relatively low quality (scattered) beams therefore there are always problems in focusing the relatively scattered beams into an ytterbium doped small fibre core. As a result, the small fibre core shown in Figure 2.4 is clad with an outer sheath so as to contain the pumped laser beams [23, 26]. The diode laser beam reflects within the ytterbium doped fibre core. This excites the ytterbium atoms, therefore, increasing the population inversion. Through stimulated emission, more photons are emitted. The photons (light) that are transmitted through the fibre bragg grating (a laser resonator) are emitted in a coherent

beam of light called fibre laser. As shown in Figure 2.3, fibre bragg grating (FBG) is a short segment of an optic fibre which by the periodical perturbation of the effective refractive index of the fibre core reflects a particular wavelength of light and transmits all others [22]. The emission of the fibre laser can either be pulsed or continuous [22]. The power of the pulsed laser is measured in Joules per pulse while the power unit of continuous wave fibre laser is Watts.

Fibre lasers have some advantages over other existing industrial lasers. The advantages are stated below [22, 23, 26];

- Unlike other industrial lasers, fibre laser generates its beam inside the fibre which makes the beam delivery very easy without any complication or requirement of any sensitive optics. As a result, fibre laser is stable and easy to use.

- Fibre laser gives beam of a very high quality because the generated beam is confined inside a small core of the fibre therefore can be focused to a very small spot.

- Since the beams can be focused to a very small spot, fibre laser can produce a laser beam of a very high power from a small power input by the pump source. Therefore, they are very efficient.

- Fibre lasers do not heat up quickly and are easy to cool since the heat is evenly distributed over the long length of the fibre.

Materials-Inconel 625

2.3 Superalloys

Superalloys are usually used in high temperature applications. They are specifically developed to retain high mechanical strength and high resistance against surface degradation at temperatures up to ~85% of their melting points [27]. The need for the superalloys started in 1940s from the frequent material failure encountered in gas turbine engines [12, 28]. The choice of high turbine entry temperature (TET) (i.e. the temperature of the turbine hot inlet gases) is the dominant factor in determining engine performance since the inside temperature falls as mechanical work is extracted from the inlet gas stream. Consequently, there was a drive to develop special materials that retain their high mechanical strength at elevated temperature in excess of 540^{o}C.

Superalloys are of three types which are nickel-iron, nickel- and cobalt–base alloys [29, 30]. A common but special feature of these alloys is the γ face-centred-cubic (FCC) crystal structure of their matrix phases [31]. They are strengthened by at least one of the following strengthening mechanisms.

- Solid solution strengthening
- Precipitation hardening
- Carbides precipitates

2.3.1 Ni-based superalloys

Ni-based superalloys usually contain more than ten alloying elements with Ni being the primary constituent (at least 50% composition). The density, resistance to oxidation and corrosion, and the creep-rupture strength of these superalloys are determined by their

chemical compositions. Therefore, the superalloys have been developed with a variety of alloying additions to provide high resistance to a wide variety of corrosive environments. The major alloying elements in Ni-based superalloys are Cr (10-20%), Al and Ti (combined up to 8%), Mo, Co, Nb and W [12, 28]. The choice of nickel as the principal element is due to its following properties[28, 29]

- FCC crystal structure
- High toughness and ductility
- Moderate cost
- Low rates of thermally activated processes

Nickel-base superalloys can withstand loading at an operating temperature 'T_o' (1273K) closed to the nickel melting temperature 'T_m' (1718K) therefore having a homologous temperature 'τ' (see equation 2.1) of about 0.75[28]. A homologous temperature of above 0.6 makes the alloy suitable for high strength service at elevated temperature[28].

$$\tau = \frac{T_o}{T_m} \tag{2.1}$$

These alloys also possess substantial resistance to mechanical degradation over extended periods of time. They possess high fracture toughness, ultimate tensile strength (UTS) and yield strength at room temperature while their creep resistance and rupture strength at elevated temperature are considerably high [28, 29].

2.3.2 Inconel 625

The chemical composition and the properties of the alloy 625 are presented in Table 2.1 and Table 2.2 respectively.

Table 2.1: Chemical compositions of Inconel 625 (wt.%) [32]

Ni	Cr	Mo	Nb	Fe	C	Mn	Si	P	S	Al	Ti	Co
58.0 min	20.0-23.0	8.0-10.0	3.15-4.15	5.0 max	0.1 max	0.5 max	0.5 max	0.015 max	0.015 max	0.4 max	0.4 max	1.0 max

Table 2.2: Typical properties of Inconel 625 [33]

Property	Value
Density	8.44g/cm^3
Melting point	1350^{o}C
Coefficient of expansion	12.8μm/m.^{o}C (20-100^{o}C)
Modulus of rigidity	79KN/mm^2
Modulus of elasticity	205.8KN/mm^2

It is a non-magnetic nickel-chromium-molybdenum nickel-based superalloy strengthened mainly by solid solution hardening effect of the refractory metals, niobium and molybdenum in an austenitic FCC γ matrix. It is also precipitation hardenable due to the precipitation of fine metastable phase γ'' (Ni_3Nb) after annealing over a long period in the temperature range 550-580^{o}C [34, 35]. It is known for its high temperature strength and excellent corrosion resistance in a wide range of corrosive media, being especially resistant to crevice and pitting corrosion [36].

It maintains its mechanical strength and toughness in the temperature range cryogenic to 1093^{o}C. Chromium and nickel provide resistance in oxidising environments while molybdenum and nickel resist any form of non-oxidising corrosion [34, 35]. Chromium continuously passivates the external surface of the alloy by forming Cr_2O_3 which is the primary reason for resistance to corrosion. The presence of molybdenum (8-10%wt.) is good for resistance against crevice and pitting corrosion. Niobium stabilises the alloy against sensitisation during welding making it the choice for many diverse applications [34, 35]. The

alloy is highly resistant to chloride-stress corrosion cracking and oxidation at high temperature. The high ductility of Inconel 625 is responsible for its ability to withstand solidification and contraction after welding thereby reducing the possibility of cracking [37]. Inconel 625 alloy is a material of choice for gas turbine engine ducting, combustion liners, furnace hardware, spray bars and special seawater applications in aerospace, chemical, petrochemical and marine industries [35].

2.3.3 The metallurgy of Inconel 625

2.3.3.1 Dendritic γ phase

The solidification reaction of Inconel 625 usually begins with the formation of dendritic γ phase (FCC) which is notably enriched in nickel, chromium and Fe. As this is being formed, elements of high atomic mass such as niobium and molybdenum are segregated to the interdendritic region. Due to the enrichment of the interdendritic liquid in niobium, there is formation of niobium rich Laves phase and/or niobium carbide during the final stage of the solidification [38, 39].

2.3.3.2 Laves and NbC carbide formation

The formation of either nobium rich Laves phase or niobium carbide in the microstructure of Inconel 625 is largely influenced by the composition of the alloy. The solidification path and the resultant microstructure of alloy 718 have been clearly defined in a pseudo ternary equilibrium diagram shown in Figure 2.5 [38]. Inconel 625 alloy which is considered as a modification of Inconel 718 has nearly the same microstructure and is believed to follow similar solidification path. As shown in Figure 2.5, three different paths can be followed. Path 1 represents a high C/Nb ratios and leads to the formation of $\gamma + \mathrm{NbC}$ with no Laves phase. At intermediate C/NbC ratios, $\gamma + \mathrm{NbC}$ is first formed, followed by Laves phase formation at the end of the solidification. At low C/NbC ratios (i.e. path 3), $\gamma +$ Laves with no NbC is

formed. Path 3 microstructures, without NbC particles, are not common but have been in the solidification of Inconel 625 containing less than 0.01% C [38].

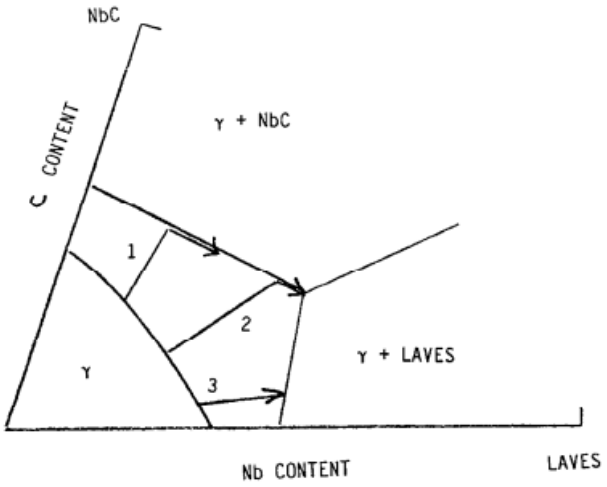

Figure 2.5: An extract from the pseudo-equilibrium diagram for Alloy 718 showing the formation of Laves phase during solidification [38]

Laves phases are hexagonal close packed, of irregular shapes and usually contain significant amount of other alloying or impurity elements [40]. Table 2.3 gives the compositions of Laves particles found in three different product forms of Inconel 625.

Table 2.3 Chemical compositions of Laves phase particles (at. %) from different Alloy 625 materials [38]

Element	Banded plate stock	Base plate heat treated 48hrs at 1600°F	6 inch GTA weldment
Ni	38	41	48
Cr	17	20	22
Mo	23	21	12
Nb	19	6	11
Fe	3	5	3
Si	6	6	4

Also, the carbides mostly appear as blocky and dendritic Chinese script morphology at the grain boundaries. Their compositions in various Alloy 625 weldments have been reported. These are presented in Table 2.4.

Table 2.4: Composition of NbC phase (wt. %) in different Alloy 625 materials [38]

Element	GTA welds		625 bar	Wrought 625 900°C/ 1 hr	Wrought 625 940°C/100 hr
	Blocky NbC	Dendritic NbC			
Ni	0.1-4.1	2.1-4.5	2.6	-	6.7
Cr	1.3-7.4	4.1-8.6	1.2	3.6	3.6
Mo	4.4-13.2	6.5-17.6	2.8	20.1	4.4
Nb	65.0-82.6	60.0-73.4	89.3	79.7	79.7
Fe	0-0.4	0.1-0.3	-	-	-
Ti	-	-	4.0	-	-

Other compositional effect on the microstructure of Inconel 625 has been observed. The formation of Laves has been observed to be promoted by increasing the Fe and Si. Therefore, lowering Fe and Si contents in Inconel 625 welding filler wire has been helpful to the ductility in weldments because the formation Laves phase is minimised [41]. There are no obvious benefits of the presence of Laves or NbC in the final microstructure of Inconel 625. Although carbides provide Alloy 625 limited strengthening by stabilizing the grain boundaries against shear. Nevertheless, it is important to control the evolution of the microstructure of so as to avoid the excessive or highly localised concentrations of these phases so as to promote the chemical stability of the alloy and improves its ductility [29].

2.3.3.3 Other precipitate phases during thermal exposures

A time-temperature-transformation (T-T-T) diagram for Inconel 625 is presented in Figure 2.6. It is shown that a number of different carbides and intermetallic compounds can precipitate in Inconel 625 after thermal exposures, for times on the order of 0.1 to 100 hours.

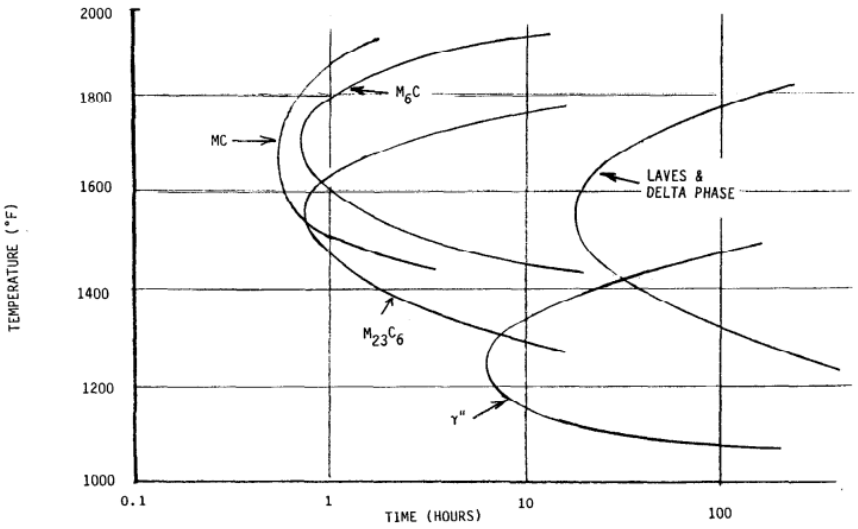

Figure 2.6: An approximate time-temperature-transformation diagram for phases forming at higher temperatures in Alloy 625 [38]

Beyond this time range, further changes may be observed. The crystal structures and typical compositions in atomic percent values of these phases are summarised in Table 2.5.

Table 2.5: Structures and typical compositions of the possible precipitate phases in Inconel 625 alloy during thermal exposures [38]

Phase	Structure	Typical composition
MC	Cubic, Fm3m	Matrix blocky MC $(Ti_{0.07}Cr_{0.04}Fe_{0.02}Ni_{0.09}Nb_{0.75}Ni_{0.03})C$ $(Ti_{0.53}Cr_{0.03}Ni_{0.04}Nb_{0.39}Mo_{0.01})C$ Globular MC $(Ti_{0.15}Cr_{0.04}Fe_{0.01}Ni_{0.08}Nb_{0.67}Mo_{0.01})C$
M_6C	Cubic, Fd3m	$(Cr_{0.21}Fe_{0.02}Ni_{0.37}Nb_{0.08}Mo_{0.24}Si_{0.08})_6C$
$M_{23}C_6$	Cubic, Fm3m	$(Cr_{0.85}Fe_{0.01}Ni_{0.07}Mo_{0.07})_{23}C_6$
γ"	Ordered tetragonal, 14/mmm	$Ni_3(Nb_{>0.5}Ti_{<0.5}Al_{<0.5})$
δ	Orthogonal, Pmmm	Ni_3Nb
Laves	Hexagonal, $P6_3mmc$	$(Cr_{0.31}Fe_{0.08}Ni_{0.41})_2(Si_{0.17}Ti_{0.01}Nb_{0.19}Mo_{0.63})$

The precipitation of MC, M_6C and $M_{23}C_6$ in the grain boundaries of Inconel 625 after heat treating depends upon the temperature [42]. At higher temperatures in the range of 1600-

1900^{o}F, the carbides are both NbC as thin grain boundary films and M_6C. In this case, M is Ni, Cr and Mo. Between 1300-1600^{o}F, the grain boundary carbides are mainly $M_{23}C_6$ where M is almost entirely Cr. All the three grain boundary carbides can be bound below the intermediate temperature range. The M_6C and $M_{23}C_6$ carbides commonly have blocky, irregular shapes and form as series of separate, discrete grain boundary particles [38].

As shown in T-T-T diagram in Figure 2.6, prolonged thermal exposure (beyond 48 hrs) of the alloy in the temperature range 1300-1800^{o}F, both Laves and Delta phase starts precipitating. The precipitation of these phases begins in the grain boundaries which already contain carbide particles. The Laves which is similar in morphology to M_6C and $M_{23}C_6$ carbides are difficult to identity however, the Delta can be easily recognised because of its acicular morphology. Just like Laves particles, Delta is also detrimental to the mechanical properties of Alloy 625 [28, 38].

The precipitation of γ" is the dominating reaction in the temperature range 1100-1400^{o}F. Unlike Inconel 718, the precipitation of γ" phase in Inconel 625 alloy may not be expected because it is not originally developed as a precipitation hardened alloy. However, with sufficient Nb + Ti + Al in its composition, significant γ" phase precipitation can occur [38]. The γ" is an ordered tetragonal structure that is usually described chemically as Ni3(Nb > 0.05, Ti > 0.5, Al < 0.5). It typically precipitates as reasonably uniformly distributed plate or disc shaped particles. With increasing the time and temperature of the heat treatment, γ" will increase in length from approximately 0.01 to 0.1 μm [40].

2.3.4 Weldability of Inconel 625 alloy

The term weldability refers to the ability of a material to avoid metallurgical degradation (usually assessed by its susceptibility to cracking during welding or post heat treatment) and

its ability, after being welded, to perform in its intended service environment. Cracking of welded construction is a major problem limiting welding of materials during fabrication. The occurrence of cracking can be traced to two factors namely, (1) the presence of tensile stress and (2) a susceptible microstructure in the weld metal or heat affected zone (HAZ) [43]. Since it is difficult to eliminate or control the stresses during welding, cracking susceptibility is reduced by controlling the weldment microstructure.

During welding of nickel-based alloys (including Inconel 625) and fully austenitic stainless steels, four types of weld cracking mechanism has been observed. These are weld solidification cracking, HAZ liquation cracking, ductility dip cracking and strain-age cracking [43].

2.3.4.1 Weld solidification cracking

It is a form of hot cracking which occurs during the final stages of solidification when tensile shrinkage stress accumulates and the liquid film still persists along the solidification grain boundaries in the welded structure. Cracking will occur whenever the imposed shrinkage strain exceeds the inherent ductility of the solidifying weld metal. This usually occurs in the fusion zone. The propensity for this type of weld cracking can be reduced to welding under a low restraint and reduce the temperature range over which the welding is done [43]. A solidification crack in Inconel 625 weld overlay is shown in Figure 2.7.

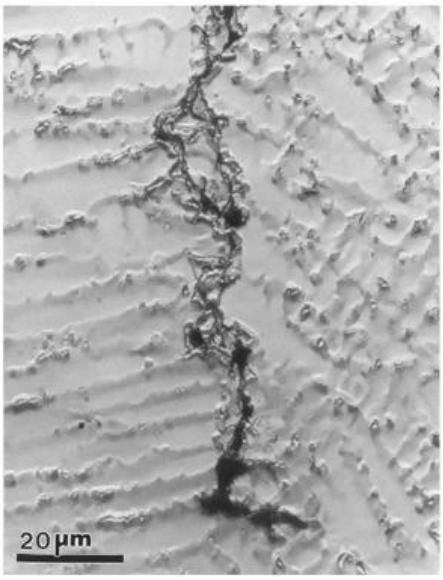

Figure 2.7: A picture of solidification crack in Inconel 625 weld overlay [41].

2.3.4.2 HAZ liquation cracking

It is another type of high-temperature weld cracking that occurs in the HAZ adjacent to the fusion boundary. The cracking is due to the presence and persistence of liquid films at grain boundaries and the inability of these films to accommodate the thermally and/or mechanical induced strain experienced during weld cooling. Although the precise mechanism of this type of weld cracking are not well understood, the simultaneous presence of a crack susceptibility microstructure and a high level restraint are known to promote cracking tendency [44]. Therefore, reduction in HAZ liquation cracking susceptibility can be achieved by adjusting the composition and microstructure of the weld metal.

2.3.4.3 Ductility–dip cracking

Ductility–dip cracking (DDC) refers to elevated temperature, solid-state cracking that occurs as a result of a sharp drop in ductility at temperatures above approximately half the melting temperature of the material [43]. This type of cracking is found in the re-heated weld metal or in the heat affected zone and fusion zone of highly restrained weldments. It is usually in connection with single phase austenitic alloys with large grain size and is intergranular in

nature. DDC can be found in Ni-base weld metal at a temperature of about 800^{o}C [45]. It always occurs along the migrated grain boundaries, for example, as shown in Figure 2.8. Migrated grain boundaries (MGBs) are crystallographic, high angle boundaries that have migrated away from their parent solidification grain boundaries during cooling below the solidification temperature range and/or during reheating in multipass welds.

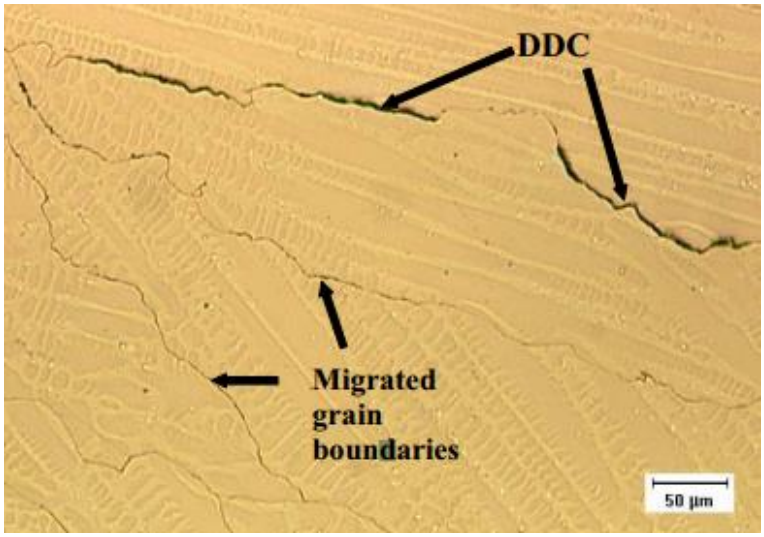

Figure 2.8: Ductility-dip cracking along migrated grain boundaries in fully austenitic weld metal [43].

DDC in Ni-base alloys depends largely on the grain size, grain boundary character and precipitation behaviour. Weld metals having large grain size with straight MGBs and few grain boundary precipitates is more prone to DDC. However, higher amount of precipitates or second phases form at elevated temperatures within the parent solidification grain boundaries will reduce susceptibility to DDC. This is due to grain boundary locking effect which resists sliding at the grain boundaries. In Ni-base filler metals, impurity segregation to MGBs and addition of hydrogen to shielding gas increase susceptibility to DDC [43, 45].

2.3.4.4 Strain-age cracking

Strain-age cracking (SAC) is a problem that usually occurs during post-weld heat treatment of Ni–base alloys that are strengthened by precipitation of γ'. The susceptibility of these alloys to SAC is related to the precipitation of γ' (Ni_3(Ti, Al)) [46]. The higher the amount of Ti + Al content (γ' forming elements), the more the alloys are prone to SAC. This is due to the fact that the precipitation of γ' reduces the ductility of the alloys to a very low level and cracking can occur if they are subjected to a level of strain that exceeds the available ductility. With a high level of restraint during welding, tensile stress is developed as a result of the volume contraction that is associated with the formation of γ' from solid solution along the grain boundaries. This problem is heightened by a coarse grain size, the presence of an oxidising atmosphere and constitutional liquation of carbides, which can further reduce ductility. Consequently, cracking will occur in the weldments because of the stress concentration along the grain boundaries in the HAZs [47].

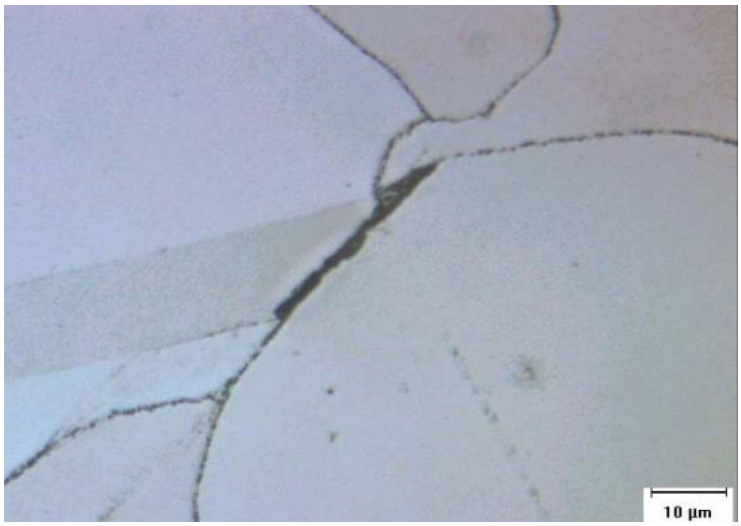

Figure 2.9: An optical micrograph of strain-age crack in Waspaloy [43]

Also, SAC can occur in the unaffected base metal in addition to the weld metal and HAZs [46]. Figure 2.9 shows a strain-age crack in Waspaloy (a Ni-base superalloy). However, Inconel 625 and 718 are not prone to SAC because of the lower content of Ti + Al (< 6%) in

their composition. The relative weldability Ni-base alloys as a function of their Ti + Al composition is presented in the map shown in Figure 2.10.

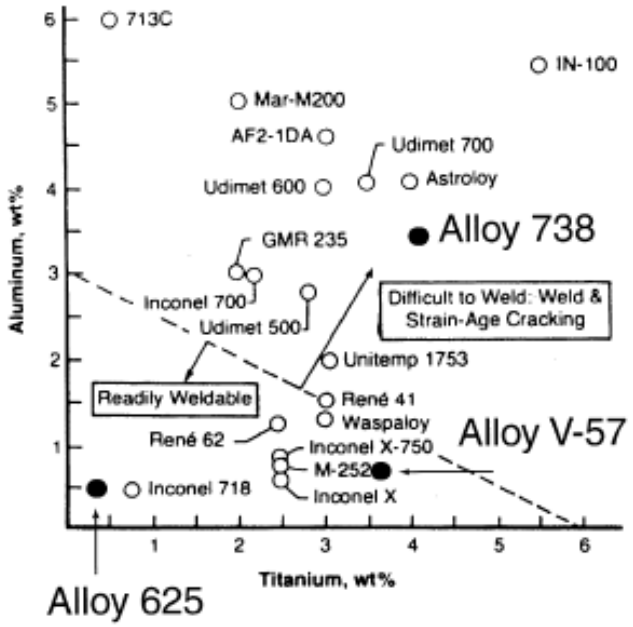

Figure 2.10: Relative weldability of various superalloys [47]

Coating technology

2.4 Surface engineering techniques

The surface properties of engineering materials have significant effects on the functionality and lifetime of a component, therefore, its importance in materials is paramount. Surface modification (i.e. surface engineering) of components is increasingly gaining attention in the manufacturing industry. Surface engineering refers to a wide range of technologies designed to modify the surface properties of metallic and non-metallic components for specific and sometimes unique engineering purposes. The role of surface engineering in the manufacturing of engineering components or products such as engine valves, petroleum pipes, etc is illustrated in Figure 2.11.

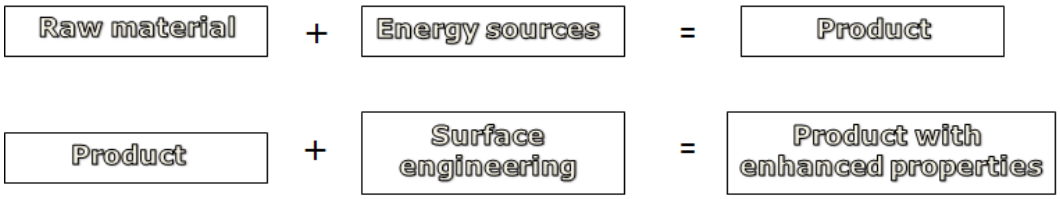

Figure 2.11: Role of surface engineering in the manufacturing of engineering components [48]

Modification of the surface properties of components can be achieved using a number of processes. Some processes involve the modification of the pre-existing surface without a change in composition whereas others involve the alteration of the composition of the pre-existing surface. There are also some processes which involve the deposition of a new material on the pre-existing surface. This is generally termed as coating deposition [32]. Depending on the technique used, surface modification can change the initial dimensions of the substrate component. On this basis, surface modification techniques can be grouped as subtractive (decreasing the dimension, e.g. machining), non-subtractive (no change in

dimension, e.g. ion implantation), or additive (increasing the dimensions such as laser cladding) [32, 48]. Figure 2.12 illustrates this classification of surface engineering techniques.

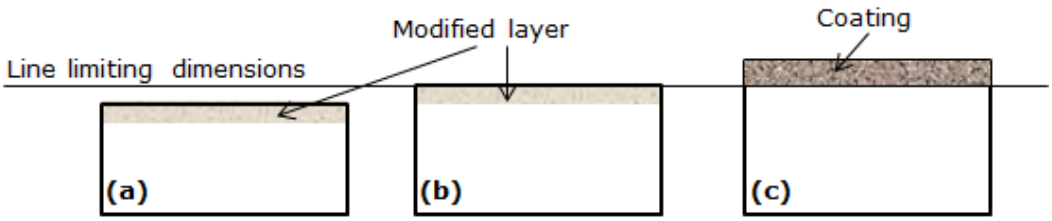

Figure 2.12: Different methods of obtaining modified superfacial layers, (a) subtractive, (b) non-subtractive and (c) additive or coating deposition [48].

2.4.1 Coating deposition

Application of coatings to engineering components can be achieved by any of the following surface engineering techniques;

- Thermal spraying
- Weld overlays
- Plasma and thermal spray
- Friction surfacing
- Chemical vapour deposition
- Physical vapour deposition
- Ion implantation
- Electroplating, and now
- Laser cladding

2.4.2 Laser cladding

Laser cladding has shown that high quality, distortion free clad layers, and even thick layers, can be deposited successfully on base materials (i.e. substrate) for enhanced surface performance [49]. The technique was first introduced to industrial applications in the 1970s for cladding valves and valve seats [14]. One of the earliest production applications was in

the Japanese car industry, where cladding the valve seats of aluminium alloy engines improved their wear properties while keeping the manufacturing cost in check. In this process, laser (heat source) is used to create a melt pool by simultaneously melting an additive material and a thin layer of a substrate. The relative movement of the heat source and the substrate forms a clad bead (or track). Figure 2.13 shows a schematic of a laser cladding process using powder as the feedstock. On the other hand, the feedstock material can be in a wire form.

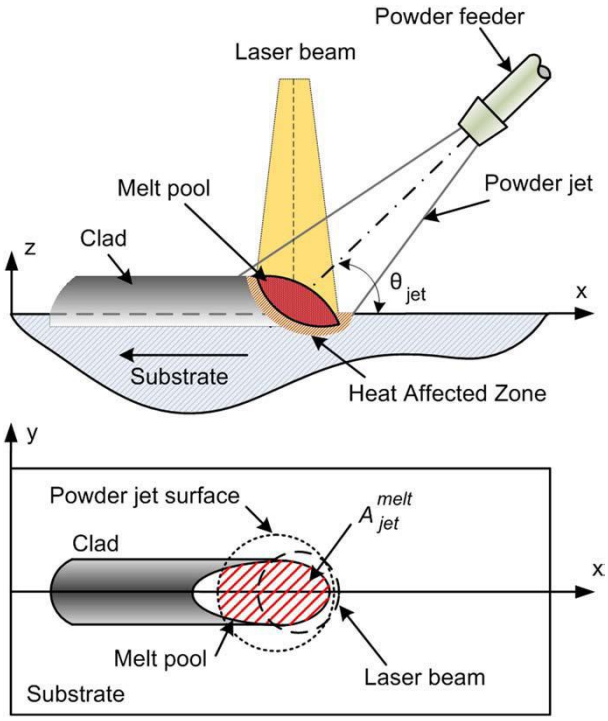

Figure 2.13: A schematic of laser cladding process with powder injection [50]

Laser cladding has found applications for rapid manufacture, repair and surface modification of metallic components especially those with complex geometries [1, 50, 51]. Compared to other coating deposition techniques, laser cladding can potentially offer a number of advantages. These include strong metallurgical bond at the clad-substrate interface [52, 53], minimal distortion of the substrate when compared with arc welds [3, 54], low substrate dilution [4], minimal porosity [5, 55] and controllable heat input often producing a small

heat affected zone (HAZ) and greater processing flexibility [56, 57]. All these are as a result of controllable low thermal input, high solidification rate of the process and focusability of the laser beam to a specific local area [58].

Usually, the substrate (i.e. the metallic component, often made of a cheaper material compared to the coating or additive material) is held by a special fixture attached to a CNC table (especially for small to medium components) while the laser beam is fixed and directed towards the substrate. The CNC table can be moved in the x, y and z directions and/or rotated depending on the process requirements and component geometry. For large components and/or laser cladding using robotics, the substrate is generally fixed at a position while the laser beam position varies. In order to prevent oxide formation, laser cladding process is performed in an oxygen-free environment. Accordingly, laser coating is deposited in a closed chamber usually filled with argon or helium gas. This technique is also called Laser Aided Rapid Manufacturing (LARM) or Laser Engineering Net Shaping (LENS) or Direct Light Fabrication (DLF) when it is applied in building metallic components [34].

Laser cladding processes can also be used to deposit hybrid materials making it more suitable for some specialised applications. Currently, laser cladding of metal matrix composite coatings has been established as an effective surface engineering technique for improving the surface performance of metallic components operating in environments that are inherently corrosive and abrasive [17]. Depending on the nature of the feedstock material utilised, laser cladding techniques can be broadly classified into two namely laser cladding with powder and laser cladding with wire.

2.4.2.1 Laser cladding with powder

There are three powder feeding systems in laser cladding technique. They are:

- Pre-placed powder

- Lateral or side feeding of powder
- Co-axial feeding of powder

Pre-placing powder feeding system: This type of material feeding system automatically makes laser cladding a two-stage process. With this method, additive material in powder is preplaced on the substrate as a powder bed or plasma spray coat before laser beam transfers its energy to the powdered metal and liquefies it. The second stage is the heat transfer of the liquid coating to the substrate. Compared with lateral side feeding and coaxially feeding of powder, this method of powder deposition for laser cladding is fading out because of its shortcomings. Apart from the fact that it is time consuming because of the multiple stages involved, it is difficult to pre-place powder on a complex geometrical shape [59]. Also, it is limited in its flexibility to produce an optimized clad quality due to the fact that it is difficult to vary the powder feeding in this laser cladding process [60].

Lateral powder feeding technique: This involves setting a powder nozzle at an appropriate angle and depositing the powder directly into the melt pool created by laser beam as shown in Figure 2.13. Unlike pre-placed powder feeding, this method gives a higher cladding efficiency, larger processing window and it is suitable for complex geometrical shapes applications [18, 60].

The effect of feeding direction is very significant in laser cladding with lateral powder feeding system. Syed et al [61] reveals that front feeding, as described in Figure 2.14a, with LDL 160-1500 diode laser gave higher powder catchment efficiency of about 20–45% when compared to rear feeding orientation shown in Figure 2.14b. As shown in Figure 2.14b, the meltpool is partly shielded from the incoming powder stream by the solidifying track. This was reported to have caused the reduction in powder catchment efficiency for rear feeding of powder during laser cladding.

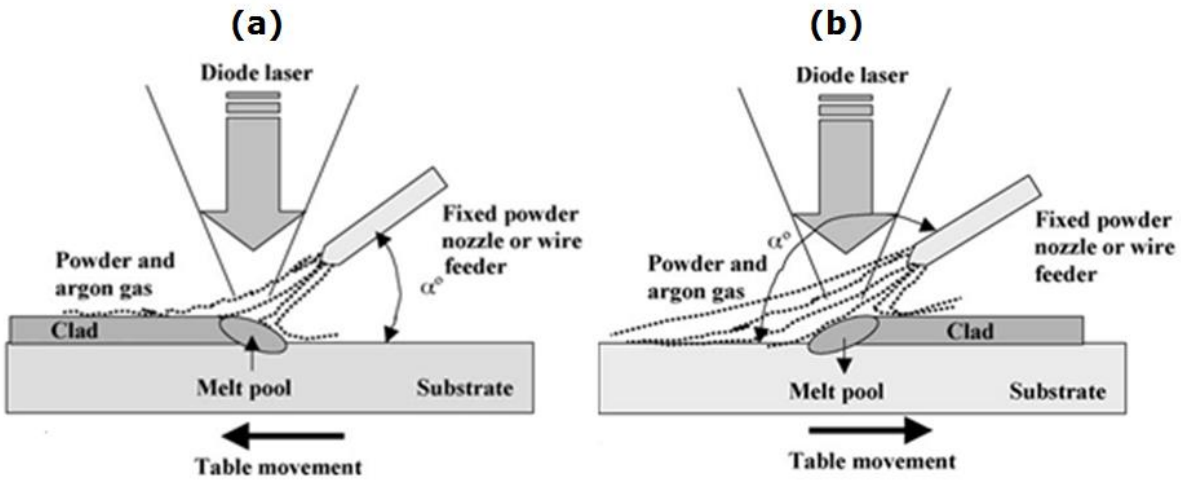

Figure 2.14: A schematic diagram for powder feeding orientation (a) front feeding (b) rear feeding [61]

Coaxial powder feeding: Laser cladding with coaxial powder feeding system is sometimes preferred over the lateral powder feeding system because of its flexibility in deposition of materials and use of multidirectional feeding process [62]. For laser cladding with coaxial powder feeding, a cladding head like the one shown in Figure 2.15 is required to guide and focus both the laser beam and the powder jet simultaneously on the surface of the work piece resulting in homogeneous powder distribution in the meltpool. This is one of the most important criteria for achieving a good clad quality. The set-up is very suitable for online monitoring and control of the metal deposition process because different sensors and optical devices can be easily integrated to the cladding head [62], for example, as shown in Figure 2.15. Consequently, co-axial laser cladding is utilised for building metallic parts from 3D designs thus increasing the scope of industrial application of laser cladding in the global manufacturing industry [60, 62]. In the set up shown in Fig 2.15, the shielding gas performs two functions. Firstly, it blows the powder through a coaxial nozzle surrounding the laser heat source and secondly, it envelopes the entire cladding process from the atmosphere thus preventing the formation of oxides.

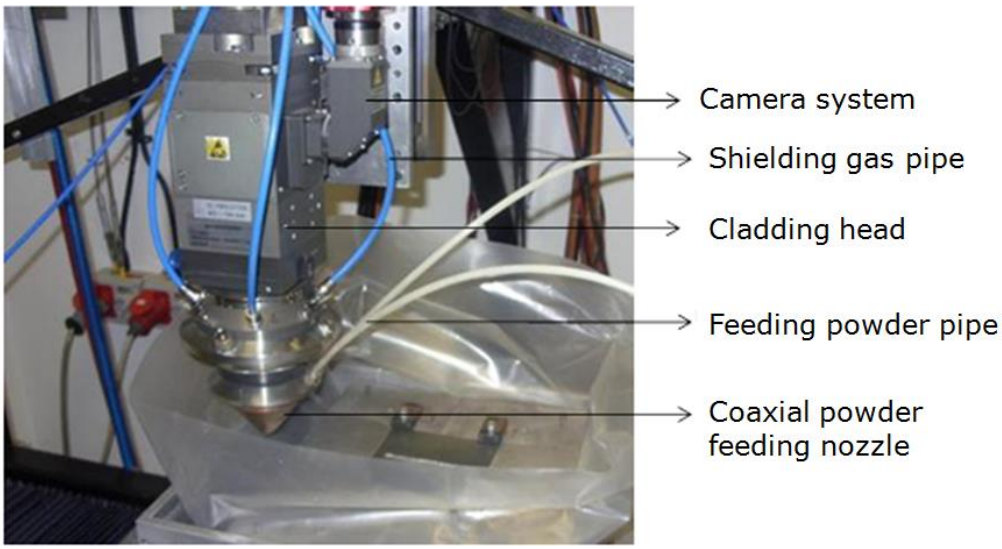

Figure 2.15: A picture of laser cladding with coaxial cladding head

2.4.2.2 Laser cladding with wire

This method is similar to lateral or side feeding powder delivery systems except that wire is fed into the meltpool in this case. Laser cladding by wire delivery is increasingly becoming popular and useful due to its advantages over powder feeding systems [63]. The advantages include increased material usage efficiency [64], improved surface quality of the deposit [61], lower cost of preparing the wire materials [64] and excellent material deposition rate [65]. However, laser cladding by wire delivery is highly sensitive to changes in processing condition. As a result, it is important to establish a balance of several impacting processing parameters such as wire tip position in the meltpool, feed angle, feed direction, laser spot size, laser power (P), wire feed rate (WFR) and traverse speed (V) before a stable deposition process, hence, a good quality track can be achieved.

In wire feeding systems, the choice of the feeding angle, feeding direction and positioning of the wire tip relative to the meltpool largely influence the quality of the clad and stability of the process [64, 66, 67]. Comparing the front and rear feeding directions, it was established that the front feeding direction produced better surface roughness and higher clad quality

because little or no disturbance of the meltpool occurred as the table moved away from the feeding nozzle [67]. However, the perturbation of the meltpool in the case of rear feeding resulted in the deposition of clad of relatively higher surface roughness. Syed et al. [67] found that diode laser cladding with rear feeding orientation produced undulations called serrations on all clad surfaces for all wire positions and feeding angles whereas with the front orientation no serration was observed for all feeding angles. The undulations shown in Figure 2.16 resemble periodic cuts across the track (clad).

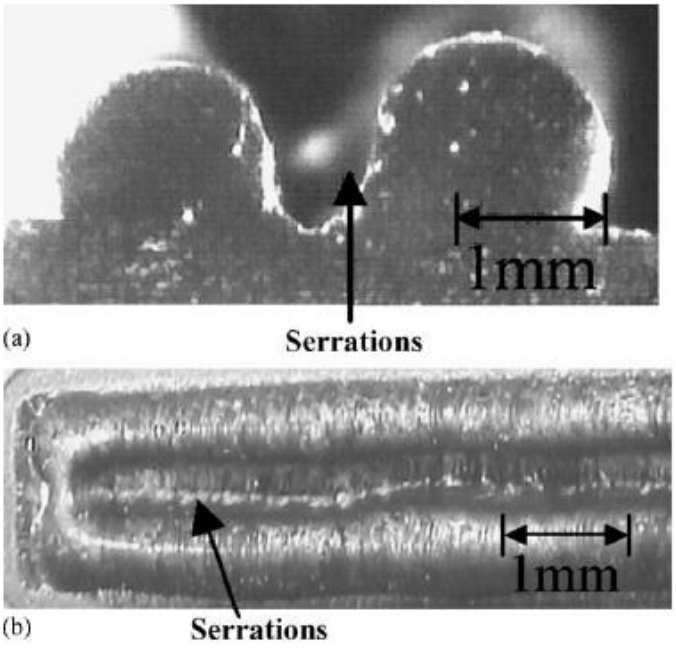

Figure 2.16: A picture showing serrations on a single track, rear fed diode laser cladding of 316L stainless steel with wire placement at the leading edge (a) sectioned view (b) top view [67]

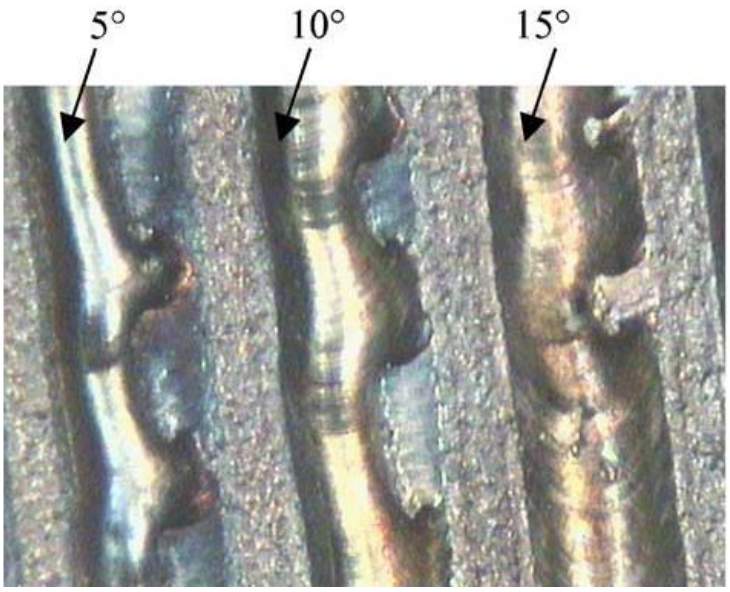

Figure 2.17: Irregular shaped beads deposited at low wire feeding angles [61]

Feed angle is critical for laser cladding with wire. When the feed angle (i.e. angle between the wire nozzle and the table) is below 20^{o}, tracks with an irregular shape are produced, for example, as shown in Figure 2.17. Experimental work had found a range of $20\text{-}60^{o}$ as feed angle that can produce continuous track of uniform height [61]. Mok et al. [68] established that a feed angle of 45^{o} for a diode laser metal deposition of Ti-6Al-4V with front feeding orientation produced the highest wire deposition volume.

Three wire tip positions (i.e. the center, leading and trailing edges) in the meltpool have been identified [67]. The leading edge of the meltpool was found to produce the most stable deposition process and excellent clad (i.e. continuous track) quality during diode laser cladding with stainless steel 316 wire of Ø0.8 mm [67]. With this position and wire size, the feed wire interacted briefly with the laser beam outside the meltpool. Therefore, the melt pool heat was the main energy source that melted the wire. Discontinuous tracks were obtained when the wire tip pointed to the trailing edge of the meltpool.

Conversely, for laser cladding with stainless steel 308L wire (Ø 1.2 mm), wire tip pointing at the centre of the meltpool gave continuous tracks of uniform height [26]. A fibre laser of about 3.6 mm beam diameter was used. Due to the larger size of the wire (Ø 1.2 mm), aiming the wire tip at the meltpool centre allowed the feed wire to interact longer with the laser beam therefore gaining more heat energy. As a result, the wire melted at the point of its intersection with the meltpool resulting in a smooth wire transfer.

Heralic et al. [65] reported that wire can be deposited in three ways which are: by droplet-like transfer, smooth transfer or by plunging. Only smooth wire transfer gives a stable laser deposition processes but it requires rather careful adjustment of the wire feeder and the process parameters such that the wire is melted close to the intersection with the melt pool. This ensures a smooth metal transfer from solid wire to liquid metal. Another parameter significant to achieving a high quality clad profile and component with appropriate metallurgical properties is the wire protrusion distance from the feeding nozzle. This must be carefully selected for a particular set-up.

In general, both powder and wire cladding processes can produce high surface quality and defect-free clad beads at optimised cladding conditions. The optimised cladding conditions for each material system differs. Compared with the laser cladding with wire, higher surface roughness value (R_a) is found in powder cladding deposits. This can be attributed to some of the powder particles sticking to the solidified clad surfaces.

2.4.3 Laser cladding of metal matrix composite coating

Metal matrix composite (MMC) coating of metallic components has made significant progress, as a result of its potential applications in industries. For example, the current challenge in the oil and gas industry is to manufacture low cost metallic components that can reduce incessant equipment failure usually caused by the combination of erosive and

abrasive-wear, and corrosive environment [69]. Hardfacing stainless steel components such as oil-drill bits, drilling cones, etc. with MMC is currently utilised as solution to this challenge.

MMC coatings can withstand high tensile and compressive stresses depending on how the applied load is transferred from the ductile matrix to the reinforcement phase. Deuis et al. [70] reported that the transfer of load is possible due to the bond between the particulate reinforcement and the matrix metal. However, the nature of the interfacial bond between the ductile matrix and the reinforcement particulate depends on the processing route (i.e. the processing time and temperature) and the matrix composition.

Over the years, a spectrum of processing techniques has evolved in an attempt to optimise the microstructure and surface properties of the composite coatings. The most commonly used processing techniques for depositing MMC on ferrous and non-ferrous substrates are thermal spraying, arc welding and laser cladding [70]. Due to its advantages over other techniques, as previously mentioned in section 2.4.2, laser cladding has been widely utilised [71]. Laser cladding has the potential to produce MMC coatings with minimal porosity, strong metallurgical clad-substrate bonding and absence of splat structures. Generally, the rapid solidification and high cooling rate which characterise the technique promotes homogeneity of the microstructure. This reduces the chances of forming intermetallic phases in the composite coating hence, improving their corrosion performance. On the other hand, high cooling rate creates stresses thus increasing cracking sensitivity in laser cladding process [50, 72, 73]. The cracking tendency can be reduced by improving the toughness of the matrix which is often achieved by a good choice of highly ductile metal alloy.

Aluminium and its alloys are commonly used as matrix material for MMC coatings and they are mostly used with SiC or Al_2O_3 in discontinuous reinforcement particulate [74]. In

aerospace industry especially gas-turbine aero-engine components, titanium alloys (α, β and metastable β alloys) are widely used as a matrix alloy because of their high tensile strength-to-weight ratio as well as high strength retention at elevated temperatures (600-800^{o}C) [75]. Ni-based alloys reinforced with WC reinforcement particulate are increasingly being applied for many industrial components in petrochemical industry, aerospace and offshore applications to provide long-time protection against wear and corrosion [17]. Ni-based alloys are generally known for high oxidation and corrosion resistance. More importantly, Inconel 625, a Ni-Cr-Mo alloy, has a better combination of favourable properties including high temperature strength, high ductility and superior resistance to oxidation and corrosion.

Just like the laser cladding of single metal, a high energy laser beam is used to melt a thin layer of the substrate as the ceramic and metal (which could be in powder or wire form) are simultaneously injected into the meltpool. A composite track is formed as the substrate moves relative to the laser source or vice versa. The metal which has lower melting point is melted first and then envelops the ceramic phase with high melting point.

2.4.3.1 Feeding methods in metal matrix composite laser cladding

The current of methods of feeding the ceramic particles and the matrix metal during laser cladding of MMC are:

- Pre-placing a mixture of the ceramic particles and the matrix metal powder on the substrate
- Lateral feeding of pre-blended powders of the ceramic particles and the matrix metal
- Coaxial feeding of pre-blended powders of the ceramic particles and the matrix metal

Ceramic particles have been mixed with matrix metal powder in different proportions. For example, 80 wt. % Ni60A powder and 20 wt. % WC particles were pre-blended and laterally fed for microstructural investigation of Ni-based WC composite coatings by laser induction

hybrid rapid cladding [19]. The microstructure and wear behaviour of laser clad composite coatings have been studied by pre-placing a mixture of 50 vol.% Ni based alloy powder (Ni35) and 50 vol.% nickel-clad WC powder (WC-Ni, 15-wt.% Ni and balance WC) on the substrate via powder flame gun [76]. Coaxial feeding of pre-mixed powders of WC and Ni-based matrix with a volume fraction of 50% were utilised for the development and characterisation of composite Ni-Cr + WC laser cladding [77]. In the past, compositionally graded materials but not MMC coatings had been fabricated via coincident wire and powder laser deposition set-up. Wang et al. [78] demonstrated that the production of functionally graded materials is successful by simultaneously and laterally feeding Ti–25V–15Cr–2Al–0.2C powder and a Ti–6Al–4V wire. Concurrent nickel wire and copper powder laser deposition on H13 tool steel using 1.5 kW diode laser power source has also been investigated [79]. The composition gradients within a layer and overall track properties were controlled by sequentially varying the feed rates of copper powder and nickel wire.

2.4.4 Defects in laser cladding

Clad-ability is defined as the formation of a continuous, high density deposit with a uniform or homogenous microstructure, possessing a strong metallurgical bond to the substrate but with low dilution [59]. Any deviation from this definition could be considered as a defect in laser clad coating. Defects limit the performance efficiency and lifespan of laser fabricated parts in service. Optimising the cladding parameters for the laser deposition process usually reduces the number of defects if not eliminating completely the defects in laser deposited layer. Therefore, searching for optimal laser cladding parameters which minimise amount of defects is always a key issue.

Typical imperfections occurring in laser clad coatings can be divided into two major groups namely: geometrical and microstructural defects [80]. Geometrical defects include:

- Irregular track height or discontinuous track
- Swollen track due to too high contact angle with the substrate
- Deeper melted depth into substrate which can cause high dilution ratio
- Serrations (in case of wire feeding)

Microstructural defects are:

- Lack of fusion
- Porosity
- Crack

2.4.4.1 Geometrical defects in laser cladding

As shown in Figure 2.18, the geometry of laser track is defined by its height (H), width (W), melted depth into substrate (h) and contact angle (β) with the substrate.

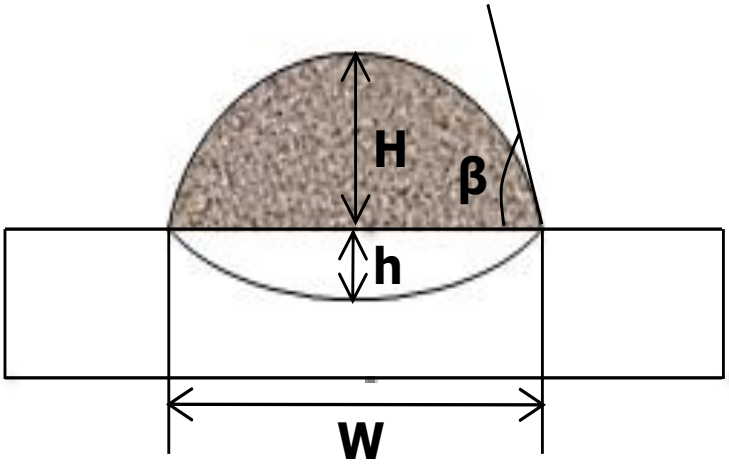

Figure 2.18: A typical laser track geometry

The melted depth into substrate is positively affected by the amount of energy available to melt both the substrate and the additive material. The energy increased with increasing the laser power and/or decreasing the traverse speed. The material feed rate also affects the melted depth into the substrate. The higher the material feed rate, the lower the depth (h). If

the melt depth into the substrate is excessively high, it becomes a defect because it indicates high substrate dilution. Generally, dilution is the percentage of the total volume of the substrate material in the track contributed by melting of the substrate. High dilution is not always wanted in a quality laser track. It must be kept to a minimum (5-8%) [81] in order to preserve the initial properties of the laser track [4, 81, 82]. Dilution increases with increasing the laser energy input but decreased with increasing the material deposition rate.

In the case of wire feeding, the position of the wire in the meltpool and the feed angle play key roles on the geometry of the track. Too low feed angle and positioning the wire tip in the trailing end of the meltpool result in discontinuous or irregular shaped tracks. This had been earlier explained in section 2.4.2.2. An ideal track/clad is defined as one with contact (or wetting) angle less than 90^{o}. Swollen track (i.e. track with contact angle more than 90^{o}), as shown in Figure 2.19, is not desirable therefore; it is a defect in laser cladding. Single track with swollen flank usually produces overlapped (i.e. multiple tracks) with inter-run porosity [60]. Inter-run porosity is detrimental to mechanical performance and corrosion behaviour of the tracks.

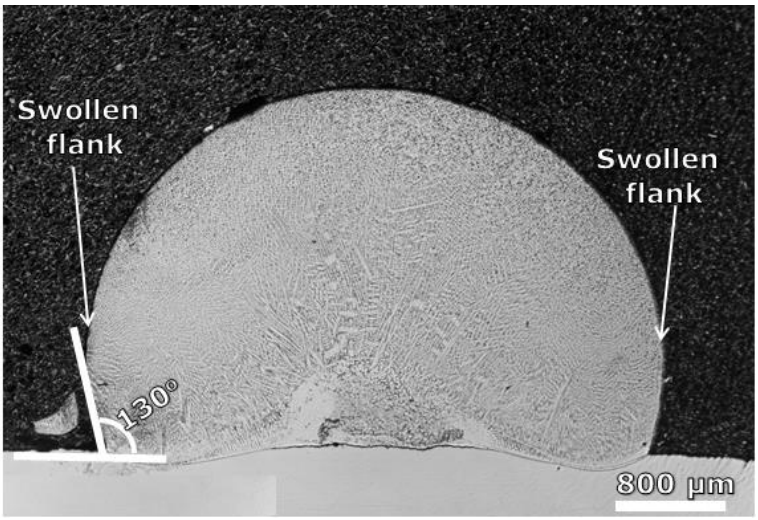

Figure 2.19: Clad cross-section with swollen flank and obtuse contact angle.

2.4.4.2 Microstructural defects in laser cladding

Poor fusion at the track-substrate interface is mainly due to insufficient melting of the substrate. Insufficient energy for a given material deposition rate and excessively high material deposition rates for a given laser energy are main causes of this defect in laser cladding [83]. In wire fed tracks, the position of wire tip relative to the size of the feed wire is another factor to be considered for depositing track with excellent bonding at the substrate [80].

Porosity is a serious problem that has been identified in laser cladding. This, depending on the causes, can be grouped into three. Inter-run porosity is caused by the horizontally aligned or offset tracks of incompatible aspect ratios (or undesirable contact angles) and forms near the base of deposited tracks [84]. Inter-layer lack of fusion porosity is caused by incomplete bonding between adjacent tracks. The third is intra-layer porosity. It is often spherical and exists within the track area. Its cause is thought to be related to gas dissolved or entrapped within the meltpool [84]. Generally, the causes of porosity include inconsistent specific energy, misplaced tracks, an oxide layer preventing or hindering fusion, and initial porosity in the powder.

Microstructure

2.5 Microstructure of coatings

Generally, the type and size of solidification structure observed in the microstructure of coatings is largely affected by the solidification conditions. The solidification conditions are affected by the processing parameters. In this work, the evolution of the microstructure of the coatings is particularly relevant therefore, the change in the solidification mode of the coatings as the solidification conditions vary is discussed in detail.

2.5.1 Solidification mode

According to Zhou et al. [19] and Kou [85], the temperature gradient (G, K. m^{-1}) and solidification growth rate (R, $m.s^{-1}$) determine the microstructure of solid parts formed through heating and solidification processes. The ratio G/R influences the mode of solidification while the product of G and R (i.e. GR) governs the size of the structure or grain formed. The temperature gradient principally depends on the temperature difference that occurs during the heating process while solidification growth rate mainly depends on the traverse speed (V) and the angle θ between the solidification front normal and the traverse direction, as expressed in equation 2.2.

$$R = V\cos\theta \qquad (2.2)$$

According to Toyserkani et al. [86]and Zhou et al. [19], R varies throughout the process from zero at the bottom of the meltpool (where θ approaches 90^o) to a maximum at the coating surface (where θ approaches 0^o) (See Figure 2.20). Also, it is known that G is highest at the bottom of the meltpool where R is zero and decreases towards the surface. This indicates that the solidification conditions vary throughout the meltpool. In order to

understand how the processing parameters affect the microstructure that forms during the solidification of molten alloys, the theory of constitutional supercooling must be followed.

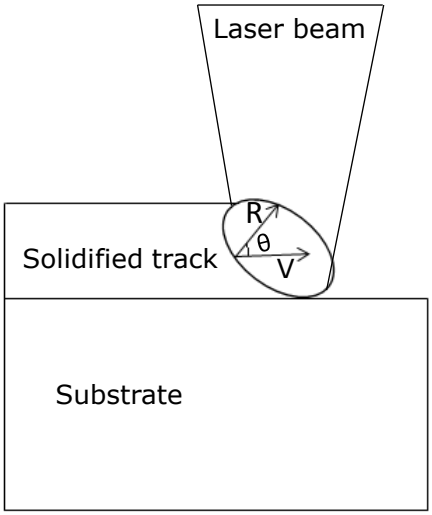

Figure 2.20: A diagram of angle relationship between the solidification front rate (R) and the traverse speed (V) [19].

2.5.2 Constitutional supercooling

There are four solidification modes namely planar, cellular, columnar dendrites and equiaxed dendrites, as described in Figure 2.21. During the solidification of a pure metal, the solidification mode at the solid/liquid (S/L) interface is usually planar except, a severe undercooling is observed. However, in the case of an alloy, the solidification mode at the S/L interface could be any of the four modes depending on the solidification condition and the material system involved [85].

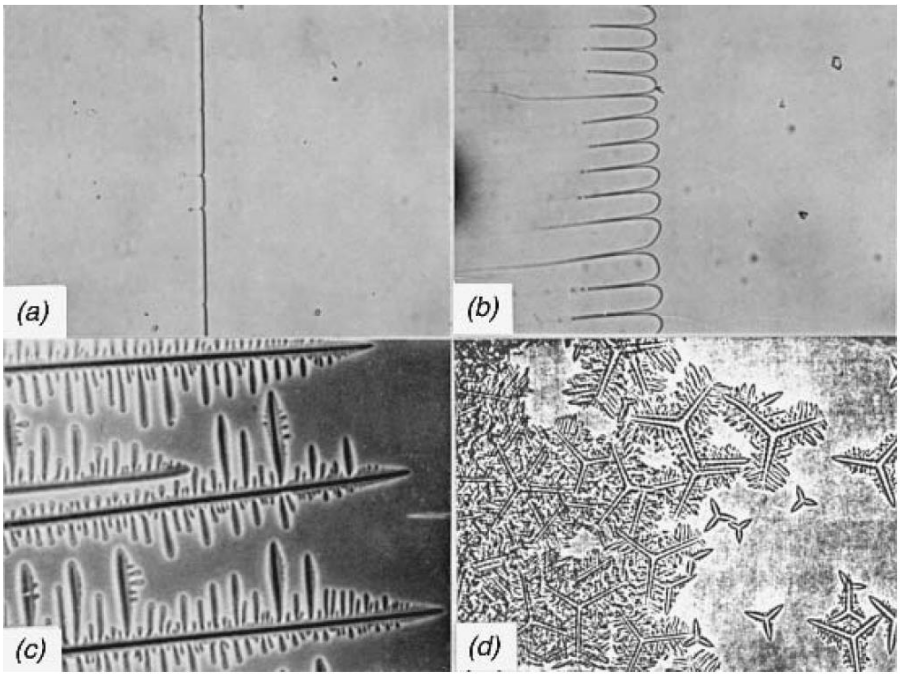

Figure 2.21: Basic solidification modes: (a) planar solidification (b) cellular solidification (c) columnar dendritic solidification (d) equiaxed dendritic solidification [85]

The binary phase diagram of an alloy C_o at a steady state with a planar S/L interface is shown in Figure 2.18. A boundary layer consisting of the liquid phase alone is thermodynamically stable only if its temperature is above the liquidus temperature. On the other hand, if its temperature is below the liquidus temperature, solid and liquid should coexist. The shaded area under the liquidus line in Figure 2.22a is the region where the actual liquid temperature is below the liquidus temperature (i.e. the region of constitutional supercooling). At this region, the liquid and solid coexist. As a result, the liquid planar S/L interface should breakdown to cellular or dendritic one so that the solid cell or dendrite can coexist with the intercellular or interdendritic liquid.

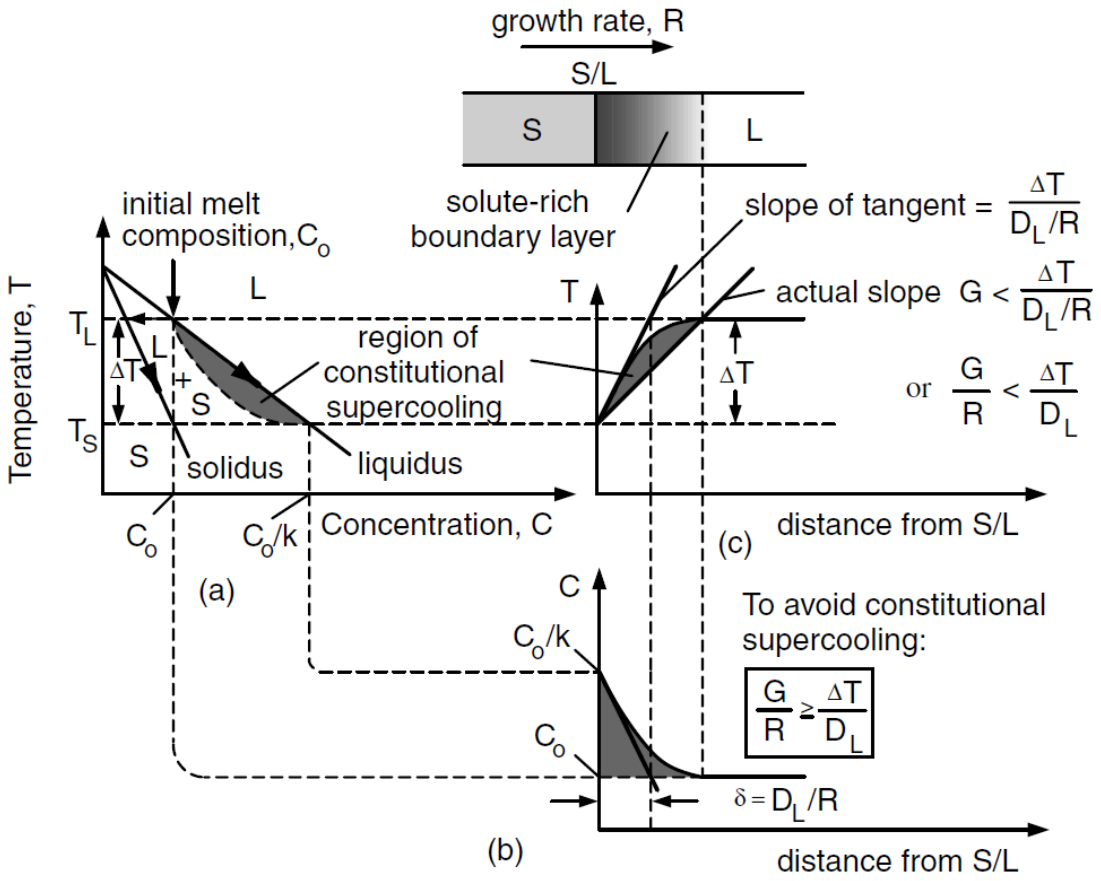

Figure 2.22: Constitutional supercooling: (a) phase diagram (b) composition profile in liquid (c) liquidus temperature profile in liquid [85].

As shown in the Figure 2.22, the temperature difference across the boundary layer is the equilibrium freezing range $\Delta T = T_L - T_S$. Also, the thickness of the boundary layer at the steady state is D_L/R where DL is diffusion coefficient of the alloy and R is the solidification growth rate. As such, the slope of the tangent to the liquidus temperature distribution at the S/L interface is $\Delta T/ (D_L/R)$ or $R\Delta T/D_L$ [85]. For the planar solidification mode to be stable at the interface, the temperature gradient G must be at least equal to $R\Delta T/D_L$. Therefore, the criterion stated in equation 2.3 must be met before a planar structure is stable at the S/L liquid interface.

$$\frac{G}{R} \geq \frac{\Delta T}{D_L} \qquad (2.3)$$

Now, the higher the temperature gradient and the lower the solidification growth rate, the easier for a planar S/L interfaces to be stable. However, if the solidification condition changes such that the degree of constitutional supercooling increases or ratio G/R decreases, the solidification mode can change to cellular or columnar dendrites or equiaxed dendrites. Figure 2.23 shows that the changes in solidification mode from planar to cellular, to columnar dendritic, and finally to equiaxed dendritic as the degree of constitutional supercooling continues to increase.

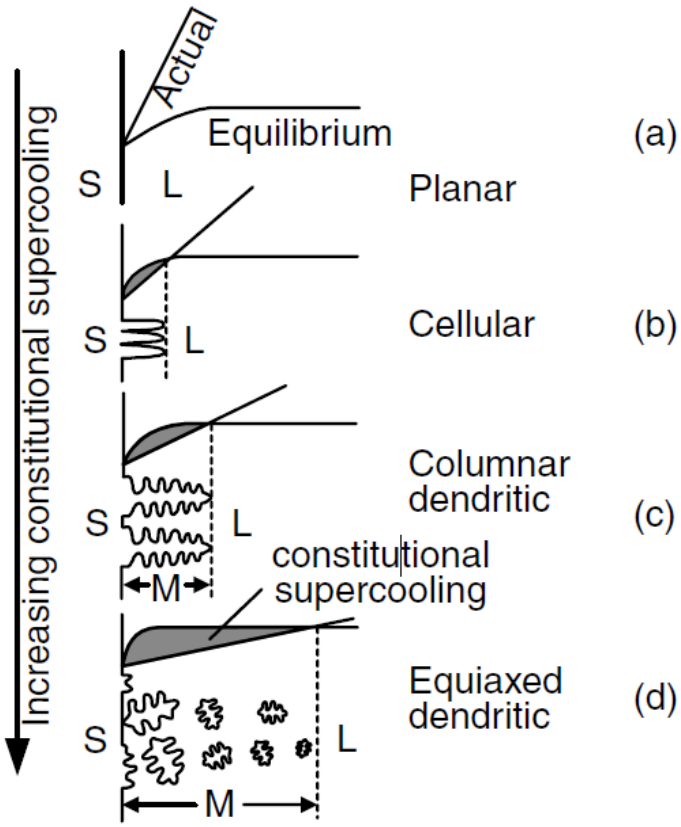

Figure 2.23: Effect of constitutional supercooling on solidification mode: (a) planar,(b) cellular, (c) columnar dendritic, (d) equiaxed dendritic (S, L, and M denote solid, liquid, and mushy zone, respectively) [85].

2.5.3 Effect of cooling rate

It has been established that the higher the cooling rate, the shorter the solidification time and the smaller the cellular or dendritic structure becomes [85-87]. The cooling rate has been

found to decrease with increasing the meltpool energy. According to Hofmeister et al. [88], cooling rate was found to decrease with increasing the meltpool size and the meltpool size decreased with decreasing energy density. The expression shown in equation 2.4 [85] revealed that the dendrite arm spacing decreases with increasing the cooling rate.

$$d = at_f^n = b(E)^{-n} \qquad (2.4)$$

Where d is the secondary dendrite arm spacing, t_f is the local solidification time, ε is the cooling rate, and a and b are proportional constants. Therefore, the higher the cooling rate, the finer the microstructure of the solidifying alloys. It is important to know that the product of G and R equals the cooling rate [19, 85]. Invariably, G and R are the two main parameters influencing the microstructure of the molten alloy after solidification.

2.5.4 Microstructure of laser deposited Inconel 625 alloy

The microstructure of laser coatings is somewhat different from that of the conventional processed materials because the materials involved undergo a rapid cooling cycle [42]. This usually results in fine microstructures and can lead to the formation of non-equilibrium phases and element distribution. There are several published articles on the Inconel 625 powder coatings but only few authors have reported on the laser cladding of Inconel 625 powder. Till date, no published article is found on the laser deposition of Inconel 625 using wire as the feedstock.

Dinda et al. [34] has investigated the microstructural evolution of Inconel 625 powder thin walls built using direct metal laser deposition technique. The processing parameters strongly affect the geometry, microstructures and hardness of the deposited walls. Pore- and crack-free walls of good metallurgical bonding with the substrate were built. The microstructure of the walls mostly consists of near vertical columnar dendrites, which grew epitaxially from the

substrate, as shown in Figure 2.24. Moreover, the growth direction of the columnar dendrites depends to the laser scanning direction.

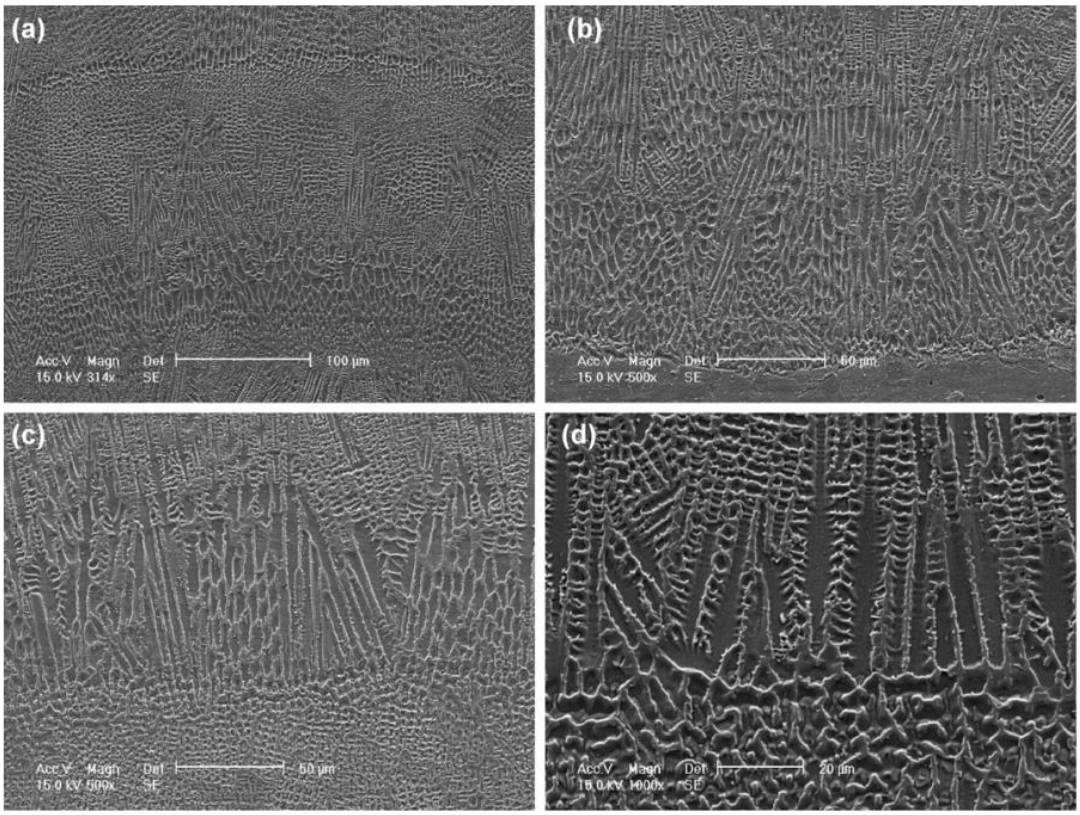

Figure 2.24: Transverse-section microstructures at different locations of an Inconel 625 powder thin wall sample built using direct laser metal deposition technique [34]

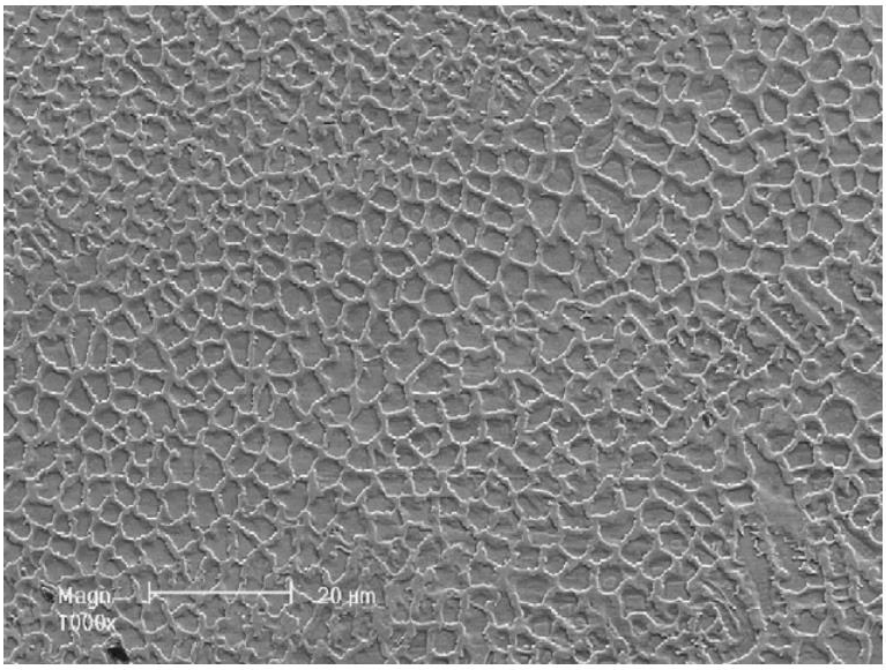

Figure 2.25: The microstructure of the horizontal section of an Inconel 625 thin wall sample built using direct laser metal deposition technique [34]

The columnar dendritic growth in the upper layer is caused by epitaxial growth of primary dendrite from the partially remelted grains of the previously deposited layer, which acts as pre-nuclei for directional growth of crystal. The morphology of the microstructure of the horizontal section (i.e. cross-section perpendicular to the build direction) was typically cellular/equiaxed dendrites, as shown in Figure 2.25. Near the surface region top layer of the deposited walls appeared horizontally growing columnar dendrites. The change in the dendrite orientation was attributed to the change in heat flux direction due to the hemispherical shape of the meltpool.

Also, the microstructure in relation to structural integrity of a three-dimensional components built by laser metal deposition with powder has been reported [42]. The built component was without defects except for small spherical gas inclusions. The microstructure of the component, as shown in Figure 2.26, was characterised with fine cellular/equiaxed dendritic structure resulting from rapid solidification which is typical of the technique used.

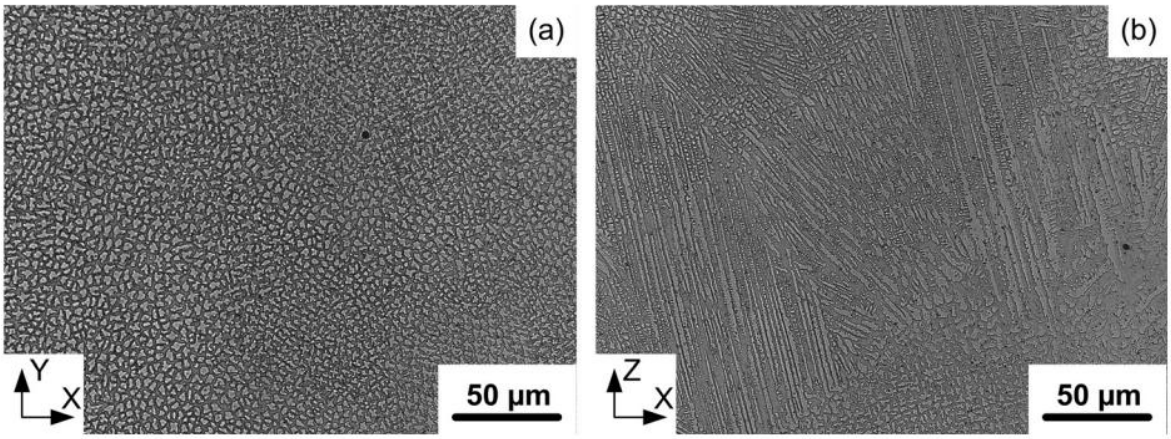

Figure 2.26: Cross-sections (a) perpendicular and (b) parallel to the build direction in the middle of Inconel 625 sample fabricated by laser metal deposition [42]

Mostly, other works on Inconel 625 powder laser cladding focused on corrosion behaviour investigations. In all the published works, the interdendritic regions of Inconel 625 coatings are usually occupied by the precipitates which are rich in Mo and Nb. The formation of these precipitates is due to the micro-segregation of these elements (of high atomic number) into interdendritic regions during the solidification of the molten alloy.

2.5.5 Solidification of Inconel 625 laser coatings

The development of the microstructure of the weldments (including laser coatings) is intimately related to the segregation of the alloy elements during solidification. Terminal solidification constituents form when the solid solubility for particular elements in the growing cells or dendrites is exceeded. In cellular or dendritic growth, these phenomena lead to the distribution of the alloying elements in accordance with the thermodynamic requirements of the system. Therefore, any element having the distribution coefficient (k) less than unity will be depleted at the cores and enriched at the interdendritic regions [39].

During the solidification of Inconel 625 powder coating, the γ dendrite core is depleted in Mo and Nb and enriched in the interdendritic region. The dendrite core is enriched in the Cr, Ni and Fe. Due to the segregation of Mo and Nb to the interdendritic region, the solidification

process of molten Inconel 625 alloy usually ends with the formation of γ dendrite core and Laves constituents at the interdendritic regions (see equation 2.5) [39, 41]. Apart from Laves, the formation of NbC (MC carbide) has been observed in the as deposited Inconel 625 laser coatings [42, 89]. The presence of MC carbide was attributed to high temperature exposure of the solidified material during laser scanning. This is known to occur at a temperature around 1250^{o}C (see equation 2.6) and a relatively small amount of NbC is produced.

$$L = \gamma + \text{Laves} \qquad (2.5)$$

$$L = \gamma + \text{NbC} \qquad (2.6)$$

The amount of Laves and NbC phases formed during solidification are sensitive to the C, Si and Fe contents. NbC is generally favoured by C whereas the presence of Laves is promoted by the Si and Fe additions [41].

2.5.6 Microstructures of tungsten carbide reinforced Ni based MMC coatings obtained by laser cladding

The use of tungsten carbide and in particular of Spherotene (WC/W_2C) as reinforcing material in Ni based alloys has been extensively researched for improving the surface properties of industrial components. This is most useful in service environments where components are potentially subjected to a combination of wear and corrosion damage, for example, in oil drilling industry [17]. Currently, laser cladding is a preferred and mostly used technique to deposit these coatings because of its advantages over other conventional methods, as mentioned in section 2.4.2.

Composite coatings (MMC) with Inconel 625 alloy as the matrix binder has not been well researched. However, other Ni-based alloys composite coatings reinforced with tungsten carbide have been extensively reported. Ni-based alloys are known to be tough, ductile and

possess high resistance to oxidation and corrosion attacks. Different ratios of the hard phase particle and the tough Ni-alloys binder may lead to a broad range of physical and mechanical properties of the coatings. The main factors affecting the surface properties of the tungsten carbide reinforced Ni-alloy composite coatings are:

- Volume fraction of the tungsten carbide particles present
- Extent of tungsten carbide particle dissolution
- Size and distribution of the tungsten carbide particle used
- Manufacturing route and shape of the tungsten carbide particle used
- Composition of the Ni-alloy binder used

Volume fraction of the tungsten carbide particles present: The effect of the tungsten carbide content on the microstructure and wear resistance of laser cladding Ni based alloys coating has been investigated [76, 90]. Wu et al. [76] and Liyanage et al. [91] have found that the volume fraction of the undissolved WC in the WC-Ni alloys composite coating increases with increasing the composition of the tungsten carbide (WC) powder in the prepared composite powder. Guo et al. [90] examined 6 different coating samples with 0%, 5%, 15%, 25%, 35% and 50% WC compositions in NiCrBSi alloy. It was found that transverse cracks were visible in the coating with 35% WC content and increased in number for the coating sample with 50% WC content. This was traced to a higher volume composition of the hard but brittle secondary carbides resulting from more WC dissolution. Also, the surface hardness and abrasive wear resistance of the WC-Ni alloy coating improves with increases in the volume fraction of the undissolved WC particle [15, 90]. The greater the WC content, the more the WC dissolution and the harder the matrix binder.

Also, higher volume fraction WC (undissolved) in MMC coatings results in reduced matrix binder mean free path (i.e. average distance in-between the WC phase in the composite

matrix) and this is significant for improved abrasive wear resistance. Three abrasive wear mechanism of MMC coatings had been identified [56]. They are micro-cutting of the matrix binder, plastic deformation due to ploughing action and fracture of hard phase debris in the matrix binder. Of the three types, micro-cutting is the dominant. Micro-cutting tends to occur when the abrasive particles degrade matrix binder of lower hardness thereby dislodging the WC particles of higher hardness from the coating surface. This is more significant whenever the matrix binder mean free path is larger than the WC phase [92].

Extent of tungsten carbide particle dissolution: The tungsten carbide dissolution which increases with increasing specific laser heat energy [19] has been found to be detrimental to corrosion properties [11] of the WC-Ni alloy coatings. The WC dissolution usually results in the formation of the secondary carbides which increases the microstructural modification and compositional in-homogeneity in coatings. These promote development of galvanic coupling leading to a reduction in corrosion resistance.

Shape of the tungsten carbide particle used: Huang et al [56] compared the abrasive wear performances of WC/Ni/Al (69.5 wt.% /29.5 wt.% / 1wt.%) composite coatings using two different WC particle shapes. The results revealed that a composite coating made with crushed (angular-shaped) WC particles exhibited better wear resistance than the clad samples made with spherical WC. The reason for the difference in the abrasive wear performances was traced to the manufacturing processes involved in the production of the two particles. Spherical powder was produced by eutectic melting of tungsten and carbon to form melt carbide. The morphology of the spherical particle contained mixture of WC and W_2C depending on the carbon content. The W_2C is less chemically stable compared to monocarbide (WC) and at high temperature dissolves easily in the molten matrix to form diverse intermetallic phases thus lowering the wear resistance property of the clad layer [56].

On the other hand, the crushed WC powder was produced by the carburisation of elemental tungsten powder which essentially consists of pure monocarbide (WC). No melting is involved in the process resulting to no intermediary eutectic sub-carbides in the carbide composition. Consequently, there is higher volume fraction of undissolved WC particles in the clad layer hence an improved wear resistance property [56].

Also, the composite coating formed with crushed WC experience significantly low micro-cutting action whereas the Spherical WC-Ni alloy coating was degraded largely by micro-cutting action. The reduced micro cutting effect in the crushed WC composite coating was due to the interlocked network of a large quantity of undissolved WC in the clad microstructure (see Figure 2.27) leaving a very small area of binder phase exposed to the abrasive action of sand particles[56, 76, 92]. However, it has been reported that the sharp edges of the crushed powder may initiate cracking in the coating because there is high stress concentration in this area [90].

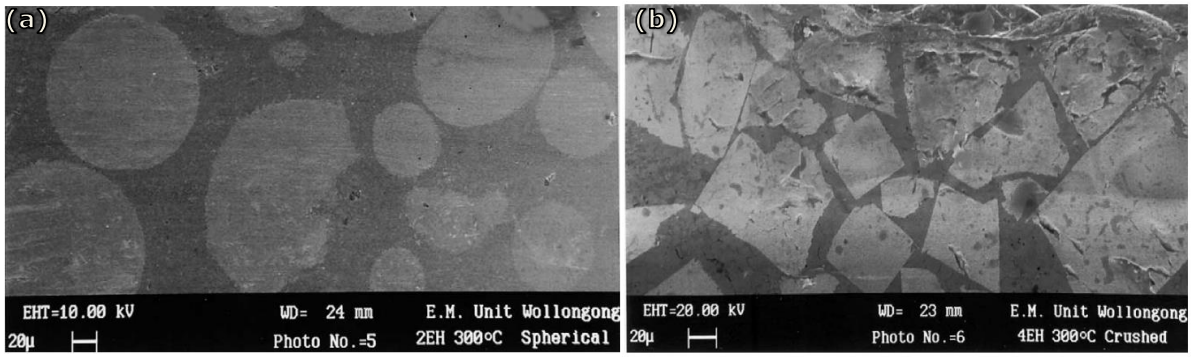

Figure 2.27: Cross-sectional microstructures of the WC-Ni alloy laser clad layer formed with (a) Spherical and (b) crushed WC particles [56]

Size and distribution of the tungsten carbide particle used: Van Acker et al [24] researched the effect of WC particle size on the wear resistance properties of WC/Ni coatings and it was found that the wear rate of the deposited coatings decreases with reducing the WC

particle size in the clad. However, the significance of the relationship depends on the wear mode the component is subjected to. Van Acker et al [24] reported that for the ball on disc tests with sliding of an Al_2O_3 ball against laser clad coatings the WC/Ni coatings made with smaller ceramic particles exhibited better wear performance. This is probably due to the stronger cohesion between the smaller WC particles (13.3-69.8μm) and the matrix binder compared to the larger carbide (115.9-206.8μm). However, the ball cratering wear test results showed no significant difference in wear rate with increasing the carbide sizes.

Composition of the Ni-alloy binder used: The composition of the alloy contents such as Cr in the Ni alloy binder plays significant role in the dissolution of the tungsten carbide [91, 93]. Possibly due to the strong Cr-C affinity, the size and amount of the precipitated carbides in the Ni alloy matrix with the higher Cr content has been found to be larger in the laser cladding of WC-Ni (Cr) composite [93]. The effects of this are an increase in cracking susceptibility and higher wear rate compared to the cladding of Ni alloys with lower Cr content [91, 93].

2.5.7 Phases in the tungsten carbide reinforced Ni based MMC coatings

X-ray diffraction is used to identify the possible phases in the materials and coatings. In the past, many authors have reported similar results on the high degree of microstructural modification in the tungsten carbide reinforced Ni based alloy composite coatings due the dissolution of the reinforcing particles. This has led to the identification of a number of phases. The appearance of both WC (undissolved) and W_2C phases is due to the dissolution of the tungsten carbide particles [11, 17, 19, 56, 90, 94].

Depending on the degree of WC dissolution and the level of substrate dilution in the Ni matrix, various secondary carbide formations had been identified by the XRD. Apart from WC and W_2C phases, Liu et al. [17] identified the formation of eutectic carbides including

$(Cr\text{-}Mo)_2C$ and Fe_3W_3C-Fe_4W_2C in the interdendritic regions during the laser surface melting of HVOF–sprayed WC-Inconel 625 coating. Table 2.6 gives the review of the phases identified in WC-Ni based alloy composite coatings.

Table 2.6: A review of the phases identified in microstructure of WC-Ni based alloy composite coatings.

Coating technique	Matrix	Substrate	Phases present	Reference
Laser cladding	Pure nickel	H13 tool steel	WC, W_2C, WC_{1-x}, Ni_2W_4C, CrFeNi	[56]
Laser surface alloying	Ni and NiCr	AISI 304L	WC, W_2C, $M_{23}C_6$, M_6C, γ-Ni matrix	[94]
Laser cladding	NiCrBSi	Stainless steel (1Cr18Ni9Ti)	WC, W_2C, Ni_2W_4C, CrB, $Cr_{23}C_6$, Ni_4W, γ-Ni	[90]
Laser induction hybrid rapid cladding	NiCrBSi	A3 mild steel	WC, W_2C, Fe_3W_3C, Ni_3B, Ni_4B_3, $(W,Cr,Ni)_{23}C_6$, γ-Ni	[19]
Laser cladding	Inconel 625	Inconel 625	WC, W_2C, M_2C, M_6C, γ-Ni matrix	[11]
Laser cladding	NiCrBSi	Low carbon steel	WC, W_2C, $Cr_{23}C_6$, CrB_2, Ni_3B, Cr_7C_3, γ-Ni	[95]
Laser surface melting	Inconel 625	AISI 316L	WC, W_2C, WC_{1-x}, Ni_2W_4C, $(Cr\text{-}Mo)_2C$, Fe_3W_3C-Fe_4W_2C	[17]

2.5.7.1 The W-C system

Generally, there are two main phases present in the W-C system. They are the higher tungsten monocarbide δ-WC (WC) and the lower β-WC (W_2C). Both have hexagonal structure and their XRD patterns are shown in Figure 2.28. It has been reported that, in the temperature range 300-1200 K, δ-WC undergoes no phase transformation and it is stable between 300 and 3030 K [96]. However, the W_2C does not exist in the W-C system at temperatures below 1523 K. Above 1523 K, it exists in three polymorphs namely: low temperature (β"), intermediate (β') and high-temperature (β). Depending on the carbon atoms arrangement, W_2C may be dis-ordered at high temperatures or ordered at low temperatures [96].

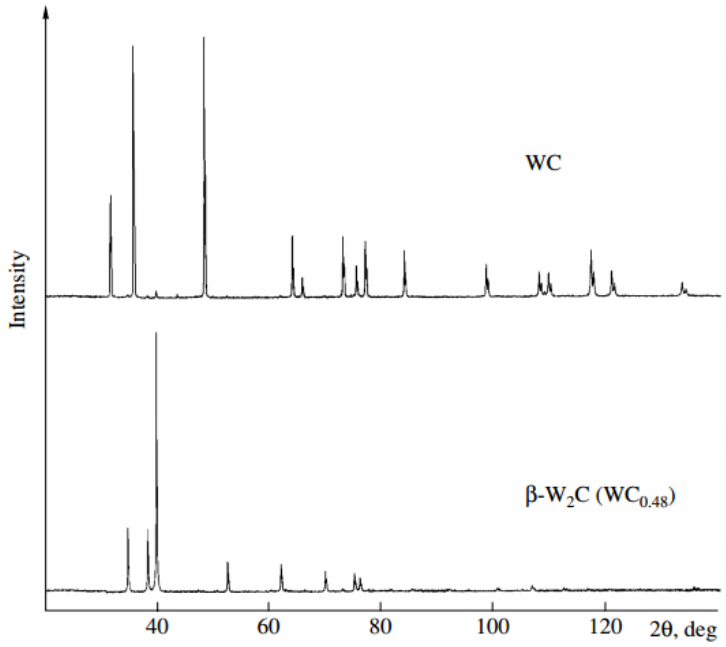

Figure 2.28: XRD spectra of the hexagonal δ-WC ($WC_{1.0}$) and hexagonal β-W_2C ($WC_{0.48}$) [96].

The phase diagram of the W-C system is shown in Figure 2.29. The special points in the phase diagram at temperatures above 1300K are summarised in Table 2.7.

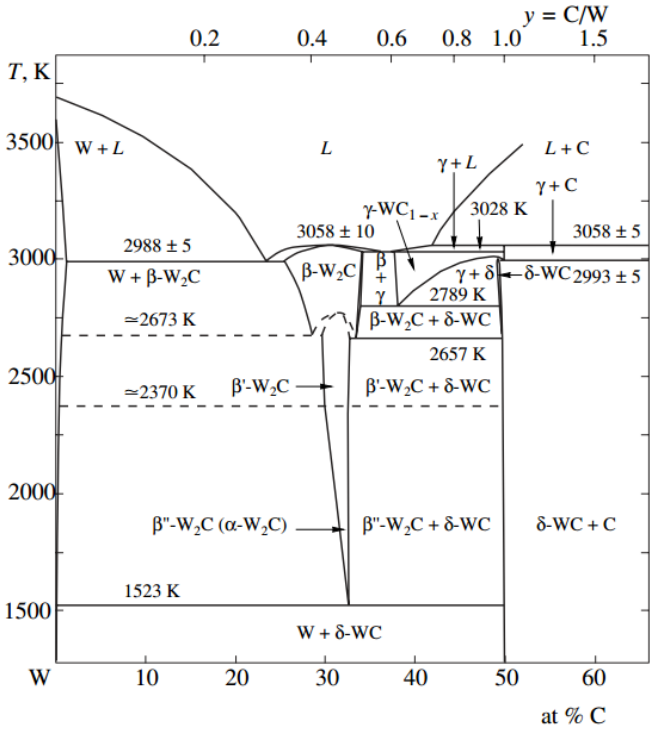

Figure 2.29: Phase diagram of the W-C system [96].

Table 2.7: Special points in the phase diagram of the W-C system shown in Figure 2.4 at temperatures above 1300 K [96].

Reaction	at % C in the phases involved			Temperature (K)	Reaction type
L ↔ W	0	0	-	3755 ± 5	Melting
L ↔ β-W_2C	≈ 30.6	≈30.6	-	3058 ± 10	Congruent melting
L + C ↔ γ-WC_{1-x}	≈ 42.0	100.0	50.0	3058 ± 5	Peritectic
L ↔ W + β-W_2C	≈ 23.5	≈ 1.2	≈ 25.5	2988 ± 5	Eutectic
L ↔ β-W_2C + γ-WC_{1-x}	≈ 37.0	≈ 34.3	≈ 37.8	3028 ± 5	Eutectic
γ-WC_{1-x} ↔ δ-WC	≈ 49.3	≈ 49.3	-	3008 ± 5	Polymorphic transformation
γ-WC_{1-x} ↔ δ-WC + C	50.0	≈ 49.8	100.0	2993 ± 5	Eutectoid decomposition
γ-WC_{1-x} ↔ β-W_2C + δ-WC	≈ 38.2	≈ 34.0	≈ 49.5	2798 ± 5	Eutectoid decomposition
β-W_2C ↔ W + β'-W_2C	≈ 28.6	≈ 0.7	≈ 29.7	2673 ± 10	Eutectoid decomposition
β-W_2C ↔ β'-W_2C	≈ 31.6	≈ 31.6	-	2768 ± 10	Disorder-order transformation
β-W_2C ↔ β'-W_2C + δ-WC	≈ 33.5	≈ 32.8	≈ 49.8	2657 ± 10	Eutectoid decomposition
β'-W_2C↔ β"-W_2C	30.0-32.5	30.0-32.5	-	2370 ± 15	Order-order transformation
β"-W_2C ↔ W + δ-WC	≈ 32.6	0	50.0	1523 ± 5	Eutectoid decomposition

It is clear from the W-C phase diagram shown in Figure 2.29 that the δ-WC phase has an insignificant homogeneity range and is stable between 300-3028 K. However, the three polymorphs of W_2C have broad homogeneity ranges. The dis-ordered high temperature β-W_2C has a homogeneity range from $WC_{0.34}$ to $WC_{0.52}$ and is stable in the range from 2670-2720 K to its melting point (3000-3050 K). The intermediate β'-W_2C has a homogeneity range from $WC_{0.34}$ to $WC_{0.49}$ and exists between 2370 and 2670-2750 K. The low temperature β"-W_2C phase has a homogeneity range of $WC_{0.34}$ to $WC_{0.48}$. As the temperature reduces, the homogeneity range narrows down such that at 1523K, there is no homogeneity range. The composition of β"-W_2C at this point is $WC_{0.48}$. Below 1523 K, β"-W_2C phase decomposes into W and δ-WC [96].

2.5.8 Scanning electron microscopy (SEM) characterisation of the tungsten carbide reinforced Ni based MMC coatings

SEM is frequently utilised to characterise the morphology and microstructure of the powder feedstock and coating. With the back scattered electron signal, one may see the contrast between the phases present due to the difference in the atomic number of the phase constituent. Secondary electron mode reveals clearly the morphology of a coating sample. In combination with the Energy-dispersive X-ray spectroscopy, the elemental composition of the phases present in a coating sample can be determined.

In the past, several authors have discussed the dissolution mechanism of tungsten carbide in the molten Ni based alloys. The dissolution or carburisation of the WC has been identified as a surface phenomenon [11, 56]. This means that the dissolution occurs mainly at the edges of the tungsten carbide particles resulting in the production of W_2C and graphite (see equation 2.7), for example, as shown in the SEM/BSE micrograph presented in Figure 2.30. The W_2C phase often appears predominantly around the edges of the undissolved WC, The phase is always of bright contrast because it is highly rich in tungsten.

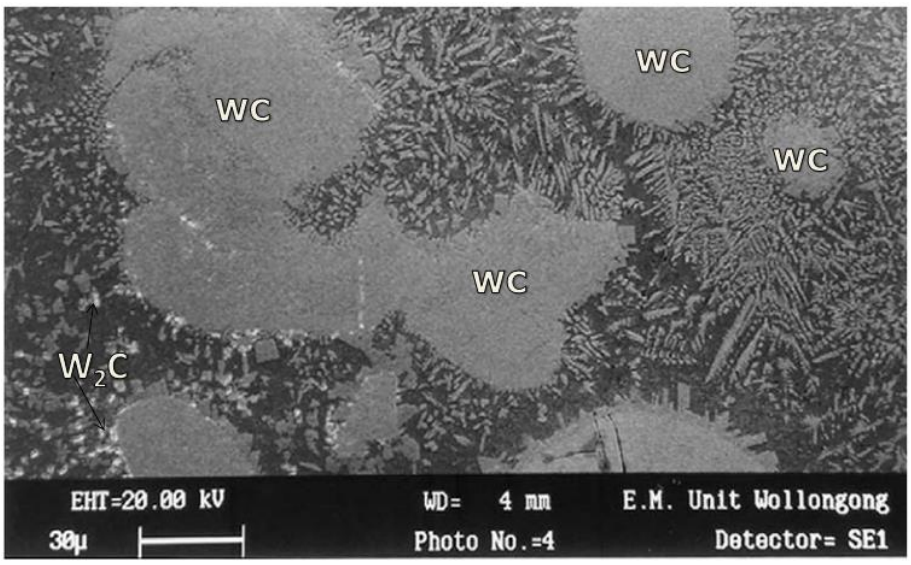

Figure 2.30: The dissolution of tungsten carbide in the molten Ni alloy matrix [56]

Another effect of the WC dissolution is the enrichment of the molten Ni-matrix alloy (Ni based) in W and C. According to Cooper et al. [11], the solidification of the W and C rich Ni matrix begins with the formation of continuous Ni rich dendrites followed by the precipitation of the eutectic carbides in the inter-dendritic regions. This is usually the case when the dissolution is moderate. This observation is supported by Liu et al. [17, 94] who explained that the solidification of the composite matrix of the partially melted HVOF sprayed WC-Inconel 625 coating started with the formation of dendritic γ-Ni matrix and followed by the precipitation of a mixture of various carbides (Ni_2W_4C, $(Cr\text{-}Mo)_2C$, Fe_3W_3C-Fe_4W_2C) termed as eutectic carbides in the interdendritic regions. However, if the WC dissolution is very high, the dendritic carbide which precipitates randomly within the coating is first formed. This is followed by Ni-rich dendrites formation and ends with the precipitation of various eutectic carbides in the interdendritic regions [11].

The various eutectic and dendritic carbides formed during the solidification of the composite matrix are termed as M_2C, M_6C and $M_{23}C_6$ with M referring to the other elements present apart from C. M_6C is formed randomly as angular (blocky) carbides within the coating. It

appears as Fe_3W_3C showing that the influence of Fe content (probably from the substrate) in the composite matrix is high or as Ni_2W_4C where the Fe composition of the molten matrix is low [17]. A typical microstructure of WC-Ni based alloy matrix composite formed by laser surface alloying showing the random precipitation of M_6C blocky carbides is shown in Figure 2.31 [90]. $M_{23}C_6$ mostly occurs as thin film within the interdendritic region. It occurs as frequently as $Cr_{23}C_6$ indicating that it is very rich in Cr. Usually, it is detected by the use of transmission electron microscopy (TEM) because of its tiny form. Figure 2.31c shows the high resolution TEM micrograph showing the presence of Cr- rich $M_{23}C_6$ carbide in-between the γ-Ni dendrites.

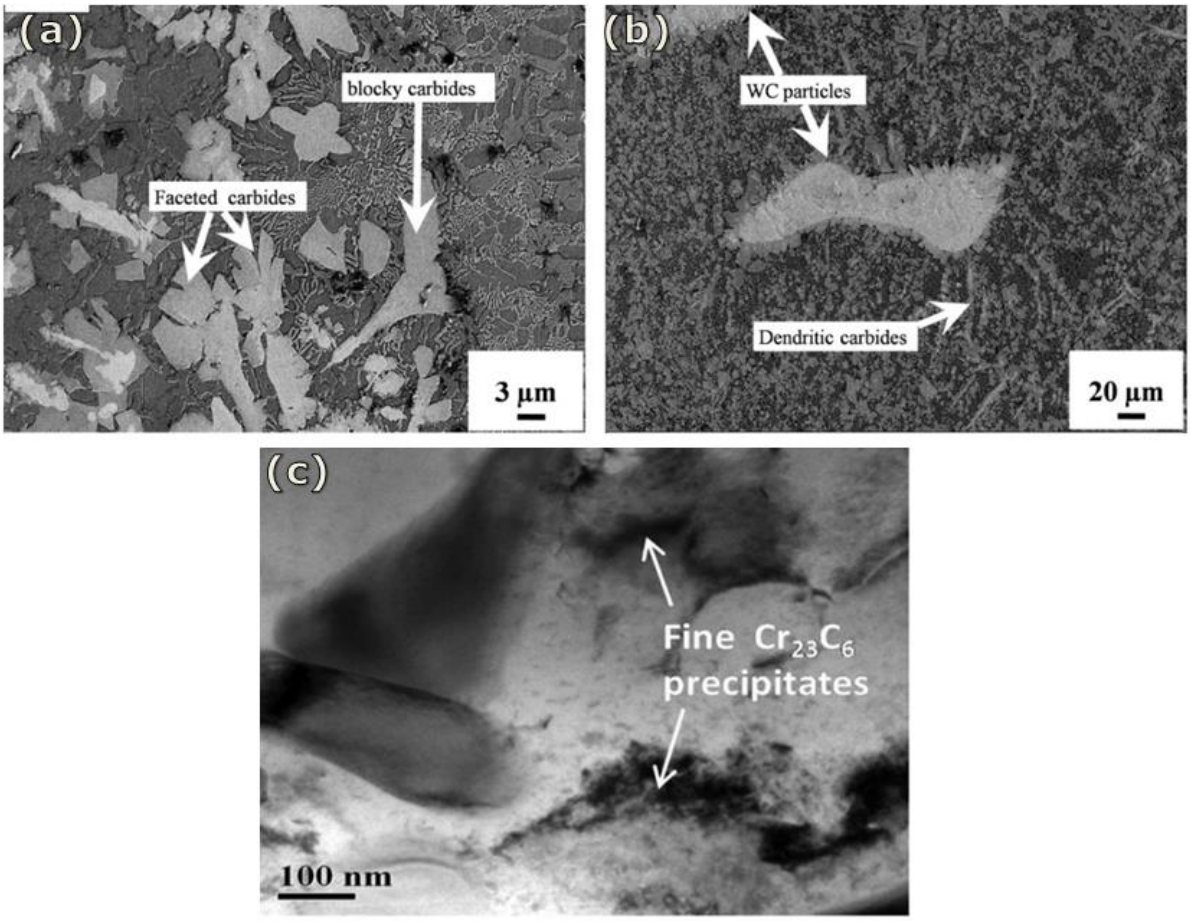

Figure 2.31: Microstructure of laser surface alloyed AISI 304L stainless steel with 70WC + 15Ni + 15NiCr lased with a power of 2.2kW and scan speed of 0.008m/s. (a) SEM/BSE image showing blocky and faceted M_6C carbides, (b) SEM/BSE images showing undissolved WC in the Ni-matrix and (c) TEM micrograph showing the presence of $Cr_{23}C_6$ in the interdendritic regions [94]

2.5.9 Distribution of WC in the composite coating

An even distribution of WC or other ceramics is essential not only for excellent wear resistance but also for the high quality and processing of the coatings [97]. WC, has often been found to be more concentrated in the base of the laser deposited coatings [97]. This is often caused by the high density of the hard phase ceramics and the stirring motion of the meltpool. However, a proper control and selection of cladding parameters have yielded uniform distribution of WC particles throughout the entire volume of the coatings [97]. It was discovered that rapid cooling rate and low meltpool temperature (higher viscosity) which can be obtained at high traverse speed restrict the time available for WC particles to sink to the bottom of the meltpool. Therefore, uniform distribution of ceramic particles is usually achieved at lower energy density.

Amado et al. [21] researched the laser cladding of tungsten carbides (Spherotene) hardfacing alloys for the mining and mineral industry. It was discovered that the Gaussian mode of beam delivery of some high power laser (e.g. Fibre) can be responsible for the uneven distribution of hard particles in the matrix binder. Figure 2.32 presents micrographs showing the distribution of WC in Ni matrix at different cladding conditions.

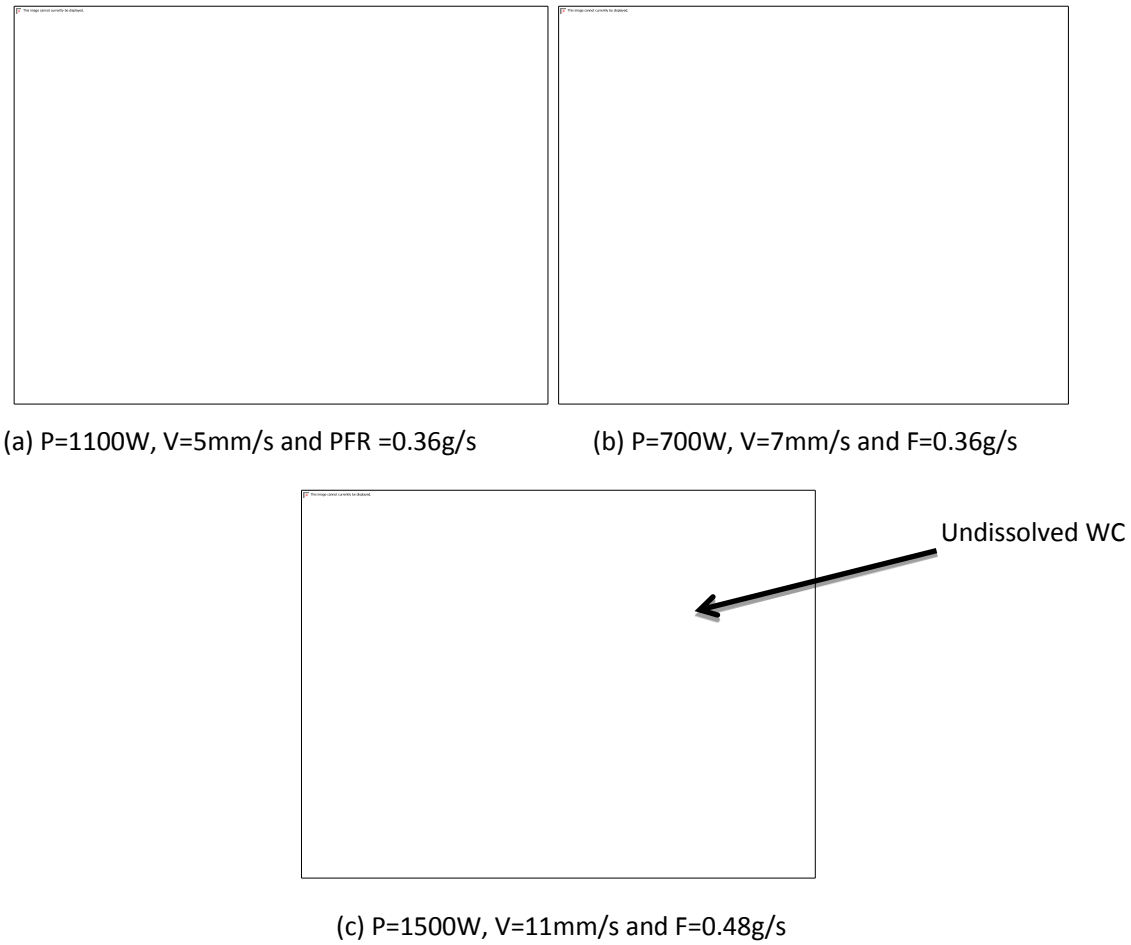

Figure 2.32: Micrographs of cladding cross sections at varying process parameters [21]

As described in Figure 2.32a, there is always a high dissolution rate of WC particles in the centre of the meltpool compared to any other part of the clad. This can be attributed to the Gaussian distribution mode of the laser beam. With a Gaussian delivery mode of the laser beam, heat energy is more intense in the centre especially when cladding at the focus. The effect is significant when cladding at high energy input, for example, as shown in Figure 2.32a. The WC particles in the centre of the meltpool suffer more severely from the heat therefore dissolving completely in the molten matrix. However, the higher volume fraction of WC particles at the top and periphery of the clad volume in Figure 2.32a is due to faster cooling rate resulting from heat transfer to the atmosphere through convection and radiation

modes. Few WC particles (undissolved) in the bottom of clad volume are due to faster cooling resulting from large heat rejection to the substrate.

Nevertheless, a relatively more WC concentration can be found at the clad core by defocusing the laser beam thereby increasing the spread of the beam. Fig 2.33 presents a diagram showing the distribution of the laser beam (a) at the focus and (b) at some distance away from the focus.

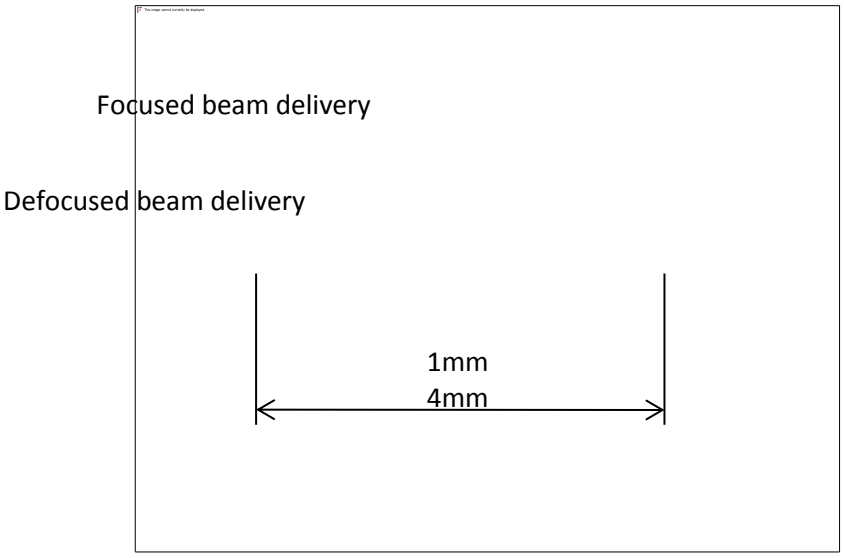

Figure 2.33: Laser beam distribution at the focus and some distance away from the focus

Corrosion

2.6 Definition and basic corrosion theory

Generally, engineering metals are unstable in nature. They tend to react with the earth's environment such as oxygen, water, warm temperatures etc. to form more stable compounds.

Metals in the un-combined form are in high-energy states. Thermodynamically, they try to lower their energy by spontaneously reacting with their environment to form solutions or compounds that have greater thermodynamic stability. This is done through a process called corrosion. Corrosion has been defined as the degradation of a metal by an electrochemical reaction with its environment [98].

The driving force for metallic corrosion is the Gibbs energy change (ΔG). This is the change in free energy of the metal brought about by the corrosion process [99]. A negative ΔG implies that the reaction is spontaneous (i.e. energy change is downhill). ΔG is measured in Joules per mole (J/mol). However, in corrosion measurements, the driving force is more often expressed in volts (V) which can be derived from equation 2.7 [99].

$$\Delta G = -nFE \qquad (2.7)$$

Then,

$$E = \frac{-\Delta G}{nF} \qquad (2.8)$$

The symbol E is the driving force for the corrosion process, n is the number of moles of electrons per mole of metal involved in the process and F is a Faraday's constant which is the electrical charge carried by a mole of electrons (= 96500 C). When this driving force (i.e. voltage 'E') is measured without the application of external voltage, it is referred to as the open circuit potential (E_{oc}).

Aqueous corrosion is electrochemical. For this to occur, the following four components must be in place.

- The anode, which is the corroding metal.
- The cathode, which is a metal or other electronic conductor whose surface provides sites for the environment to react.

- The electrolyte (i.e. the aqueous environment), in contact with the anode and cathode. This provides the path for the ionic conduction.
- The electrical connection between the electrodes (anode and cathode) allowing electrons flow between them.

All these constitute an electrochemical corrosion cell as illustrated diagrammatically in Figure 2.34. The anodes and cathodes are usually located close to each other and in some cases, may be on the same piece of metal.

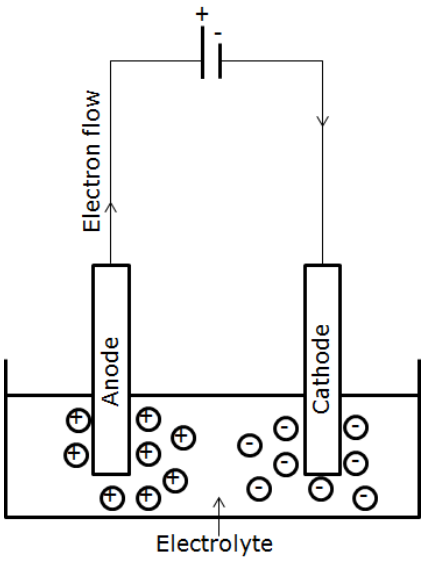

Figure 2.34: The components of an electrochemical corrosion cell

2.6.1 Corrosion reactions

Corrosion normally occurs at a rate determined by equilibrium between two opposing electrochemical (corrosion) reactions. Corrosion reactions are divided into anode and cathode half-cell reactions.

2.6.1.1 Anodic reaction

When an anode metal (denoted as M) is immersed in an electrolyte, it corrodes and goes into a solution as metal ions as described in equation 2.9. An example of anodic-half reaction for a steel corroding in seawater is given in equation 2.10.

$$M \rightarrow M^{n+} + ne^{-} \quad (2.9)$$

$$Fe \rightarrow Fe^{2+} + 2e^{-} \quad (2.10)$$

This is an oxidation reaction because there is loss of electrons by the metal. These electrons reside around the corroding metal where they migrate through electronic conductor to the cathode, as shown in Figure 2.28.

2.6.1.2 Cathodic reaction

Reduction occurs at the cathode because the electrons produced at the anode are consumed at the cathode. If this does not occur, the anode will be so much loaded with electrons and all the reactions would stop. The cathode itself does not react however, it is some reducible species (corrosive environments such as O_2, H_2, Cl^-) in the electrolyte that reacts on the cathode. Since there many different corrosive environments, several cathode reactions are possible. Some common cathodic reactions are described in the following equations [99].

$$O_2 + 2H_2O + 4e^{-} \rightarrow 4OH^{-} \quad \textit{(In neutral or basic solutions with dissolved oxygen)} \quad (2.11)$$

$$2H^{+} + 2e^{-} \rightarrow H_2(g) \quad \textit{(In acid solutions)} \quad (2.12)$$

$$O_2 + 4H^{+} + 4e^{-} \rightarrow 2H_2O \quad \textit{(In aerated acids or oxidizing acids e.g. } HNO_3\textit{)} \quad (2.13)$$

2.6.1.3 Cell reactions

The cell reaction combines the anodic and cathodic reactions together. For example, a cell reaction for corroding steel in seawater is a combination of equations 2.10 and 2.11. This, as represented in equations 2.14 and 2.15, results in production of rust.

$$2Fe + 2H_2O + O_2 \rightarrow 2Fe^{2+} + 4OH^- \rightarrow 2Fe(OH)_2 \quad (2.14)$$

$$2Fe(OH)_2 + \tfrac{1}{2}O_2 \rightarrow H_2O + Fe_2O_3 \bullet H_2O \quad (2.15)$$

2.6.2 Corrosion products and passivity

The corrosion products can be soluble or insoluble compounds or a gas (usually H_2) [99, 100]. Soluble compounds or gases do not usually affect subsequent corrosion reactions. However, insoluble compounds precipitate on the surface of the anode or cathode or somewhere in-between the two electrodes, depending on relative mobilities of the ions. If the cations (i.e. the negative ion produced at the cathode) reach the anode before the positive metal ions (i.e. anions) migrate from it, the insoluble compounds tends to form on the anode.

Consequently, a deposit of the corrosion products on the anode will slow down the diffusion of the metal ions to the cathode therefore decreasing the rate at which corrosion is taking place. This can be referred to as passivity. In a simple term, passivity refers to the loss of chemical reactivity experienced by certain metals or alloys under particular environmental conditions [100]. This means that some metals, when in contact with corrosive environments, become essentially inert and act as if they were noble metals such as platinum and gold.

If a metal demonstrates passivity, it reacts with its environment to form thin layer of corrosion products acting as a barrier and slowing the corrosion process by several order of magnitude [100]. For example, Cr_2O_3 is formed in a case of stainless steel. The behaviour of this type of metal including Inconel 625 alloy can be divided into three as presented in Figure 2.35. In active region, the corrosion behaviour is similar to that of the normal metals or alloys. In the passive region, the corrosion rate decreases or showed no significant increase even with the addition of more oxidizing agents. Finally, at very high concentration of the oxidizing agents or in the presence of very powerful oxidizers, the corrosion increases with increasing the oxidizer power. The region at which this occurs is termed as transpassive

region. These characteristics are used to determine the corrosion resistance of metals and alloys.

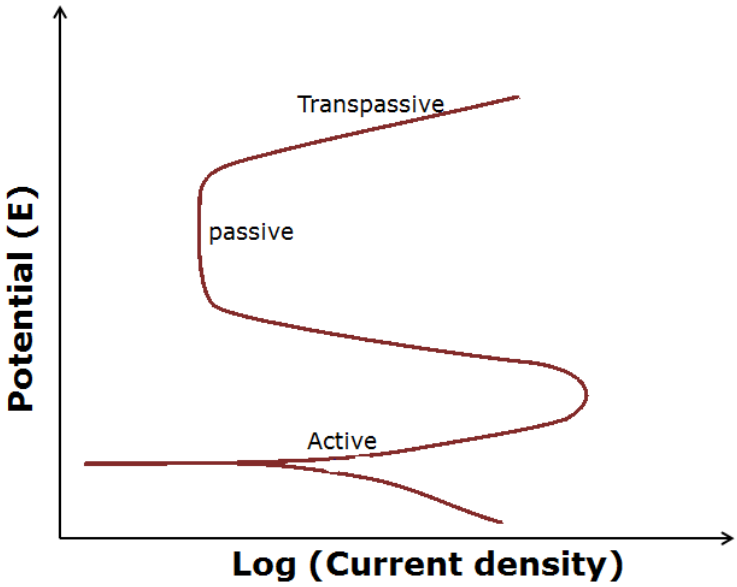

Figure 2.35: Corrosion behaviour of a metal exhibiting passivation in a corrosive environment

2.6.3 Environmental factors affecting corrosion rates of metals

Metals behaved differently in different environments. Environmental effects on the corrosion rate of the metals or alloys have been studied. The various factors affecting the corrosion rates are briefly discussed.

Fluid velocity: The relative velocity between the corrosive environment and the metal can affect the corrosion rate. Going from stagnant to moderate velocities may lower the corrosion rate, especially localised corrosion. The reason is that the environment is more uniform and the settlement of suspended solids that may possibly cause localised corrosion. The effect of localised corrosion can be reduced by increasing the velocity of environment, for example, in case of solution flowing through a duct [49].

On the other hand, the corrosion rate of an active metal has been found to increase with increasing velocity. At higher velocity, the rate at which the reactants (e.g. O_2) are supplied to the cathode increased. At a particular stage, an increase in velocity has no significant change in the corrosion rate.

Metals that passivate provide another scenario. First, increase in velocity cause increase corrosion until a condition is reached when passive film is formed on the metal surface. From this point, the velocity virtually has no effect until it become so great that it damages the film [99, 100]. When the metal is protected by a thick layer of corrosion products, the effect of the velocity on the corrosion rate presents another scenario. The velocity showed no noticeable effect until the thick layer is eroded away by a very high velocity.

Temperature: Since the increase in temperature increases the reaction rates, diffusion rates and the rate of dissolution of gases in water, it is expected that the corrosion rate will increase as the temperature increases. Increasing temperature also increases the oxidizing power, for example, of nitric acid solution [100]. It also increases the ionization of water therefore improves its ionic conduction.

Other factors influencing the corrosion of metals are the effects of galvanic coupling, effect of oxidizers, corrosive concentration of the environment, grain structure of the metal, cathode/anode area ratio, presence of any crystal defects, solid solution alloys, etc [99, 100].

2.6.4 Classification of corrosion

Based on the appearance of the corroded metal, corrosion has been classified into eight different forms [100]. They are: (1) Uniform or general attack, (2) galvanic, (3) crevice corrosion, (4) pitting, (5) intergranular, (6) selective leaching, (7) erosion and (8) stress corrosion. For the purpose of this work, the first four type of corrosion will be discussed in

terms of their formation mechanism and characteristics which have the most relevance to this study.

2.6.4.1 Uniform attack

It is the most common type of corrosion and normally characterised by a chemical or electrochemical reaction that occurs uniformly over the surface of a metal. A typical example of this type of corrosion is the atmospheric corrosion of an old galvanised steel barn roof. This type of corrosion, from a technical point of view, is the least serious, because the corrosion rate can be easily determined and the lifespan of the equipment can be accurately estimated. Uniform attack can be prevented or reduced by coating the surface of the metal with a material of superior corrosion properties.

2.6.4.2 Galvanic corrosion

Electron flow is initiated whenever two dissimilar metals are immersed in a corrosive or conductive solution. This is due to a potential difference between the metals. A galvanic cell is said to have formed because of the electron flow between the metals. The less corrosion-resistant metal acts as the anode and its corrosion is increased compared to the metal behaviour when a galvanic cell is not formed. On the other hand, the more corrosion-resistant metal corrodes a little or not at all because it acts as the cathode in the cell. The galvanic effect can be reduced or eliminated by insulating dissimilar wherever practicable in a conductive solution, selecting combinations of metals whose electrochemical potentials are very close in the galvanic series [100].

2.6.4.3 Crevice

This type of corrosion is a localised attack and it occurred within the crevices and other shielded areas on metal surfaces exposed to corrosives, especially environments that are rich in chloride ions [100, 101]. Deposits such as sand, dirt, corrosion products and other solids do

cover the crevice thereby leaving small volume of stagnant solution underneath. For crevice corrosion to occur, a crevice must be wide enough to permit liquid entry but sufficiently narrow enough to maintain stagnant zone [100]. The corrosion starts as uniform attack over the entire surface, including the interior crevice of a metal exposed to seawater. As the metal ions are formed, the electrons produced are immediately consumed by the oxygen therefore producing hydroxyl ions. After some time, the oxygen is depleted in the crevice because of the restricted convection. Consequently, oxygen reduction will stop therefore leading to production of excess metal ion because the oxidation of the metal continues. For corrosion to continue in the crevice, there is migration of chloride ions which combine with the metal ions to form metal chloride. The metal chloride hydrolyses in water producing insoluble hydroxide and acid. The PH value in the crevice is lowered and the dissolution of metal is increased. The corrosion within the crevice is increased because of the concentration of chloride and hydrogen ions whereas the metal surface adjacent to the crevice suffers little corrosion. Metals that passivate especially, stainless steels are susceptible to this type of corrosion. The passive films are usually destroyed by high concentration of chloride or hydrogen ions within a small surface region [100, 102]. To avoid crevice corrosion, crevice must be avoided on the metal surface [101].

Pitting corrosion: this form of corrosion is similar to crevice corrosion except that it creates its own holes. These holes may be small or large in diameter, but in most cases they are relatively small and their growth is in the direction of gravity. Pitting is one of the most destructive and insidious forms of corrosion. Just like the crevice form of corrosion, pitting is an autocatalytic process [100]. This means that the corrosion process within a pit produce conditions that are both stimulating and necessary for the continuing activity of the pit. Also, the mechanism is as a result of oxygen depletion leading to concentration of chloride ion within a localised area on the surface of anode (corroding metal). As explained before, this

may lead to increased metal dissolution due to high concentration of hydrogen ion and chloride ion resulting from hydrolysis of metal chloride in the localised area. Pitting is mostly associated with stagnant conditions such as corrosive liquid trapped in pipe. However, if the liquid is flowing through pipe, the chance of pitting formation is low because the locally high concentration of chloride and hydrogen ions will be swept away by the flowing liquid [49, 100]. Pitting is very common in stainless steels, particularly type 304 and 316, when exposed to chloride rich solutions [103, 104]. The effect of pitting can be reduced by addition of some useful alloying elements into their compositions [105]. The effects of each alloying element on the corrosion resistance of stainless steels are summarised in Table 2.8.

Table 2.8 Effects of alloying on pitting resistance of stainless steel alloys [100]

Element	Effect on pitting resistance
Chromium	Increases
Nickel	Increases
Molybdenum	Increases
Silicon	Decreases but increases when present with Molybdenum
Sulphur	Decreases
Carbon	Decreases especially in sensitised condition
Nitrogen	Increases

2.6.5 Review of the past works on corrosion behaviour of Inconel 625 and tungsten carbide reinforced Ni based alloy composite coatings

Many authors have reported on the corrosion behaviour of Inconel 625 powder deposited by thermal spraying techniques but significantly few articles are found using laser cladding as the coating technique. Tuominen et al. [106] investigated the electrochemical performance of Inconel 625 powder coatings deposited by HVOF and laser cladding techniques in de-aerated

3.5% NaCl solution. As shown in Figure 2.36, the laser deposited coating demonstrated better corrosion resistance in terms of lower passive current density and higher breakdown potential and corrosion potential. The relative lower performance of HVOF coating was attributed to inhomogeneous coating structure caused by pores and oxides formation and presence of interconnected paths in the coating deposition.

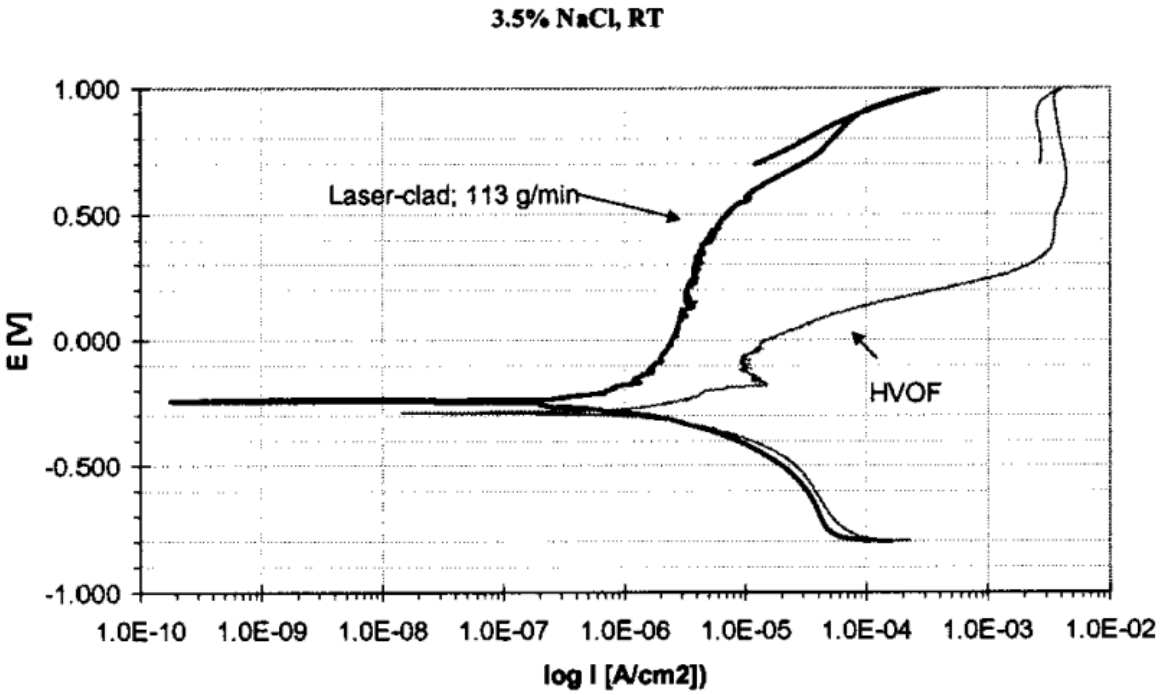

Figure 2.36: Cyclic polarisation curves for laser clad and HVOF sprayed coatings of Inconel 625 powder in 3.5% NaCl solution [106].

However, the microstructure of the laser coating is unaffected therefore it is relatively more uniform. A rapid rise in the current density of HVOF coating after passive region signifies the occurrence of localised corrosion (pitting). The cause was found to be massive Fe dilution in the coating resulting in inability to form a dense oxide layer on top of the coating. Ahmed et al. [107] studied the corrosion performance of wrought Inconel 625, HVOF deposited Inconel 625 powder coating and laser surface remelted HVOF Inconel 625 powder coating with the

purpose of providing a more detailed understanding of how specific microstructural features result in the performance gap between bulk and sprayed Inconel 625.

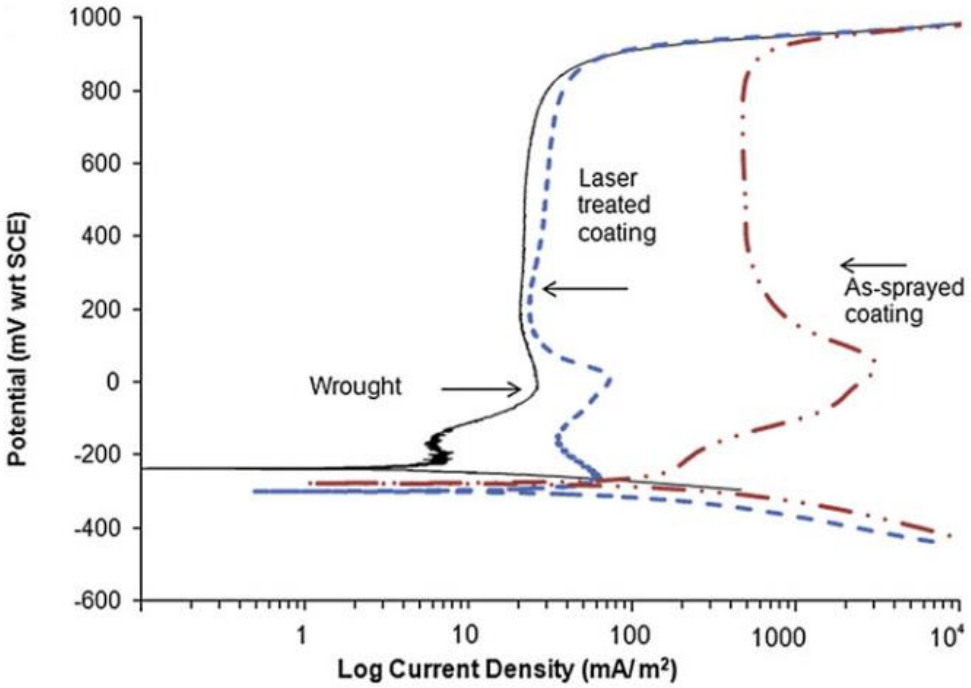

Figure 2.37: Potentiodynamic scans of wrought Inconel 625, HVOF sprayed Inconel 625 coating and laser treated HVOF sprayed Inconel 625 coating in 0.5M H_2SO_4 acid solution [107].

As shown in Figure 2.37, it was discovered that the HVOF coating exhibited much higher current density but the HVOF coatings subjected to laser surface remelting are found to have a lower passive current density close to that of wrought material. Laser surface melting of HVOF coatings of Inconel 625 eliminates the performance gap due to the elimination of both porosity and localised regions of material depleted in Cr in HVOF coatings. This observation is similar to the findings of Shrestha and Sturgeon [108] who established that the corrosion performance of thermally sprayed Inconel 625 powder coatings could, at best, match the performance of wrought stainless steel (type 316).

Though there are several published articles on the wear performances of tungsten carbide reinforced Ni-based alloy composite coatings the corrosion behaviour of the composite coatings has not been well researched. Cooper et al. [11] studied the corrosion performance of the WC-Inconel 625 powder composite coatings. The corrosion damage was found to be complex and mainly resulted from the galvanic couple mechanism between intermetallic carbides, and between these carbides and the Cr-depleted region of the Ni-matrix adjacent to the carbides. Corrosion also occurred as a result of galvanic couples between the partially dissolved WC and the Ni-matrix surrounding it. An investigation of the corrosion and wear performances of the HVOF-sprayed Inconel 625 and WC-Inconel 625 coatings by high power diode laser treatments has also been undertaken [17]. The type of corrosion mechanism found in these coatings is similar to the findings of Cooper et al [11]. The corrosion behaviour of the HVOF-sprayed composite coatings improve by homogenisation of their microstructure after laser treatments.

2.7 Summary of the literature review

Laser

- In the production of fibre laser, optical fibres are usually doped with rare earth ions such as erbium (Er^{3+}), neodymium (Nd^{3+}), ytterbium (Yb^{3+}), thulium (Tm^{3+}), or praseodymium (Pr^{3+}). Ytterbium doped fibre lasers have been found as the most powerful. In general, fibre laser can produce beam of a very high power because fibre laser beam can be focused to a very small spot.

Wrought Inconel 625

- The superalloys (i.e. nickel-iron, cobalt- and nickel-base alloys) are specifically developed to retain high mechanical strength and high resistance against surface degradation at temperatures up to ~85% of their melting points. They are mechanically strengthened by solid solution strengthening and/or precipitation hardening and/or carbides precipitates.

- Inconel 625 is a non-magnetic Ni-based superalloy containing significant proportion of Cr (20-23 wt. %), Mo (8-10 wt. %) and Nb (3-4 wt. %). It derives its unique mechanical properties such as high temperature strength, and creep-rupture strength mainly from the solution strengthening effect of the refractory metals, niobium and molybdenum in a FCC nickel (γ) matrix. Additional strengthening of the alloy is the precipitation hardening effect resulting from the formation of intermetallic compounds (i.e. ordered γ' and γ'') at high temperature in the continuous γ matrix. A small volume of carbide phases ($M_{23}C_6$, M_6C, MC, etc) which can be present as globular, script or blocky grain boundary particles also provides additional strength to the superalloy.

- The high corrosion and oxidation resistance of Inconel 625 is derived from the high Cr (20-23%), Mo (8-10%) and Nb (3-4%) content of the superalloy. Cr forms Cr_2O_3 with the atmosphere thus passivates the surface of the alloy against oxidizing environment, Mo and Ni resist any form of non–oxidizing corrosion. Nb stabilizes the alloy against sensitization at high temperature by preventing Cr from reacting with carbon thus avoiding any form of inter-granular corrosion at the grain boundaries.

- The weldability of nickel-base superalloys including Inconel 625 is largely influenced by the composition of γ' forming element in the alloys. Depending on its volume fraction, the γ' precipitate along the grain boundaries in the weld heat affected zones may result in hot cracking and post weld heat treatment (PWHT) cracking. Inconel 625 is considered very weldable because the sum of the γ' forming element (i.e. 2Al + Ti) present in the alloy is much lower than 6wt. %.

- WC is an extremely hard (1780Kg/mm^2) ceramic having a melting point of 2720^{o}C and quite stable at elevated temperature (2600^{o}C). WC is much denser (15.63g/cm^3) than any other commonly used carbide such as TiC, SiC and Cr_3C_2, thus having a higher powder flowability and catchment efficiency for laser cladding process. It has good wettability with Ni alloys

Laser cladding

- Laser cladding has several advantages over other competing coating deposition techniques such as plasma cladding, arc welding and thermal spraying. These include strong metallurgical bonding at the clad-substrate, minimal distortion of the substrate, low substrate dilution, minimal porosity and controllable heat input often producing a small heat affected zone (HAZ) and greater processing flexibility.

- Laser cladding with wire has not been widely used as powder feeding method. However, wire, as feedstock material, has a number of advantages over powder for laser cladding applications such as component surface modification, repair, manufacture and feature addition. Wire gives higher deposition rate, lower clad surface roughness and cleaner process environment, reduced material economy and lowers the processing cost and clad gas porosity content.

- Laser cladding, especially using wire as the feedstock material, is sensitive to changes in processing conditions. Therefore, determining suitable processing conditions for attaining stable process is essential for producing high quality clads.

- Laser cladding with front feeding orientation has been established as a better practice for both wire and powder feeding. Front feeding method produces process of higher powder catchment efficiency of about 20-45% and clads of improved surface roughness for both wire and powder since there is lower meltpool disturbance with this set-up.
- Three wire tip positions in the meltpool have been identified. The leading edge for smaller wire diameter (Ø 0.8mm) and aiming at the centre of the meltpool for wire of about Ø 1.2mm can produce good deposits and stable processes whereas placing the wire tip at the trailing edge will produce irregular tracks.
- It is found that wire feeding angle range of 20-60^{o} will produce good clad quality and stable process for front feeding orientation.

- Laser cladding of metal matrix composite (MMC) coatings has been extensively researched, particularly WC-Ni based alloy composites, for improved wear resistance. The feedstock materials are usually pre-mixed powders.

Microstructure

Inconel 625 coatings

- The solidification mode and grain size in the microstructure of solidifying coatings are determined by the temperature gradient and solidification growth rate. In laser cladding, the cooling growth rate is rapid therefore the microstructure is somewhat finer and mostly dendritic compared to other coatings made by other techniques.

- Usually, the microstructure of laser deposited Inconel 625 powder is finer and dendritic in morphology. The cracking tendency is very low because of the high ductility resulting from high Ni composition of the alloy. XRD has revealed continuous γ-Ni dendrites with some precipitates formation at the interdendritic regions. The precipitates, depending on the composition of the alloy, can be Laves or NbC. EDAX results showed that these precipitates are richer in Mo and Nb.

Ni based alloy tungsten carbide reinforced composite coatings

- Few authors have reported on the WC-Inconel 625 composite coatings, however, extensive work had been reported on Ni based alloys tungsten carbide reinforced composite coatings. The microstructure is more complex due to the dissolution of the hard tungsten carbide particles. XRD has revealed the formation of various secondary (intermetallic) carbides including M_6C, $M_{23}C_6$, etc in the coating. The M_6C usually appears as blocky carbide randomly formed within the continuous γ-Ni matrix whereas the $M_{23}C_6$ appears as tiny film in the interdendritic region. Other phases usually present are WC phase and tungsten rich W_2C phase.

- The extent of tungsten carbide particle dissolution increases with increasing the quantity of the particle injected and the amount of heat energy available for meltpool

creation. The more the dissolution, the greater the amount of the secondary carbides formed and the higher the cracking propensity of the coating.

Corrosion properties

Inconel 625 coatings

- Inconel 625 powder coatings shows excellent resistance to corrosion in both acidic and chloride rich environments. Compared to thermal sprayed coatings, laser coatings made of Inconel 625 powder shows improved resistance to corrosion in 3.5% NaCl solution. The corrosion is usually a uniform attack.
- The main contributing factors to the corrosion performance of Inconel 625 coatings are pores formation, the extent of Cr depletion in the continuous γ- Ni matrix and the amount of Fe dilution in the coating. These factors have deteriorating effect on the corrosion.

Ni based alloy tungsten carbide reinforced composite coatings

- The corrosion behaviours of Ni alloy tungsten carbide reinforced composite coatings are largely influenced by the micro-galvanic and interfacial mechanisms, as well as amount of porosity present in the coatings
- WC-Inconel 625 coatings exhibited increased uniform corrosion damage compared to Inconel 625 alloys coating in seawater application. This was traced to the presence of different secondary carbides of different electrochemical potentials in the microstructure of the composite coating.

2.8 Gaps in Literature

Despite the extensive work that has been undertaken on the laser cladding of Inconel 625 and WC/Ni-alloy MMC, there are still issues that need to be resolved. Based on the literature, it was discovered that:

- An investigation of the process stability and characterisation of fibre laser cladding of Inconel 625 using wire as the feedstock material has not been achieved.
- The effects of the processing parameters including laser power, traverse speed and wire feed rate on the geometry and microstructure of the Inconel 625 wire laser deposited coating have not been investigated.
- The corrosion performance of laser clad Inconel 625 wire has not been investigated.
- Tungsten carbide reinforced Ni based alloys composite laser coatings have been extensively studied for wear performance. The electrochemical properties of these coatings have not been well researched.
- Till date, no literature on the study of laser deposition of metal matrix composite coatings has reported a case where metal matrix binder is fed in wire form with the aim of promoting the wettability at the ceramic-matrix interface. This is probably due to the high sensitivity of wire cladding process to the change in the processing parameters.
- Inconel 625 alloy either in powder or wire forms has not been extensively used as the matrix binder for MMC coatings. As a result, the study of the microstructure of the tungsten carbide/Inconel 625 alloy composite laser coating at varying processing parameters has not been presented.

- The corrosion performance of the WC-Ni based alloys is affected by the complex galvanic couple mechanism occurring due to microstructural modification and compositional inhomogeneity resulting from carbide dissolution. The direct effect of the amount of the tungsten carbide dissolution on the hardness and corrosion performance of the composite coating has not been explored.

3.0 Methodology

3.1 Introduction

This chapter details the materials and equipment used in the experimental work explored in this thesis. Processes including the laser cladding of Inconel 625 wire, Inconel 625 powder, and concurrent laser cladding of Spherotene (WC/W_2C) powder-Inconel 625 wire composite as well as the parameters used for each experiment are presented. Process characterisation, geometrical characterisation, dilution analysis, microstructural characterisation and corrosion measurements of the samples were done using various methods. The procedure for each method is described in this chapter.

3.2 Materials

3.2.1 AISI 304L stainless steel (substrate)

Austenitic stainless steel AISI 304 supplied by Smith Metals Nottingham was used as the substrate material. Plates of dimension 100 mm ×180 mm × 6 mm were prepared and then grit blasted and degreased with acetone before the cladding process so as to improve the substrate surface laser absorptivity and remove contaminants respectively. The chemical composition of the stainless steel, as received, is given in Table 3.1.

Table 3.1: Chemical composition (wt. %) of AISI 304L stainless steel

Ni	Cr	Mn	Si	Fe	C	P	S
7.86	18.58	1.78	0.42	71.15	0.08	0.10	0.03

3.2.2 Inconel 625 wire

Inconel 625 wire of diameter 1.2 mm was supplied by VBC group, Loughborough, UK. The chemical composition of the wire, as received, is shown in Table 3.2. The chemical composition, especially the Fe content (0.14 wt. %) is within the limiting range of the alloy 625, as given in Table 2.1 in chapter 2.3.2.

Table 3.2: Chemical composition (wt. %) of Inconel 625 wire (as received)

Ni	Cr	Mo	Nb	Fe	C	Al	Ti
64.56	22.46	8.84	3.46	0.14	0.02	0.26	0.26

3.2.3 Inconel 625 powder

Gas atomised Inconel 625 powder was obtained from Laser Cladding Technology, Sheffield, UK. The chemical composition of the powder, as determined by Energy Dispersive X-ray (EDX) analysis, is presented in Table 3.3. The values presented in Table 3.3 are averages of five measurements. The composition is within the limiting chemical composition of the alloy and very close to the values presented in Table 3.2.

Table 3.3: Chemical composition (wt. %) of Inconel 625 wire (as received)

Element	Ni	Cr	Si	Fe	Nb	Mo
Mean	63.4	22.0	0.4	0.2	3.9	10.2
Standard deviation	± 0.6	± 0.2	± 0.1	± 0.1	± 0.3	± 0.4

As defined by the supplier, the powder particle size range was 35-140 µm. The powder is spherical in shape. Figure 3.1a shows the morphology of the Inconel 625 powder, as received from the supplier.

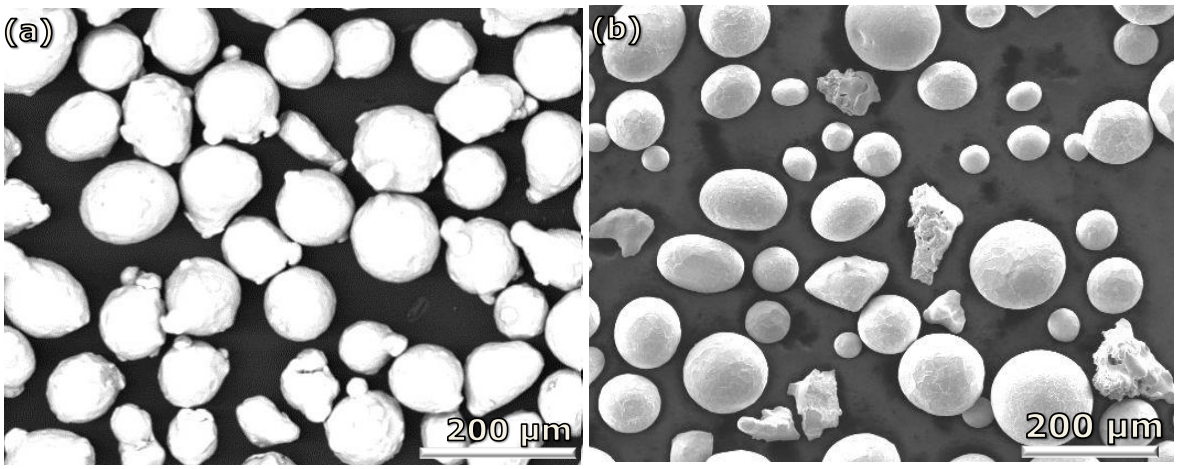

Figure 3.1: The morphology of the as-received (a) Inconel 625 powder and (b) Spherotene

3.2.4 Spherotene (WC/W_2C) powder

The WC/W_2C powder, commercially named as Spherotene, was supplied by Technogenia, France through laser cladding technology, Sheffield, UK. The powder is nearly spherical as shown in Figure 3.1b. It was produced using a unique, patented process called cold crucible induction fusion system. The powder size range is 40-260µm, as defined by the manufacturer.

3.3 Powder size distributions

The powder size distribution was determined using a Malvern Mastersizer-S (Malvern Instruments Limited, Malvern, UK). The powders are dispersed and circulated by water through the machine. The powder particles pass through the laser beam (optical unit) causing the light to scatter. The Mastersizers' optical unit (comprises annular detectors) capture the actual scattering pattern from a field of particles. Based on the Fraunhofer diffraction model, the powder size is predicted from the scattering pattern (called measurement) of the light beam. The raw data contained in the measurement is analysed by the Malvern software (V

2.18) interfaced with Mastersizer-S to obtain results in the form of particle vol % in different size ranges.

3.4 Laser processing – Experimental set-up

The laser cladding experiments were carried out with a 2-kW Ytterbium doped fibre laser (IPG Photonics) operating at 1070 nm ± 6 wavelength. The beam was focused to a round spot of about 3.1mm at 20 mm away from focus giving a 212 mm working distance with a Gaussian energy distribution. The fibre laser head (Prectec YW50) was mounted on a 4-axis gantry system with a worktable controlled by CNC. To prevent oxidation, all the deposition runs were performed inside a transparent enclosure which was evacuated and back-filled with high purity argon gas supplied at 25 l min^{-1}. A WF200DC wire feeder (Redman Controls and Electronic Ltd) and a Miller Thermal (Model 1264) powder feeder were used for all the depositions made in this work. The detailed procedure and the selected range of processing parameters for each laser cladding process are explained in the following sections.

3.4.1 Laser deposition of Inconel 625 wire single tracks

The objectives of the experiment were to:

1) Develop a stable process for Inconel 625 wire laser cladding. This includes the development of a process window within which continuous laser tracks of Inconel 625 can be deposited.
2) Investigate the process characteristics of Inconel 625 wire laser cladding within the developed process window
3) Control the Fe dilution in the deposited tracks which is known to affect corrosion properties.

4) Investigate the microstructural features of the tracks at a range of processing parameters, hence, determine their effect on the micro-hardness of the tracks.

Figure 3.2 shows a picture of the experimental set-up for this experiment. Inconel 625 wire was "front fed" at an angle of $42^{o} \pm 1$ to the horizontal so as to aim the wire tip at the centre of the meltpool. Single track depositions were performed at varying laser cladding parameters. Prior the start of the depositions, a working distance of 10 mm was kept between the substrate and the feed wire tip. In order to make sure that the substrate temperature is close to the room temperature for each deposition run, a minimum of 5 minutes cooling time was allowed between two successive runs. Also, a space of 10 mm was allowed between two consecutive tracks on the same plate. The ranges of processing parameters used were selected following preliminary trials so as to reduce the number of experimental runs required. The utilised parameters are given below:

Laser power (kW) – 1, 1.2, 1.4, 1.6, 1.8

Traverse speed (mm min^{-1}) – 100, 200, 300

Wire feed rate (mm min^{-1}) – 400, 600, 800, 1000, 1200

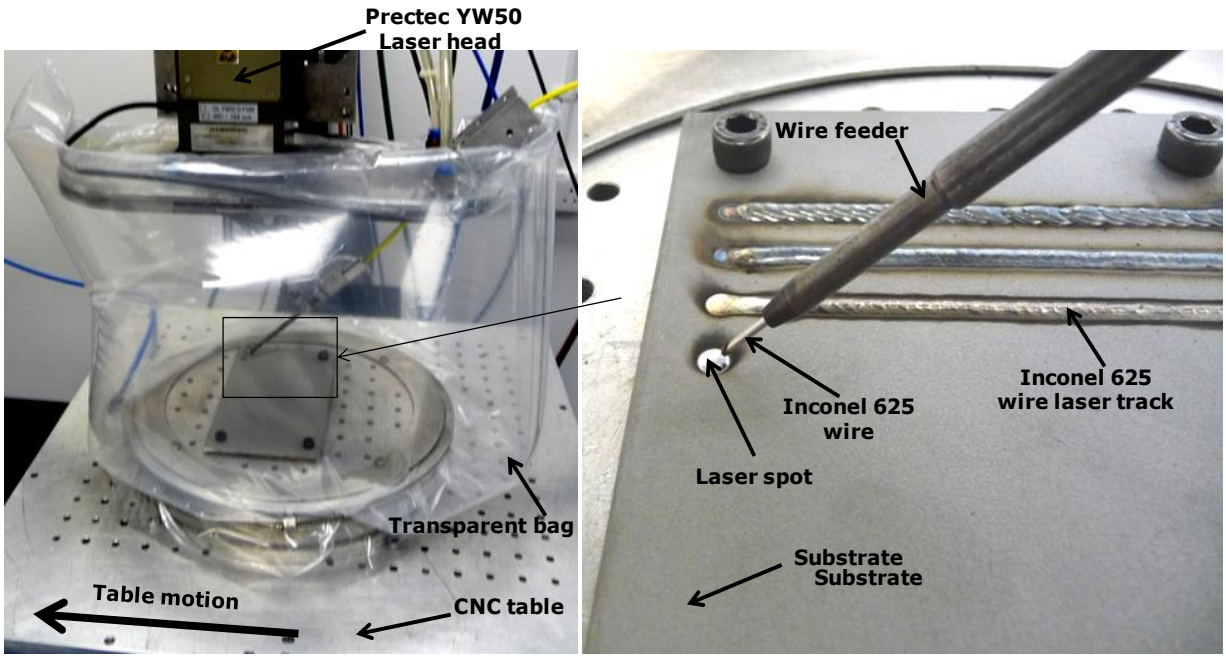

Figure 3.2: Experimental set-up for Inconel 625 wire laser deposition

Single tracks were deposited with combinations of laser powers and traverse speeds at varying wire feed rates ranging from 400 mm min^{-1} until stubbing was observed i.e. the wire hitting the substrate. This process was repeated for all possible parameters (i.e. processing conditions) within the selected range of laser power and traverse speed (totalling 84 processing conditions). Two tracks were deposited at each processing condition to provide a degree of verification. Table A1 in Appendix A presents the processing conditions employed in this experiment.

3.4.2 Laser deposition of Inconel 625 powder single tracks

The objectives of this experiment are to:

1. Deposit continuous single laser tracks of Inconel 625 powder at the processing conditions comparable with those utilised for the Inconel 625 wire laser cladding described in section 3.4.1.

2. Compare the laser cladding processes with wire and powder feeding system in terms of track qualities including degree of substrate (Fe) dilution ratio, microstructural evolution, micro-hardness and corrosion behaviour.
3. The economy of the two processes will also be compared.

Single laser tracks of Inconel 625 powder were deposited with an experimental set-up similar to the one in section 3.4.1 except that the wire feeding system was entirely replaced with the powder feeding system. The powder was fed by argon gas into the meltpool through a Praxair (Model 1264) powder feeder. The side-fed powder nozzle was oriented at 67° to the horizontal so as to improve the deposition efficiency of the powder. The ranges of laser power and traverse speed used were similar to those utilised in section 3.4.1 above. However, due to the lower deposition efficiency of the powder, compared with the wire, the powder feed rate (PFR) was ranged between 10 and 30 g min^{-1}. Table A3 in Appendix A presents the varying processing conditions utilised for the laser cladding of Inconel 625 powder.

3.4.3 Laser cladding of Spherotene (WC/W_2C) powder -Inconel 625 wire composite

The objectives of the experiment are to:

1) Deposit continuous and well bonded WC/W_2C powder-Inconel 625 wire composite tracks that are crack- and pore-free.
2) Study the effects of Spherotene powder injection on the process characteristics of Inconel 625 wire laser cladding
3) Investigate the extent of Fe dilution and Spherotene particle dissolution in the composite tracks as a function of the processing parameters. The results obtained from these will be related to the micro-hardness and corrosion performance of the tracks.

4) Identify the phases present and determine their effects on the micro-hardness and corrosion behaviour of the tracks.

Figure 3.3 shows a picture of the concurrent wire and powder laser deposition system used in this work. The wire was "front fed" (ahead of the laser) at an angle of $42^{o}\pm1$ to the horizontal so as to aim the wire tip at the centre of the meltpool. Spherotene powder was simultaneously back-fed into the meltpool by argon gas flowing at 10 l min^{-1}. The powder nozzle was set to an angle of 67^{o} to the horizontal. Single tracks were deposited at all processing conditions used for the Inconel 625 wire laser deposition except for those where wire stubbing was observed. The processing conditions are listed in Table A4 in Appendix A. In order to effectively study the extent of the Spherotene dissolution as a function of the laser power, traverse speed and wire feed rate, the powder feed rate was kept constant at 25 g min^{-1} throughout this experiment.

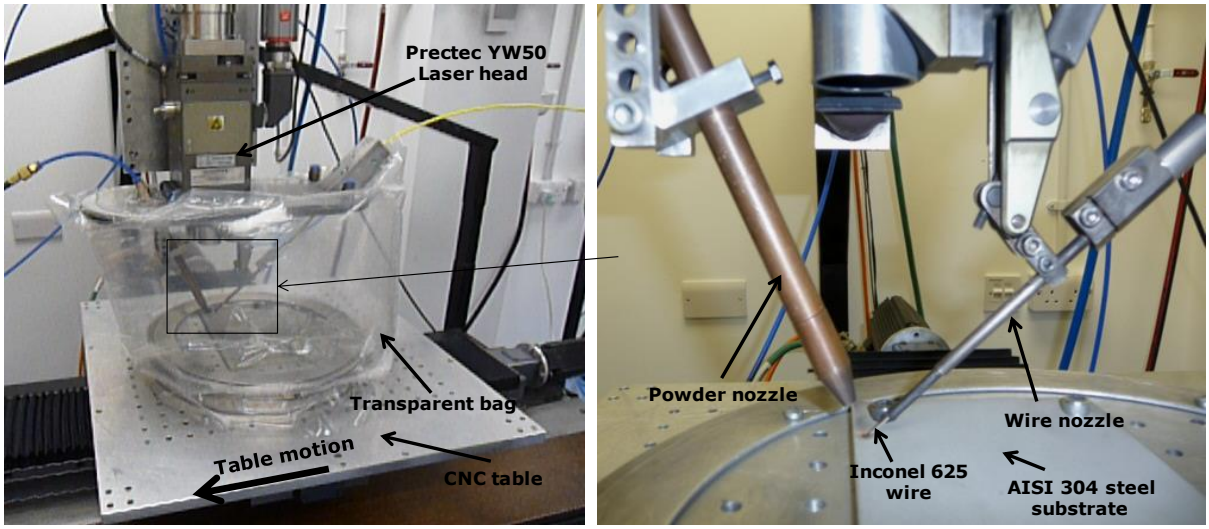

Figure 3.3: Experimental set-up for WC/W_2C powder-Inconel 625 wire laser deposition

3.4.4 Laser cladding of overlapped-track layers

Overlapped-track layers of Inconel 625 wire, Inconel 625 powder and WC/W_2C powder-Inconel 625 wire composites were made from the continuous single tracks using the

procedures described in sections 3.4.1, 3.4.2 and 3.4.3 respectively. 60% overlapping ratio was used and at least five parallel tracks were deposited in each case.

3.4.5 Combined deposition parameters for the process map

One of the aims of this work is to develop maps which predict the process characteristics of Inconel 625 wire laser cladding and concurrent laser cladding of Spherotene powder-Inconel 625 wire within a process window. In order to accommodate all the main processing parameters (i.e. laser power, traverse speed and wire feed rate) in the process maps, combined processing parameters was applied. Laser energy per unit length of track (E_L) in J mm^{-1} and wire deposition volume per unit length of track (W_{vol}) in mm^3 mm^{-1} were determined from equations 3.1 and 3.2 respectively. In the equations, P is the laser power in Watts, V is the traverse speed in mm min^{-1}, WFR is the wire feed rate in mm min^{-1} and A is the cross-sectional area of the feed wire in mm^2.

$$E_L = 60\frac{P}{V} \tag{3.1}$$

$$W_{vol} = \frac{A \times WFR}{V} \tag{3.2}$$

3.5 Track geometry: height and width measurement

Typical track geometry is described in Figure 3.4 where H is the track height (mm), h is the depth of meltpool (mm), W is the track width (mm) and β is the contact angle (degrees)**.** The heights and widths of the deposited tracks were measured using surface profiler Taylor Hobson Precision Machine (Talysurf CLI 1000).

The surface profiler traversely scanned each track at three equally spaced points within a set travel range of 50 mm. With the aid of Talysurf CLI 1000 software, each track profile was

displayed graphically and levelled so as to eliminate errors due to distortion of the substrate after laser processing. The heights and widths at the three points along the length of a track were displayed on the profile. The three heights were averaged and the three width values were also averaged. The mean values represent the height and width of the track. The contact angle or clad angle was determined using equation 3.3 [52].

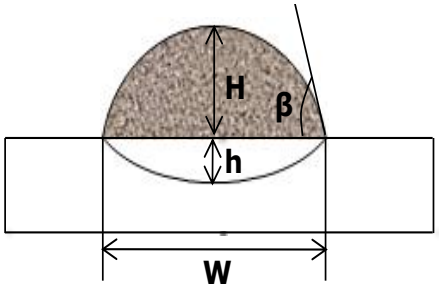

Figure 3.4: Typical track geometry

$$\beta = 2\arctan\left(\frac{2H}{W}\right) \qquad (3.3)$$

3.6 Metallographic techniques and sample preparation

Each track sample underwent standard procedures of specimen preparation including cutting, mounting, grinding, polishing and etching. Thereafter, microstructural analysis and hardness tests were conducted.

3.6.1 Cutting, mounting, grinding and polishing of samples

In order to investigate the microstructural features across the track length, 10 mm long samples were transversely and longitudinally cut from the deposited tracks. The cuts were made around the mid-length of the track because experience has shown that it takes 2-3 seconds for laser deposition process to become stable. Figure 3.5 describes how the tracks were sectioned.

For the purpose of carrying out X-ray diffraction analysis, some selected samples were further cut such that a planar surface was produced on the top of the samples. All samples were cut using wire electro-discharge machining (wire-EDM) and cut-off machine. There were no significant microstructural changes after cutting with EDM and if any change was present, it was removed after grinding and polishing of the samples.

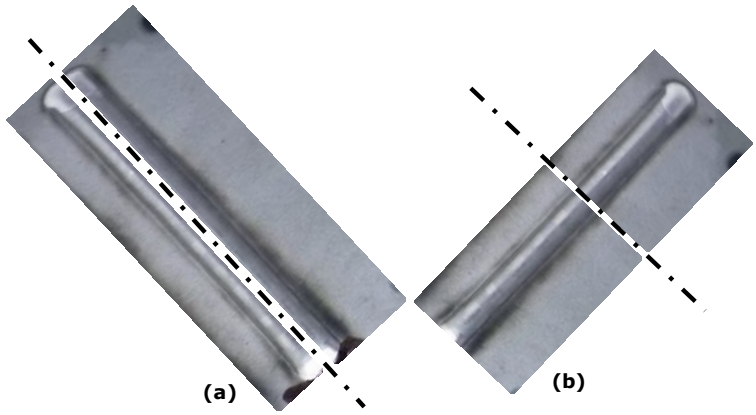

Figure 3.5: Sectioning of a track sample in (a) longitudinal and (b) traverse direction

The cut samples were hot mounted in conductive resin. The mounted samples were sequentially polished with SiC papers of grades 240, 400, 800 and 1200 using a Struers Labopol-21 grinding machine. Thereafter, ground samples were polished using a 1 μm diamond paste.

3.6.2 Etching

The samples were examined in polished and in etched conditions depending on microstructural features intended to be studied. Polished samples were etched electrolytically with 70% orthophosphoric acid in water with the cathode and anode being a stainless steel plate and the track sample respectively. The voltage was set at 6 V for 3-5 seconds depending on the time taken for the desired microstructure feature to be clearly revealed.

3.7 Metallographic techniques

3.7.1 Optical microscopy

Optical microscopy was utilised to reveal the microstructure of the samples. The grain growth and directions of the deposited samples were clearly revealed using a Nikon optical microscope with objective lens of 5, 10, 20 and 40 X. The DXM1200F digital camera of the microscopy was connected to computer acquisition software so as to clearly view, capture, record and store the micrographs of samples in digital form. In order to obtain optimum resolution of the track microstructures, contrast was enhanced by adjusting the dark field illumination, polarised light and the phase contrast of the microscopic system.

3.7.2 Scanning electron microscopy

Further microstructural examination was performed on polished samples using scanning electron microscopy (SEM; FEI XL30) with both secondary electron (SE) and backscattered electron (BSE) signals. SEM was also used in combination with energy dispersive X-ray (EDX) so as to determine the elemental composition of microstructural features (or phases) observed in the track samples.

3.7.3 X-ray diffraction

X-ray diffraction (XRD) was utilised in order to identify the phases present in the track samples and determine their crystal structures. A Bruba D500 with Cu-K_α radiation of wavelength 0.1 nm was used. For all the analysis, XRD scans were performed at 40 kV with a step size of 0.01^o and a dwell time of 5.6 seconds per step in the 2θ range of $25\text{-}110^o$.

3.8 Dilution measurement

Dilution of the Inconel 625 wire and Inconel 625 powder tracks were measured from the compositions of the track samples. Track samples were examined by scanning electron microscopy (SEM) using the BSE signal. Energy dispersive X-ray analysis was then utilised to determine the elemental composition of the sectioned track samples by conducting 200 μm x 200 μm area scan along and across the track height, as shown in Figure 3.6. Since Fe is the solvent element of the substrate and its content in Inconel 625 is nearly negligible, the dilution ratio was calculated from the increased Fe content in the deposited tracks. The average of Fe composition (wt.%) obtained from the scanned areas within a track area above the clad-substrate interface was determined. Thereafter, the clad-substrate dilution (D) was estimated using equation 3.4 [86].

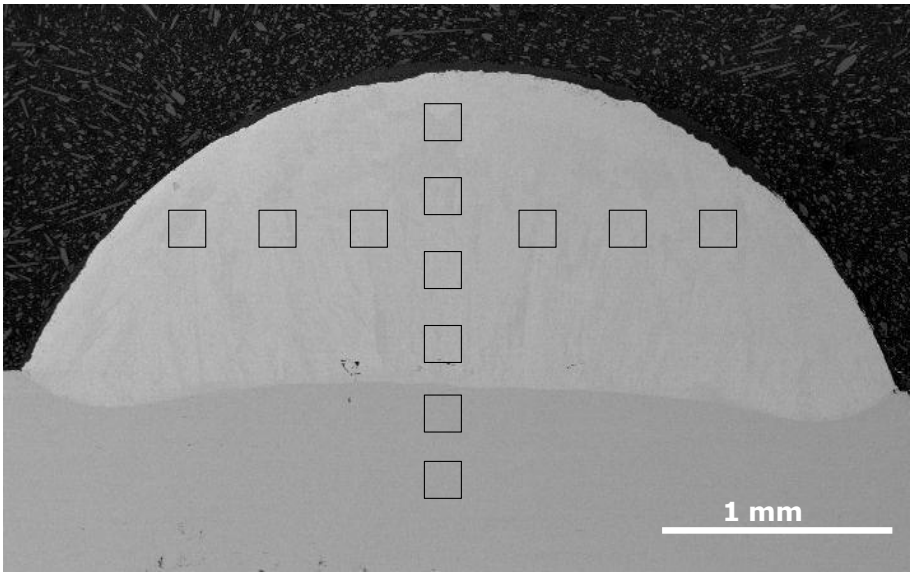

Figure 3.6: SEM micrograph showing EDX area scan analysis conducted on a transversely sectioned Inconel 625 wire track

$$D = \frac{\rho_A (X_T - X_A)}{\rho_S (X_S - X_T) + \rho_A (X_T - X_A)} \qquad (3.4)$$

Where ρ_A and ρ_S are the densities in g mm^{-3} of the additive and substrate materials respectively. X_T and X_S are the mean weight percentage of Fe in the track and substrate respectively while X_A is the weight percentage of Fe in the additive material. In this case, it is Inconel 625.

3.9 Spherotene powder deposition efficiency

The powder deposition efficiency in the composite tracks was determined using weighing method. However, the following underlying assumptions were made for this method.

- The flow of powder is constant throughout the deposition process
- There is zero dissolution of the injected Spherotene powder
- Volume change during solidification process is negligible

The step by step procedures for determining the Spherotene powder deposition efficiency are described below.

(1) Mass of the substrate: Firstly, the volume (length × width × height, mm^3) of the substrate was calculated and the result was multiplied by its density (8.0×10^{-3} g mm^{-3}) to give the mass (g) of the substrate. Alternatively, the mass of the substrate was confirmed by weighing the substrate plate before the deposition. The mass difference in the results obtained from the two methods was negligible. The mass of the substrate was denoted as M_1.

(2) Mass of the deposited wire: 80 mm long Inconel 625 wire single track was deposited on the substrate whose weight had been pre-determined as M_1. The deposited Inconel 625 wire track and the substrate were weighed and the mass (g) was recorded as M_2. The mass (g) of the deposited wire (M_{wire}) was determined as shown in equation 3.5.

$$M_{wire} = M_2 - M_1 \qquad (3.5)$$

(3) Mass of the Spherotene powder captured: Spherotene powder-Inconel 625 wire composite single track of length 80 mm was deposited on another but similar substrate of mass M_1. The processing parameters used in step 2 above were the same except for the concurrent injection of Spherotene powder at PFR of 25 g min^{-1}. The composite track including the substrate was weighed and the mass (g) was recorded as M_3. The mass of the powder captured (M_{PC}) was determined by mass difference as illustrated in equation 3.6.

$$M_{PC} = M_3 - M_2 \qquad (3.6)$$

(4) Mass of Spherotene delivered: The mass of the Spherotene powder delivered (M_{PD}) from the nozzle was calculated from the equation 3.7.

$$M_{PD} = \frac{PFR \times L}{V} \qquad (3.7)$$

L in equation 3.6 is 80 mm and it is the length of the composite track. V is the traverse speed in mm min^{-1}.

(5) Spherotene powder deposition efficiency: The Spherotene powder deposition efficiency (P_{eff}) was determined using equation 3.8.

$$P_{eff} = \frac{M_{PC}}{M_{PD}} \times 100 \qquad (3.8)$$

3.10 Spherotene (WC/W2C) volume fraction

3.10.1 Volume fraction of Spherotene captured in the composite track

The percentage fraction of the volume of the Spherotene captured to the total volume of the composite track was defined as the volume fraction of the Spherotene captured. However, the following underlying assumptions were made in its calculation.

- There is no dissolution of Spherotene powder in the composited track
- There is no volume expansion in the track
- The flow of Spherotene is constant throughout the deposition
- There is negligible substrate dilution

The procedures involved are:

(1) Volume of Spherotene Captured (V_{PC}): The volume spherotene captured was determined by multiplying the mass of the Spherotene captured (M_{PC}) by the density of the Spherotene powder (16.3×10^{-3} g mm^{-3}).

(2) Volume of the wire deposited (V_{wire}): Likewise, the volume of the Inconel 625 wire deposited was found by multiplying the mass of the wire deposited (M_{wire}) by the density of Inconel 625 (8.44×10^{-3} g mm^{-3}).

(3) Volume fraction of Spherotene captured (VF_{PC}): This was determined using the equation 3.9 below.

$$VF_{PC} = \frac{V_{PC}}{V_{PC} + V_{wire}} \times 100 \qquad (3.9)$$

3.10.2 Volume of Spherotene retained in the composite track

This was measured from the cross-sectional areas of the deposited composite tracks. At least, 14 BSE/SEM micrographs, each at 200 × magnification, were taken with a scanning electron microscope at different parts of the transversely sectioned single track samples, as shown in Figure 3.7. The volume fraction of the retained Spherotene (VF_{PR}) in each micrograph was analysed using Image J processing software. The software measures the percentage fraction of bright contrast to the entire track area in the micrograph. The retained Spherotene particles appeared much brighter than the matrix. The recorded volume fraction of the Spherotene

retained in each composite track is an average of at least 14 measurements taken randomly across the track cross-section.

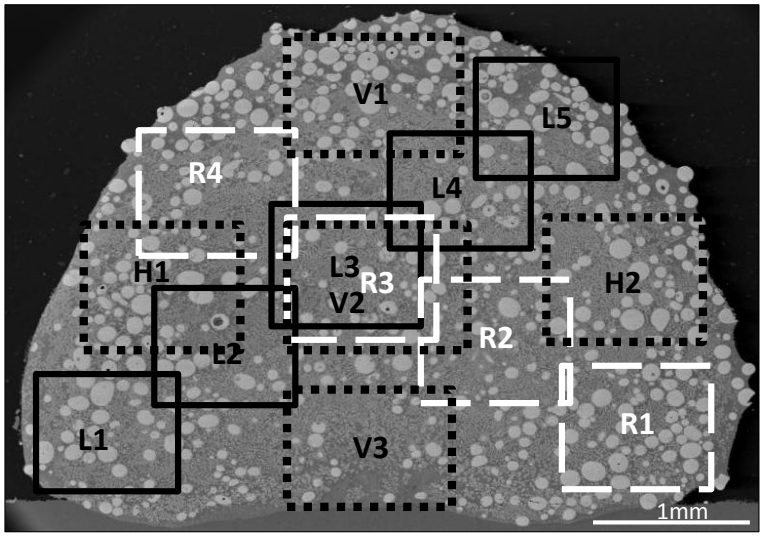

Figure 3.7: A transversely sectioned WC powder-Inconel 625 wire single track showing measurement areas for image analysis of WC.

3.10.3 Dissolution ratio

The term 'dissolution ratio' in this study indicates the relative amount of Spherotene dissolution in the composite tracks. It was determined using equation 3.10. The difference between the volume fractions of the Spherotene particle captured and Spherotene particle retained is considered as the volume fraction of the Spherotene particle dissolved in the composite tracks.

$$D_{Ratio} = \frac{VF_{PC} - VF_{PR}}{VF_{PC}} \qquad (3.10)$$

This ratio of this difference to the volume fraction of the Spherotene particle captured is the dissolution ratio. It was later converted to a percentage.

3.11 Pores and cracks identification

The transverse and longitudinal cross-sections of the continuous track samples and the deposited overlapped-track layers of Inconel 625 powder, Inconel 625 wire and WC/W_2C powder-Inconel 625 wire composite were polished. These samples were examined under SEM for the crack and pores identification.

3.12 Hardness measurements

Micro-hardness tests were conducted on polished cross-sectional area of the track using a LECO M400 Vickers micro-hardness tester with a load of 300 gf (i.e. 5N) applied for 15 seconds. The indentations were made, starting from the substrate, along the centreline of the transversely cut tracks up to the track top at 150 μm intervals. In the case of the composite coating, indentations were randomly made on the matrix and the retained Spherotene particles separately.

3.13 Corrosion study

The corrosion behaviour of the AISI 304L substrate and coatings of Inconel 625 (Inconel 625 wire and Inconel 625 powder laser coatings, and concurrently fed WC/W_2C powder-Inconel 625 wire composite laser coatings) were investigated using open circuit potential and potentiodynamic polarisation tests. These tests were carried out for all the samples according to the guidelines stated in ASTM standards G5-94 and G61-86 respectively [109].

3.13.1 Sample preparation

At least, four 100 mm^2 square samples were cut, using EDM, from the overlapped track layers of each of the coatings whose corrosion behaviours were to be measured. The samples from each coating were ground to the same thickness (mid-height from the substrate). This

was done so as to reduce variations in the microstructures of the samples' top surfaces. The results obtained from the microstructural characterisation of the deposits show that the solidification mode changed along the height of the track. Therefore, it is believed that large variations in the microstructure could significantly alter the corrosion results of the samples obtained from the same track layer. Thereafter, the samples were hot-mounted in non-conductive resin. A hole was drilled through the back of the hot-mounted sample until there was a contact with the material sample in the resin. The hole was threaded and a brass rod was screwed into the hole until an electrical contact was established between the specimen and the rod. Plastic tubing was used to prevent contact between the rod and the electrolyte during the tests.

The mounted samples were sequentially polished with SiC papers of grades 240, 400, 800 and 1200 and then polished to 1 μm surface finish using diamond paste. The boundary between each of the samples and the mounting resin was covered by applying stop-off lacquer. The reason was to avoid the possibility of crevice corrosion effects on the corrosion results.

3.13.2 Corrosion test

Electrochemical measurements of all the samples were performed in saline media (3.5% NaCl) at room temperature using a three electrode cell, as shown in Figure 3.8. The electrolyte was de-aerated by nitrogen gas purging for at least 30 minutes prior to sample immersion in order to ensure that the experiment is carried out in an oxygen free environment. This continued throughout the experiment.

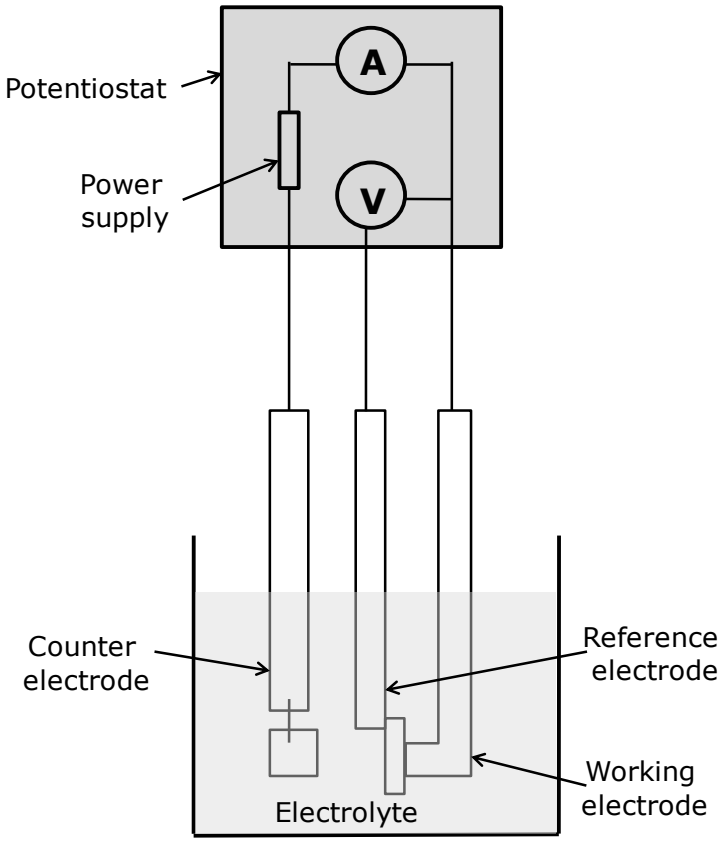

Figure 3.8: A schematic diagram of experimental set-up for three-electrode cell utilised for corrosion tests

The sample, which is the working electrode (WE), was immersed in the electrolyte and was allowed to stabilise for 60 minutes before polarising the potential against a reference electrode. Ag/AgCl electrode and the platinum plate were used as the reference and counter electrode, respectively. With the use of a potentiostat (ACM instruments, Cumbria, UK), potentiodynamic polarisation scans were performed for all the samples with the sweep rate of 20 mV min^{-1} from 1-hour open circuit potential (E_{oc}). The potential scanned over the range of -200 mV to 1500 mV. The corresponding current flow between the WE and the platinum counter electrode (CE) was recorded for each scan. After each scan, the corroded area of the sample was measured using image J processing software. The recorded current values were divided by the measured area to give current density (mA cm^{-2}). The polarisation curve for each scan was plotted with potential (mV wrt Ag/AgCl electrode) as ordinate and logarithm

of absolute current density as abscissa. For each track layer, the tests were repeated at least three times to verify the reproducibility.

Table 3.4: Parameters used for the corrosion measurement

Symbol	Meaning	Unit
E_{corr}	Corrosion potential	mV
E_{oc}	Open circuit potential	mV
E_b	Breakdown potential	mV
I_p	passive current density	mA cm^{-2}

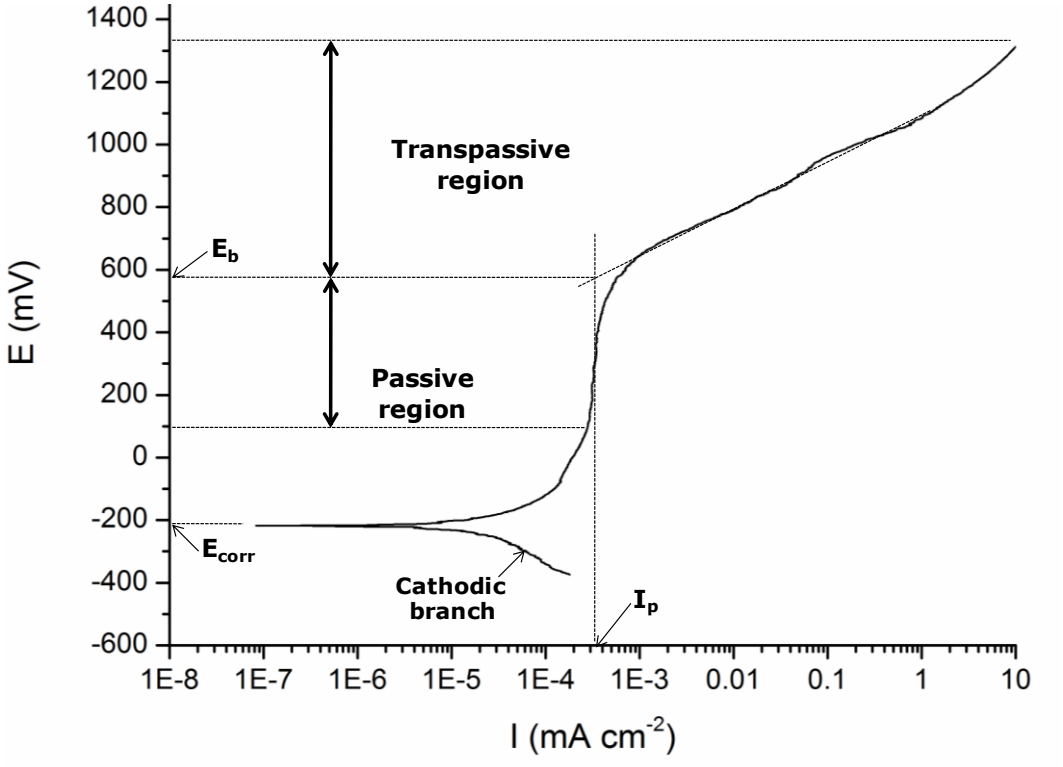

Figure 3.9: Representative polarisation curve and location of different parameters

Table 3.4 defines the different parameters used for the corrosion study. The representative polarisation curve showing the locations of these parameters is presented in Figure 3.9. It is

essential to know that the corrosion potential (E_{corr}) and open circuit potential (E_{oc}) have been used interchangeably in the literature. In this study, the E_{oc} is defined as the corrosion potential without the application of any external potential source whereas E_{corr} is taken as the potential when there is no current flow at cathodic to anodic transformation during the polarisation scan with external voltage source.

4.0 Process, geometrical and microstructural characterisations of Inconel 625 wire and Inconel 625 powder laser cladding

4.1 Introduction

This chapter investigates the fibre laser cladding with lateral feeding of Inconel 625 wire and Inconel 625 powder on AISI 304L stainless steel. Firstly, optimisation of the Inconel 625 wire laser cladding within a process window was performed and is reported. Secondly, geometrical and microstructural characterisations of the continuous tracks, produced within the process window, are detailed. The results presented include dilution ratio, melt depth into the substrate, microstructural evolution and micro-hardness as a function of the processing parameters. Thereafter, the geometries, microstructure and micro-hardness of a typical Inconel 625 wire track are compared with the similar track qualities of a corresponding Inconel 625 powder single laser track formed using a comparable processing condition. The results of the microstructural examination of (1) Inconel 625 wire and (2) Inconel 625 powder overlapped-track layers including coating-substrate interfacial bonding, pore and crack formation and dilution ratio are also presented. This chapter contains the results, discussion and a summary of the important findings for fibre laser cladding using Inconel 625.

4.2 Laser deposition of Inconel 625 wire

4.2.1 Laser deposition with wire: Process stability

Single laser tracks of Inconel 625 wire (Ø 1.2 mm) were deposited using the experimental set up described in section 3.4 with the wire tip aiming at the centre of the meltpool. This was achieved by creating a laser spot on the substrate prior wire depositions. Thereafter, the wire

tip was set to the centre of the spot. Most of the depositions performed with the wire tip aiming at the meltpool leading edge resulted in discontinuous tracks, for example, as shown in Figure 4.1a. When the wire tip was aimed at the centre of the meltpool, continuous laser tracks were formed at appropriate processing parameters, as shown in Figure 4.1b and 4.1c. This indicates that the stability of the wire cladding process is dependent on the position of the wire tip in the meltpool.

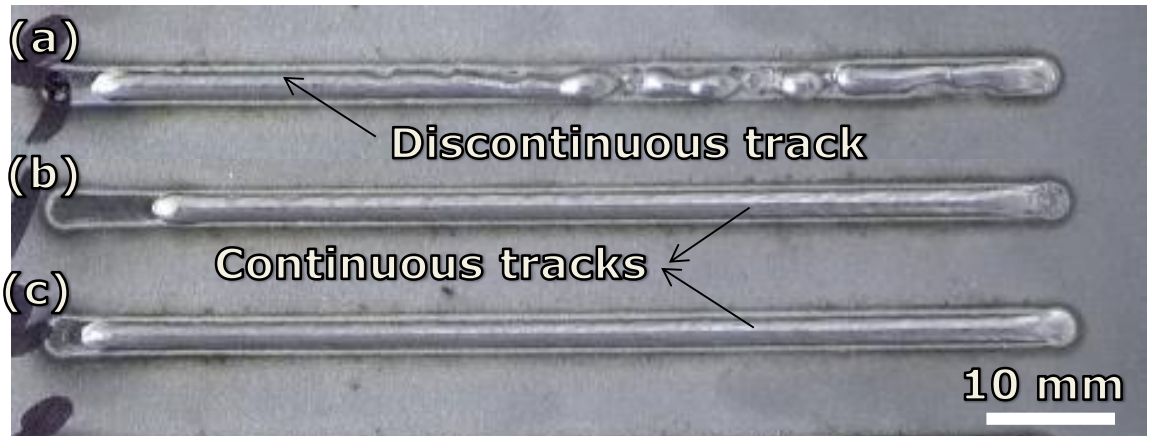

P = 1 kW, V = 200 mm min^{-1}, WFR = 400 mm min^{-1}

Figure 4.1: Macrographs of Inconel 625 wire (Ø1.2 mm) laser tracks formed with wire tip aiming at the (a) leading edge and (b-c) centre of the meltpool

In order to determine a suitable process window for Inconel 625 wire laser cladding, trial experiments were conducted at various processing parameters with the wire tip aiming at the meltpool centre. The laser power was varied between 1.0-1.8 kW and the selected range for the traverse speed was 100-500 mm min^{-1}. Laser deposition was performed at various possible combinations of laser power and traverse speed. For each combination, wire feed rate was gradually increased from 400 mm min^{-1} until wire stubbing was observed.

One of the reasons for the choice of laser power (1.0-1.8 kW) was that maximum output power of the fibre laser used is 2.0 kW. Also, experience has shown that with low laser power and/or high traverse speed, successful laser cladding process is usually not possible because

of low laser energy density which may result in insufficient melting of the large volume of material fed into the meltpool.

P = 0.8 kW, V = 100 mm min^{-1}, WFR = 600 mm min^{-1}

Figure 4.2: Photographs of discontinuous Inconel 625 wire laser tracks caused by the feed wire tip hitting the base of the meltpool therefore oscillating about the meltpool centre

(a): P = 1.2 kW, V = 500 mm min^{-1}, WFR = 600 mm min^{-1}
(b): P = 1.2 kW, V = 500 mm min^{-1}, WFR = 800 mm min^{-1}

Figure 4.3: A photograph of poor quality tracks showing un-melted Inconel 625 wire at low laser power and extremely high traverse speed

For example, as shown in Figure 4.2, most of the cladding conducted at <1.0 kW laser power, at varying traverse speed and wire feed rate selected for the trial experiment, produced discontinuous tracks. Likewise, as shown in Figure 4.3, nearly all the depositions conducted in the trial experiment using the selected range of laser power (1.0-1.8 kW) and wire feed rates from 400 mm min^{-1} with traverse speed above 300 mm min^{-1} produced poor quality (i.e. un-melted wire) tracks. The reason can be attributed to extremely low energy density at high traverse speed.

4.2.2 Laser deposition with wire: Process characteristics

Following initial trials, a process window for the laser deposition of Inconel 625 wire was established as shown below.

Laser power (kW): 1.0, 1.2, 1.4, 1.6, 1.8

Traverse speed (mm min^{-1}): 100, 200, 300

Wire fee rate (mm min^{-1}): 400, 600, 800, 1000, 1200

Single laser tracks were deposited with combinations of laser power (P) and traverse speed (V) with varying wire feed rate (WFR). All combinations of the processing parameters are within the established process window. Figure 4.4 presents some examples of single laser tracks deposited on an AISI 304L substrate.

At each processing condition, the behaviour of wire at the point of entering the meltpool was observed. Three behaviours of wire including wire dripping, smooth wire transfer and wire stubbing were noticed. The process characteristics were defined based on these behaviours. Wire dripping often termed as droplet transfer of wire is the intermittent dropping of wire into the meltpool. This was caused whenever the incident energy was excessive for the wire feed rate. On the other hand, wire stubbing occurred whenever the wire feed rate was excessive for the available incident energy. At this condition, the feed wire entered the meltpool un-melted therefore, hitting the substrate at the base of the meltpool. The cladding process was considered to be characterised by smooth wire deposition each time there was smooth flow of wire into the meltpool.

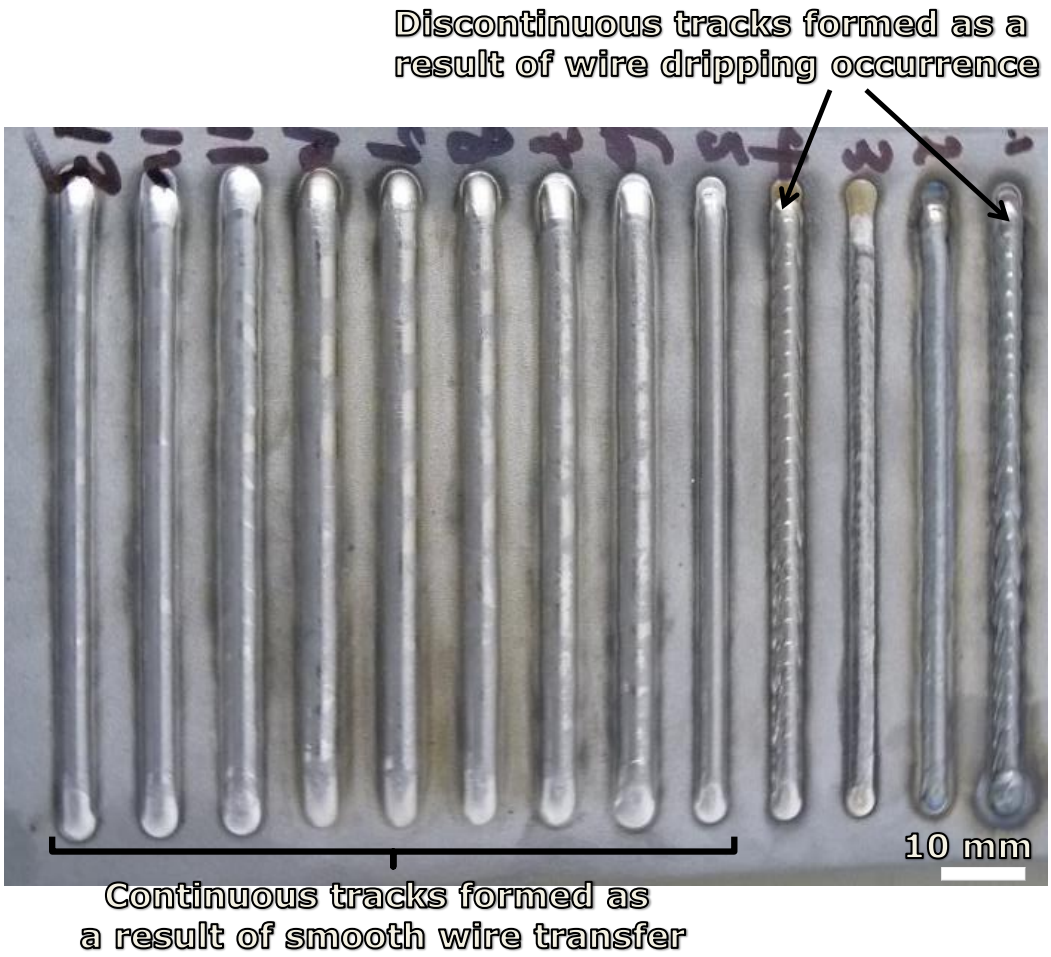

Figure 4.4: Examples of Inconel 625 wire single laser tracks deposited within the process window

In order to provide some degree of verification, the process was repeated for all possible combinations of the processing parameters within the process window. Table A1 of Appendix A presents each processing condition (i.e., a combination of the laser power, traverse speed and wire feed rate) and the corresponding process characteristic (i.e. behaviour of the feed wire). The summary of the results of the geometrical characterisation of the Inconel 625 wire laser tracks is presented in Table A2 of Appendix A. This includes the height, width, cross-sectional area, aspect ratio and contact angle of the single tracks.

4.2.3 A process map

As shown in Figure 4.5, a process map which characterises the results of Inconel 625 laser cladding at varying processing conditions was developed. The map is valid for the process window established earlier in section 4.2.2 using the experimental set-up presented in Chapter 3.4.1. Five different regions are defined in the map with 1-5 representing: dripping, dripping may occur, smooth wire deposition, stubbing may occur and stubbing regions respectively. In order to accommodate all the three main processing parameters (i.e. laser power (P), traverse speed (V) and wire feed rate (WFR)) in the map, the combined processing parameters defined in section 3.4.5 of chapter 3 were used. Energy per unit length of track (60P/V) in J mm^{-1} was plotted against wire deposition volume per unit length of track (A*WFR/V) in mm^3 mm^{-1}. 'A' represents the cross-sectional area (mm^2) of the feed wire. Each processing condition is represented by a point on the map.

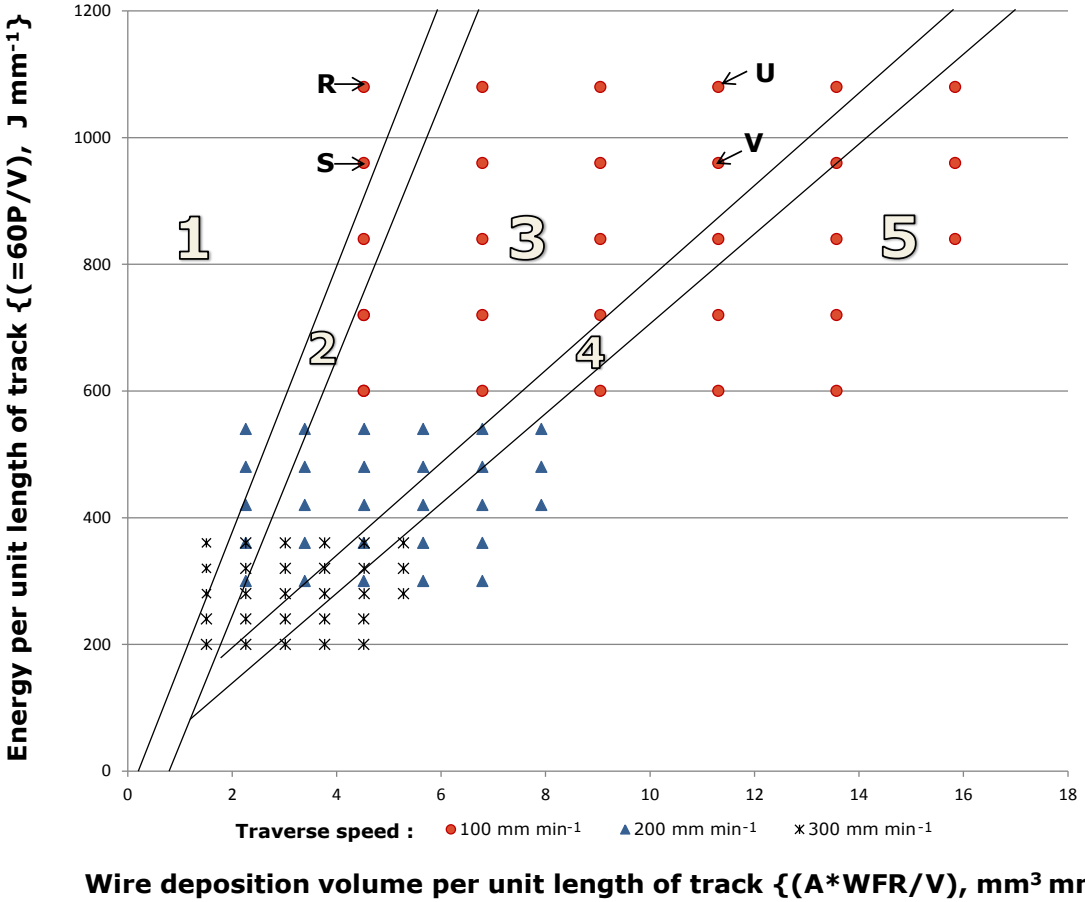

(1) Dripping, (2) Dripping may occur, (3) Smooth wire deposition, (4) Stubbing may occur and (5) Stubbing regions

Figure 4.5: A process map showing the process characteristics of Inconel 625 wire laser cladding

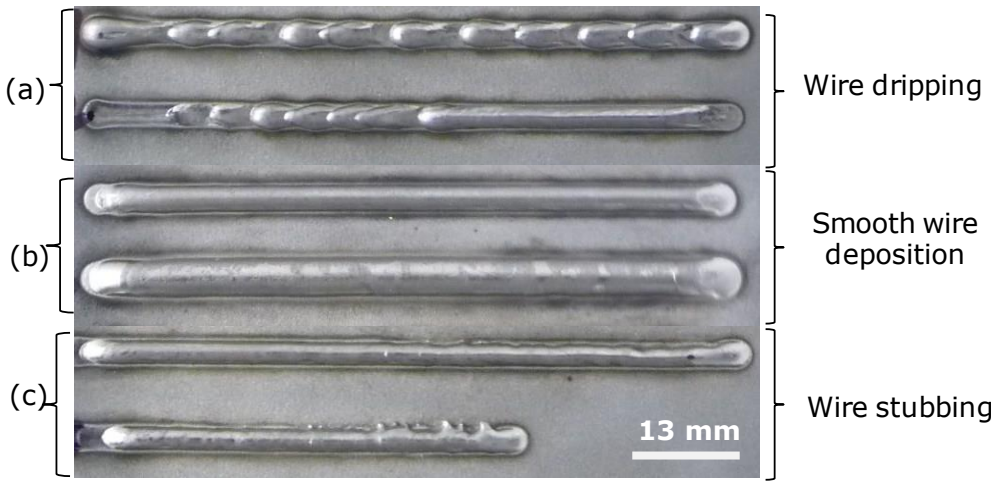

Figure 4.6: Typical laser tracks of Inconel 625 laser cladding

Table 4.1 presents the processing conditions and the corresponding process characteristics of the points spotted ‘R’, ‘S’, ‘U’ and ‘V’ on the map. Points R and S are contained in the dripping region and the tracks produced at these conditions are discontinuous, for example, as seen in Figure 4.6. The typical examples of tracks deposited by the cladding processes characterised by smooth transfer of wire (see points U and V in the map) and stubbing of wire are also presented in Figure 4.6. As evidenced in Figure 4.6, continuous tracks were formed only when there was smooth wire deposition. More of the continuous tracks were formed at higher energy per unit length of track and lower traverse speed. As the traverse speed increases and energy per unit decreases, the region 3 (i.e. smooth wire deposition region) becomes narrower.

Table 4.1: The processing conditions and corresponding process characteristics of some marked points on the map shown in Figure 4.5

Point	Laser power (kW)	Traverse speed (mm min^{-1})	Wire feed rate (mm min^{-1})	Energy per unit length of track (J mm^{-1})	Wire deposition volume per unit length of track (mm^3 mm^{-1})	Deposition process characteristic without powder injection
R	1.8	100	400	1080	4.5	wire dripping
S	1.6	100	400	960	4.5	wire dripping
U	1.8	100	1000	1080	11.3	smooth wire transfer
V	1.6	100	1000	960	11.3	smooth wire transfer

The main objective behind the development of the process window and map was to determine and predict the processing conditions that produce continuous single tracks of Inconel 625 wire. The conditions that were characterised with wire stubbing and dripping are unsuitable for Inconel 625 wire laser cladding. The ideal scenario (i.e. smooth wire deposition) was observed whenever the feed wire melted at the point or close to the point of its intersection

with the meltpool. At these conditions (i.e. those represented in region 3 of the process map), the feed wire flows smoothly and continuously into the molten pool.

It is observed in the map that as the wire deposition volume per unit length of track increases, the cladding process characteristics change from wire dripping to smooth wire deposition to wire stubbing. This shows that at conditions where wire dripping was observed, the deposition process characteristics can be changed to smooth wire depositions by increasing the wire feed rate (i.e. wire deposition volume per unit length of track). Likewise, decreasing the wire feed rate at laser processing conditions where stubbing was observed can reverse the process characteristics to an ideal scenario.

As the energy per unit length of track increases, region 1 (i.e. wire dripping) and region 3 widen whereas region 5 (wire stubbing) becomes narrower. This is probably due to additional heat energy gained by the feed wire at increased energy per unit of length of track. The increased energy gain is believed to have expedited the melting of the wire therefore reducing the propensity of wire stubbing to occur.

Region 2 (i.e. dripping may occur region) formed the boundary between the dripping region and smooth wire deposition region. Laser deposition processes performed at the conditions corresponding to this region produced inconsistent characteristics because each of these processes were characterised with dripping and smooth wire transfer effects after at least two trials. As a result, it was difficult to correctly classify them either into dripping or smooth deposition region.

Also, region 4 is the boundary between smooth deposition region and wire stubbing region. Due to inconsistencies in their process characteristics, processing conditions that gave deposition run of wire stubbing effect and smooth wire transfer phenomenon after at least two different trials were grouped in this region. Finally, the map predicts that smooth wire

transfer may not be possible, with this arrangement, when cladding below energy per unit length of track of 200 J mm^{-1}.

4.3 Effects of the processing parameters on the dilution ratio of the Inconel 625 wire laser tracks

The substrate dilution should be controlled because Fe contamination in the Inconel 625 coatings affects its corrosion performance [82]. In this study, the dilution ratio of each continuous track was determined from the amount of Fe measured in the track area (see equation 3.4). The Fe wt. % compositions in the feed wire and the substrate are both known. The reason behind this is that Fe (71.5 wt. %) is the bulk element in the AISI 304L substrate. Therefore, the composition of the Inconel 625 wire in the meltpool can mainly be contaminated by Fe through inter-mixing of the molten wire with the substrate. The detailed procedure used for calculating the substrate dilution ratio in the tracks can be found in Chapter 3.8. Within the process window used in this study, the minimum and maximum Fe contents of the deposited tracks are 0.3 ± 0.1 and 21.8 ± 0.4 wt. % respectively. This gave dilution ratios of 0.2 and 24% respectively. The result of the dilution ratio for the Inconel 625 wire laser tracks is presented in Table B1 of Appendix B.

As presented in Figure 4.7, the result obtained from the elemental composition analysis (i.e. EDXA) established that the Fe content, hence, the percentage dilution of the examined track samples increases with increasing laser power and traverse speed but with decreasing wire feed rate.

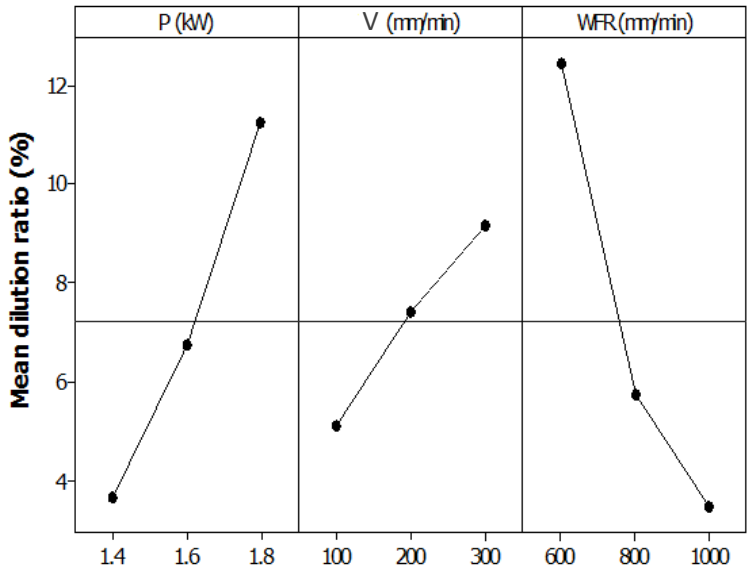

Figure 4.7: Main effects plot for dilution ratio of Inconel 625 wire laser tracks

The relative significance of the effects of each of the processing parameters on the track dilution ratio was studied using analysis of variance (ANOVA). Three levels of each parameter (i.e. laser power, traverse speed and wire feed rate) were selected for the analysis (see Appendix B). The ANOVA was achieved by analysing the mean dilution ratio of the tracks using Minitab software. The results were validated using the procedure described in Appendix B. Table 4.2 presents the degree of freedom (DOF), sum of squares (SS), mean square (MS), F value and P value calculated for each factor (i.e. the main processing parameters).

Table 4.2: Analysis of variance for dilution in the Inconel 625 wire tracks

Source	DOF	SS	MS	F	P	$F_{Critical}$
Laser power (kW)	2	261.9	130.94	20.39	0.000	3.4928
Traverse speed (mm min^{-1})	2	74.4	37.20	5.79	0.010	3.4928
Wire feed rate (mm min^{-1})	2	388.7	194.35	30.27	0.000	3.4928
Error	20	128.4	6.42			
Total	26	853.4				
S = 2.47207		R^2 = 85.80%		R^2(adj) = 81.54%		

From Table 4.1, the F value for each factor was compared with the critical F value as found in standard F-tables (see Table B2 in Appendix B) [110] for a significance level of $\alpha = 0.05$ (95% confidence). When the computed F value is lower than the critical value at the selected level of significance, the factor does not contribute to the sum of squares within the confidence level. As a result, it is considered insignificant. As seen in Table 4.2, the DOF for each of the three factors is 2 whereas the error term has 20 DOF. Therefore, at 95% confidence, critical F value F (2, 20) was found to be 3.5 for each factor. The computed F value of each of the three factors is greater than the critical showing that each of the three main processing parameters significantly influenced the dilution ratio. Wire feed rate with an F value of 30.27 has the most significant influence whereas the traverse speed with an F value of 5.79 relatively has the least significant influence on the dilution ratio of the Inconel 625 wire tracks. The F value for laser power is 20.39. R^2 of 0.86 obtained for this analysis indicates that there is a good correlation between the factors and the dilution ratio. The interaction effect was not considered because the intention was to study the individual effect of each of the parameters on the Fe dilution from the substrate.

4.4 Microstructural characterisation of Inconel 625 wire single laser tracks

Defects such as porosity, cracking and poor fusion at the track-substrate interface are important problems in laser cladding. Therefore, preventing these defects during laser processing is crucial to depositing high quality tracks. All the continuous tracks deposited with smooth wire deposition characteristics (as found in region 3 of the process map shown in Figure 4.1) were transversely sectioned. It was found that all were free of cracks and pores, and had good fusion with the substrate showing that it is possible to deposit defect-free

Inconel 625 tracks by laser cladding with wire. Figure 4.8 presents the optical images showing the transverse sections of some of the continuous tracks.

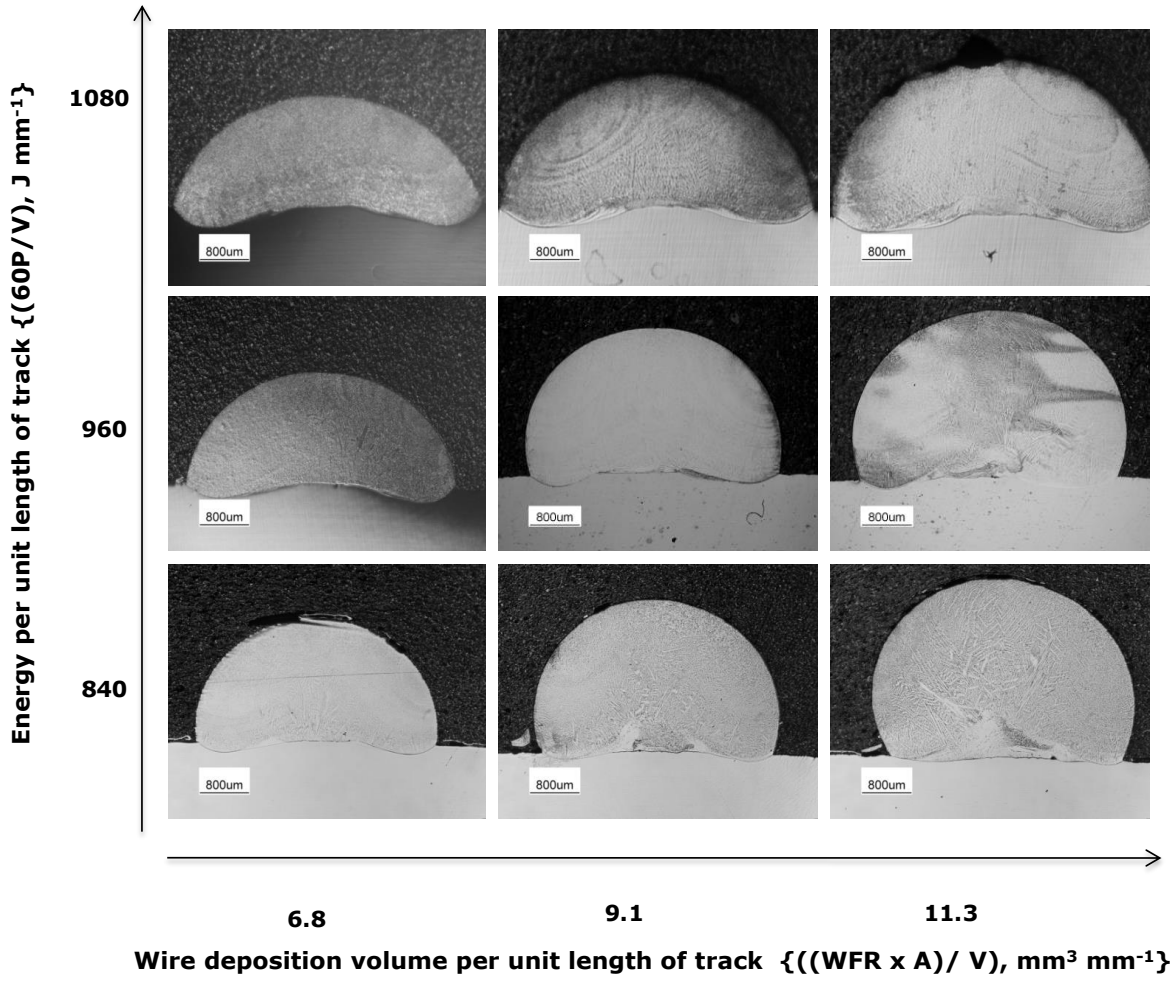

Figure 4.8: Etched optical macro-photographs of laser tracks cross-sections for Inconel 625 wire on AISI 304 stainless steel at traverse speed of 100 mm min^{-1}. P is laser power in W, V is traverse speed in mm min^{-1}, WFR is wire feed rate in mm min^{-1} and A is the cross-sectional area of the wire (Ø=1.2 mm).

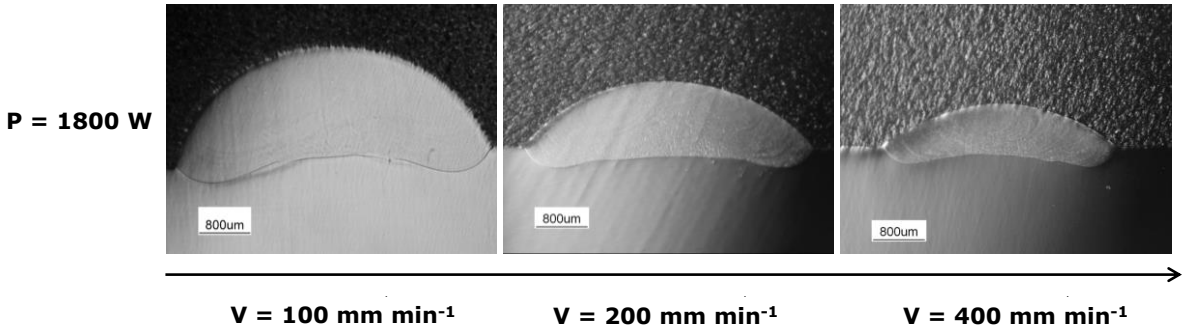

Figure 4.9: Etched optical macro-photographs of laser tracks cross-sections for Inconel 625 wire on AISI 304 stainless steel at different traverse speeds

Apart from the absence of these common defects in the track samples shown in Figure 4.8, visual observation of the cross-sectioned track samples in Figure 4.8 shows that melt depth into the substrate decreased whereas contact angle and track height increased with increasing wire deposition volume per unit length of track. Conversely, melt depth into the substrate increased but contact angle and track height decreased with increasing energy per unit length of track. Figure 4.9 shows that track height and contact angle significantly decreased with increasing traverse speed. However, melt depth into the substrate decreased slightly with the traverse speed.

As seen in Figures 4.8 and 4.9, the meltpool shape for all continuous tracks is convex to the substrate. This is thought to result from the interruption of the laser beam by the feed wire pointing to the centre of the meltpool. As a result, the substrate at the centre of the meltpool was obscured from the laser beam source and so less heating was experienced at the centre of the substrate.

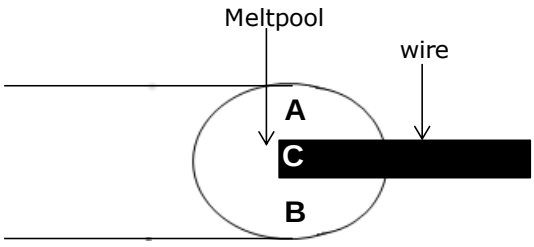

Figure 4.10: A schematic diagram showing the top view of the meltpool during laser cladding with wire

Schematic diagram of the top view of the meltpool is shown in Figure 4.10. Evidently, more heat energy was available to melt the substrate at regions A and B whereas region C is partly obscured from the laser beam by the feed wire.

4.4.1 Microstructural characterisation of Inconel 625 wire single laser tracks at low and high traverse speed

In order to investigate the effect of traverse speed on the microstructural evolution of the Inconel 625 wire laser track, two typical single track samples were selected for metallurgical analysis. The selected track samples were deposited at low (P = 1.8 kW, **V = 100 mm min^{-1}**, WFR = 600 mm mm^{-1}) and high (P =1.8 kW, **V = 300 mm min^{-1}**, WFR = 600 mm mm^{-1}) traverse speed settings. Both tracks were continuous. Optical micrographs showing the longitudinal views of the two track samples are shown in Figure 4.11.

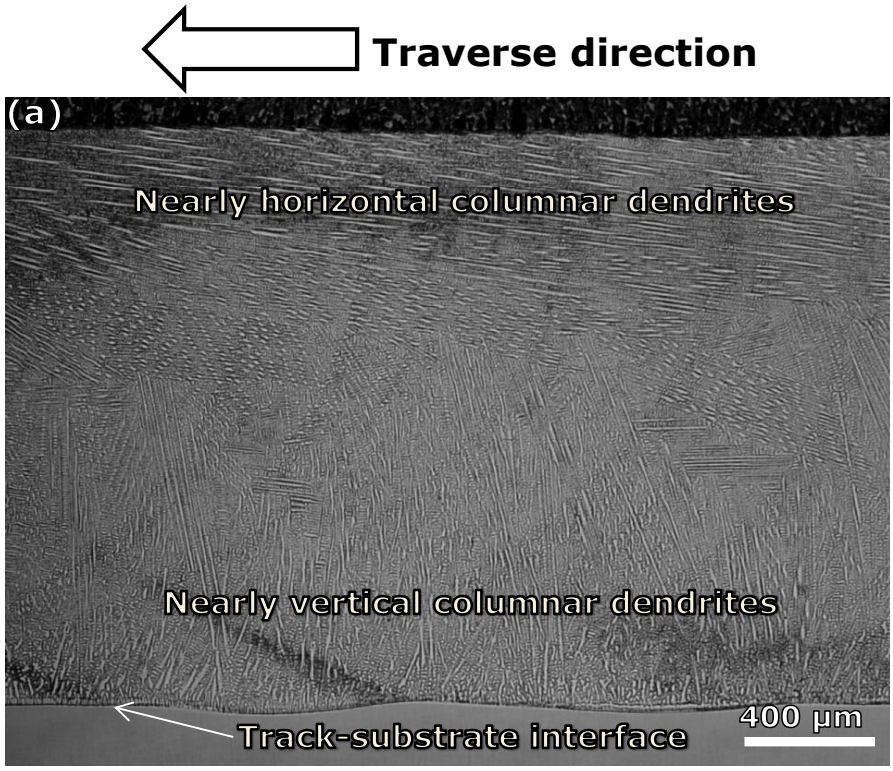

P = 1.8 kW, V = 100 mm min^{-1}, WFR = 600 mm min^{-1}

P = 1.8 kW, V = 300 mm min^{-1}, WFR = 600 mm min^{-1}

Figure 4.11: Optical micrographs showing longitudinal section of Inconel 625 wire laser tracks microstructures at different traverse speeds (a) 100 mm min^{-1} and (b) 300 mm min^{-1}

From the track-substrate interface of both samples, there was an evolution of columnar dendrites growing nearly vertical to the substrate. At lower traverse speed, the dendrites were slightly inclined towards the laser beam scanning direction. Just above the interface, the inclination was not apparent. However, close to the surface of the track, the inclination was clear, as seen in Figure 4.11a. At the top region of the sample (100 mm min^{-1}) was an evolution of near horizontal columnar dendrites. With a 300mm min^{-1} traverse speed, the near horizontal columnar dendrites were replaced by an equiaxed solidification mode, as shown in Figure 4.11b.

Figure 4.12 and 4.13 show the respective tracks (at 100 and 300 mm min^{-1} traverse speeds) at higher magnification. The transition from near vertical to near horizontal columnar dendrites is seen in Figure 4.12. Figure 4.13 shows clearly the transition from vertically growing columnar dendrites to a predominantly equiaxed structure.

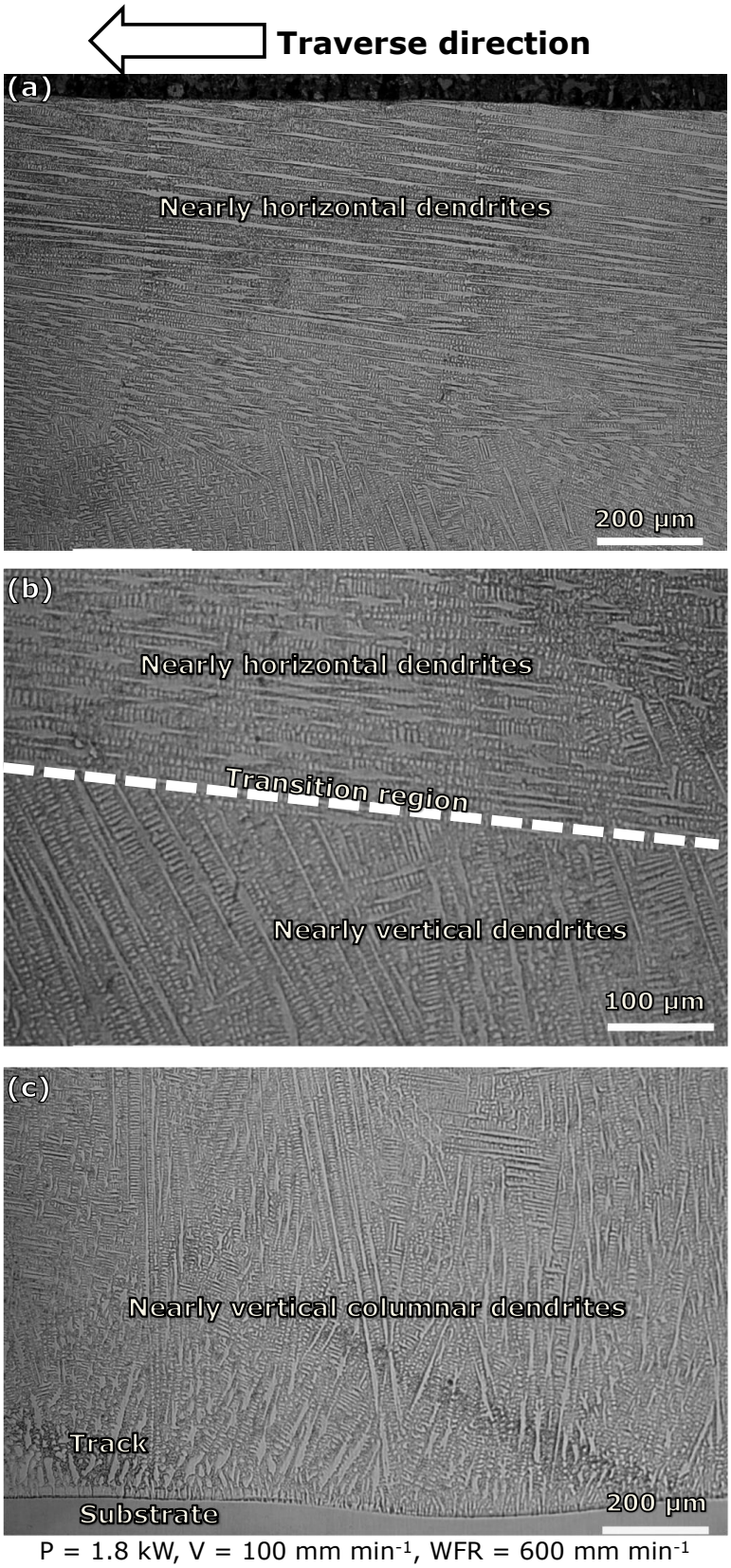

P = 1.8 kW, V = 100 mm min^{-1}, WFR = 600 mm min^{-1}

Figure 4.12: Optical images showing different regions of the Inconel 625 wire laser track of Figure 4.11(a). (a) Near surface region, (b) transition from vertical columnar dendrites to horizontal columnar dendrites and (c) bottom region

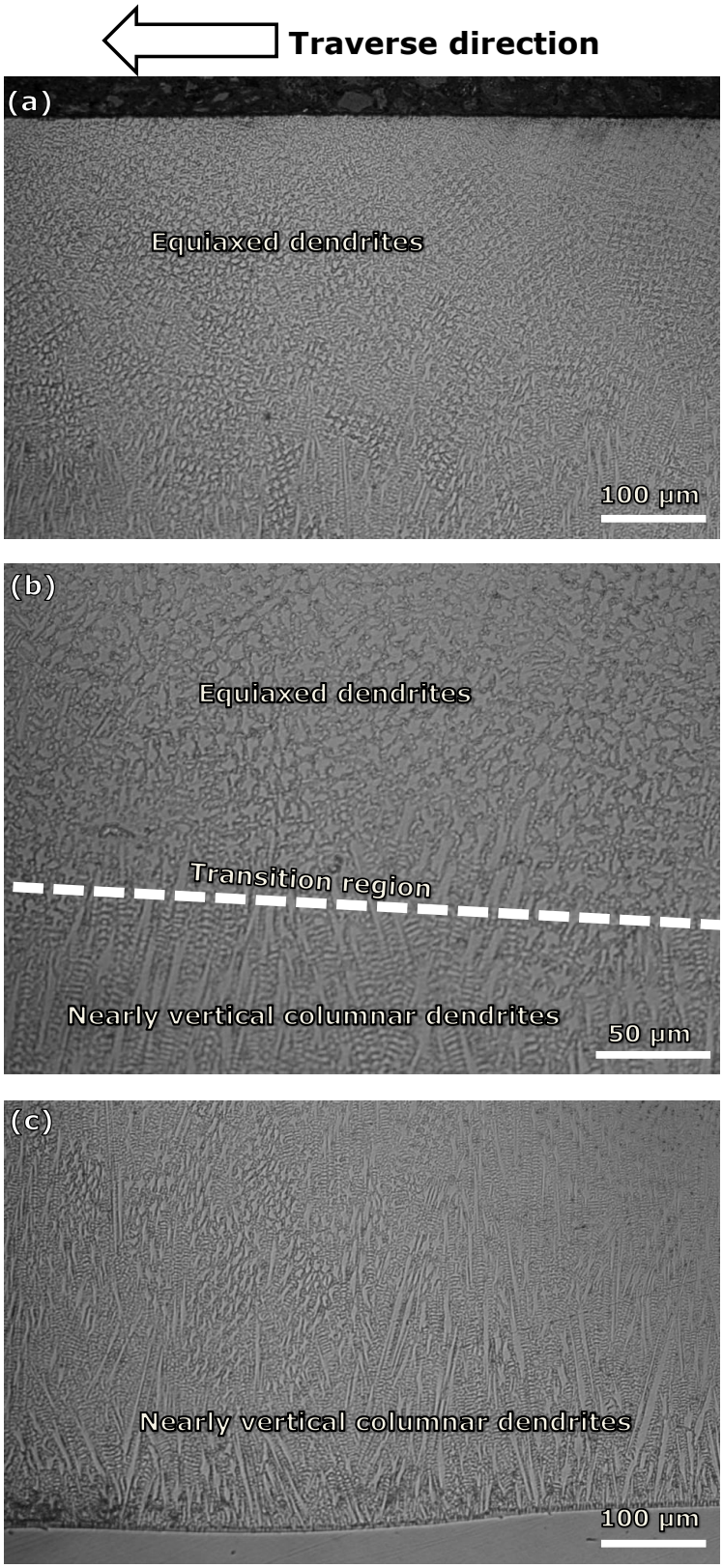

P = 1.8 kW, V = 300 mm min^{-1}, WFR = 600 mm min^{-1}

Figure 4.13: Optical images showing different regions of the Inconel 625 wire laser track of Figure 4.11(b). (a) Near surface region, (b) region of the transition of columnar dendrites into equiaxed dendrites and (c) bottom region

4.4.2 Phase identification of Inconel 625 wire laser tracks

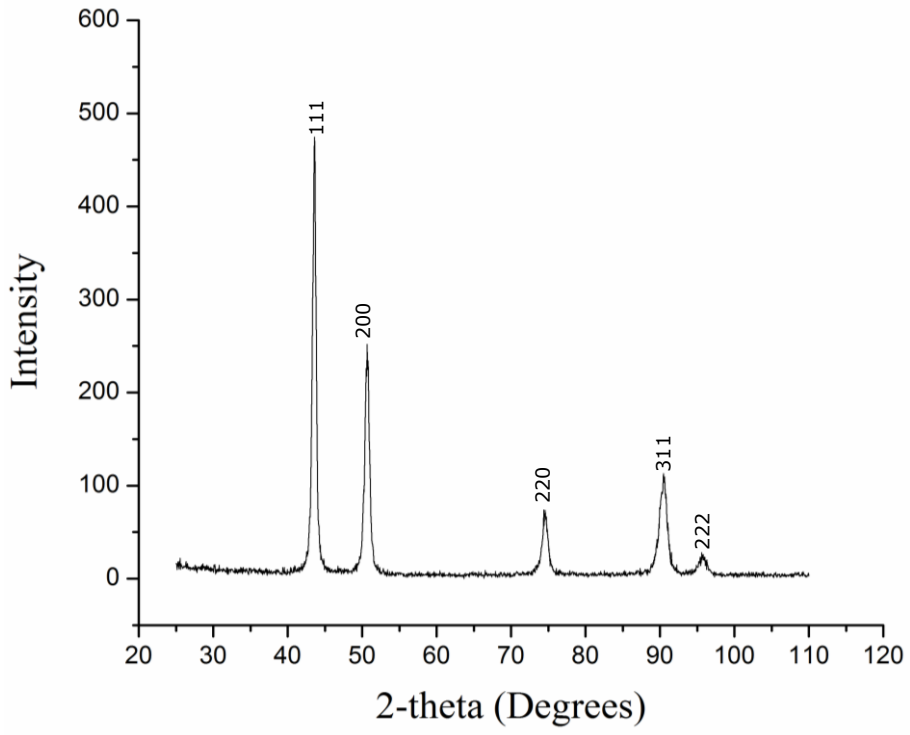

Figure 4.14: XRD spectrum showing the FCC structure of Inconel 625 wire laser track

The results obtained from the XRD analysis conducted on the top surface of the two track samples are identical. Figure 4.14 shows the XRD spectrum for the top surface of the two tracks. The major peaks in the spectra were found at $2\theta = 43.5^{o}$, 50.7^{o}, 74.6^{o}, 90.5^{o} and 95.8^{o}. The JCPDS file number is presented in Appendix C (Figure 1) However, the peak positions for pure Ni from the ICDD-database were found at $2\theta = 44.5^{o}$, 51.9^{o}, 76.4^{o}, 92.9^{o} and 98.5^{o} (see Appendix C, Figure 3). Apparently, pure FCC Ni phase occurred at slightly higher values of 2-theta when compared with the positions where major peaks were observed in the XRD spectra of the laser tracks of Inconel 625 wire. The difference in the lattice parameters is due to alloying elements in the solid solution of Inconel 625. This affected the inter-planar spacing of the γ-Ni present in the coating. No phases other than an FCC γ-Ni phase with lattice parameter close to pure Ni could be detected. However, the limit of detection for secondary phases by XRD is approximately 1-2%.

4.4.3 Elemental composition of phases present in a typical Inconel 625 wire laser track

Scanning electron microscopy (SEM) images, with secondary electron (SE) signal, of the single track layers show a light contrast precipitate in the interdendritic regions, as seen in Figure 4.15. EDX spot analysis was performed on the dark continuous matrix region A and region B (light contrast precipitate). The results are summarised in Table 4.3 which is the average of 5 measurements. It is evident that matrix composition is significantly richer in Fe (9.2 wt. %) when compared with the wire feedstock which has a Fe composition of 0.14 wt. %. This can be attributed to dilution of Fe from the stainless steel substrate. It is also evident that the precipitate is richer in Mo and Nb compared to the matrix. However, the precipitate is depleted in Fe, Cr and Ni compared to the Ni-matrix. In the previous studies on solidification of Inconel 625 and Inconel 718, the secondary phase or the precipitates (most notably enriched in Mo and Nb) has been identified as either Laves phase or NbC depending on the composition of C, Si and Fe in the alloy composition [41]. In this case, the light contrast precipitate is considered to be Mo- and Nb-rich precipitate.

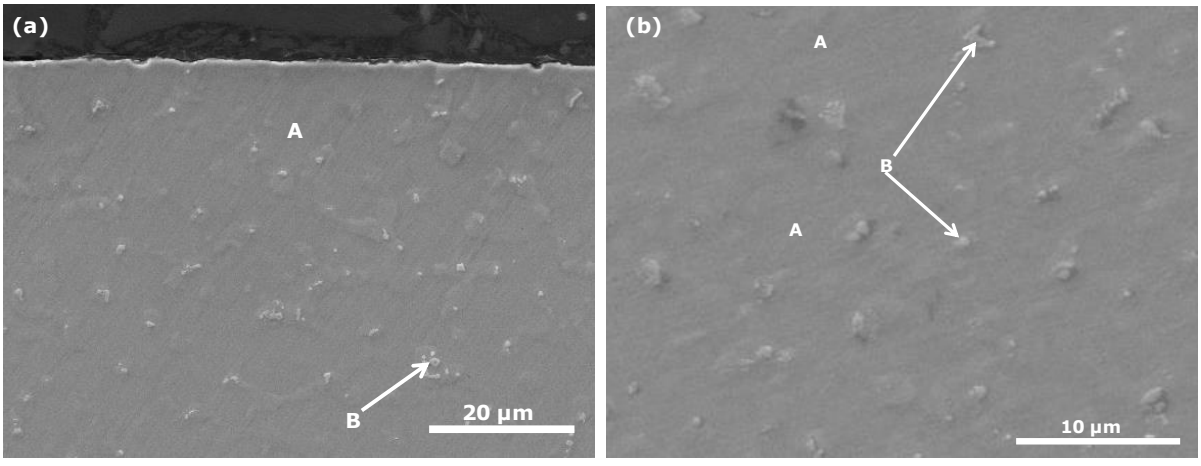

Figure 4.15: Secondary electron images showing the phases in the microstructure of the typical Inconel 625 wire laser tracks

Table 4.3: Elemental composition (wt. %) of phases present in single track deposit of Inconel 625 wire laser cladding

Traverse speed setting	Symbol	Phase	Cr	Fe	Ni	Nb	Mo
100 mm min^{-1}	A	FCC Ni matrix	23.2 ±0.2	9.2 ±0.4	56.4 ±0.5	2.3 ±0.4	8.6 ±0.3
	B	Precipitate	19.2 ±0.4	6.8 ±0.3	46.7 ±0.5	12.6 ±1.3	14.2 ±0.8

At a traverse speed of 100 mm min^{-1} (P = 1.8 kW, WFR = 600 mm min^{-1}), average Fe content in the track was 9.2 ± 0.4 wt. % (± SD). However, at higher traverse speed (300 mm min^{-1}), the iron composition in the track varied from 10.15 to 11.11 wt. % giving an average composition of 10.5 ± 0.3% (±SD). Dilution ratio of 11.9% and 13.3% were found for the Fe composition of 9.2 wt. % and 10.5 wt. % in the tracks. The increase in dilution ratio with increasing traverse speed is confirmed by the significant decrease in track height but only slight decrease in melted depth into the substrate at higher traverse speed, as shown in Figure 4.9.

4.4.4 Microstructural characterisation of Inconel 625 wire single laser tracks at high and low wire feed rates

Figure 4.16 shows the optical micrographs of Inconel 625 wire single laser tracks at different settings of wire feed rate but the same laser power of 1.8 kW and traverse speed of 100 mm min^{-1}. At a lower wire feed rate of 600 mm min^{-1}, near vertical columnar dendrites developed from the track-substrate interface up to the near top region of the track. With a higher wire feed rate of 1000 mm min^{-1}, cellular solidification mode was observed at the bottom region of the track. At about 0.3mm above the interface, there was a transition from cellular solidification mode to vertically growing columnar dendrites. Also, the microstructure of the track formed at the higher wire feed rate appeared to have a relatively coarse microstructure when compared with the microstructure of the track sample deposited at lower wire feed rate.

The reason for the coarser microstructure found at 1000 mm min^{-1} wire feed rate could be attributed to reduced cooling rate.

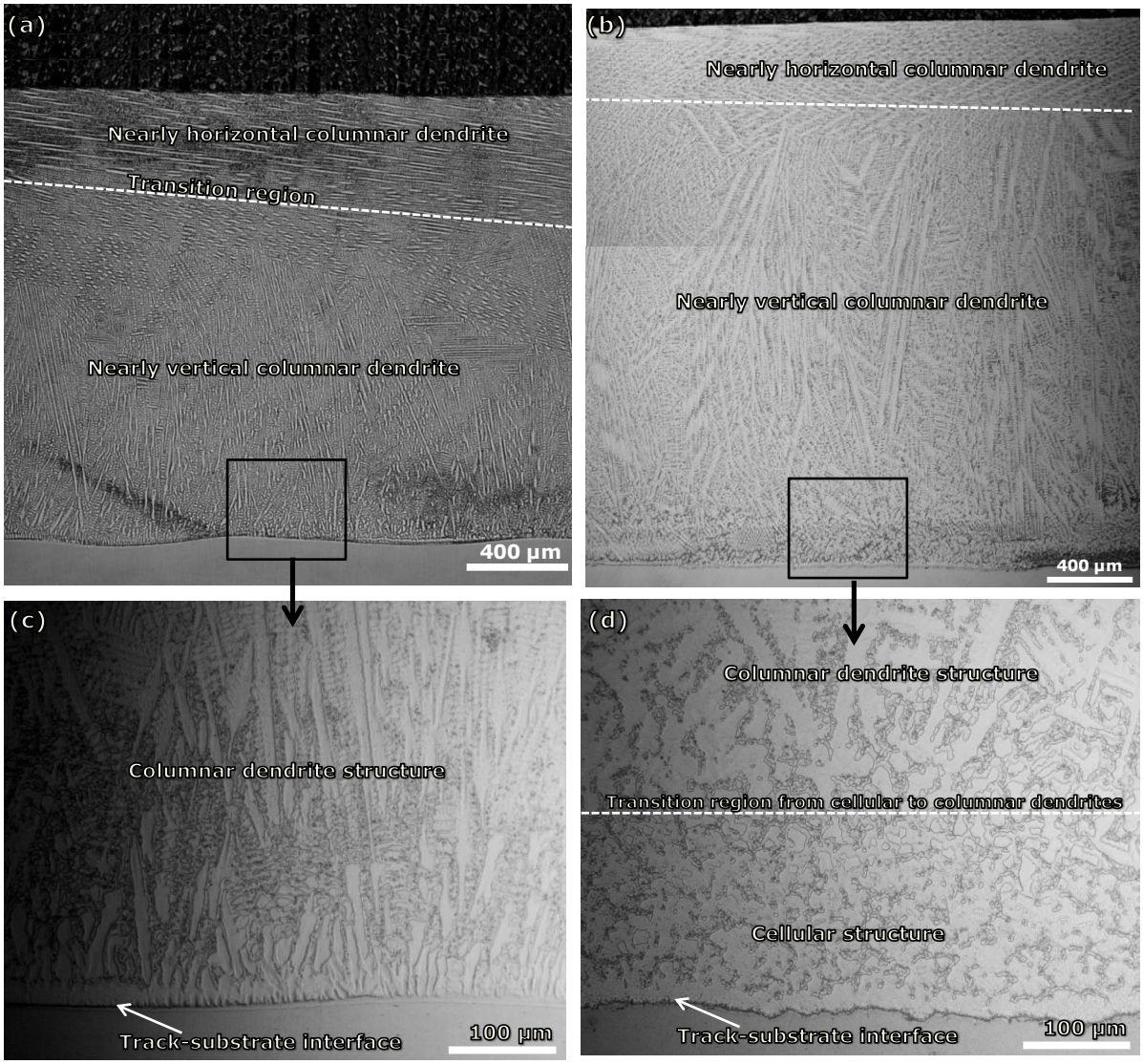

Figure 4.16: Optical micrographs showing longitudinal section of Inconel 625 wire laser tracks microstructures at wire feed rates of (a) 600 mm min^{-1} (b) 1000 mm min^{-1}

Figure 4.17 clearly shows the near horizontal dendrites occupying the entire top region of the track microstructures shown in Figure 4.16. The size of the region containing the near horizontal columnar dendrites decreased from 636 ± 20 µm to 383 ± 14 µm as the wire feed rate increased from 600 to 1000 mm min^{-1}.

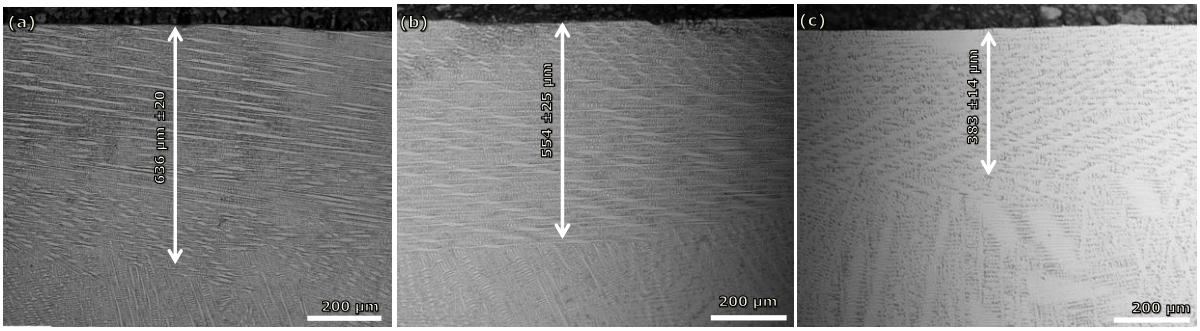

Figure 4.17: Formation of near horizontal columnar dendrites near the track surface at wire feed rates of (a) 600 mm min^{-1}, (b) 800 mm min^{-1} and (c) 1000 mm min^{-1}.

4.4.5 Microstructural characterisation of Inconel 625 wire single laser tracks at high and low laser power

Figure 4.18 presents the optical images of tracks deposited at low (1.4 kW) and high (1.8 kW) laser power settings. Both tracks were deposited at the same traverse speed of 100 mm min^{-1} and wire feed rate of 600 mm min^{-1}. Comparing the two images, the microstructure of the track deposited at 1.4 kW was predominantly characterised by equiaxed dendrites from the interface up to the near top region. At the top region, the equiaxed dendrites were replaced with columnar dendrites growing parallel (i.e horizontally) to the track-substrate interface. On the other hand, the track formed at 1.8 kW appeared to be relatively coarse and mainly characterised with the vertical growth of columnar dendrites evolving from the track-substrate interface. At the top regions of the two tracks, horizontal columnar dendrites blocked-off the vertical dendrites preventing them from reaching the tracks surfaces.

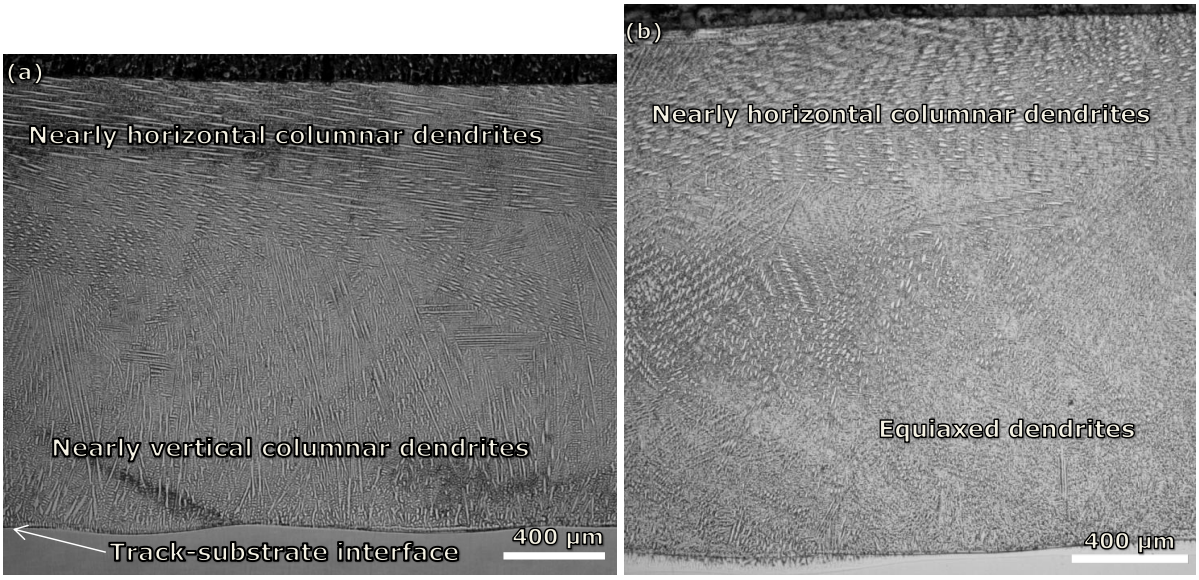

Figure 4.18: Optical micrographs showing longitudinal section of tracks microstructures at laser power settings of (a) 1.8 kW (b) 1.4 kW

4.5 Micro-hardness of Inconel 625 wire single laser tracks

Following the procedure detailed in Chapter 3.12, Vickers micro-hardness measurements were obtained, starting from the substrate, along the centreline of the transverse section of the track samples. Figures 4.19, 4.20 and 4.21 present the micro-hardness profiles of the typical tracks at low and high traverse speed, low and high wire feed rate, and low and high laser power settings respectively. It is apparent that all the coatings exhibit higher hardness than the substrate. The substrate hardness before the deposition was 201 ± 2.4 $HV_{0.3}$.

Single wire track deposited at higher traverse speed demonstrated higher hardness than the track formed at lower traverse speed. The average micro-hardness of track deposited at higher speed was 248 ± 3.8 $HV_{0.3}$ whereas at lower traverse speed, an average of 232 ± 4.5 $HV_{0.3}$ was found. In addition, the hardness of the substrate, after cladding, was found to be 205 ± 1.5 $HV_{0.3}$ and 202 ± 1.4 $HV_{0.3}$ for both high and low traverse speed settings. In other words, the substrate hardness was not significantly altered.

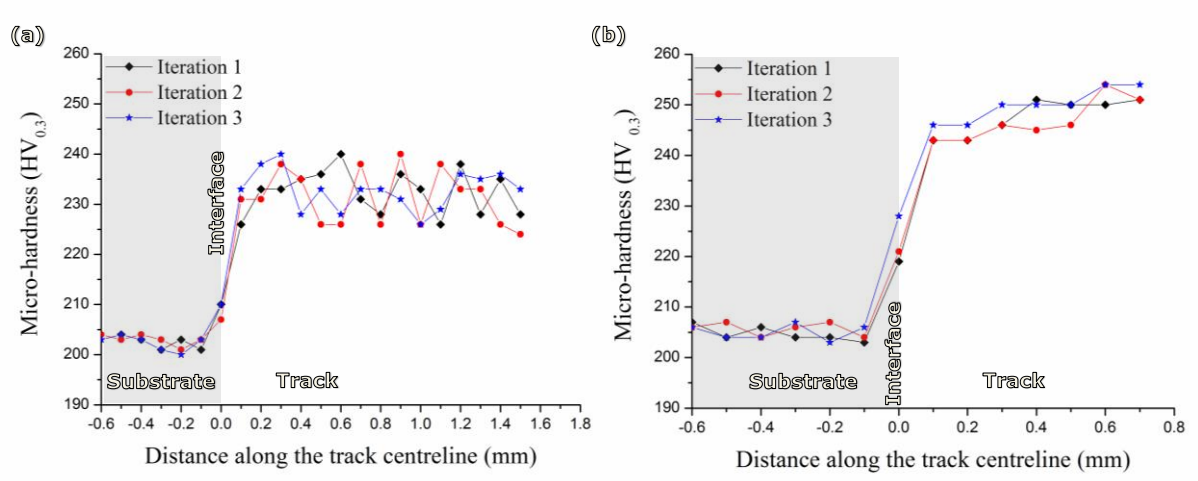

Figure 4.19: Micro-hardness profile of the Inconel 625 wire single laser tracks deposited (a) low (100 mm min^{-1}) and (b) high (400 mm min^{-1}) traverse speeds. Laser power and wire feed rate were fixed at 1.8 kW and 600 mm min^{-1} respectively

Figure 4.20 shows the micro-hardness profile of the typical tracks deposited at low and high wire feed rates. The results revealed that at high wire feed rate setting (1000 mm min^{-1}) laser track exhibited a lower hardness value of 224 ± 5.0 $HV_{0.3}$. The micro-hardness of the track at lower wire feed rate of 600 mm min^{-1} was 232 ± 4.5 $HV_{0.3}$. The average hardness values of the substrate after cladding was 204 ± 1.1 $HV_{0.3}$ for the track formed at high wire feed rate setting.

As shown in Figure 4.21, track formed at 1.4 kW laser power exhibited a slightly higher hardness than the track formed at 1.8 kW setting. At 1.4 kW laser power, track hardness value of 236 ± 4.4 $HV_{0.3}$ was found whereas 232 ± 4.5 $HV_{0.3}$ was demonstrated by the track formed at 1.8 kW laser power. The micro-hardness of the substrate after cladding was 204 ± 1.0 $HV_{0.3}$ when the laser power setting was 1.4 kW.

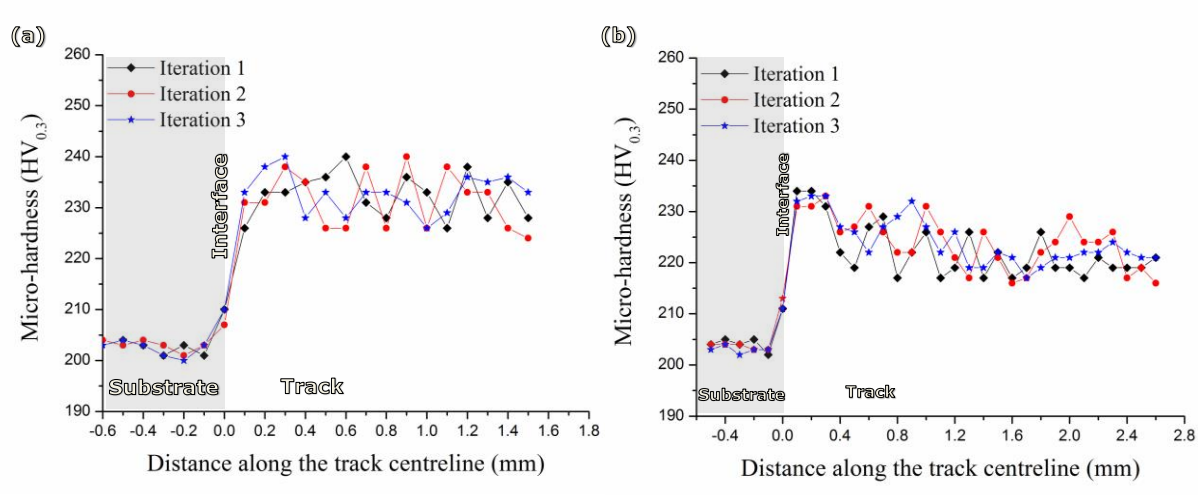

Figure 4.20: Micro-hardness profile of the Inconel 625 wire single laser tracks deposited at (a) low (600 mm min^{-1}) and (b) high (1000 mm min^{-1}) wire feed rates. Laser power and traverse speed were fixed at 1.8 kW and 100 mm min^{-1} respectively.

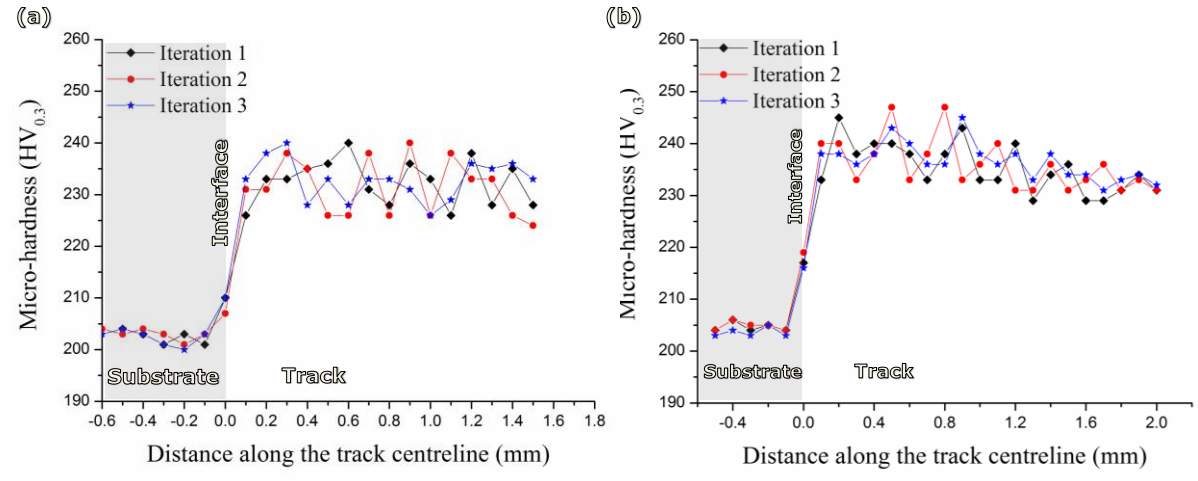

Figure 4.21: Micro-hardness profile of the Inconel 625 wire single laser tracks deposited at (a) 1.8 kW and (b) 1.4 kW laser power. Traverse speed and wire feed rate were fixed at 100 mm min^{-1} and 600 mm min^{-1} respectively

4.6 Laser deposition of Inconel 625 powder

Single laser tracks of Inconel 625 powder were formed using the process window established for Inconel 625 wire laser cladding except that the powder feed rate (PFR), in this case, ranged from 10 to 30 g min^{-1}. All the Inconel 625 powder single laser tracks formed within the process window were continuous and of uniform heights, for example, as shown in Figure 4.22. This shows that Inconel 625 powder laser cladding has a wider process window and is less sensitive to variation in process conditions than Inconel 625 wire laser cladding. As expected and revealed in Figure 4.22, the tracks surfaces were relatively rough compared with the single tracks formed with Inconel 625 wire.

Figure 4.22: Examples of continuous single laser tracks of Inconel 625 powder showing relatively rough surface finish

Likewise, the cladding environment was messy with powder feeding. The un-captured powder, due to powder spreading, resulted in the untidy environment while the rough surface finish was caused by the powder sticking to the solidifying track surface as the table traversed. The track geometries including the height, width, aspect ratio, contact angle and

cross-sectional area under varying processing conditions are presented in Table A3 of Appendix A. Also, the amount of Fe dilution (%) from the substrate at each condition is given in Table B2 of Appendix B.

4.6.1 Effects of the processing parameters on the dilution ratio of the Inconel 625 powder single laser tracks

ANOVA was run for the Inconel 625 powder track dilution ratio using a similar method used for Inconel 625 wire. This was undertaken so as to determine the effect and relative level of significance of the effect of each processing parameter on the Fe dilution in the powder tracks. The result of the compositional (EDX) analysis (detailed in Chapter 3.8) shown in Table B3 in Appendix B revealed that the Fe content of the tracks varied between 8 ± 0.3 wt. % and 48 ± 0.6 wt. %. These give percentage dilution ratios of 10% and 41% in the tracks respectively. As shown in the main effect plots shown in Figure 4.23, the dilution ratio of the powder tracks is proportional with the laser power and traverse speed but varied inversely with the powder feed rate. Similar observations were found for the Inconel 625 wire laser tracks. However, the ANOVA results for the powder tracks showed something different in terms of the order of relative level of significance of the processing parameters. As presented in Table 4.4, the F values of all the factors are greater than the critical value (3.5) for 5% significant level implying that all the parameters are significant. The PFR has the most significant effect (F = 378) followed by the traverse speed with the F value of 184. The laser power has the least influence on the dilution of the track for the range of parameters used in this experiment. R^2 of 0.97 obtained for this analysis indicates that there is a good correlation between the factors and the dilution ratio. The interaction effect was not considered because the intention was to study the individual effect of each of the parameters on the Fe dilution from the substrate.

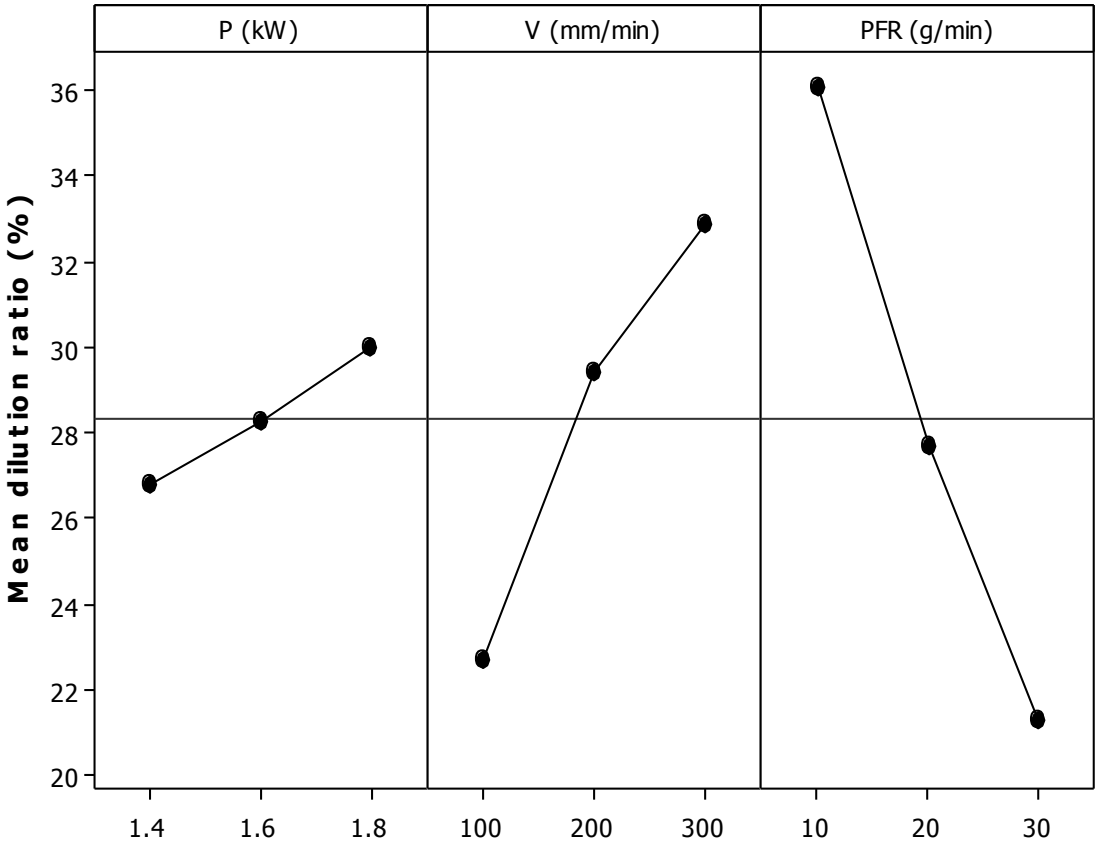

Figure 4.23: Main effect plot for dilution ratio of powder laser tracks

Table 4.4: Analysis of variance for dilution in the Inconel 625 wire tracks

Source	DOF	SS	MS	F	P	$F_{Critical}$
Laser power (kW)	2	44.94	22.47	17.25	0.000	3.4928
Traverse speed (mm min^{-1})	2	477.81	238.90	183.47	0.000	3.4928
Powder feed rate (g min^{-1})	2	984.49	492.25	378.02	0.000	3.4928
Error	20	26.02	1.30			
Total	26	1533.28				
S = 1.54760 R^2 = 97.10% R^2 (adj) = 96.45%						

4.7 Microstructural characterisation of Inconel 625 powder single laser tracks

All the deposited Inconel 625 powder tracks had good fusion at the track-substrate interface, for example, as shown in Figures 4.24 and 4.25. As observed in Inconel 625 wire laser tracks, the tracks formed via Inconel 625 powder deposition system were without cracking and porosity. The cross-sections of Inconel 625 powder single laser tracks revealing their microstructures are presented in Figure 4.24 and 4.25. These observations thus reveal that Inconel 625 powder is a suitable material for laser deposition.

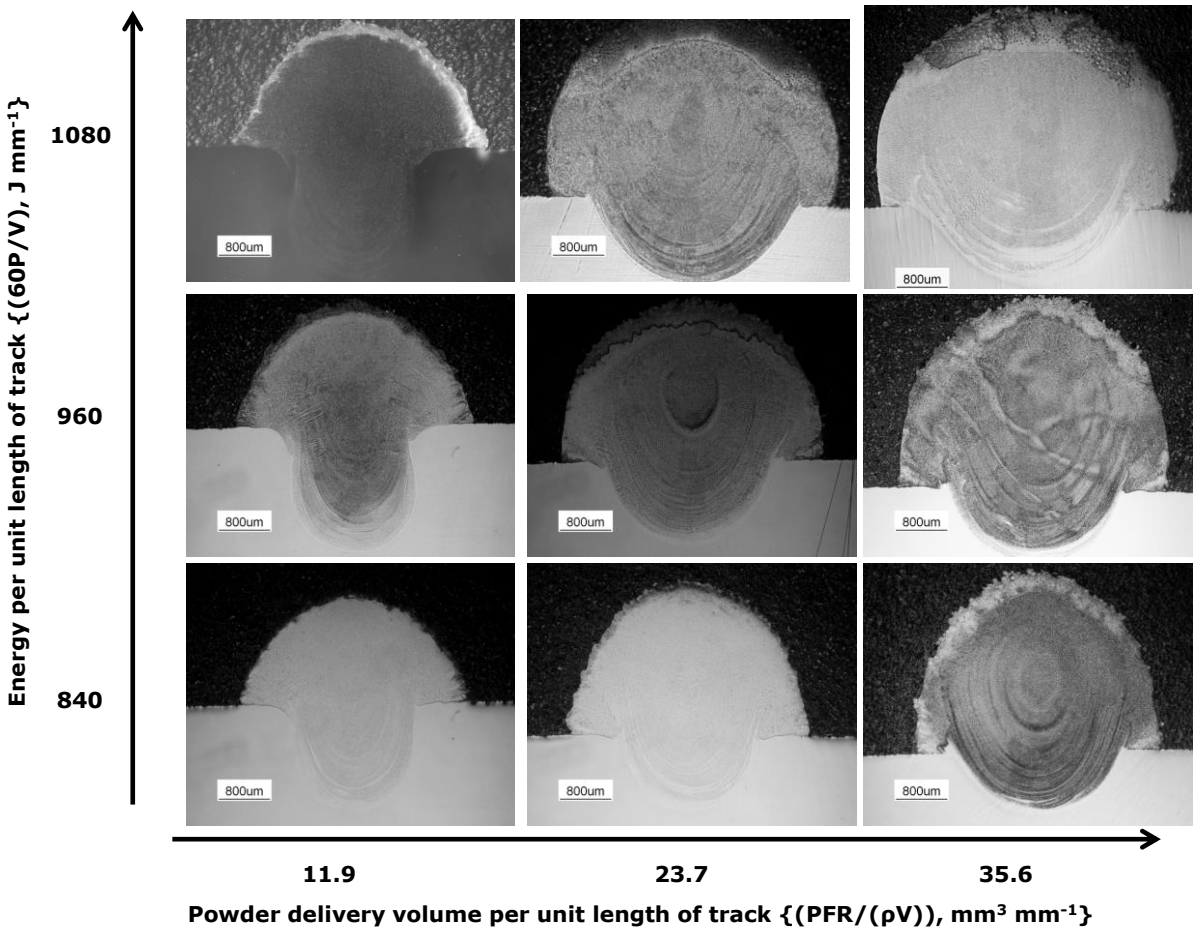

Figure 4.24: Etched optical macro-photographs of laser tracks cross-sections for Inconel 625 powder on AISI 304 stainless steel at traverse speed of 100 mm min^{-1}. P is laser power in W, V is traverse speed in mm min^{-1}, PFR is powder feed rate in g min^{-1} and ρ is the density of Inconel 625 (8.44 × 10^{-3} g mm^{-3}).

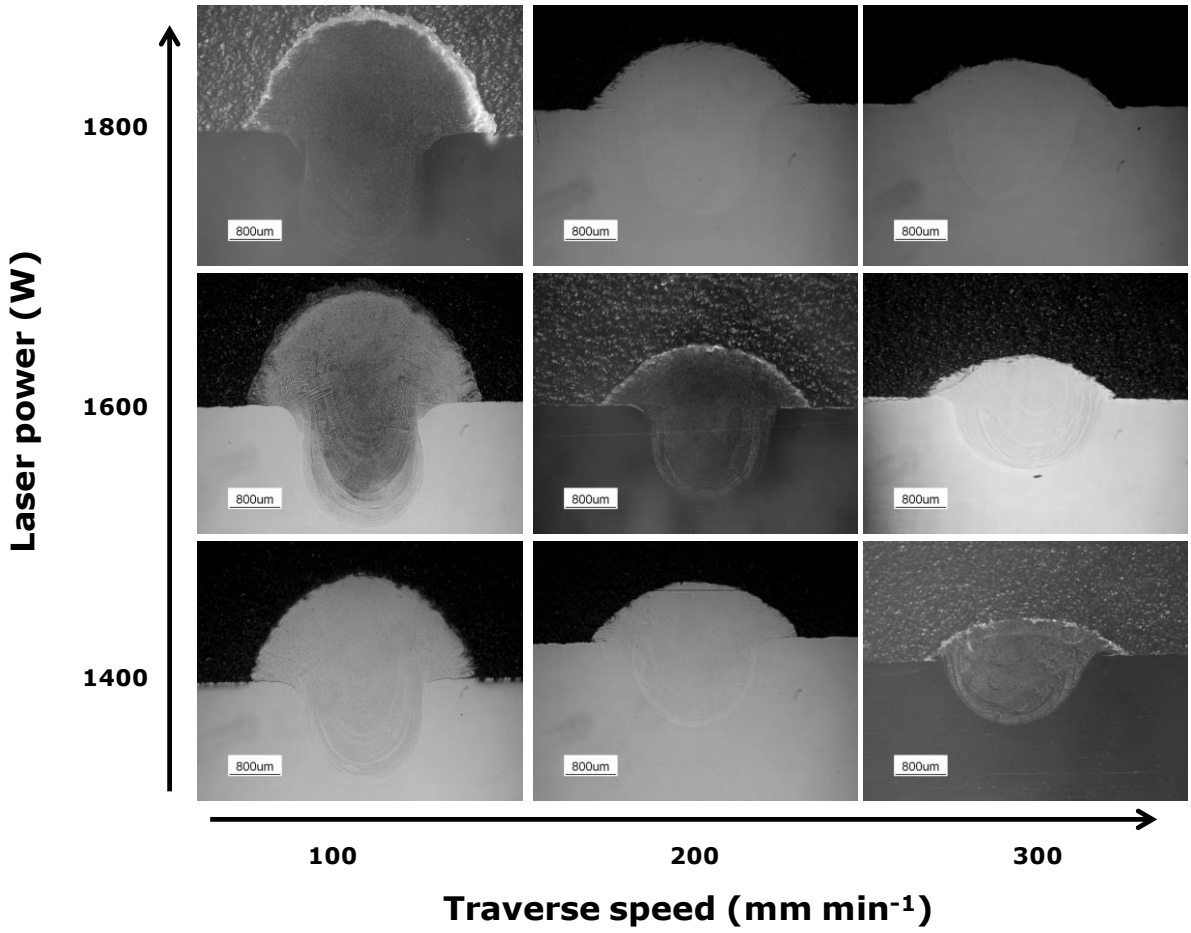

Figure 4.25: Etched optical macro-photographs of laser tracks cross-sections for Inconel 625 powder on AISI 304 stainless steel at powder feed rate of 10 g min^{-1}

Compared with the Inconel 625 wire laser tracks shown in Figures 4.8 and 4.9, Inconel 625 powder laser tracks, due to lower laser beam attenuation by the powder stream, have significantly deeper melt depth into the substrate. This increased as the laser power increased but decreased with increasing powder feed rates (i.e. powder delivery volume per unit length of track). Also, the melt depth into the substrate decreased with the traverse speed.

Additionally, the track cross-sections in Figure 4.24 revealed that the track height increased with increasing powder delivery volume per unit length of track. The powder delivery volume per unit length of track is directly proportional to the PFR. The height increased with

increasing the laser power but decreased as the traverse speed increased, as shown in Figure 4.25.

4.7.1 Microstructural characterisation of a typical Inconel 625 powder laser track

In order to investigate and compare the microstructure and micro-hardness of Inconel 625 powder laser track with the microstructure and micro-hardness of a corresponding single laser track formed using Inconel 625 wire, a typical Inconel 625 powder laser track was selected. For the purpose of effective and reasonable comparison, it was considered that the processing condition of the typical powder track must be similar to that of the wire track.

The range of laser power and traverse speed utilized for the wire and powder laser deposition systems are the same. However, it was difficult to compare the tracks based on the material feed rates utilised because not all the powder was trapped in the laser meltpool but it was expected that all the feed wire entered the meltpool. As a result, track area (i.e. area of track above the substrate) was used in place of material feed rate as a criterion for comparison. Table 4.5 presents the processing parameters and track geometrical properties of the Inconel 625 powder and Inconel 625 wire laser tracks selected for comparison.

Table 4.5: Processing parameters and geometrical properties of Inconel 625 powder and Inconel 625 wire laser tracks selected for comparison

a	b	c	d	e	f	g	h	i = (g/h)*100
Material form	**Laser power (kW)**	**Traverse speed (mm mm^{-1})**	**Material feed rate**	**Average track height (mm)**	**Average track width (mm)**	**Average track area (mm^2)**	**Material volume deposited (mm^3 mm^{-1})**	**Material utilisation efficiency (%)**
Powder	1.8	100	20 g min^{-1}	3.2	4.3	10.9	23.6	45
Wire	1.8	100	1000 mm min^{-1} (12 g min^{-1})	2.7	4.7	10.7	11.32	95

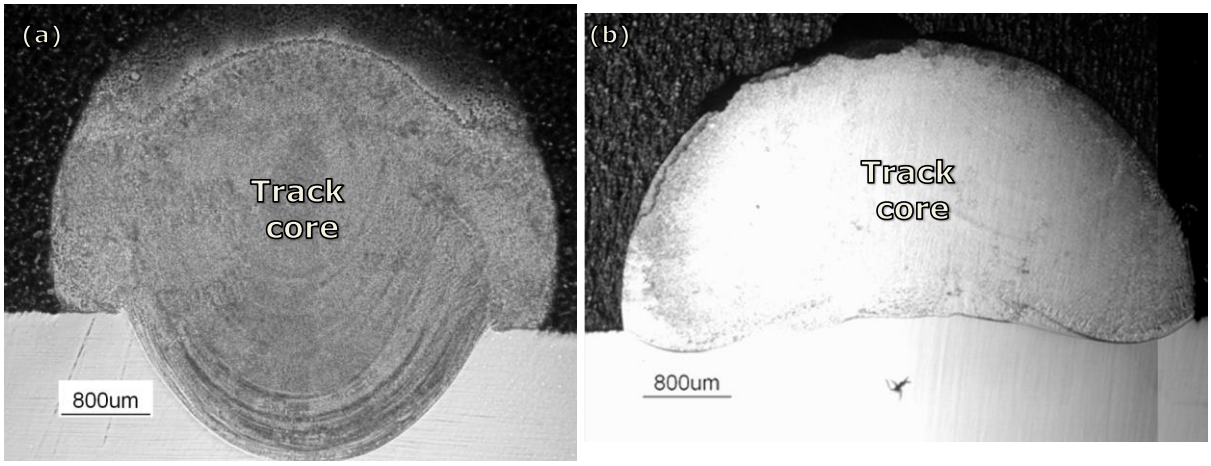

P =1.8 kW, V = 100 mm min^{-1}, PFR = 20 g min^{-1} P =1.8 kW, V = 100 mm min^{-1}, WFR = 1000 mm min^{-1}

Figure 4.26: Etched optical macro-photographs of laser tracks cross-sections for (a) Inconel 625 powder and (b) Inconel 625 wire on AISI 304 stainless steel

Figure 4.26 shows the transverse sections of the Inconel 625 powder and wire single laser tracks selected for comparison. Though there are clear differences in the heights and widths of the two tracks, the track cross-sectional area which is a function of the volume of material captured in the meltpool is 11mm^2 for the two tracks.

In order to investigate the microstructural evolution of the two tracks, the microstructures (longitudinal view) of the two tracks were compared. The longitudinal section of the selected Inconel 625 wire track, as shown in Figure 4.16, had been discussed in section 4.4.4. Figure 4.27 presents the longitudinal view of the corresponding Inconel 625 powder laser track.

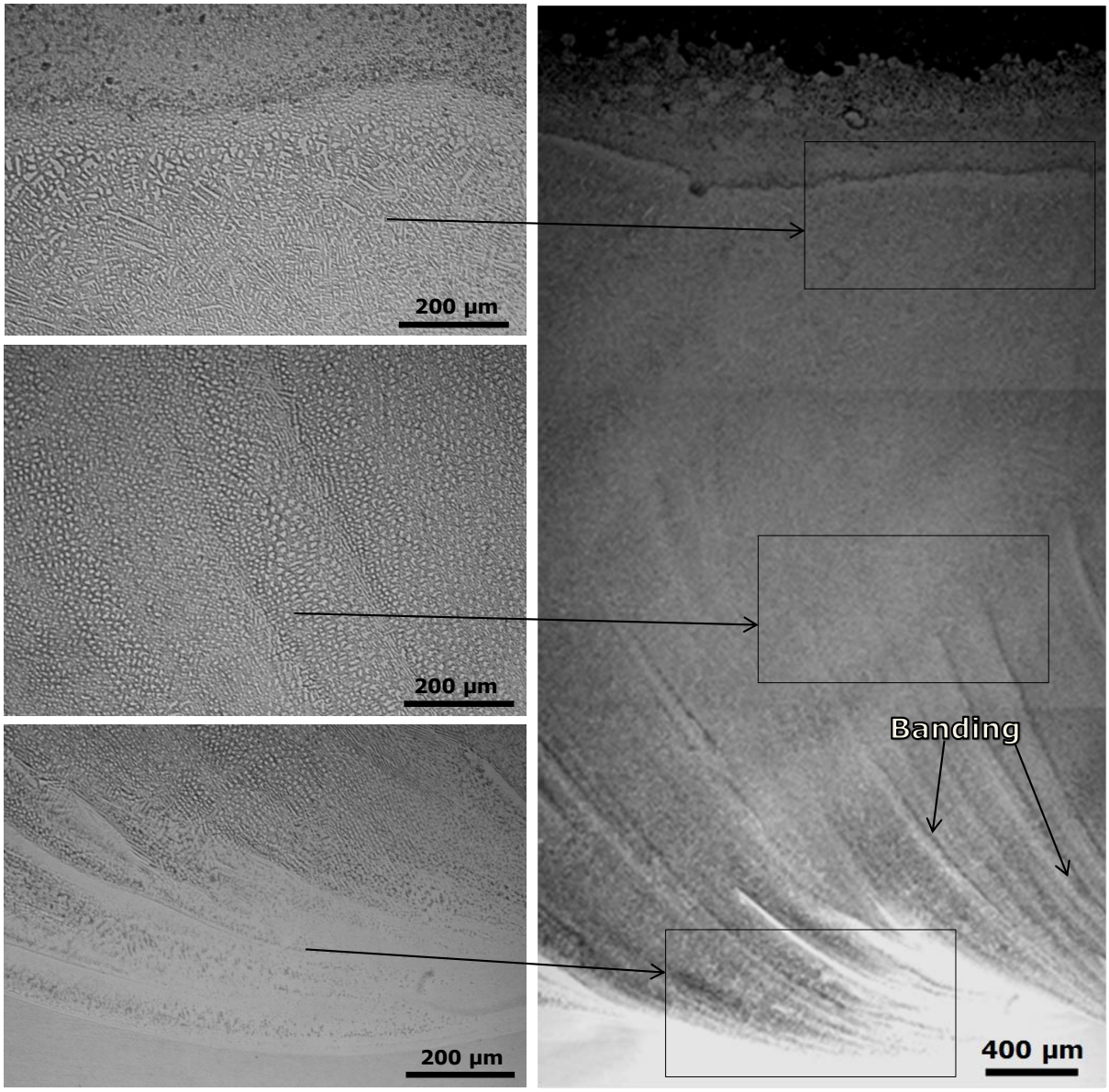

Figure 4.27: Optical micrographs showing a longitudinal section of a typical Inconel 625 powder laser track

As shown in the magnified views of Figure 4.27, the solidification mode of the typical Inconel 625 powder track appears to be entirely cellular/equiaxed dendrites. The banding in the microstructure is thought to result from irregular powder feeding. Actually, the mass of the powder delivered per unit time by the nozzle varied due to some melted powder particles sticking to the orifice of the nozzle. Generally, the microstructure of Inconel 625 powder

laser track appeared to be finer than Inconel 625 wire laser track except for the banding. Magnified view of the track on the SEM, as seen in Figure 4.28, shows that the topmost region consisted of the partially melted powder particles.

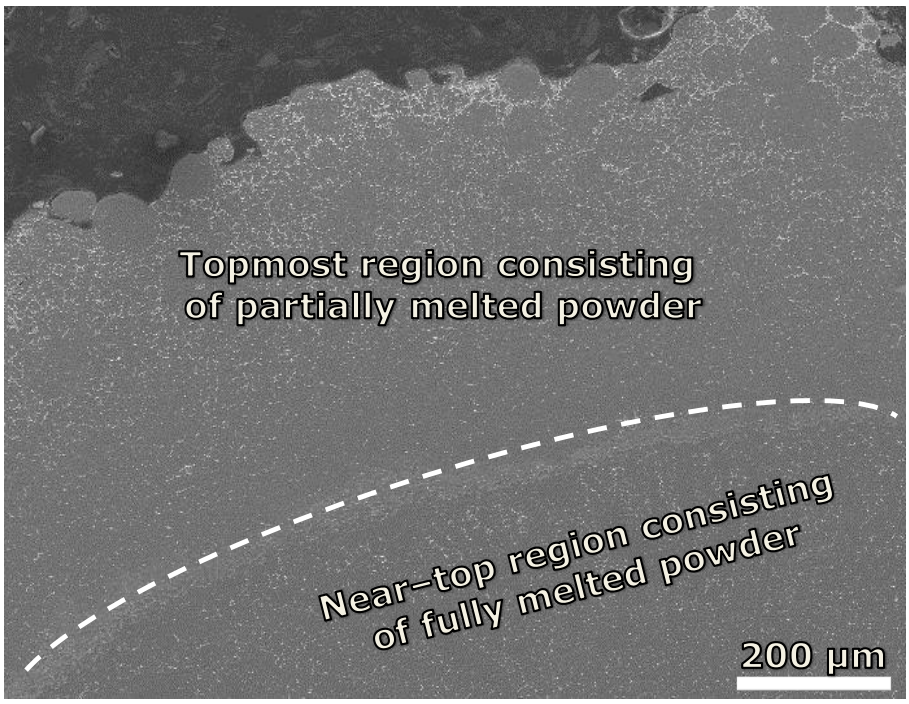

Figure 4.28: SEM image revealing the partially melted powder at the topmost region of the typical track shown in Figure 4.27.

In order to confirm this observation, 200 × 200µm area scan EDX analysis was conducted randomly on the topmost region and near-top region of the track. The results, as presented in Table 4.6, revealed that the composition of the topmost region is very close to the composition of the as received Inconel 625 powder. This suggests that the powder particles at the topmost region were partially melted.

Table 4.6: Compositions of the topmost and near-mid region of the typical Inconel 625 powder laser track

Element	Ni	Cr	Si	Fe	Nb	Mo
Topmost region	61.9 ±0.5	21.8 ±0.2	0.5 ±0.1	0.8 ±0.1	5.0 ±0.3	10.1±0.1
Near-top region	52.1 ±0.5	21.4 ±0.1	0.5 ±0.1	14.4 ±0.2	3.6 ±0.3	8.0 ±0.3

4.7.2 Phase Identification of typical Inconel 625 powder laser track

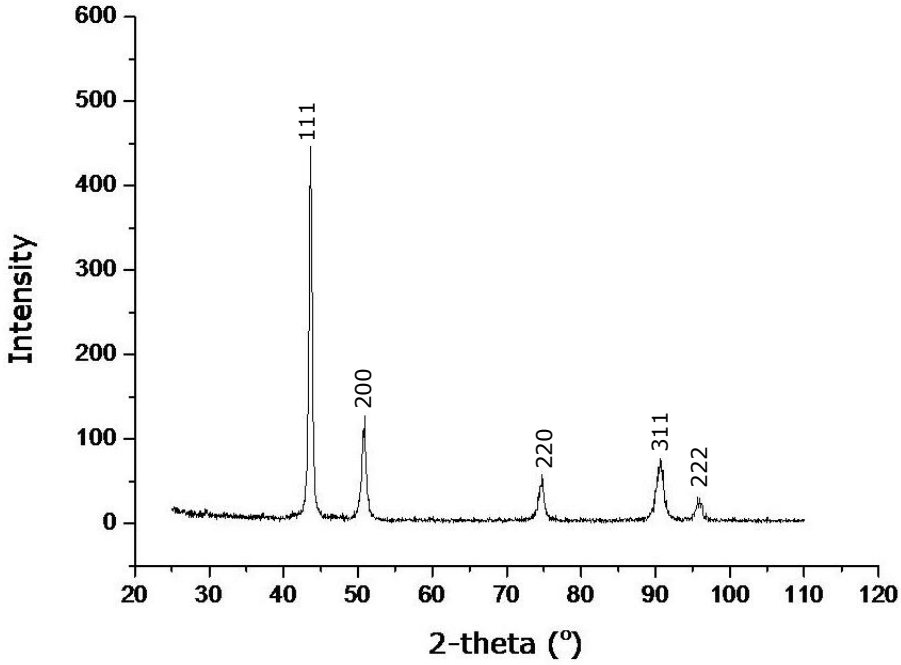

Figure 4.29: XRD spectrum showing FCC structure of Inconel 625 powder laser track

Figure 4.29 represents the XRD spectrum for the top surface of the typical Inconel 625 powder laser track (see Appendix C, Figure 2 for the raw spectrum containing JCPDS file number). The spectrum is similar to the result obtained for the Inconel 625 wire laser track. The major peaks in the spectrum occurred at similar positions of 2-theta (2θ = 43.6, 50.8, 74.7, 90.7 and 96.0) as found in the spectra obtained for Inconel 625 wire laser track and as received Inconel 625 powder. Similar to the result obtained for Inconel 625 wire laser tracks, no phases other than an FCC phase with lattice parameter close to pure Ni could be detected. However, the limit of detection for secondary phases by XRD is approximately 1-2%. Therefore, secondary phases of extremely low volume fraction (<2%) in the track may not be detected.

4.7.3 Elemental composition of phases present in typical Inconel 625 powder laser track

SEM images (using secondary electron signal) of the core (see Figure 4.26) of the typical Inconel 625 powder laser track are shown in Figure 4.30. In the interdendritic regions exists a light contrast precipitate 'B' randomly dispersed in a continuous dark matrix 'A'. EDX analysis was performed on the matrix region A and precipitate region B. The results are summarised in Table 4.7 which is the average of 5 measurements.

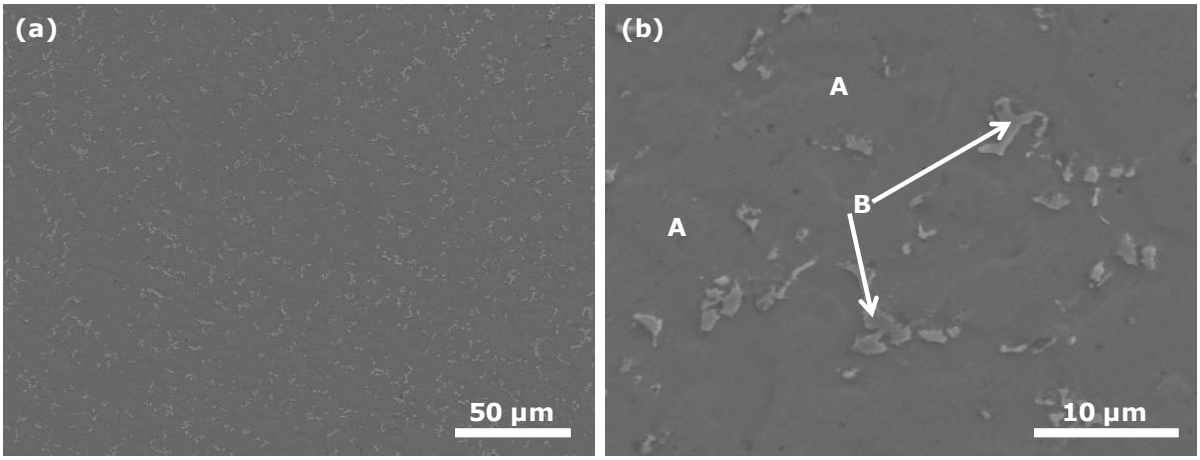

Figure 4.30: SEM/SE images showing the phases present in the microstructure of a typical Inconel 625 powder laser track

Table 4.7: Elemental composition (wt. %) of phases present in a typical single track of Inconel 625 powder laser cladding

Phase	Si	Cr	Fe	Ni	Nb	Mo
FCC Ni matrix	0.4 ±0.2	21.5 ±0.3	16.4 ±0.5	52.5 ±0.6	1.6 ±0.5	7.4 ±0.5
Precipitate	0.5 ±0.2	20.4 ±0.2	12.2 ±0.7	43.2 ±0.2	10.6 ±1.8	11.6 ±1.1

It was found that the continuous dark matrix is richer in Ni and Fe whereas the precipitate was richer in Mo and most notably, Nb. This was also noticed in the composition of the laser tracks deposited using Inconel 625 wire. Similar to previous findings on the solidification of Inconel 625 alloy reported in the literature [39, 41, 42], the segregation of high atomic mass elements such as Nb and Mo resulted in the formation of precipitates within the boundaries between the dendritic cores (i.e. grains which are richer in Ni, Cr and Fe).

For the purpose of determining the dilution ratio of the track, Fe content was measured by conducting 200 × 200µm area scan along and across the centreline of the track area. On the average, the Fe composition in the area above the interface was 15.8 ± 1.2 wt. % giving a dilution ratio of 18.9% for Inconel 625 powder laser track. However, the corresponding Inconel 625 wire track had Fe composition of 3.4 ± 0.5 wt. % producing a dilution ratio of 4.6%. This observation shows that there was higher volume of the substrate elements in the composition of Inconel 625 powder laser track than the corresponding Inconel 625 wire laser track. The possible explanation for this is that relatively higher energy attenuation by the feed wire was observed in the laser cladding with wire. In the case of the powder feeding, there was relatively lower reflectivity of the laser beam causing increased melting of the substrate.

4.8 Micro-hardness of typical Inconel 625 powder single laser track

Vickers micro-hardness measurements of the typical Inconel 625 powder laser track were performed. The measurements were conducted along the centreline of the transverse cross-section of the track. The micro-hardness profiles of the typical Inconel 625 powder laser track and the corresponding Inconel 625 wire laser track are shown in Figure 4.31. For the typical Inconel 625 powder track, the substrate hardness after cladding was 208 ± 1.2 $HV_{0.3}$. At the fusion zone, the hardness increased to 233 ± 4.4 $HV_{0.3}$ while the hardness value within the track area was 245 ± 3.0 $HV_{0.3}$. The corresponding Inconel 625 wire laser track demonstrated

lower hardness value of 224 ± 5.0 $HV_{0.3}$ within the track area and 204 ± 1.1 $HV_{0.3}$ at the substrate.

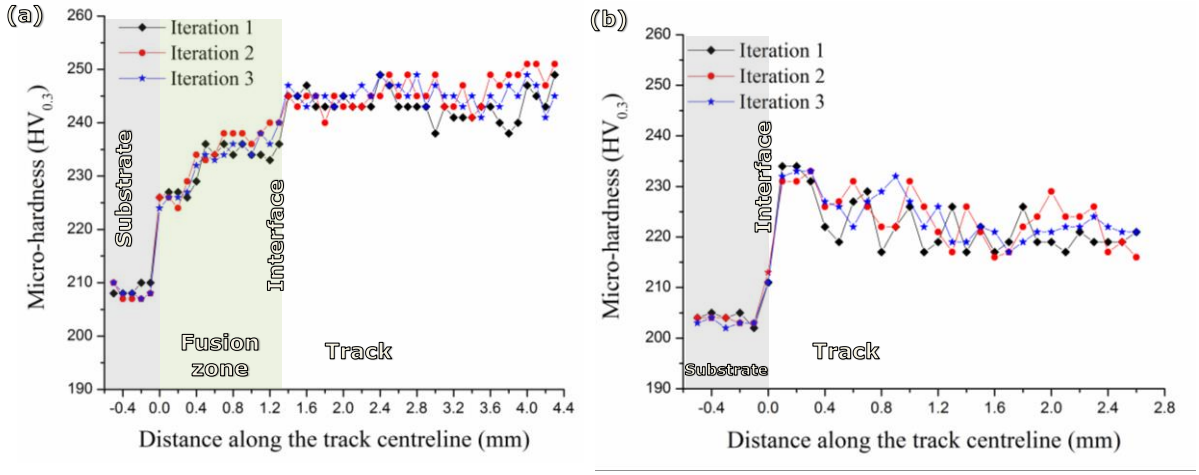

Figure 4.31: Micro-hardness profiles of the laser tracks deposited using (a) Inconel 625 powder and (b) Inconel 625 wire

From this analysis, it is apparent that the laser track formed by powder feeding demonstrated higher micro-hardness than the typical laser tracks formed by wire feeding. The difference in the hardness values of the two tracks can be related to their microstructures. In the case of the powder track, fine equiaxed/cellular dendrites were observed. However, long and coarse columnar dendrites constitute the microstructure of the typical Inconel 625 wire laser track.

4.9 Laser cladding of overlapped-track layers of Inconel 625

4.9.1 Laser cladding of Inconel 625 overlapped-laser tracks via powder and wire feeding

Overlapped-track layers of the typical Inconel 625 powder and Inconel 625 wire single laser tracks were formed. The depositions were carried out at 60% overlapping ratio as described in Chapter 3.4.4. The transverse cross-sections (SE) of the two layers are shown in Figure 4.32. No trace of cracks and pores were observed in the two layers. Although, inter-run

porosities are seen in the layer formed with wire feeding system, the two layers are well bonded with the substrate.

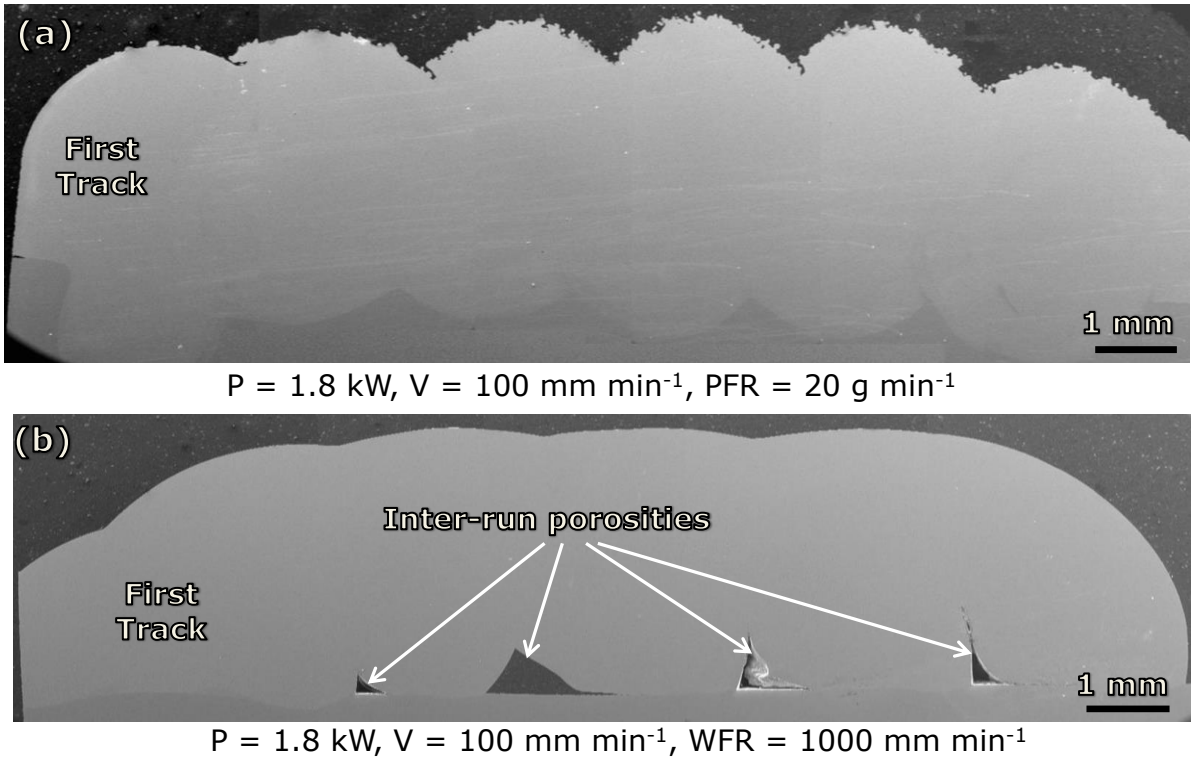

Figure 4.32: Typical Inconel 625 overlapped-laser track layers formed by (a) powder and (b) wire feeding systems

In industrial applications (e.g. protection of the oil drilling tools against corrosion and abrasion), the top surface area of the coating is essentially attacked by corrosion. As a result, the inter-run porosities which exist at the track-substrate interface will have negligible impact on the corrosion performance of the coatings surfaces. However, the clad integrity is affected.

The Fe compositions of the overlapped-track layers were determined using EDAX. Area scan (200 × 200 μm) was conducted at a minimum of 20 locations within the cross-sections of the typical overlapped-track layers. On average, a significant reduction in the Fe dilution into the layers was noticed when compared with the Fe dilution found in the corresponding single

laser tracks. Table 4.8 presents the summary of dilution ratio observed in the overlapped-track layers.

Table 4.8: Summary of the Fe dilution into the Inconel 625 single and overlapped-laser track layers formed via powder and wire feeding systems

Material feeding method	Processing parameters			Single track		Overlapped tracks		% reduction in substrate dilution
	Laser power (kW)	Traverse speed (mm min^{-1})	Material feed rate	Fe content (wt.%)	Dilution (%)	Fe content (wt.%)	Dilution (%)	
Powder delivery	1.8	100	20 g min^{-1}	15.8 ±1.2	18.9	9.9 ±4.1	12.6	35.2
Wire delivery	1.8	100	1000 mm min^{-1}	3.4 ±0.5	4.6	1.1 ±1.1	1.4	69.6

4.9.2 Overlapped-track layers of Inconel 625 wire and powder at varying processing parameters

Photographs showing the top surfaces of some of the deposited overlapped layers of Inconel 625 wire and Inconel 625 powder are shown in Figure 4.33. It can be seen that the surfaces are without cracks and rough. However, the layers made by wire feeding system are relatively smoother and neater. This is due to the smooth flow of the wire into meltpool. Good fusion between the Inconel 625 layer and the substrate and absence of inter-run porosity were achieved in some of the deposited overlapped-track layers, for example, as shown in Figure 4.34. Also, the cross-sections of the layers shown in Figure 4.34 reveal that they are free of cracking and exhibit low melt depth into the substrate.

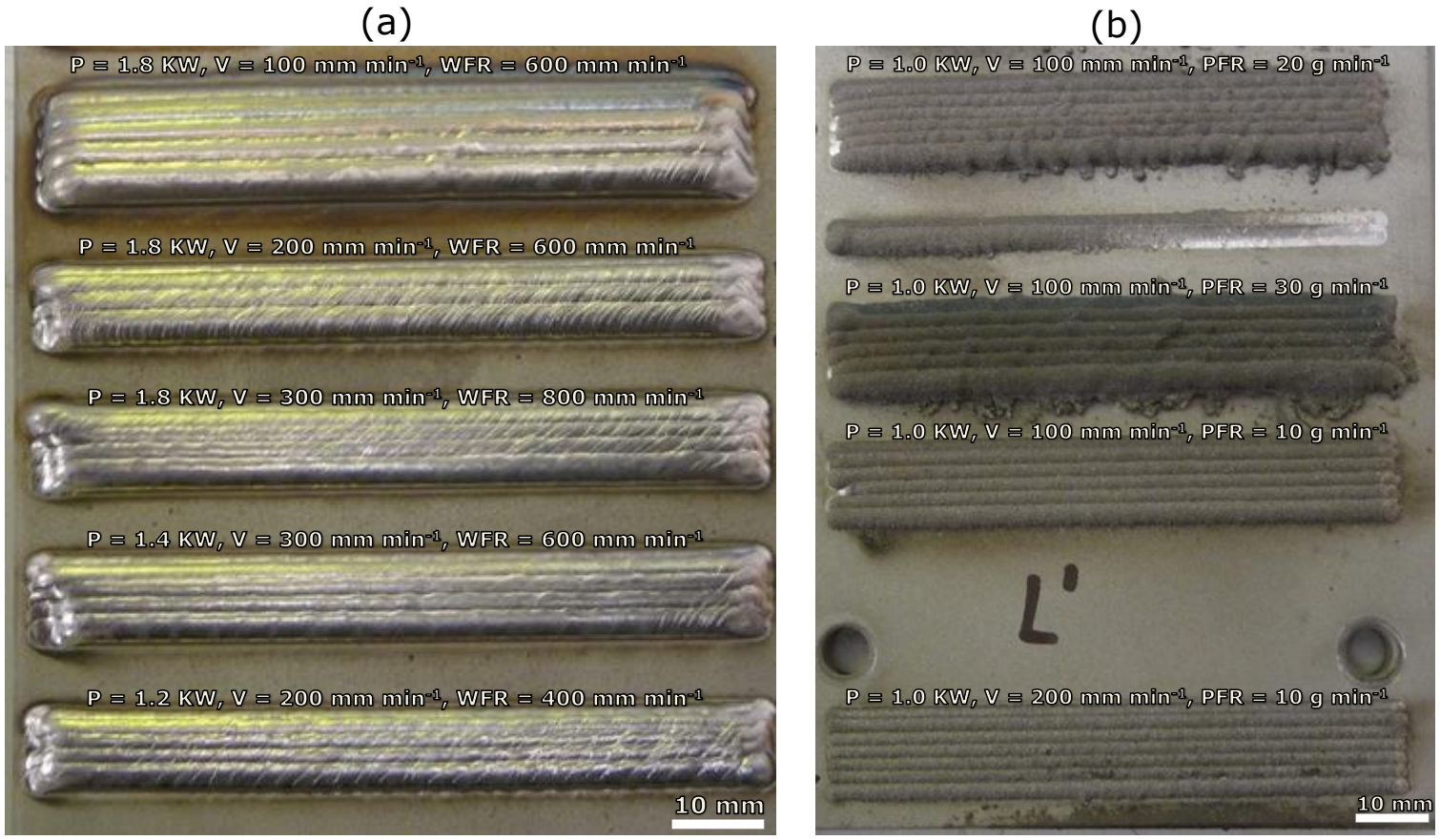

Figure 4.33: Photographs of the top surfaces of the overlapped-track layers of (a) Inconel 625 wire and (b) Inconel 625 powder showing no cracking

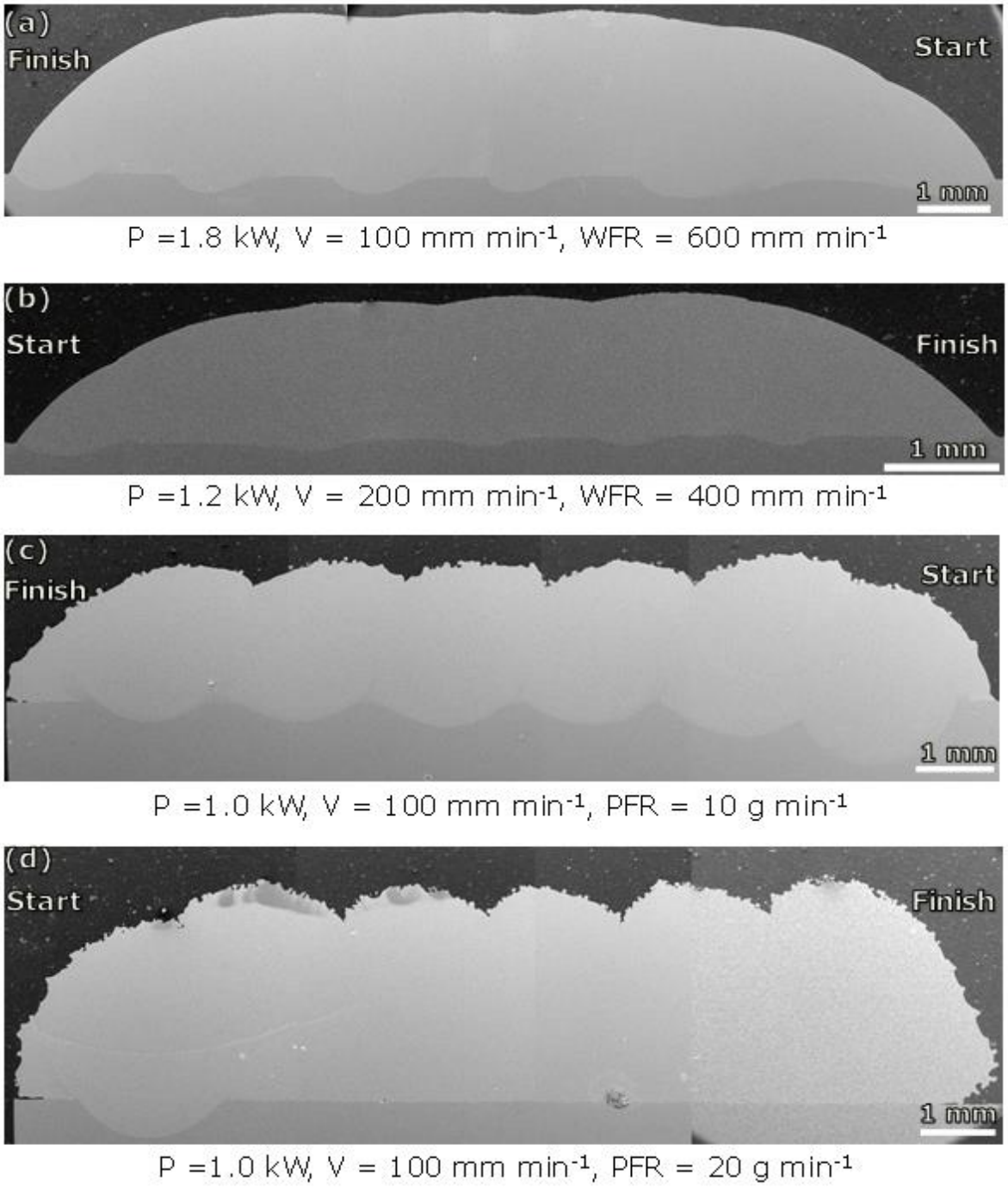

Figure 4.34: Secondary electron images showing the crack- and pore- free cross-sections of the Inconel 625 overlapped-laser track layers formed by (a-b) wire and (c-d) powder lateral feeding systems

Discussion

4.10 Laser cladding with wire: process stability and characteristics

Process stability: Laser cladding with wire is considered stable when there is smooth transfer of wire into the meltpool. This is possible in a situation where the feed wire melts at the point or close to the point of entering the meltpool. In this work, it was found that the stability of the laser cladding with wire process is very sensitive to the position of the wire tip in the meltpool. The reason is that the position of the wire tip in the meltpool influences the interaction time between the feed wire and the laser beam outside the meltpool, for example, as shown in Figure 4.35. Three positions of the wire tips including (1) trailing edge, (2) centre and (3) leading edge of the meltpool were identified in the literature [66]. However, stable laser cladding with wire process had been achieved only with wire tip pointing to the centre [26] and leading edge of the meltpool [67]. The positions, as utilised in the trial experiments, are described diagrammatically in Figures 4.35.

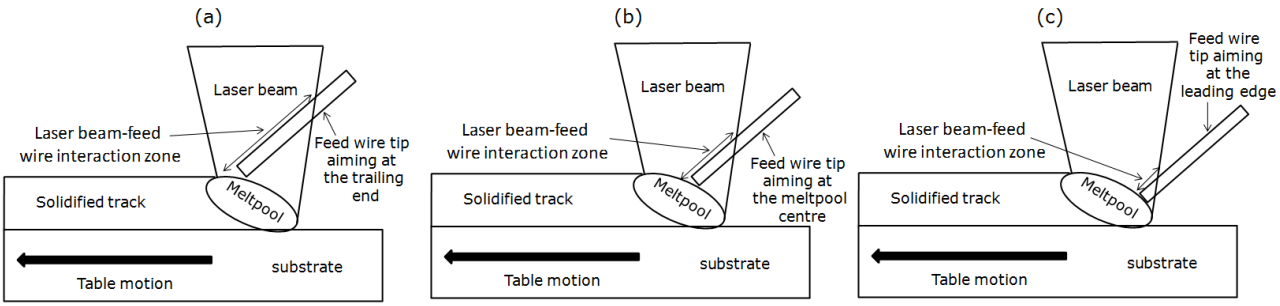

Figure 4.35: Schematic diagrams illustrating different positions of wire tip in the meltpool (a) trailing end, (b) centre and (c) leading edge

Due to excessively long interaction time between the feed wire and the laser beam outside the meltpool, as shown in Figure 4.35a, the feed wire absorbed a high amount of thermal energy. As a result the wire melted above the meltpool and dropped continually leading to formation

of a discontinuous track. A stable process was not achieved with the wire tip aimed at the trailing edge.

With the position described in Figure 4.35c, the wire interacted for only a short time with the laser beam before entering the meltpool whereas the interaction time was considered appropriate when the wire tip was aimed at the meltpool centre, as shown in Figure 4.35b. The reason is that smooth wire transfer into the meltpool was achieved whenever the wire tip was directed to the meltpool centre.

Due to the size of the wire used in this work, stable process was not achieved within the selected range of processing parameters with the set-up shown in Figure 4.35c (i.e. with the wire tip aiming at the leading edge of the meltpool). The heat energy gained outside the meltpool was not enough to melt the feed wire at the point of entry into the meltpool. As a result, the wire entered the meltpool un-melted therefore hitting the substrate. The wire hit the substrate and slipped sideways therefore forming a discontinuous track.

With the wire tip directed to the meltpool centre, the feed wire gained sufficient heat energy as it was being fed into the meltpool. Therefore, the wire melted at the point of entry into the meltpool resulting in smooth flow of wire into the meltpool.

Process characteristics: Having found the correct wire tip position for the laser cladding with wire process, the wire characteristics at the point of entering the meltpool can be altered with varying the processing parameters. In this research, three wire behaviours were identified as the parameters varied. The three process characteristics namely: wire dripping, smooth wire deposition and wire stubbing were defined based on the wire behaviour. The characteristics obtained at a particular condition depends on the relative amount of wire feed rate (i.e. wire deposition volume per unit length of track) to the available energy per unit length of track.

At the conditions where smooth wire deposition was observed, it is believed that the wire feed rate at such conditions gave correct laser beam-feed wire interaction time relative to the available energy per unit length of track. As a result, the wire absorbed the heat energy sufficient for its melting as it entered the meltpool. Continuous tracks were formed at these conditions because there was smooth wire transfer suggesting minimal meltpool disturbance.

With a decrease in wire feed rate or increase in energy per unit length of track, the wire gained too much energy. This is because the interaction time increased with a decrease in WFR. A greater amount of energy was absorbed by the wire. Therefore, droplet wire transfer termed as wire dripping occurred at conditions when the WFR was excessively low relative to energy per unit length of track. Due to the fact that the wire melted too early, the molten wire dropped intermittently into the meltpool thus a forming discontinuous track. Similar results were observed whenever the available energy per unit length of track was excessively high relative to the wire feed rate.

At excessively high WFRs, the laser beam-feed wire interaction time relative to the energy per unit of track was reduced. The heat energy absorbed by the wire outside the meltpool was not sufficient for its melting before reaching the meltpool. As a result, it entered the meltpool in a solid form hitting the substrate. Similar observations were made whenever the energy per unit length of track was excessively low relative to the wire feed rate.

4.11 Melt depth into substrate and dilution ratio analysis

Laser cladding quality is typically graded by the dilution ratio. Usually, low dilution ratio (about 3-8%) is preferred because of the influence of the substrate dilution on the coatings [44, 81]. The amount of dilution ratio depends on three main cladding parameters namely: laser power, traverse speed and material feed rate.

Laser power: The dilution ratio was found to increase with increasing laser power for the laser cladding with wire and powder feeding systems (see Figures 4.7 and 4.23). As the laser power increased, a higher volume of the substrate was melted because of the increase in energy available per unit length of track. Also, more energy was trapped within the meltpool producing a more energetic meltpool. As a result, there was increased mixing and vigorous meltpool movement. This is considered to have caused a higher volume of the molten substrate mixing with the coating thus producing increased Fe composition in the coating. The bulk of the substrate element is Fe (71.15 wt. %). A high Fe content is proposed as unfavourable for corrosion resistance of Inconel 625 alloy coatings [82].

Traverse speed: As shown in Figures 4.7 and 4.23 respectively, the substrate dilution in the wire and powder tracks varied directly with the traverse speed. In both the wire and powder laser cladding processes, two things became apparent whenever the traverse speed was increased. First, the material deposition volume per unit length of track decreased therefore a smaller track area is produced. Secondly, the energy per unit length of track decreased resulting in reduced melt depth into the substrate. In both cladding processes (wire and powder feeding), the decrease in melt depth into the substrate with the change in traverse speed was relatively insignificant compared with the reduction in track area. This indicates that there was more volume fraction of the substrate material in the track area as the traverse speed increased. As a result, dilution ratio increased with increasing the traverse speed.

Material feed rates: With increasing the WFR and PRF, it was discovered that the substrate dilution reduced, as shown in Figures 4.7 and 4.23 respectively. Whenever the wire feed rate or powder feed rate was increased, there was increased laser energy interruption by the feed material. This would have caused a significant reduction in the amount of energy reaching the substrate. Subsequently, lower melt depth into the substrate was found at higher WFR or PFR. Dilution ratio decreased with increasing the material feed rate because of the low

substrate melting and enlarged track area resulting from increased material deposition volume.

Generally, the feed wire, because it is a continuous solid, interrupted the laser beam more than the powder feed. With the powder feeding system, the laser beam infiltrated through the powder stream. This is the reason for the deeper melt depth into the substrate and higher dilution ratio observed in the Inconel 625 powder laser tracks when compared with the corresponding wire tracks.

4.12 Pores and crack formation

Porosity: The absence of pores in the continuous single tracks of Inconel 625 powder and Inconel 625 wire indicates that all the combinations of laser power and traverse speed gave sufficient energy density for full melting of all deposited material volumes used within the selected process window. The possible explanation for the presence of inter-run porosity in some of the overlapped-track layers is high contact angle or low aspect ratio (< 2.5) of the single tracks from which the layers were built. As previously explained in the literature in chapter 2.4.4.1, the higher the contact angle or the lower the aspect ratio, the more spherical a single laser track becomes. Whenever the contact angle is more than 90^{o}, a hollow groove or gap is formed at the base of the track with the substrate (see Figure 2.15). During the overlapped cladding process, it becomes difficult for the molten material to flow into this gap because the laser beam radiation is obstructed from reaching the area covered by this gap due to the protruded flanks of the adjacent track.

Crack formation: The presence of cracks in laser coatings has been a major drawback of laser cladding techniques [50, 73]. Cracks are formed as a result of residual stresses built-up during the molten track solidification. In laser cladding of metal alloys, the stress comprises

mainly of thermal stresses occurring at different regions of the meltpool. The thermal stress occurs because of the large temperature gap (i.e. temperature gradient) between the solidifying clad and the substrate [73]. Also, in a case where the substrate material is different from the additive material, the mismatch in their thermal expansion always results in the development of thermal stress at the clad-substrate interface. Whenever the sum of the thermal stresses is beyond the toughness (strength) of the solidifying clad, crack is initiated. Due to the localised heating of the laser beam and rapid solidification which characterise laser cladding processes, crack propensity is very high in laser deposited coatings. In this study, the absence of cracking in both the Inconel 625 wire and Inconel 625 powder laser coatings can be attributed to high ductility of the alloy [28, 111]. The ductility, hence, fracture toughness of the alloy 625 is believed to withstand the thermal stresses built up during the solidification and contraction of the clads. Therefore, crack-free Inconel 625 laser coatings were formed.

4.13: Microstructural evolution

4.13.1: Comparison between typical Inconel 625 wire and Inconel 625 powder laser tracks

The micro structures of the typical Inconel 625 powder and Inconel 625 wire tracks are somewhat different. The Inconel 625 powder track exhibited fine cellular/equiaxed dendrite grain structure with the occurrence of banding around the base region. The occurrence of fine cellular/equiaxed structure can be attributed to rapid cooling rates which are typical of laser cladding. Generally, there are four main solidification modes (grain structures) namely planar, cellular, columnar dendrite and equiaxed dendrites. The type of grain structure and the grain size are influenced by the temperature gradient (G) and the solidification growth rate (R). This is described in the map shown in Figure 4.36. The temperature gradient is

principally a function of the temperature difference (ΔT) during the process whereas the solidification growth rate is proportional to the cooling rate.

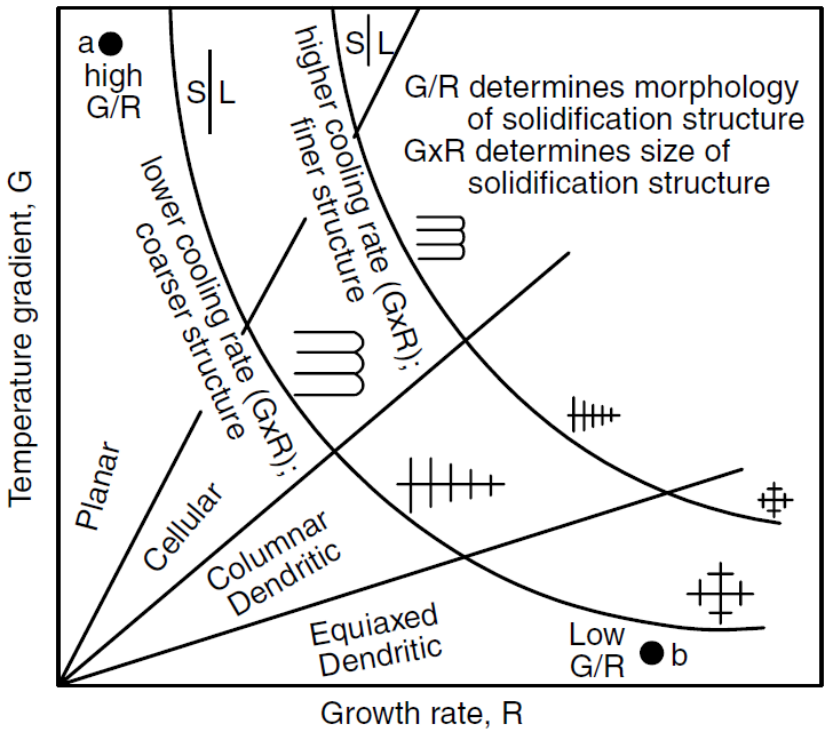

Figure 4.36: Effect of temperature gradient (G) and Solidification growth rate (R) on the morphology and size of solidification microstructure [85]

The ratio G/R determines the solid/liquid interface morphology (i.e. grain structure) while the product of the two (i.e. GR) governs the grain size. Following the theory of constitutional supercooling, a planar solid/liquid interface is stable at the steady state provided the condition described in equation 4.1 is satisfied, where D_L is the diffusion coefficient of the process material [85].

$$\frac{G}{R} \geq \frac{\Delta T}{D_L} \qquad (4.1)$$

It can be deduced from equation 4.1 that the higher the value of G and the lower the value of R, the higher the possibility of planar solidification mode at the solid/liquid interface. The absence of planar grain structure in all the tracks deposited with powder and wire feeding

systems in this work indicates that the condition given in equation 4.1 was not fulfilled. This is probably due to high cooling rate, hence, rapid solidification growth rate. The cooling rate during laser cladding process has been estimated to be 10^3-10^4 K/s [42, 112]. The cellular/equiaxed dendrites grain structure predominantly observed in the powder track confirmed that the solidification (cooling rate) was very rapid.

On the other hand, the changes in the grain structure in the middle region exhibited by the typical Inconel 625 wire track can be explained by the variation in cooling rate (i.e. solidification rate) and temperature gradient at different regions within the track. When the lower region of the track was deposited the solidification growth rate was rapid and the temperature gradient was also high. However, the evolution of a relatively coarse cellular structure shows that the cooling rate was not as rapid, at the interface, as that of the powder laser cladding (see Figure 4.36). During laser cladding with wire, cooling at the bottom (near substrate) region of the coating mainly takes place by conduction mode into the substrate which is usually assumed to be at room temperature. However, in the case of powder, additional heat loss is believed to occur by radiation and convention through the space in-between the molten powder particle before they joined together to form a larger pool.

Usually, it is known that the temperature gradient decreases continuously as solidification occurs from the base to the top of the track. A transition in the grain structure around the mid-region of the wire track indicates that the ratio G/R decreased as expected, at this position, to a value that promoted the formation of the columnar dendrites growing against the heat flux direction. Since cooling occurred mainly through the substrate at this position of the meltpool, the columnar dendrites are nearly vertical to the substrate.

For the upper part of the typical Inconel 625 wire track, there was change in dendrite orientation with the growth of columnar dendrites parallel to the substrate. This is most likely due to a change in heat flux direction at the near surface region of the meltpool.

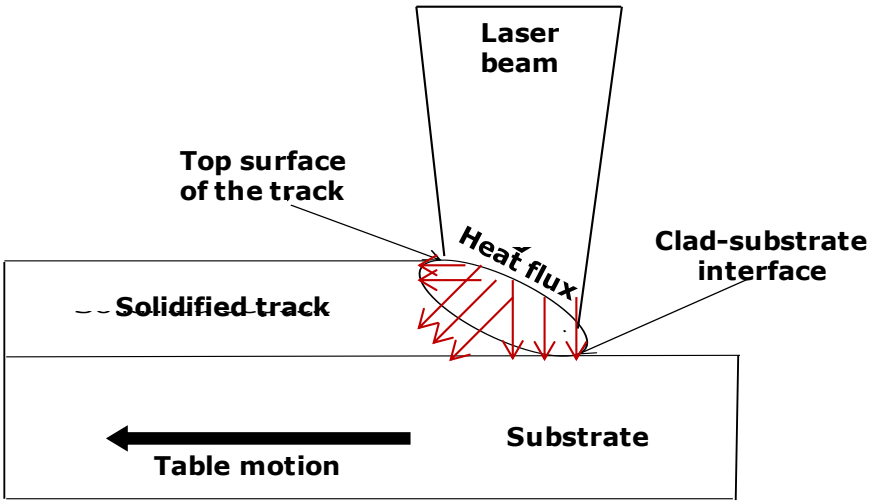

Figure 4.37: A diagram illustrating the heat flow direction in the meltpool

As explained by Dinda et al. [34], the amount of heat flux to the back of the meltpool, at this region, is greater compared to the substrate due to hemispherical shape of the meltpool, for example, as illustrated in Figure 4.37. The reason is that the temperature of the core is usually very high. Therefore, most of the heat was rejected to the solidified track region at the back of the meltpool. This led to the directional growth of the dendrites from the back of the meltpool (growing against heat flux).

4.13.2: Effect of traverse speed on microstructure evolution

Figure 4.11 presents the microstructures of two Inconel 625 wire laser tracks deposited at two traverse speed settings. The growth of nearly vertical columnar dendrites from the interface of the two tracks shows that G/R ratio, at the interface, produced by the two parameters was low, as previously discussed. However, for higher speed, G/R would be much lower because R is proportional to the traverse speed (V) as described in equation 2.2 in chapter 2.5.1.

Also, energy per unit length of track reduced with increasing the traverse speed. This implies that the temperature difference (ΔT), hence, G at the track-substrate interface is lower at higher traverse speed. The transition from columnar dendrite to equiaxed dendrite observed around the mid region of the track formed at a speed of 300 mm min^{-1} (high) shows that the G/R ratio reduced, at this position, to a critical value that promotes the formation of equiaxed dendrite solidification mode. However, at lower speed (100 mm min^{-1}), G/R ratio never reached the critical value to form these equiaxed dendrites. As a result, columnar dendrites were blocked-off from reaching the track top by the growth of nearly horizontal dendrites.

If it is assumed that the heat flow in the track can be approximated by Rosenthal's 3D equation (see equation 4.2), then the cooling rate, which determines the dendrite (grain) size, along the centre line of the track can be estimated as shown below.

$$\text{Cooling rate} = \frac{dT}{dt} = 2\pi KV\frac{(\Delta T)^2}{P} \qquad (4.2)$$

Where K is the thermal conductivity of the Inconel 625 (W m^{-1} K^{-1}), P is the laser power (W), ΔT is temperature difference between the substrate and the meltpool (K) and V is the traverse speed of the heat source (mm sec^{-1}). A valuable deduction from this equation is that the cooling rate varies indirectly with the energy per unit length of track (P/V). As the traverse speed increased from 100 to 300 mm min^{-1}, the energy per unit length of track decreased from 1080 to 360 J mm^{-1} and subsequently, the cooling rate increased. The fact that grain size decreases with increasing cooling rate [85] explains the finer microstructure observed at a traverse speed setting of 300 mm min^{-1}.

4.13.3 Effect of laser power on microstructure evolution

As presented in Figure 4.18, there are differences in the grain structures and sizes of the selected Inconel 625 wire laser tracks deposited at low (1.4 kW) and high (1.8 kW) laser

power settings. The differences are basically as a result of the effect of the laser power on the meltpool temperature. The lower the laser power, the lower the heat input and the lower the average meltpool temperature. Therefore, at low laser power (1.4 kW), a relatively lower G is believed to occur at the track-substrate interface compared to the high laser power (1.8 kW). Also, the cooling rate, hence, solidification growth rate (R) increases with decreasing laser power (see equation 4.2). Consequently, G/R is relatively lower for track formed at 1.4 kW than that of the 1.8 kW. The evolution of equiaxed dendrites from the track-substrate interface of the track formed at 1.4 kW suggests that the G/R ratio reduced to a critical value that promotes the growth of equiaxed dendrites. Conversely, columnar dendrites which are nearly vertical to the substrate evolved from the track-substrate interface of the track formed at 1.8 kW.

Additionally, fine grain size observed at 1.4 kW is due to high cooling rate as explained by Rosenthal's 3D equation. Similar findings had been reported in the literature by Hofmeister et. al [88]. In their study, cooling rate was estimated as a function of the meltpool size. It was discovered that cooling rate decreased with increase in meltpool size and the size of the meltpool increased with the laser power. Therefore, it was concluded that the higher the power, the wider the meltpool and the bigger the grain size.

4.13.4: Effect of wire feed rate on the microstructure evolution

The microstructure of the Inconel 625 wire laser tracks at two wire feed rate settings are somewhat different, as shown in Figure 4.16. Since the laser power and traverse speed are the same for the two depositions, the total thermal energy absorbed by the meltpool will be determined by the material volume deposited in the meltpool. Higher thermal energy is believed to be retained in the meltpool containing higher material volume. This is evidenced by the negative dependency of the melt depth into the substrate with the wire feed rate, as plotted in Figure 4.38.

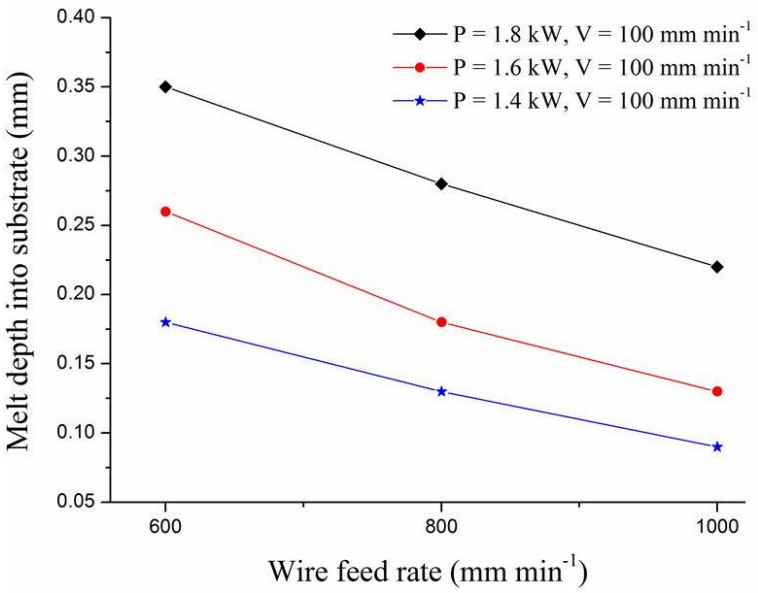

Figure 4.38: Effect of wire feed rate on melt depth into substrate

Lower melt depth into the substrate at higher WFR indicates that a large fraction of the laser beam energy was absorbed by the meltpool. Therefore, there was reduced thermal energy available for substrate melting. On the other hand, significant increase in the melt depth into the substrate found at low WFR shows that smaller fraction of the thermal energy was retained in the meltpool. A larger fraction was used for melting the substrate.

Due to a greater thermal mass, the track formed at high WFR will cool slower than the track formed at low WFR. This is probably the reason for the coarse grain structure found in the track formed at WFR of 1000 mm min^{-1} compared with the track formed at WFR of 600 mm min^{-1}.

4.14: Phase constitution and compositions

From the XRD and EDS results of the wire and powder laser tracks, it can be concluded that only two phases are present in the laser deposited tracks. The phases are continuous FCC γ-

Ni and light contrast Nb- and Mo-rich precipitate occurring in the interdendritic region. However, the XRD and EDS results obtained for the as received powder revealed that FCC γ-Ni is only present. Therefore, it can be deduced that the presence of Nb- and Mo-rich interdendritic precipitate is as a result of meltpool solidification during laser cladding process. The rapid solidification of the molten Inconel 625 alloy has been reported in the literature.

According to Rombouts et al. [42], the precipitation mechanism of Inconel 625 is complex and depends on the chemical composition and the time-temperature history of the alloy. The fractional presence of elements such as Nb, Si, and C in the chemical composition of the alloy influences the solidification products. This is due to strong propensity of these elements to form secondary phase (precipitates) within the grain boundaries at terminal stages of solidification [39, 41].

Generally, the solidification of Inconel 625 deposit starts with the formation of γ dendrites which are depleted in high atomic elements most notably Nb and Mo at their cores. As solidification continues outward from the dendrite cores, Nb and Mo continue to segregate to the liquid phase while Fe, Ni and Cr elements migrate to the solidifying γ-Ni dendrites. As the solidification proceeds further, the interdendritic liquid increases in Nb and Mo composition until γ/Laves eutectic composition is reached. At this stage, the solidification terminates with the formation of γ + laves constituents. Equation 4.3 [41] shows the solidification sequence of Inconel 625.

$$\text{Liquid} \rightarrow \text{Liquid} + \gamma \rightarrow \text{Liquid} + \gamma + \text{Laves} \rightarrow \gamma + \text{Laves} \qquad (4.3)$$

In the past, the Nb- and Mo-rich precipitates have been identified as either Laves or NbC. For example, both Laves and NbC were found in the welds of Alloy 625 after exposure to temperatures in the range of 650-1050^{o}C. The melt temperature of Inconel 625 is 1427^{o}C [11]

showing that the meltpool temperature was above 1050^{o}C during the laser cladding process. Consequently, at least either of these two phases would have been formed in this study. C promotes the formation of NbC whereas Laves is favoured by the amount of Si and Fe contained in the alloy [41]. In this work, the Nb- and Mo-rich precipitate in the typical powder track could be Laves phase because of the presence of Si and significant amount Fe (15.8 wt. %) resulting from substrate dilution. About 3.4 wt. % of Fe in the wire track might have favoured the precipitation of Laves phase. C in the track could not be quantified due inability of the SEM/EDAX technique to accurately quantify it. However, C composition in as-received Inconel 625 wire is 0.08 wt. % (negligible).

4.15: Amount of precipitates, grain refinement and micro-hardness

4.15.1: comparison between the Inconel 625 wire and Inconel 625 powder laser tracks

The typical Inconel 625 powder track exhibited higher micro-hardness value (245 $HV_{0.3}$) than the corresponding Inconel 625 wire track (224 $HV_{0.3}$), as shown in Figure 4.31. Two main issues influencing the micro-hardness of Alloy 625 deposits are the amount of secondary precipitates (hard phases) present in the interdendritic regions and the grain size of the core dendrites. The higher the amount of the precipitates and/or the finer the grain size, the higher the micro-hardness. According to DuPont [41], one of the effects of Fe in Inconel 625 deposits is to promote the precipitation of Laves (precipitates) phase. Following this finding, the volume fractions of the light contrast (interdendritic precipitate) phase present in the two tracks were determined using image processing analysis. The results, as presented in Table 4.9, revealed that higher volume fraction of the precipitate are contained in the powder track. This was expected because of the higher Fe dilution observed in the powder track.

Table 4.9: Amount of the interdendritic precipitate present in the typical Inconel 625 tracks via powder and wire feeding systems

Coating	Volume fraction of Mo- and Nb-rich precipitate (%)	Volume fraction of γ-Ni (%)
Inconel 625 powder track	2.3 ± 0.6	97. 7 ± 0.6
Inconel 625 wire track	0.7 ± 0.4	99.3 ± 0.4

Also, it has been discussed earlier in the previous section (chapter 4.13.1) that the typical Inconel 625 powder track is entirely characterised with finer grains compared to the corresponding Inconel 625 wire track because of the increased cooling rate. In summary, the higher micro-hardness exhibited by the powder track is mainly due to a finer grain structure and partly due to the higher volume fraction of interdendritic precipitates found in the track.

4.15.2: Effects of the processing parameters on the track micro-hardness

Traverse speed: The possible explanation for the rise in micro-hardness with increasing traverse speed, as observed in Inconel 625 wire track, is the finer grain structure found at higher traverse speed. The rise in Fe composition (from 3.2 to 15 wt.%), due to increased substrate dilution, probably led to more precipitation of the harder phase (Nb- and Mo-rich precipitate). This is believed to have partly contributed to the higher hardness noticed at a traverse speed of 300 mm min^{-1} (see Figure 4.19).

Laser power: As shown in Figure 4.21, the lower micro-hardness (232 $HV_{0.3}$) obtained for the track deposited at laser power setting of 1.8 kW when compared with that of 1.4 kW (236 $HV_{0.3}$) is due to the coarsening effect of increasing laser power. Though, more Fe content was found at 1.8 kW power, the decrease in micro-hardness with the increase in laser power shows that the grain refinement has a greater effect than the increase in the amount of the interdendritic precipitate.

Wire feed rate: The Fe composition, hence, the amount of interdendritic precipitate decreased with increasing the wire feed rate. Also, the grain structure became less refined as the wire feed rate increased from 600 to 1000 mm min^{-1}. The combined effects of these therefore led to reduced micro-hardness (236 to 224 HV0.3) found at higher WFR, as presented in Figure 4.20.

4.16 Summary

Stability and characteristics of Inconel 625 wire laser cladding

- The stability of laser cladding with wire process depends on the position of the feed wire tip in the meltpool because the wire tip position influences the amount of heat gained by the wire outside the meltpool. In this study, a stable fibre laser cladding process was achieved for Inconel 625 wire of Ø 1.2 mm with the wire tip directed at the centre of the meltpool. At this position, smooth transfer of wire into the meltpool was obtained at suitable cladding conditions.

- A map predicting the process characteristics of the Inconel 625 wire laser cladding within a process window was successfully developed. Three distinct characteristics namely wire dripping, smooth wire transfer and wire stubbing were found to occur depending on the balance between the energy per unit length of track and wire deposition volume per unit length of track. The main parameters have their individual influence but the map was better described by the use of the two combined parameters.

- Smooth wire transfer into the meltpool was considered to be the ideal laser cladding process because continuous tracks of uniform height were formed with these characteristics. It occurred whenever there was correct balance between the energy per unit length of track (P/V, J min^{-1}) and wire deposition volume per unit length of track (WFR*A/V, mm^3 mm^{-1}).

- The wire melted and entered the meltpool as continual droplets whenever the energy per unit length of track (P/V) was excessive for the wire deposition per unit length of track. Tracks of uneven height and width are formed at these cladding conditions.

However, the process can be corrected to smooth wire deposition by either increasing the wire feed rate or reducing the laser power.

- Wire stubbing occurred whenever an excess wire feed rate was used for a combination of laser power and traverse speed. Due to high wire feed rate, laser beam-wire interaction time was too short such that the wire entered the meltpool in a solid form hitting the substrate below. The feed wire oscillated and formed a discontinuous track.

Dilution ratio and melt depth into the substrate

- Wire feed rate and powder feed rate were found as the most significant factors affecting the dilution ratio in both wire and powder laser cladding processes.

- Dilution ratio and melt depth into the substrate showed negative dependency on the wire feed rate or powder feed rate. This is because the reflectivity of the laser beam energy by the feedstock increased with increasing the material feed rates.

- In the two processes, Fe dilution and melt depth into the substrate increased with increasing the laser power because there was more substrate melting resulting from increased energy per unit length of track.

- The melt depth into the substrate showed no noticeable change with the traverse speed. However, the dilution ratio increased with increasing the traverse speed because the track volume decreased significantly as the traverse speed increased.

- Significantly higher dilution (ranging from 10-41%) and deeper melt depth into the substrate were observed in powder laser tracks when compared with wire laser tracks (ranging from <1-24%).

Microstructures

- Defect-free single laser tracks of Inconel 625 powder and Inconel 625 wire (only with smooth wire deposition) were successfully deposited. The absence of common defects including pores, cracks and poor fusion shows that the selected range of parameters were suitable for laser cladding of Inconel 625 powder and wire.

- The microstructural characterisation of the Inconel 625 powder and wire laser tracks revealed the presence of γ-Ni (FCC) and light contrast interdendritic Mo- and Nb- rich precipitates in the tracks. The XRD analysis could detect only γ-Ni (FCC). The precipitates were not detected because the limit of detection for secondary phases by XRD is approximately 1-2%.

- Inconel 625 powder track and Inconel 625 wire track, deposited at the same parameters, showed different solidification modes and grain sizes. The cause was attributed to different cooling rates occurring when cladding with wire and powder feeding systems.

- Typical Inconel 625 powder laser tracks comprised entirely of fine cellular/equiaxed dendrites. Conversely, the corresponding (in terms of processing parameters) Inconel 625 wire laser track showed cellular solidification mode near the substrate. This transited to vertical columnar dendrites which were blocked off by the horizontal dendrites, parallel to the substrate, near the top surface of the track.

- The growth of the horizontal dendrites near the surface region of the Inconel 625 wire laser tracks is due to the change in the heat flux direction occurring at the top region of the meltpool.

- Due to increased cooling rates, Inconel 625 wire laser tracks formed at higher traverse speed exhibited finer microstructure. The grain structure is characterised with short growth of vertical columnar dendrites at the bottom clad region and transited to equiaxed dendrites at the clad top. The corresponding laser track formed at lower traverse speed was predominantly characterised with long growth of vertical columnar dendrites which was intercepted by horizontal columnar dendrites near the top region.

- Inconel 625 wire track formed at higher WFR is coarser compared with the similar track formed at low WFR. The reason is that larger meltpools absorb more thermal energy resulting in slower solidification rate.

- Fine equiaxed structure exhibited by the Inconel 625 wire formed at low laser power was also a result of rapid cooling rate. Cooling rate reduces with increasing laser power.

Micro-hardness

- The deposited Inconel 625 powder and wire laser tracks demonstrated higher micro-hardness when compared to the AISI 304L substrate.

- Typical Inconel 625 powder exhibited higher micro-hardness than the corresponding Inconel 625 wire track. This is because the powder laser tracks cool faster and contain higher volume fraction of interdendritic (Mo- and Nb- rich) precipitates.

- Traverse speed showed positive influence whereas laser power showed negative influence on the micro-hardness of Inconel 625 wire tracks. This is due to the fact that better grain refinement is obtained at reduced energy per unit length of track (P/V).

- The decreased micro-hardness at higher wire feed rate was as a result of the coarsening of the microstructure with increasing wire feed rate.

Overlapped tracks

- Overlapped-track layers of Inconel 625 powder and wire were successfully deposited. Except for the presence of inter-run porosity in few layers, the layers were free of defects such cracks, poor fusion at the interface and lack of fusion porosity.

- There was significant reduction in the total Fe content in the overlapped-track layers compared with the single tracks.

5.0 Process and microstructural characterisations of Spherotene (WC/W_2C) powder-Inconel 625 wire composite laser coatings

5.1 Introduction

This chapter reports the laser cladding of WC/W_2C (Spherotene) powder-Inconel 625 wire composite coatings on AISI 304L stainless steel. Single laser tracks and overlapped-track layers were deposited at varying processing parameters via concurrent lateral feeding of Spherotene powder and Inconel 625 wire. Effects of the simultaneous injection of the powder on the process characteristics of Inconel 625 wire laser cladding are reported. The Spherotene dissolution analysis, microstructural characterisation and micro-hardness of the single tracks are detailed using several techniques including image processing software, optical microscopy, SEM/EDAX, XRD and Vickers hardness test. The results presented are the dilution ratio, Spherotene particle dissolution and micro-hardness as a function of processing parameters. The typical phases present and their compositions are also reported. Overlapped-track layers are mainly characterised for good fusion with the substrate, cracks, pores and even distribution of the retained Spherotene particles. This chapter presents the results and then the discussions. Summary of the important findings closes the chapter.

5.2 Spherotene (WC/W_2C) powder analysis

5.2.1 Size distribution of the Spherotene powder

The WC/W_2C powder, commercially named as Spherotene, was supplied by Technogenia, France. The powder size distribution was obtained by Malvern Mastersizer-S (Malvern Instruments Limited, Malvern, UK) using laser diffractometry. The powder size distribution is shown in Figure 5.1. The powder size ranged from +40 to 270 µm with a mean size of ~150 µm. It is revealed in Figure 5.1 that 10% (d_{90}) of the powder was above 190 µm and 10% (d_{10}) below 95 µm with a d_{50} (median size) of 140 µm.

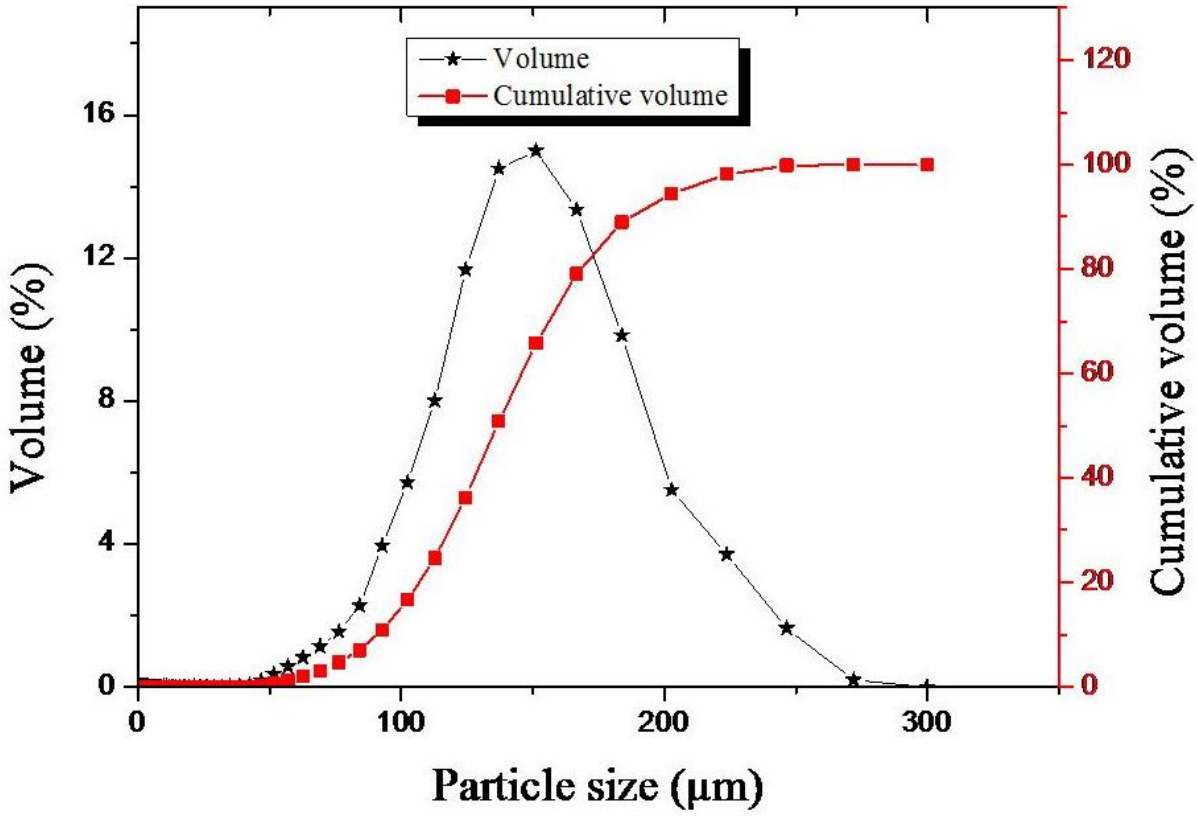

Figure 5.1: Plot of powder distribution and cumulative vol % against particle size for Spherotene (WC/W_2C) powder

5.2.2 Spherotene powder morphology and composition

The supplier (Technogenia) manufactured the spherical cast Spherotene powder using a unique, patented process called cold crucible induction fusion system [113]. The spherical powder is specified to have a micro-hardness of 3000 ± 500 HV. The phases present in the powder before laser processing were determined by X-ray diffraction. As shown in Figure 5.2**,** W_2C and WC phases were identified. WC peaks occurred at 2θ = 31.5, 36.6, 48.3, 64.0, 65.8, 73.1, 75.5, 77.1, and 84.1 (JCPDS = 00-025-1047). The W_2C phase gave a fit to peaks at 2θ = 34.5, 38.0, 39.6, 52.3, 61.9, 69.8, 72.8, 74.9, 75.9, 81.3 and 85.2 (JCPDS = 00-035-0776). The corresponding raw spectrum containing the JCPDS files numbers of the two phases are shown in Appendix C (Figure 4). Evidently, W_2C is the major phase because it has the highest peak at 2θ = 39.6^o (see Figure 5.2)

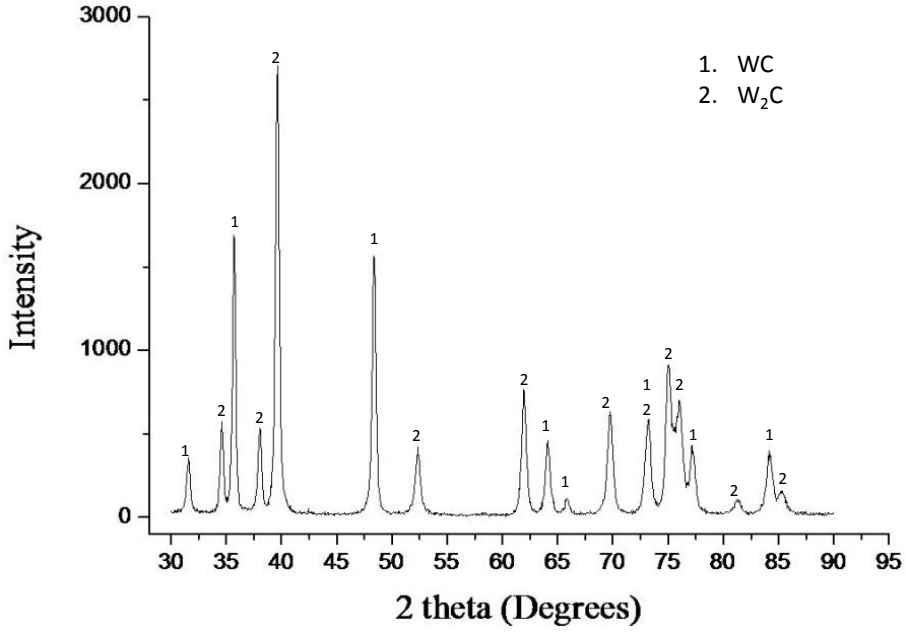

Figure 5.2: XRD spectrum of the WC/W_2C (Spherotene) powder before laser processing

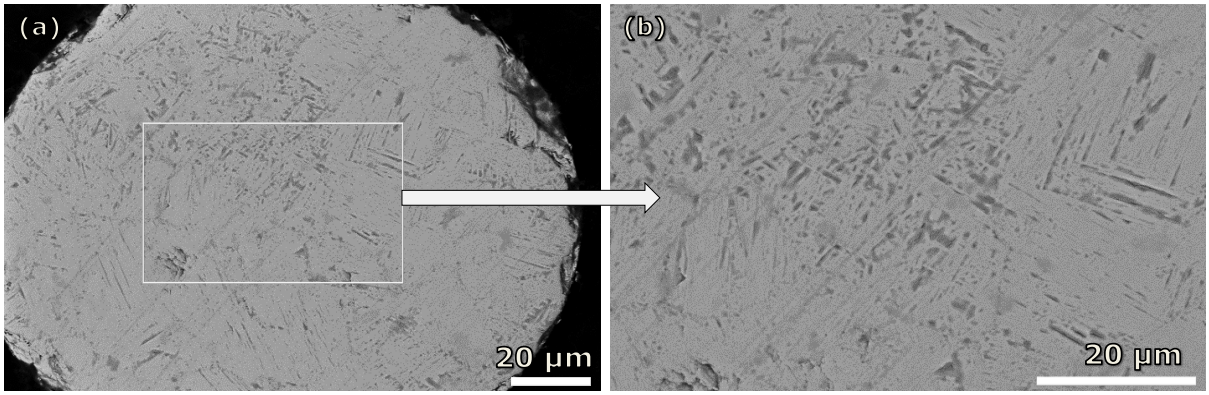

Figure 5.3: Back scattered electron (BSE/SEM) image of the cross-section of the spherical cast Spherotene (WC/W_2C) powder as supplied by Technogenia, France.

Back scattered electron (BSE) images of the powder shown in Figure 5.3 revealed its main metallurgical feature termed, by the manufacturer [113], as tangled needles. The composition of the powder obtained from the London & Scandinavian Metallurgical Co Limited Rotherham, England showed 92.24 wt. % W and 3.96 wt. % C. The test certificate is included in Appendix D. The summation of the percentage composition of the two elements is lower than 100 suggesting that traces of other elements might be present in the Spherotene particle. As a result, EDX analysis (area scan) of the as received Spherotene was carried out. The result, as presented in Table 5.1, revealed that no other element apart from W and C was detected. Figure 5.4 shows the spectrum obtained from the EDX analysis showing the peaks corresponding to W and C only.

Table 5.1: The composition of Spherotene by chemical and EDX analysis

Analysis method	**Element (wt. %)**	
	W	**C**
Chemical	92.2	4
EDX	92.9 ± 0.5	7.1 ± 0.5

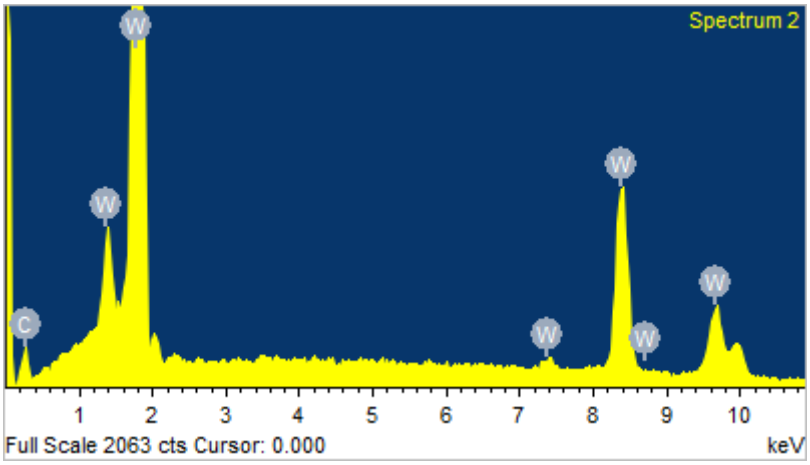

Figure 5.4: EDX spectrum showing the peaks corresponding to W and C during Spherotene compositional analysis

Since no additional element could be identified by EDX analysis method, the weight compositions obtained from the chemical analysis method was normalised to 100% giving 95.8 wt. % W and 4.2 wt. % C. The weight fractions of WC and W_2C in the Spherotene were then calculated from the normalised Spherotene compositions obtained via chemical analysis method. The procedure used is described in Appendix E. 35.3 wt. % and 64.7 wt. % of WC and W_2C were found respectively.

5.3 Laser deposition of Spherotene (WC/W_2C) powder-Inconel 625 wire single tracks

The experimental arrangement and procedure are detailed in chapter 3.4.3. In this study, powder feed rate (PFR) was kept constant for all combinations of laser power (P), traverse speed (V) and wire feed rate (WFR) so as to investigate the effects of the simultaneous injection of the Spherotene powder on the process characteristics and microstructures of the Inconel 625 wire laser cladding. The resulting process characteristics and geometries for all the experiments are summarised in Table A4 and A5 of Appendix A respectively.

Powder feed rate (PFR) of 25g min^{-1} was used for most of the work. The reason for this is that at higher PFR (e.g. 35 g min^{-1}), micro-cracks were observed in nearly all the tracks as shown, for example, in Figures 5.5a and 5.5b.

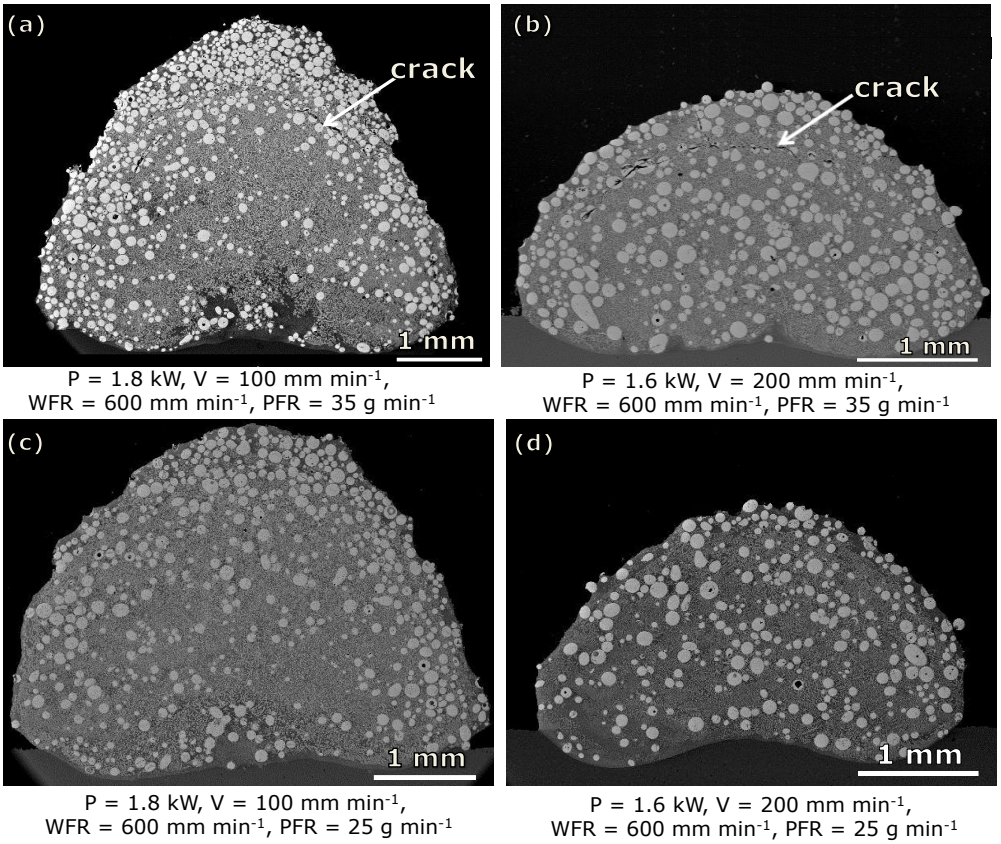

Figure 5.5: BSE/SEM images of the cross-sections of the concurrently fed WC/W_2C powder-Inconel 625 wire single laser tracks showing micro-cracks at (a), (b) PFR of 35 g min^{-1} and (c), (d) no cracks at PFR of 25 g min^{-1}

However, crack like defects were not found in nearly all the tracks formed at lower PFR (e.g. 25 g min^{-1}), for example, as shown in Figures 5.5c and 5.5d. In the few tracks where cracks were observed, the number of surface cracks was limited to 2 per 80 mm length of the track. Cracking, in this case, is possibly due to the build-up of residual stress resulting mainly from increased volume of carbides in the tracks.

5.4 Effects of the concurrent injection of Spherotene powder on the process characteristics of Inconel 625 wire laser cladding

Concurrent laser cladding of Spherotene (WC/W_2C) powder-Inconel 625 wire composite tracks were performed at similar conditions utilised for the cladding of Inconel 625 wire reported in Chapter 4.2.3. As mentioned earlier, the reason for this is to study the effects of simultaneous injection of Spherotene powder on the process characteristics of Inconel 625 wire laser cladding.

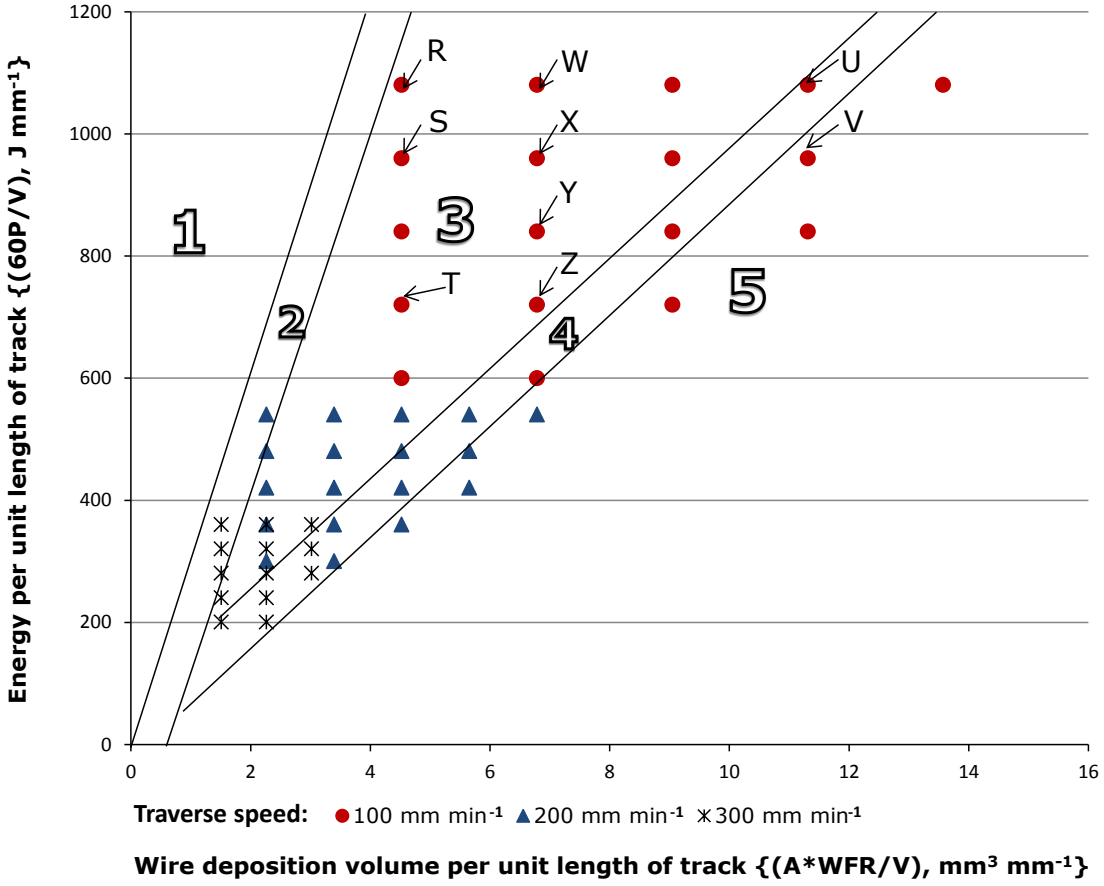

(1) Dripping, (2) Dripping may occur, (3) Smooth wire deposition, (4) Stubbing may occur and (5) Stubbing regions

Figure 5.6: A process map showing the fibre laser cladding characteristics of Spherotene (WC/W_2C) powder-Inconel 625 wire single tracks at P = 1.0 - 1.8 kW, V = 100 - 300 mm min^{-1}, WFR = 400-1000 mm min^{-1} and PFR = 25 g min^{-1}.

Figure 5.7: Typical Spherotene (WC/W_2C) powder-Inconel 625 wire laser deposited single composite tracks

Figure 5.6 shows the process map illustrating the characteristics observed, at all processing conditions employed in this experiment for the Spherotene powder-Inconel 625 wire composite cladding where A is the wire cross-sectional area. Five different regions are clearly defined in the map with 1–5 representing: dripping, dripping may occur, smooth wire flow, stubbing may occur and stubbing regions respectively. Each processing condition (i.e. a combination of laser power, traverse speed and wire feed rate) was represented by a point on the map. PFR was kept at 25 g min^{-1} for all experiments. Continuous composite tracks of uniform heights were produced at processing conditions contained in region 3 (i.e. smooth wire deposition), for example, as shown in Figure 5.7. Both the wire dripping (region 1) and wire stubbing (region 5) process characteristics produced discontinuous tracks.

Table 5.2: Examples of transition in the process characteristics of Inconel 625 laser cladding caused by the concurrent injection of WC powder into the meltpool

Point	Laser power (kW)	Traverse speed (mm min^{-1})	Wire feed rate (mm min^{-1})	Energy per unit length of track (J mm^{-1})	Wire deposition volume per unit length of track (mm^3 mm^{-1})	Deposition process characteristic without powder injection	Deposition process characteristic with powder injection
R	1.8	100	400	1080	4.5	wire dripping	smooth wire transfer
S	1.6	100	400	960	4.5	wire dripping	smooth wire transfer
U	1.8	100	1000	1080	11.3	smooth wire transfer	wire stubbing may occur
V	1.6	100	1000	960	11.3	smooth wire transfer	wire stubbing

Compared with the process map previously developed for Inconel 625 wire laser cladding (see Figure 4.5), a rightward shift is noticeable in the map shown in Figure 5.6. For example, the corresponding processing conditions for points marked ‘R’, ‘S’, ‘U’ and ‘V’ in the process map shown in Figure 5.6 are presented in Table 5.2. Without powder injection, Inconel 625 wire deposition performed at conditions marked as ‘R’ and ‘S’ were characterised with wire dripping, as shown in Figure 4.5 and Table 4.1. With simultaneous injection of Spherotene powder, the process characteristic changed to smooth wire deposition, as seen in Figure 5.6. Similarly, the Inconel 625 wire process characteristics transited from smooth wire deposition to wire stubbing may occur and wire stubbing with the concurrent injection of Spherotene powder at parameters corresponding to points ‘U’ and ‘V’, respectively, in the process maps.

5.5 Analysis of the Spherotene volume fraction in the composite track

Usually, one of the major issues with the wear and corrosion performance of the WC/Ni alloy composite coating is the degradation or dissolution of the tungsten carbide particles. In this study, Spherotene particle dissolution was observed but at different degrees as the processing parameters varied, for example, as shown in Figure 5.8. Most of the analysis in this section will consider two typical continuous composite tracks whose cross-sections are shown in Figure 5.8.

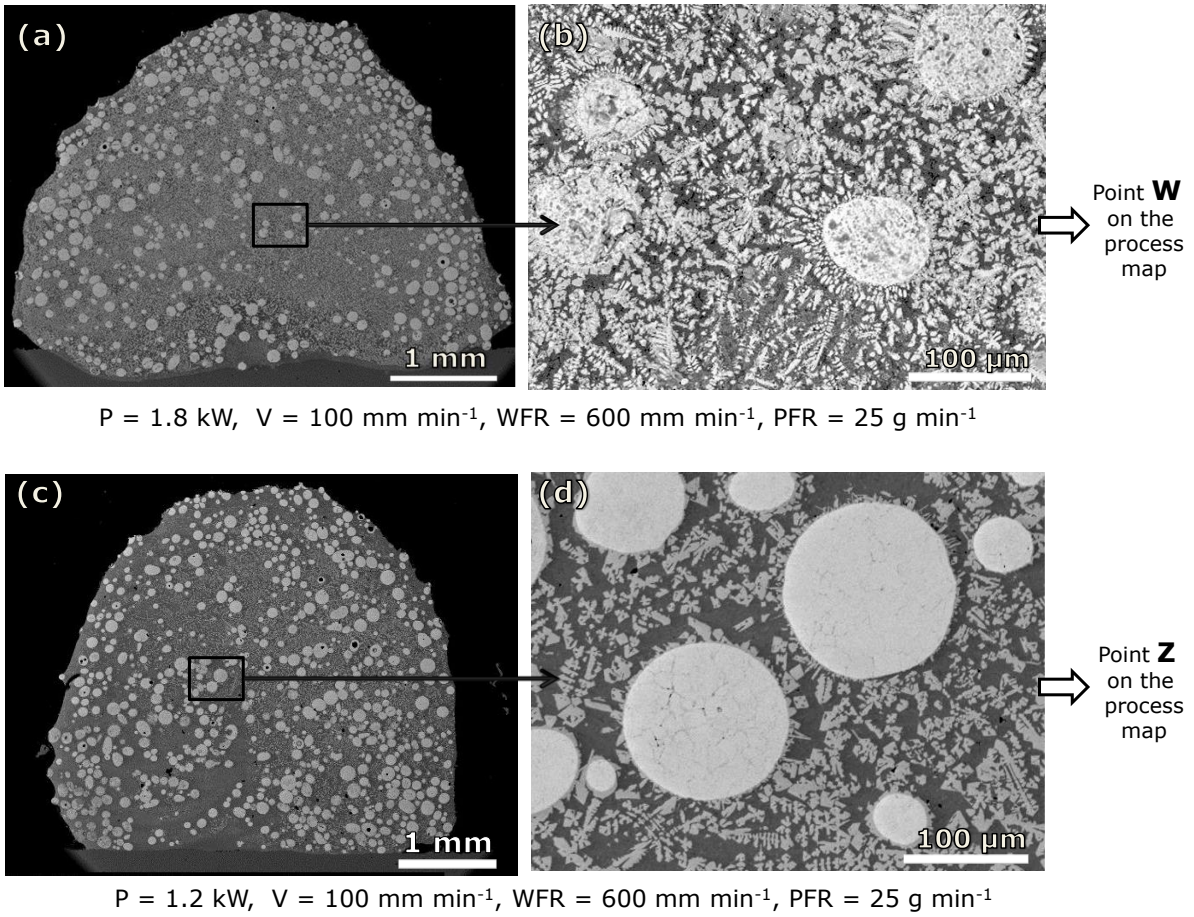

Figure 5.8: BSE/SEM images of the composite track cross-sections showing Spherotene dissolution at (a,b) 1080 J mm^{-1} and (c,d) 720 J mm^{-1} energy per unit length of track

They were deposited at high (corresponding to point W in Figure 5.6) and low (corresponding to point Z in Figure 5.6) energy per unit length of track. One of the reasons for their selection is that their cladding conditions are within the region 3 of the process map shown in Figure 5.6. Also, clear differences in the extent of Spherotene dissolution and other microstructural features were noticed between the two tracks.

In order to effectively determine the amount of Spherotene dissolution in the composite tracks, the mass (g) of the Spherotene particle captured by the meltpool was calculated. The reason is that not all the Spherotene delivered from the powder nozzle was captured by the meltpool.

5.5.1 Deposition efficiency and amount of Spherotene particle captured

The procedure for this is detailed in Chapter 3.9. Mass of the Spherotene delivered (g) was calculated by dividing the PFR (g min^{-1}) by the traverse speed (mm min^{-1}) and then multiply the result by the track length (80 mm). Mass of the Spherotene captured was obtained by a weighing method whereas the deposition efficiency was a ratio of the mass of the Spherotene captured to the mass of the Spherotene delivered. The results, as presented in Table 5.3, give the powder deposition efficiency at each laser cladding condition. The conditions, in this case, include those used for depositing the tracks whose cross-sections are shown in Figure 5.8 (printed in red colour) and some others which are contained in region 3 of the process map.

Table 5.3: The calculated values of the Spherotene powder deposition efficiency and volume captured in the meltpool assuming no dissolution

Laser power (kW)	Traverse speed (mm min^{-1})	wire feed rate (mm min^{-1})	Mass of Spherotene delivered (g)	Mass of Inconel 625 track + the substrate (g)	Mass of composite track + the substrate (g)	Mass of Spherotene captured (g)	Spherotene powder deposition efficiency (%)
W 1.8	100	600	20.0	42.2	48.9	6.4 ± 0.7	32 ± 3.3
1.8	100	800	20.0	43.7	51.0	7.0 ± 0.3	35 ± 1.6
1.8	100	1000	20.0	45.3	52.7	7.7 ± 0.3	38 ± 1.4
1.8	200	600	10.0	39.9	42.1	2.4 ± 0.5	24 ± 4.7
1.8	300	600	6.7	39.2	40.2	1.0 ± 0.2	15 ± 2.9
X 1.6	100	600	20.0	42.2	48.3	5.7 ± 0.4	29 ±1.9
Y 1.4	100	600	20.0	42.2	47.7	5.1 ± 0.5	25 ± 2.4
1.2	100	400	20.0	40.7	45.3	4.4 ± 0.2	22 ± 1.0
Z 1.2	100	600	20.0	42.2	46.9	4.7 ± 0.2	23 ± 0.8
1.2	100	800	20.0	43.7	48.6	5.4 ± 0.5	27 ± 2.3
1.2	200	600	10.0	39.9	41.4	1.7 ± 0.2	17 ± 2.2
1.2	300	600	6.7	38.9	39.6	0.8 ± 0.2	12 ± 3.0
1.0	100	600	20.0	42.1	45.7	3.6 ± 0.1	18 ± 0.3

From Table 5.3, it is found that the Spherotene deposition efficiency ranged between 12 and 38%. However, the wire deposition efficiency was ~ 100% since all the wire delivered were presumably captured by the meltpool.

The variations of the Spherotene deposition efficiency and mass of spherotene captured in the meltpool with the processing parameters are plotted in Figure 5.9. Both the Spherotene deposition efficiency and mass of Spherotene captured show similar trends with the processing parameters. The amount of Spherotene captured is proportional to the laser power and wire feed rate. However, with the traverse speed, an inverse relationship was established. These changes could be attributed to the size of the meltpool which changed as the parameters varied. For example, the higher the laser power, the bigger the meltpool size and the higher the mass of Spherotene captured and the deposition efficiency. However, the higher the traverse speed, the smaller the meltpool size due to the decrease in energy per unit

length of track. Therefore, a reduced amount of Spherotene is expected to be captured. The increase in Spherotene deposition efficiency with the WFR can be attributed to variations in powder attenuation as the parameter changed. This is fully explained in section 5.12 of this chapter.

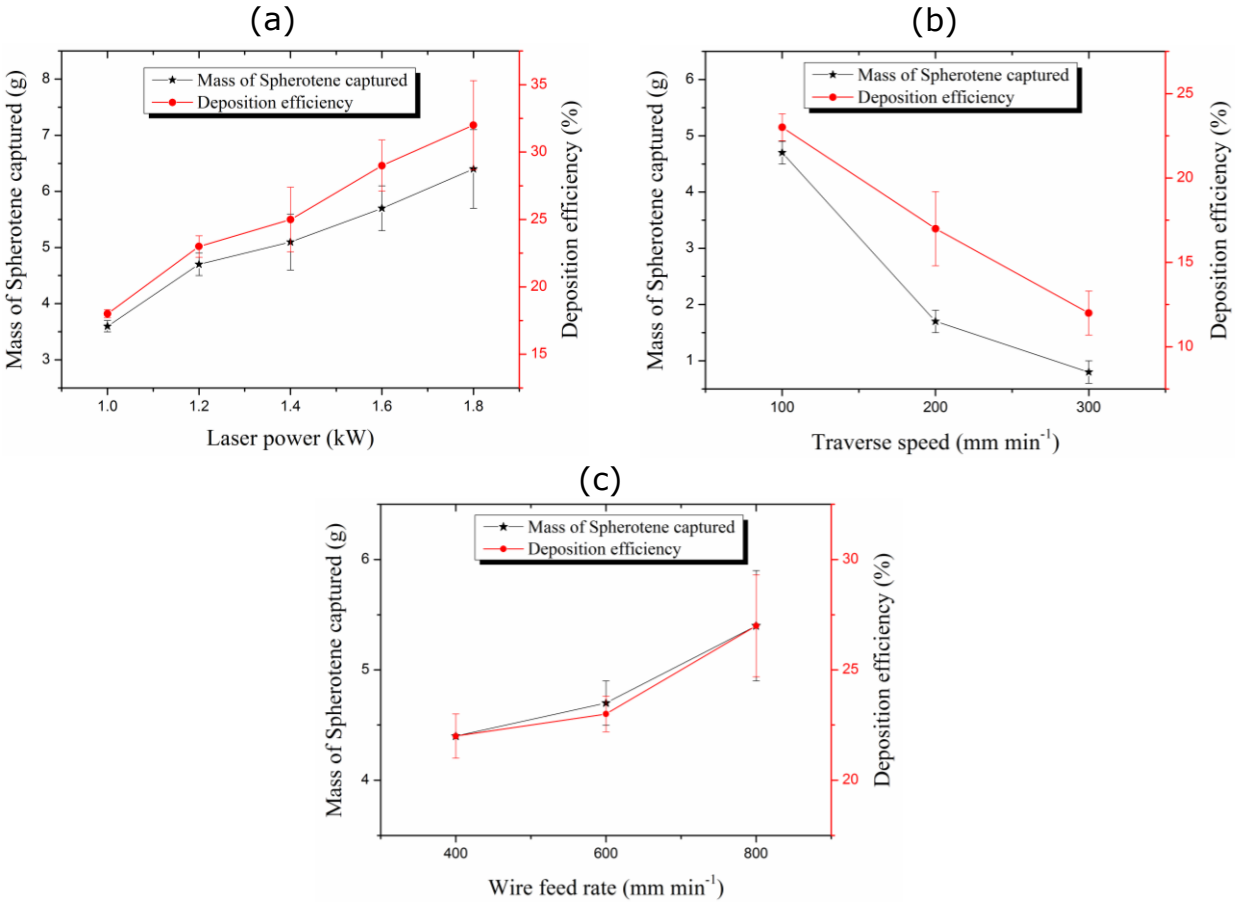

Figure 5.9: Variation of the deposition efficiency and mass of Spherotene captured in the meltpool with the processing parameters assuming no carbide dissolution

5.5.2 Amount of Spherotene dissolution in the composite track

In this study, the dissolution ratio, as presented in Table 5.4, is considered to give relative amount of Spherotene dissolution at each processing condition. The dissolution ratio (%) was found by dividing the volume fraction of Spherotene dissolved by the volume fraction of

Spherotene captured. The procedure for determining the volume fraction of Spherotene dissolved and captured is outlined below.

- The volume fraction of Spherotene dissolved equals the difference between the volume fraction Spherotene captured and retained
- The volume fraction of Spherotene retained was measured using image processing analysis (image J)
- The volume fraction of Spherotene captured equals the volume of Spherotene captured divided by the total track volume (volume of Spherotene captured + volume of Inconel 625 wire deposited).

Detailed procedures about these calculations are contained in Chapter 3.10 and the results are presented in Table 5.4. As shown in Table 5.4, the typical track deposited at high energy setting (1080 J mm^{-1}, corresponding to point W) has the highest dissolution ratio of 57%. Relating the dissolution ratio to the BSE/SEM track images shown in Figure 5.8a-b, it is believed that, at this cladding condition, the Spherotene particles suffered intensely from laser beam energy. This had caused the smaller Spherotene particles to dissolve completely while the larger particles dissolved to smaller sizes.

Conversely, in the case of the composite track formed at 720 J mm^{-1} (i.e. low energy setting corresponding to point Z), the retained Spherotene particle was of higher number density and appeared relatively larger in the cross-sectioned track, as shown in Figure 5.8c-d. This indicates low Spherotene dissolution which is confirmed by the lower dissolution ratio of 18%, as presented in Table 5.4.

Table 5.4: Summary of the analysis of the Spherotene dissolution in the composite tracks

(Density of the Inconel 625 wire 'ρ_{wire}' = 8.44 × 10^{-3} g mm^{-3}, Density of Spherotene 'ρ_{powder}' = 16.3 × 10^{-3} g mm^{-3})

	a	b	c	d	e = $\frac{d}{(\rho_{wire} \times 80)}$	f	g = $\frac{f}{(\rho_{powder} \times 80)}$	h = $\frac{g}{(g+e)}$	i	j = $\left(\frac{h-i}{h}\right) \times 100$
Laser power (kW)	**Traverse speed (mm min^{-1})**	**Wire feed rate (mm min^{-1})**	**Energy per unit length of track (J mm^{-1})**	**Mass of wire deposited in 80 mm track length (g)**	**Volume of wire deposited (mm^3 mm^{-1})**	**Mass of Spherotene captured in 80 mm track length (g)**	**Volume of Spherotene captured ($mm^3 mm^{-1}$)**	**Volume fraction of Spherotene captured (%)**	**Volume fraction of Spherotene retained (%)**	**Dissolution ratio**
W 1.8	100	600	1080	4.6	6.8	6.4 ± 0.7	4.9 ± 0.5	42 ± 2.6	18 ± 2.4	57
1.8	100	800	1080	6.1	9.0	7.0 ± 0.3	5.4 ± 0.3	37 ± 1.1	17 ± 0.9	54
1.8	100	1000	1080	7.6	11.3	7.7 ± 0.3	5.9 ± 0.2	34 ± 0.8	16 ± 1.2	51
1.8	200	600	540	2.3	3.4	2.4 ± 0.5	1.8 ± 0.4	35 ± 4.4	17 ± 0.9	50
1.8	300	600	360	1.5	2.3	1.0 ± 0.2	0.7 ± 0.1	25 ± 3.7	16 ± 0.9	34
1.6	100	600	960	4.6	6.8	5.7 ± 0.4	4.4 ± 0.3	39 ± 1.6	21 ± 1.7	47
1.4	100	600	840	4.6	6.8	5.1 ± 0.5	3.9 ± 0.4	37 ± 2.2	23 ± 1.8	38
1.2	100	400	720	3.1	4.5	4.4 ± 0.2	3.4 ± 0.2	43 ± 1.1	30 ± 1.9	31
Z 1.2	100	600	720	4.6	6.8	4.7 ± 0.2	3.6 ± 0.1	35 ± 0.8	28 ± 1.5	18
1.2	100	800	720	6.1	9.0	5.4 ± 0.5	4.1 ± 0.4	31 ± 1.9	27 ± 1.4	12
1.2	200	600	360	2.3	3.4	1.7 ± 0.2	1.3 ± 0.2	28 ± 2.6	25 ± 1.1	8
1.2	300	600	240	1.3	2.0	0.8 ± 0.2	0.6 ± 0.2	23 ± 4.5	22 ± 0.9	5
1.0	100	600	600	4.6	6.8	3.6 ± 0.1	2.8 ± 0.1	29 ± 0.3	29 ± 1.1	2

Also, it can be deduced from Table 5.4 that the retained Spherotene volume fraction ranges between 16-30 vol.%. The transverse cross-sectional area of the track with the 30 vol. % of the retained Spherotene particle is shown in Figure 5.10.

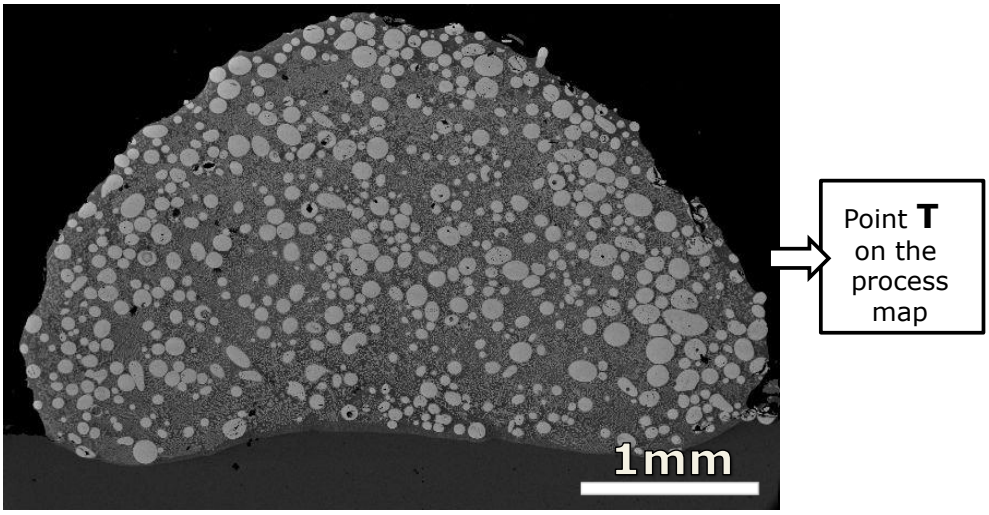

P = 1.2 kW, V = 100 mm min^{-1}, WFR = 400 mm min^{-1}, PFR = 25 g min^{-1}

Figure 5.10: SEM image showing the cross-sectioned composite laser track with 30 vol. % of retained Spherotene particle

The graphs showing the variations of the retained and captured Spherotene volume fractions, and the dissolution ratio with the processing parameters are shown in Figure 5.11. It was found the dissolution rate increases with increasing the laser power but decreases with increasing the traverse speed and wire feed rate.

The captured Spherotene volume fraction also shows positive dependency on the laser power but decreases with the traverse speed and wire feed rate. The retained Spherotene volume fraction decreases as the laser power increases because more Spherotene dissolution occurred at higher energy per unit length of track. With increasing the traverse speed, the retained Spherotene volume fraction decreased. Although lower Spherotene dissolution is expected at higher traverse speed, the decreasing powder deposition efficiency plays a role.

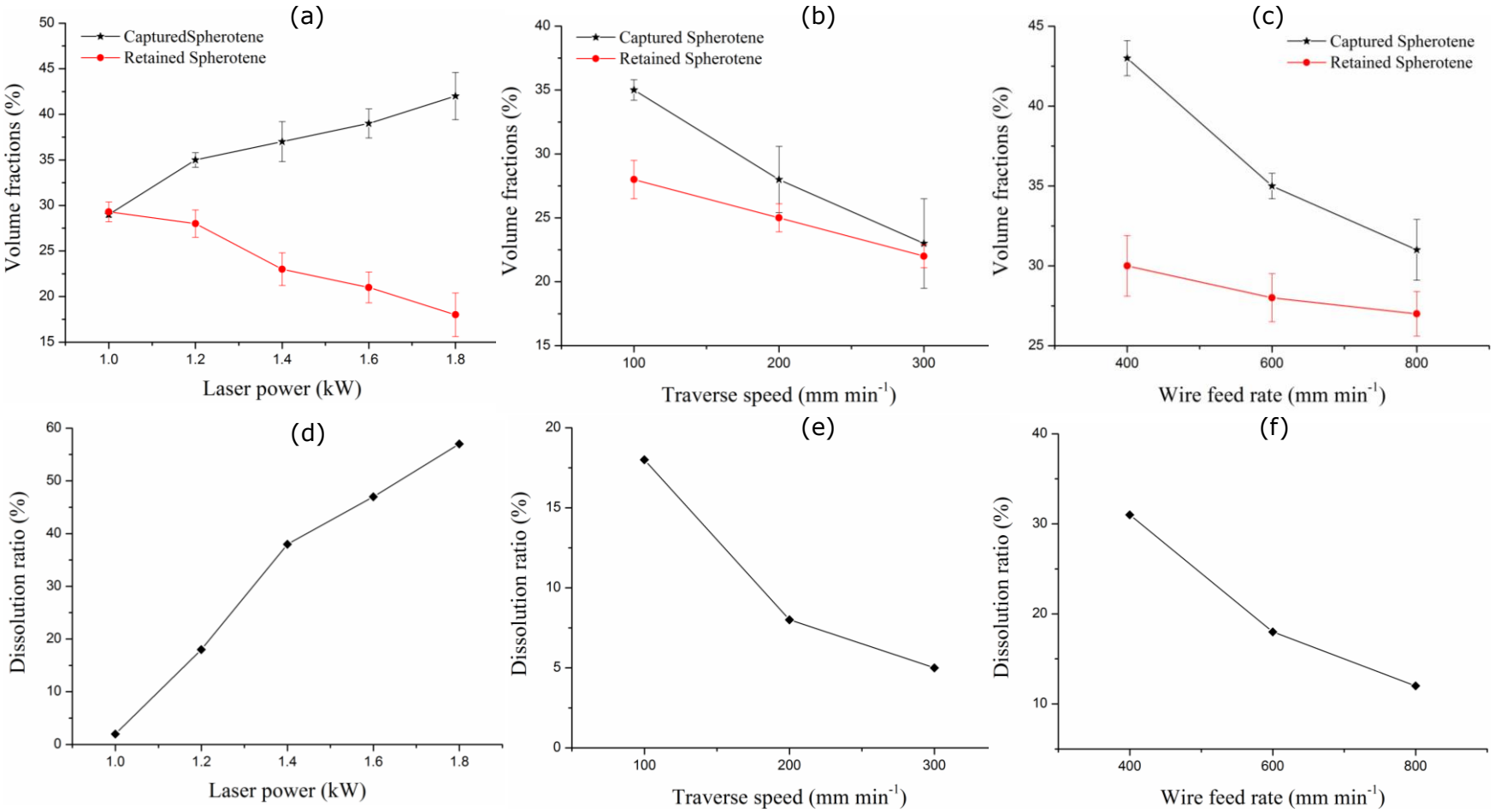

Figure 5.11: Variation of the captured and retained Spherotene volume fractions and dissolution ratio with the processing parameters: (a & d) V = 100 mm min^{-1}, WFR = 600 mm min^{-1}, PFR = 25 g min^{-1}; (b & e) P = 1.2 kW, WFR = 600 mm min^{-1}, PFR = 25 g min^{-1}, (c & f) P = 1.2 kW, V = 100 mm min^{-1}, PFR = 25 g min^{-1}

As shown in Figure 5.11, the volume fraction of the retained Spherotene particle decreases with increasing the wire feed rate. The reason is possibly due to increased deposition volume of the Inconel 625 wire at higher WFR. Though Spherotene powder deposition efficiency also increased with the WFR but the relatively higher deposition efficiency (100%) of the wire has greater impact.

5.5.3 Distribution of retained Spherotene in the composite track

The distribution of the retained Spherotene in the composites tracks was relatively uniform, for example, as shown in Figure 5.8. A more even distribution was observed at lower energy per unit length of track (e.g. at 720 J mm^{-1} corresponding to point Z on the process map). A slightly higher concentration of the retained Spherotene was seen around the periphery of the tracks formed at higher energy per unit length of track, for example 1080 J mm^{-1} corresponding to point W on the process map. At higher incident energy, more Spherotene dissolution occurred at the core of the track. This was probably due to Gaussian mode of beam delivery of the fibre laser utilised in this work (i.e. energy concentration is higher at the centre of the meltpool). Since the energy concentration at the meltpool core is higher, the surface tension is believed to be smaller compared to the periphery of the meltpool. Due to the surface tension gradient, a stirring effect called marangoni will set up. This probably caused the migration of some retained Spherotene particles from the clad core to the periphery.

Figure 5.12 presents the BSE images of the boundary and core of the composite tracks formed at 1080 J mm^{-1}. It was found that the retained Spherotene concentration decreased from the boundary to the core of the track. Also, severe dissolution of the Spherotene particles was noticed in the track core.

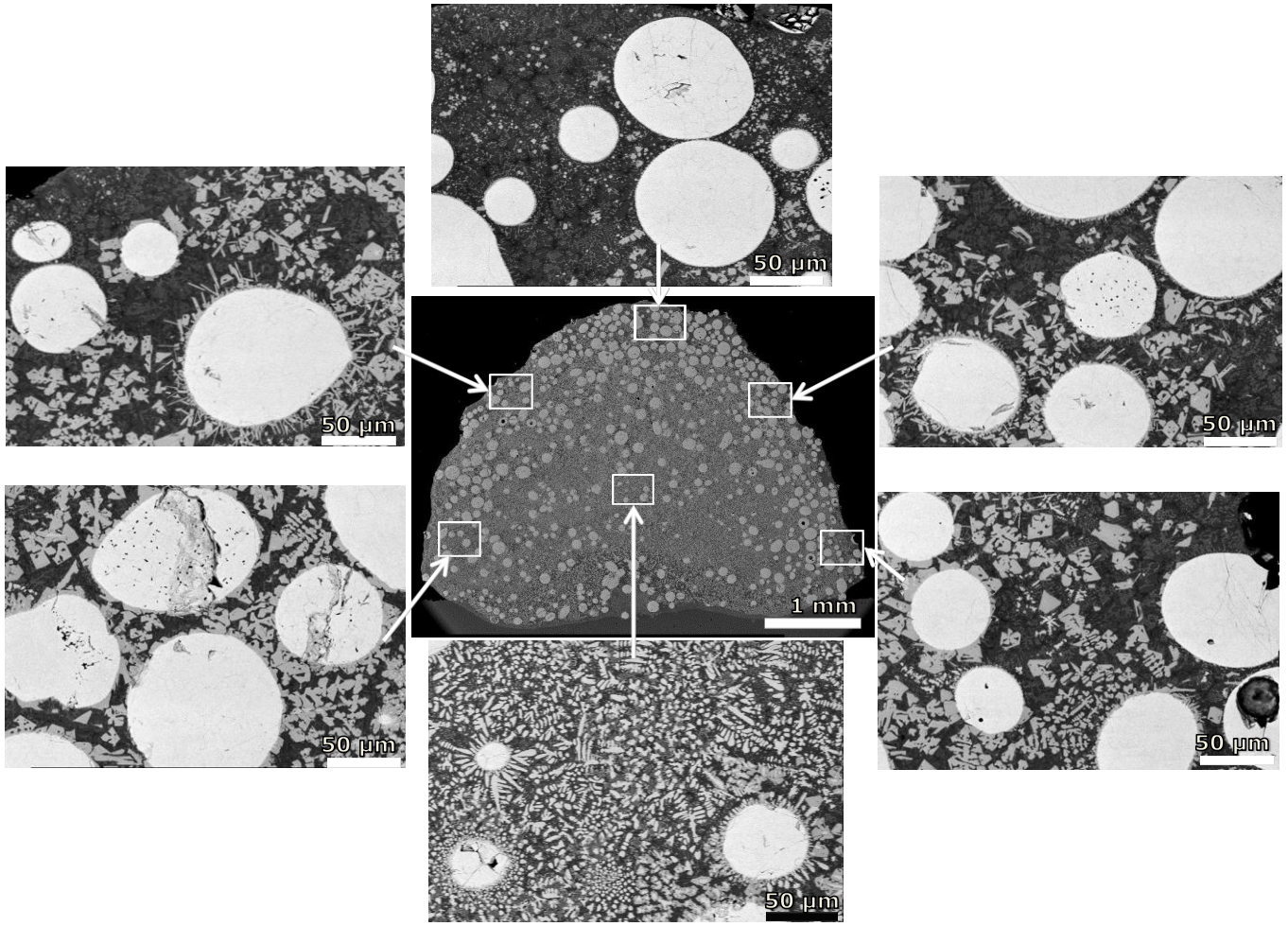

P = 1.8 kW, V = 100 mm min^{-1}, WFR = 600 mm min^{-1}, PFR = 25 g min^{-1}

Figure 5.12: SEM image showing the WC distribution and dissolution amount at the centre and boundary of a cross-sectioned track formed at high energy density

5.5.4 Spherotene powder/Inconel 625 wire matrix interfacial bonding in the composite tracks

At all processing conditions contained in region 3 of the process map, good interfacial bonding existed between the retained carbide (Spherotene) and Inconel 625 wire matrix in the composite tracks. This is evidenced by the formation of phases at the interface sections of the composite tracks, for example, as shown in Figure 5.13.

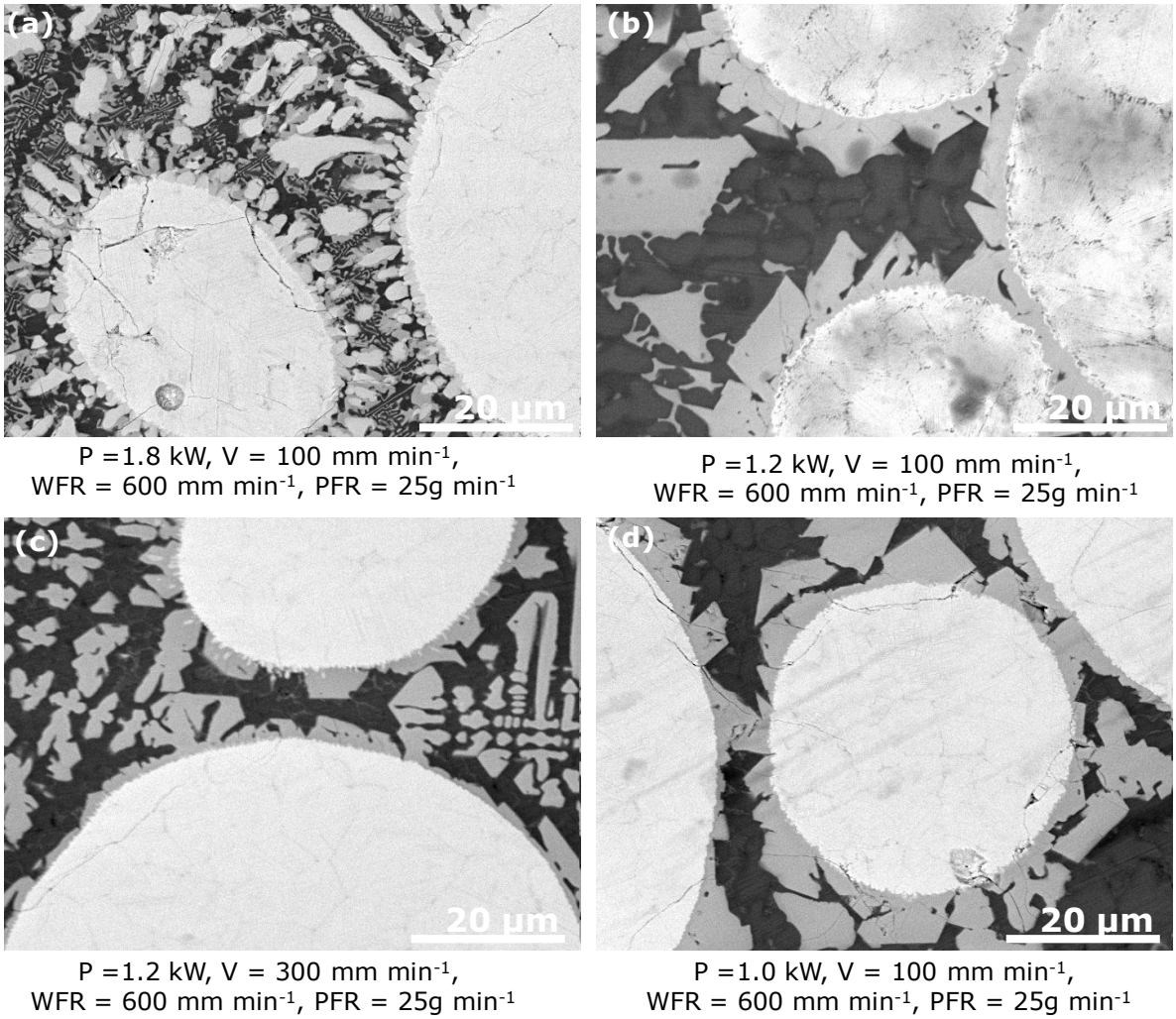

P =1.8 kW, V = 100 mm min^{-1}, WFR = 600 mm min^{-1}, PFR = 25g min^{-1}

P =1.2 kW, V = 100 mm min^{-1}, WFR = 600 mm min^{-1}, PFR = 25g min^{-1}

P =1.2 kW, V = 300 mm min^{-1}, WFR = 600 mm min^{-1}, PFR = 25g min^{-1}

P =1.0 kW, V = 100 mm min^{-1}, WFR = 600 mm min^{-1}, PFR = 25g min^{-1}

Figure 5.13: SEM/BSE images showing new phases at the interface between the retained Spherotene particle and Inconel 625 wire matrix

All the micrographs shown in Figure 5.13 were taken around the centre of the tracks cross-sections. The formation of light contrast secondary phases around the edges of the retained Spherotene powder suggests that there was partial dissolution of the powder which enhanced good bonding with the Ni-matrix. The identification of these phases in the composite tracks is reported in the next section.

5.6 Microstructural characterisation of Spherotene (WC/W_2C) powder–Inconel 625 wire composite single laser tracks

This section describes the microstructural features of the composite tracks at varying processing parameters. The results of the detailed microstructural characterisation carried out on the two typical composite tracks (corresponding to point W (1080 J mm^{-1}) and point Z (720 J mm^{-1}) on the process map shown in Figure 5.6) are presented.

5.6.1 Identification of the phases present in the composite tracks

Figure 5.14 presents the XRD spectra of the top surfaces of some selected Spherotene (WC/W_2C) powder-Inconel 625 wire composite tracks. The raw spectra containing the JCPDS file numbers of each phase are presented in Appendix C (Figure 5-8). The tracks were formed at different processing conditions (i.e. varying energy per unit length of track) corresponding to points W, X, Y and Z on the process map shown in Figure 5.6. In order to properly identify all the phases present in the composite tracks, each of the XRD samples was ground from the top surface to the mid-region because more Spherotene dissolution occurred around the track core. Table 5.5 shows the processing conditions and the phases present in the corresponding composite tracks.

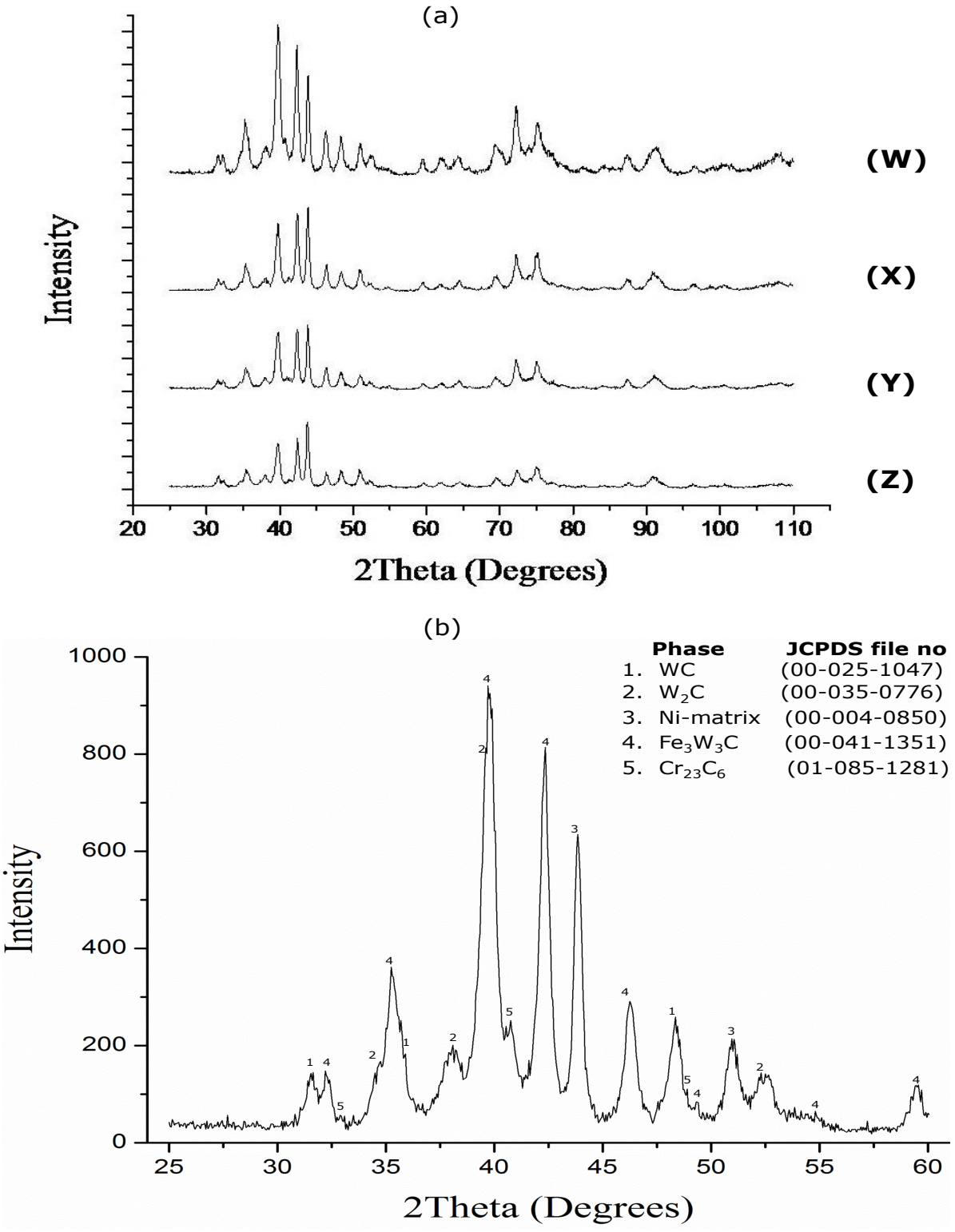

Figure 5.14: XRD spectra of the top surface of the concurrently laser deposited Spherotene (WC/W_2C) powder-Inconel 625 wire composite single tracks (a) at different parameters (b) an expanded view of W showing peaks identification.

Table 5.5: Summary of XRD profiles of the concurrently deposited Spherotene powder-Inconel 625 wire composite tracks

Point	Laser power (kW)	Traverse speed (mm min^{-1})	Wire feed rate (mm min^{-1})	Energy per unit length of track (J mm^{-1})	Phases identified
W	1.8	100	600	1080	WC, W_2C, Ni-matrix, Fe_3W_3C, $Cr_{23}C_6$
X	1.6	100	600	960	WC, W_2C, Ni-matrix, Fe_3W_3C, $Cr_{23}C_6$
Y	1.4	100	600	840	WC, W_2C, Ni-matrix, Fe_3W_3C, $Cr_{23}C_6$
Z	1.2	100	600	720	WC, W_2C, Ni-matrix, Fe_3W_3C, $Cr_{23}C_6$

The XRD results presented in Figure 5.14 reveal that the composite tracks are constituted of five different phases. The phases are: Ni-matrix (FCC), WC (hexagonal), W_2C (hexagonal), Fe_3W_3C (FCC) and $Cr_{23}C_6$. The peaks occurred at similar positions of 2θ in all the spectra. However, clear differences in the spectra are observed in the conditions corresponding to point W (1080J mm^{-1}) and spectrum corresponding to Z (720 J mm^{-1}). Possibly, the reason may be the difference in the volume fractions of the Spherotene captured which have dissolution ratios of 57 and 18% respectively.

5.6.2 Elemental composition of the phases identified in the composite tracks

Back scattered electron images of the two typical tracks (at 1080 J mm^{-1} (W) and 720 J mm^{-1} (Z)) showing the phases present are revealed in Figure 5.15. The white contrast phase with near circular shape marked as ‘A’ is seen to be of high number density and relatively uniformly distributed in the tracks cross-sections. This phase is believed to be the retained Spherotene (WC/W_2C) because of its light contrast, circular shape and its distribution within the tracks cross-sections.

The dark phase dendritic core which is marked as ‘B’ is observed to be continuous throughout the track area. At the boundaries in-between the continuous dark phase dendrites

are film-like light contrast precipitate. This is marked as ‘C’ in Figure 5.15. The light grey phase with a trapezoidal shape marked as ‘D’ appears to be randomly distributed all over the track cross-section whereas the smaller sized but a light angular phase marked as ‘E’ is predominantly seen around the edges of the retained WC/W_2C. Due to their light contrast and angular shapes, the phases marked as ‘D’ and ‘E’ are thought to be secondary carbides formed as a result of the dissolution of the Spherotene particles. The phase marked E is clearly seen and predominant around the retained Spherotene in the track formed at 1080 J mm^{-1} but is rarely found in the track formed at lower energy per unit length of track (720 J mm^{-1}).

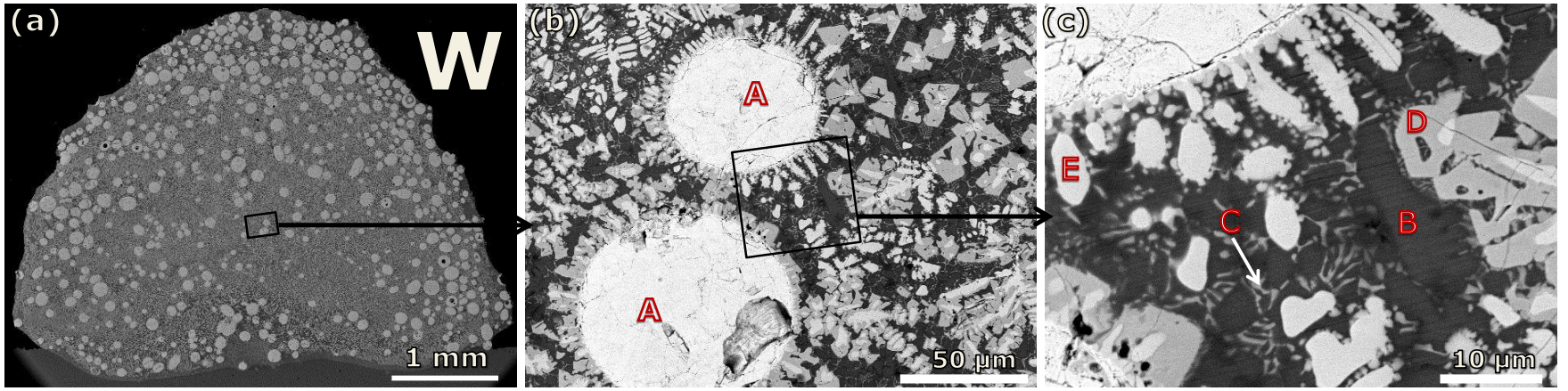

P = 1.8 kW, V = 100 mm min^{-1}, WFR = 600 mm min^{-1}, PFR = 25 g min^{-1}

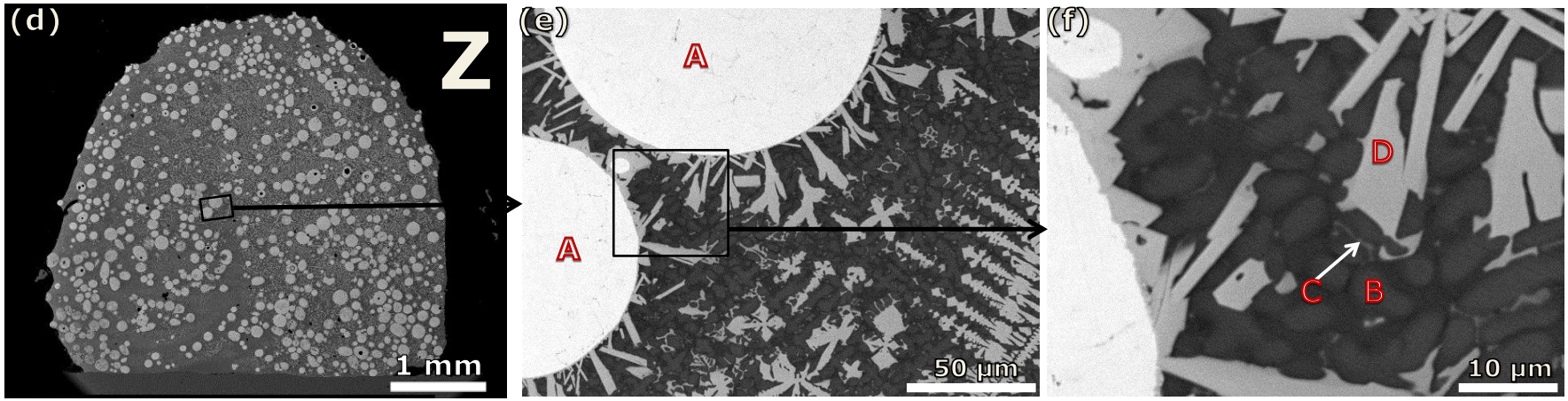

P = 1.2 kW, V = 100 mm min^{-1}, WFR = 600 mm min^{-1}, PFR = 25 g min^{-1}

Figure 5.15: BSE/SEM images showing the identified phases present in the cross-sections of the typical composite tracks formed at (a) 1080 J mm^{-1}, and (b) 720 J mm^{-1}

Table 5.6: Chemical composition (wt. %) of the phases identified in Figure 5.12

Symbol	Probable Phase	W	C	Cr	Fe	Ni	Nb	Mo
A	WC/W_2C	92.7 ± 0.9	7.3 ± 0.4	-	-	-	-	-
B	Ni matrix	13.0 ± 1.1	-	14.2 ± 1.1	7.9 ± 0.5	61.2 ± 1.3	1.3 ± 0.7	2.5 ± 0.5
D	Fe_3W_3C	63.2 ± 2.6	-	8.8 ± 0.9	2.5 ± 0.2	19.0 ± 1.1	-	6.5 ± 0.7
E	W_2C	89.6 ± 3.2	-	7.3 ± 0.6		3.2 ± 0.8	-	-

The results of EDAX analysis conducted on each of the phases present in the composite tracks are presented in Table 5.6. All the data presented in Table 5.6 are averages of at least five measurements.

Area scan analysis on the phase marked ‘A’ produced an average composition of 93 wt. % W and 7 wt. % C. This phase can be categorically identified as WC/W_2C due to the fact that its composition (wt. %) is similar to that of the Spherotene particle (as received) (see Table 5.1). The dark phase marked as ‘B’ was also identified as Ni-matrix because of its high Cr (14 wt. %) and Ni (61 wt. %) contents. It is also the only phase having some quantity of Nb in its composition. Spherotene dissolution observed in the composite track is believed to have caused the Ni matrix to be enriched in W (13 wt. %). The phase also contains about 8 wt. % of Fe which must have resulted from the substrate dilution.

The EDAX result obtained for the tiny phase marked ‘C’ in Figure 5.14 was believed to be inaccurate because of the larger interaction volume electron beam. It was considered that the compositions of the surrounding phases especially Ni-matrix dendrites were picked therefore the result was not included in Table 5.6. However, the phase could be $M_{23}C_6$ ($Cr_{23}C_6$) because it precipitated as films at the grain (Ni-matrix dendrites) boundaries. In the literature, $M_{23}C_6$ has always appeared as a light contrast small precipitate existing usually at the grain boundaries of continuous Ni-matrix [91, 94]. Since this phase appeared predominantly in the interdendritic regions, it is termed eutectic carbide.

The average composition (wt.%) of the light grey trapezoidal phase ‘D’ shows that it contained significant amount of W (63%) with some traces of other elements like Cr (9%), Fe (3%), Ni (19%) and Mo (7%). C was excluded because of the limitation of the SEM/EDAX technique for accurate quantification of the element. This phase is thought to be Fe_3W_3C (M_6C) because it contains noticeable quantity of W and Fe. The presence of other elements

such as Cr, Mo and Ni in its composition is normal because M element in M_6C (FCC) is generally W with some solubility for Fe, Cr, Ni and Mo [29]. Also, M_6C (FCC) is usually distributed randomly which is the case for the light grey trapezoidal phase 'D' in the composite track. Fe_3W_3C (considered to be the phase D) is believed to have precipitated, during the solidification of the track, from a Ni rich molten phase which contained significant quantities of dissolved W, C and Fe.

The result of the EDX spot analysis carried out on the phase marked as 'E' is also presented in Table 5.6. The composition of the phase indicates that it is rich in W (89 wt. %). The light phase E also contains some amount of C but it was not quantified because of the limitation of SEM/EDAX technique to give accurate composition of carbon in a test sample. The fact that the phase is predominantly found around the edges of the WC/W_2C phase suggests that it is a product of Spherotene dissolution. Therefore, the phase E is possibly W_2C with other elements in solute.

5.6.3 W enrichment and Cr depletion in the composite tracks

The W and Cr compositions in the composite tracks were measured by determining the composition of the matrix in-between the retained Spherotene using SEM/EDAX technique. Area scans of about 50 × 50 μm were performed. The result, as shown in Table 5.7, is the average of 5 measurements. From table 5.7, it is observed that the more the matrix is enriched in W element the more the Cr element is depleted from the matrix.

The variations of the W enrichment and Cr depletion with the processing parameters were plotted and are shown in Figure 5.16.

Table 5.7: Elemental composition of the matrix in-between the retained Spherotene particles

Laser power (kW)	Traverse speed (mm min^{-1})	Wire feed rate (mm min^{-1})	Energy per unit length of track (J mm^{-1})	W	Cr	Ni	Fe	Mo	Nb
1.8	100	600	1080	50 ± 0.5	11 ± 0.2	29 ± 0.4	5 ± 0.3	4 ± 0.2	2 ± 0.1
1.6	100	600	960	44 ± 0.2	12 ± 0.4	33 ± 0.5	4 ± 0.1	4 ± 0.4	1 ± 0.6
1.4	100	600	840	41 ± 1.8	13 ± 0.4	36 ± 1.4	2 ± 0.3	5 ± 0.5	2 ± 0.3
1.2	100	400	720	51 ± 0.18	11 ± 0.2	29 ± 2.5	5 ± 1.8	4 ± 0.6	1 ± 0.3
1.2	100	600	720	35 ± 2.5	14 ± 0.6	42 ± 1.8	1 ±0.3	6 ± 0.3	2 ± 0.2
1.2	100	800	720	31 ± 2.3	16 ± 1.1	45 ± 2.0	0.2 ± 0.1	6 ± 0.2	2 ± 0.1
1.2	200	600	360	33 ± 1.6	15 ± 0.4	43 ± 1.1	2 ± 0.1	6 ± 0.3	2 ± 0.2
1.2	300	600	240	30 ± 2.6	16 ± 0.6	44 ± 2.1	2 ± 0.2	6 ± 0.5	2 ± 0.3
1	100	600	600	32 ± 0.9	16 ± 0.2	44 ± 0.4	0.3 ± 0.1	6 ± 0.1	2 ± 0.4

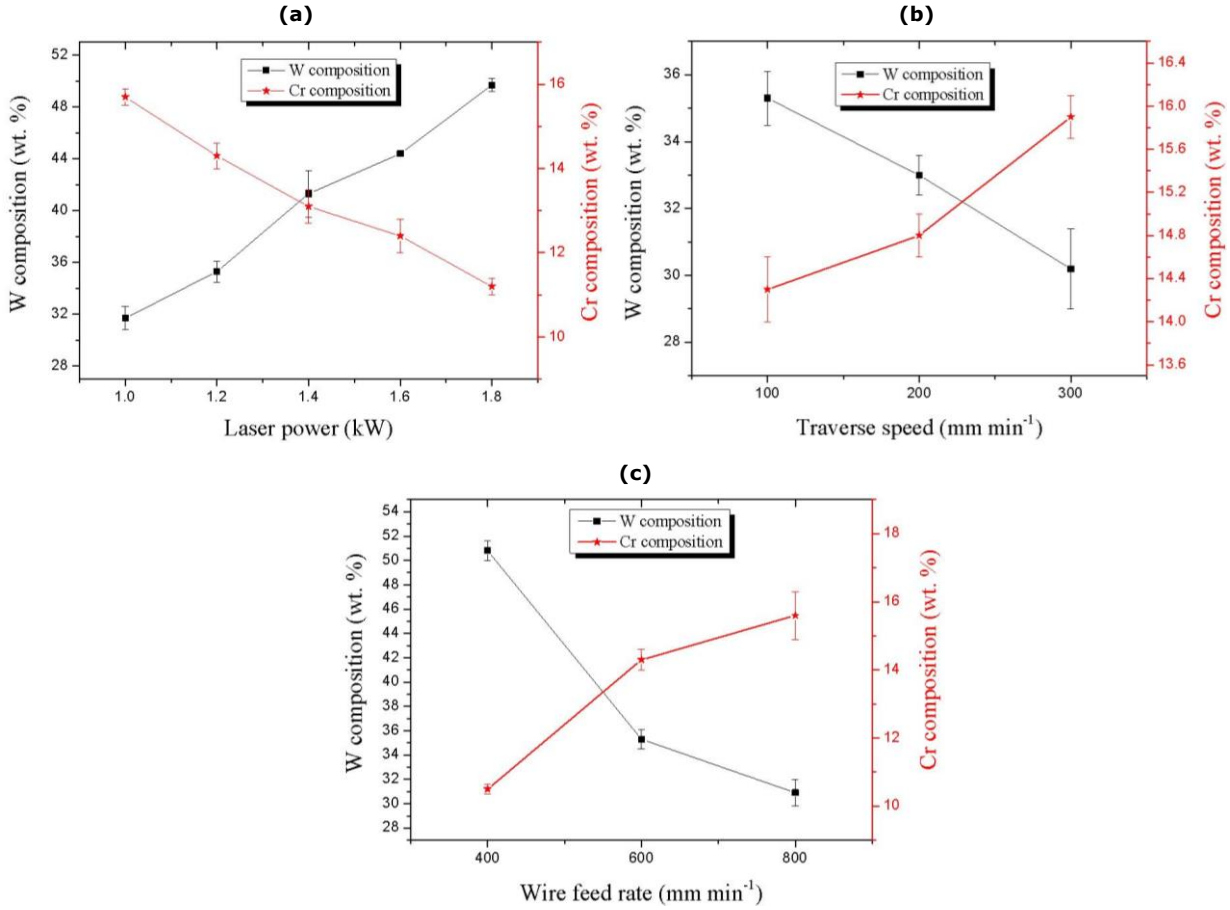

Figure 5.16: Plots of the variation of W and Cr content of the WC/W_2C powder-Inconel 625 laser tracks matrix with the processing parameters. (a) V = 100 mm min^{-1}, WFR = 600 mm min^{-1}, PFR = 25 g min^{-1}. (b) P = 1.2 kW, WFR = 600 mm min^{-1}, PFR = 25 g min^{-1}. (c) P = 1.2 kW, V = 100 mm min^{-1}, PFR = 25 g min^{-1}

The W content of the matrix, after cladding, increased with the laser power but decreased with the traverse speed. This simply confirms the previous observation that the Spherotene dissolution increased with increasing energy per unit length of track (= 60P/V). Conversely, the Cr composition of the composite tracks decreased with increasing the laser power but increased with increasing the traverse speed. This indicates that increased Spherotene dissolution increases the Cr depletion.

From Figure 5.16c, it can be deduced that, with this laser cladding set-up, increasing wire feed rate reduced the W composition but increased the Cr content of the composite tracks.

5.7 Micro-hardness of the composite laser tracks

Vickers micro-hardness measurements of the track samples were made randomly on their cross-sectional areas and the results are presented in the Table 5.8. Compared with the hardness value of the stainless steel plate (201 $HV_{0.3}$) and laser deposited Inconel 625 wire and Inconel 625 powder single tracks (ranging between 224 and 248 $HV_{0.3}$), the hardness of the matrix of the composite track ranged from 540-690 $HV_{0.3}$. The average Spherotene particle hardness in the composite track ranged between 2100 and 2400 $HV_{0.3}$. The improved hardness demonstrated by the matrix of the composite tracks is due to the injection of Spherotene particles whose dissolution resulted in the formation of hard secondary phases (W_2C Fe_3W_3C and $Cr_{23}C_6$) [94] in the tracks.

Table 5.8: A summary of the micro-hardness measurement for the WC powder-Inconel 625 wire composite tracks

Processing parameters				Micro-hardness value ($HV_{0.3}$)	
Laser power (kW)	**Transverse speed (mm min^{-1})**	**Wire feed rate (mm min^{-1})**	**Powder feed rate (g min^{-1})**	**Matrix**	**WC particle**
1.8	100	600	25	693 ±68	2276 ±363
1.6	100	600	25	636 ±68	2267 ±226
1.4	100	600	25	619 ±62	2113 ±209
1.2	100	600	25	611 ±55	2146 ±193
1	100	600	25	563 ±60	2235 ±260
1.2	100	400	25	655 ±81	2332 ±200
1.2	100	800	25	593 ±71	2308 ±431
1.2	200	600	25	581 ±61	2408 ±167
1.2	300	600	25	560 ±73	2153 ±212

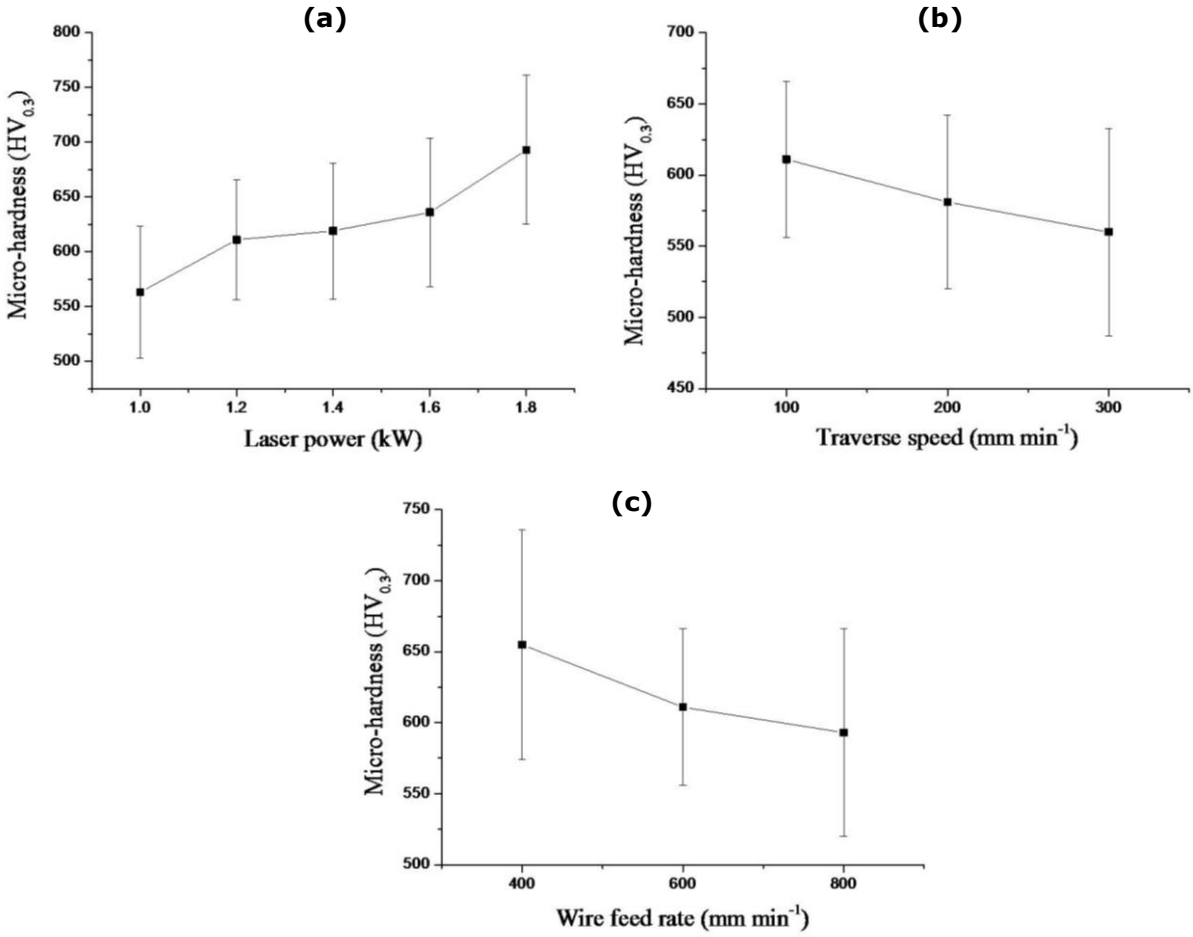

Figure 5.17: Plots of the variation of the WC powder-Inconel 625 laser tracks matrix micro-hardness with the processing parameters. (a) V = 100 mm min^{-1}, WFR = 600 mm min^{-1}, PFR = 25 g min^{-1}. (b) P = 1.2 kW, WFR = 600 mm min^{-1}, PFR = 25 g min^{-1}. (c) P = 1.2 kW, V = 100 mm min^{-1}, PFR = 25 g min^{-1}

The results are graphically presented in Figure 5.17**.** It is evident that the hardness of the composite tracks varied directly with the laser power but inversely with the traverse speed. More so, the hardness was found to vary inversely with the wire feed rate. The variations can be related to the amount of Spherotene dissolution in the tracks at each processing condition. The hardness of the retained Spherotene particle did not show any particular pattern with the processing parameters. However, it was within the bracket of 2100 and 2400 $HV_{0.3}$ for all the cross-sectioned tracks.

5.8 Deposition of overlapped-track layers of WC powder-Inconel 625 wire composite laser coatings

Overlapped-track composite layers were formed from the single composite tracks deposited at the selected parameters listed in Table 5.9. Most of the conditions in Table 5.9 were chosen at low laser power (1.2 kW) because low Spherotene dissolution and significantly low substrate dilution (see Table 5.7) were noticed at low energy input.

Table 5.9: Laser cladding parameters of the composite single tracks selected for overlapped-track layer depositions

Laser power (kW)	Traverse speed (mm min^{-1})	wire feed rate (mm min^{-1})	Powder feed rate (g min^{-1})
1.0	100	0.6	25
1.2	100	0.6	25
1.2	100	0.4	25
1.2	200	0.6	25
1.2	300	0.6	25
1.8	100	0.6	25

60% overlapping ratio was used for all the multi-track cladding. As seen in Figure 5.18, the pictures of the top surface of the overlapped-track layers show that they are nearly flat and free of cracks. Each of the deposited layers was about 25-30% thicker than its corresponding single track.

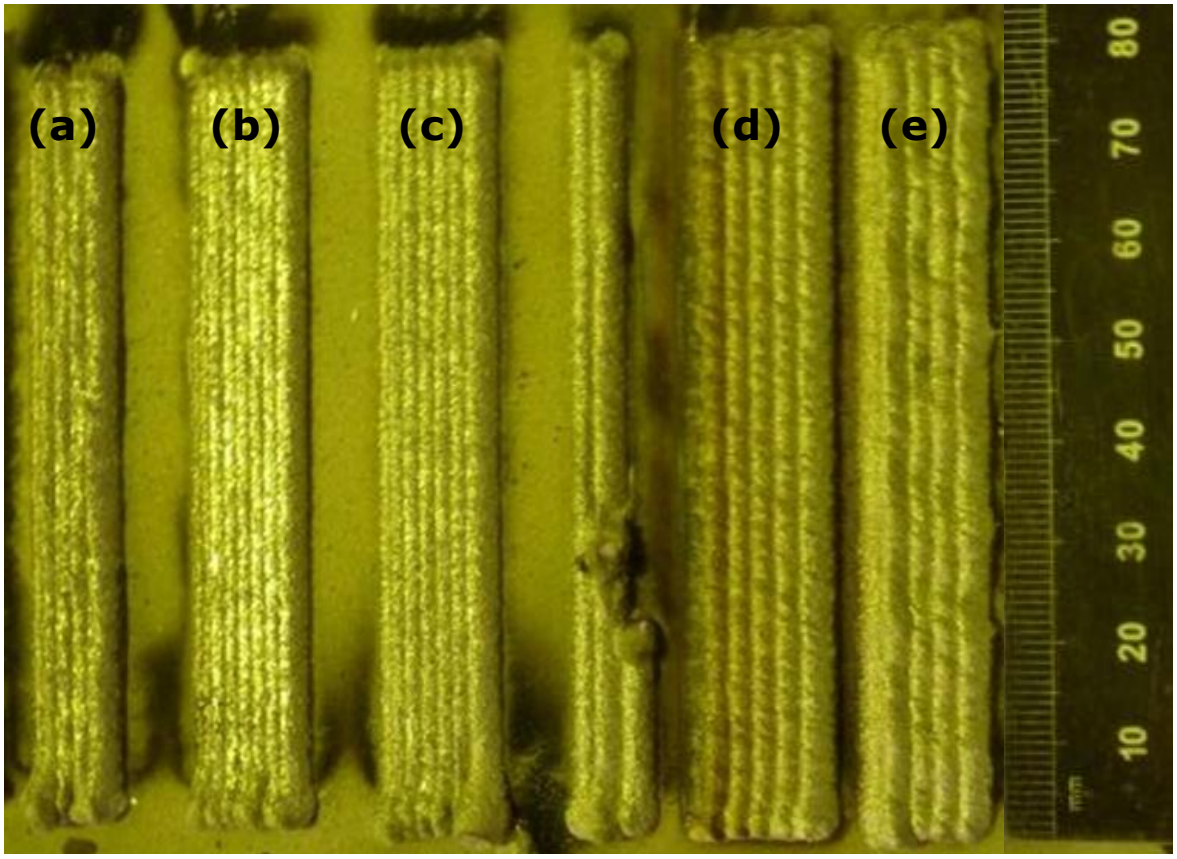

Figure 5.18: As-deposited overlapped track-layers of WC/W_2C (Spherotene) powder-Inconel 625 wire composite showing nearly flat and crack-free top surface

The transverse and longitudinal cross-sections of each the overlapped-track layers were examined for defects such as pores, cracks and good fusion with the substrate. As seen in Figure 5.19, the composite layers formed at laser power of 1.0 kW and 1.2 kW with a combination of 100 mm min^{-1} traverse speed and 600 mm min^{-1} wire feed rate showed poor fusion with the substrate. This was considered unsuitable as poor fusion often leads to low coating-substrate bonding strength and sometimes delamination of the coating from the base component. The poor fusion found in both layers was due to the fact that the total material delivery volume was too high for the available energy input.

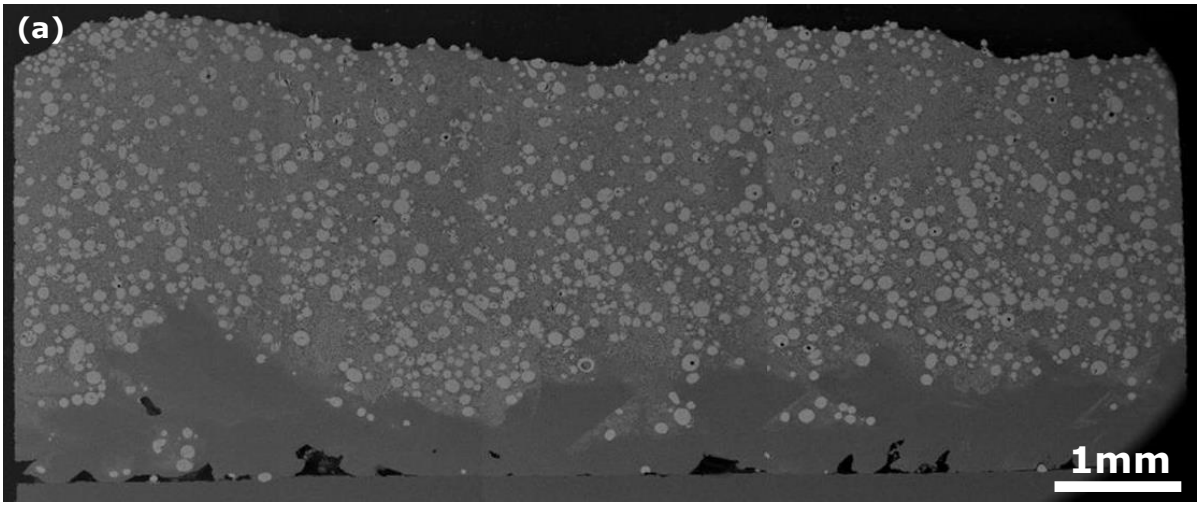

P = 1.0 kW, V = 100 mm min^{-1}, WFR = 600 mm min^{-1}, PFR = 25 g min^{-1}

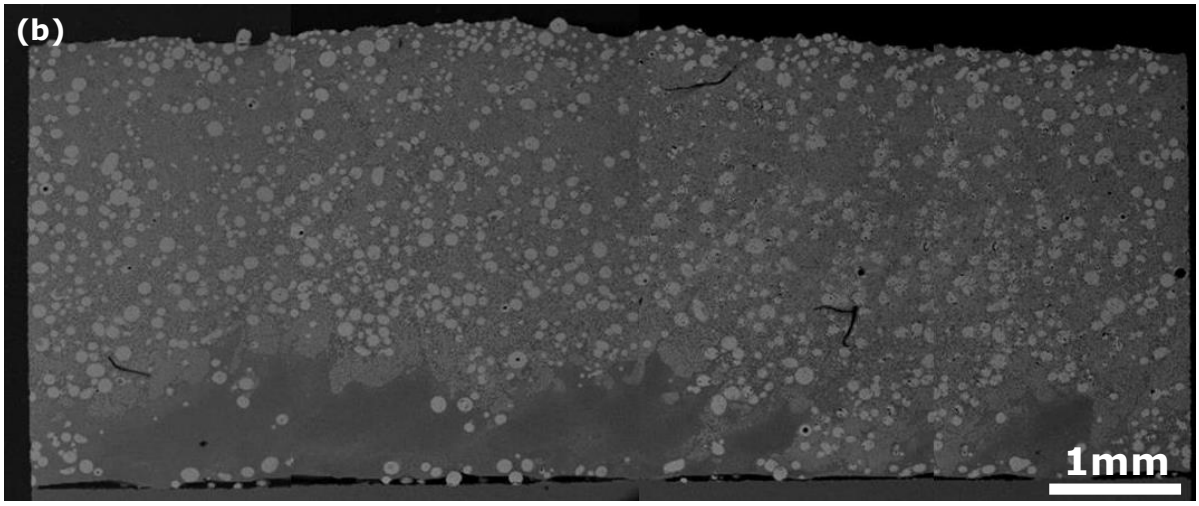

P = 1.2 kW, V = 100 mm min^{-1}, WFR = 600 mm min^{-1}, PFR = 25 g min^{-1}

Figure 5.19: Longitudinal views showing poor fusion between the overlapped-track coating and the substrate due to high material deposition volume at low incident energy

As shown in Figure 5.20, fully bonded overlapped-track layers were formed at all other processing conditions listed in Table 5.9. All the deposited layers were free of cracks and pores within the track layer. Absence of pores in the layer and good layer-substrate fusion shows that there was sufficient melting of the delivered material by the incident energy at these conditions.

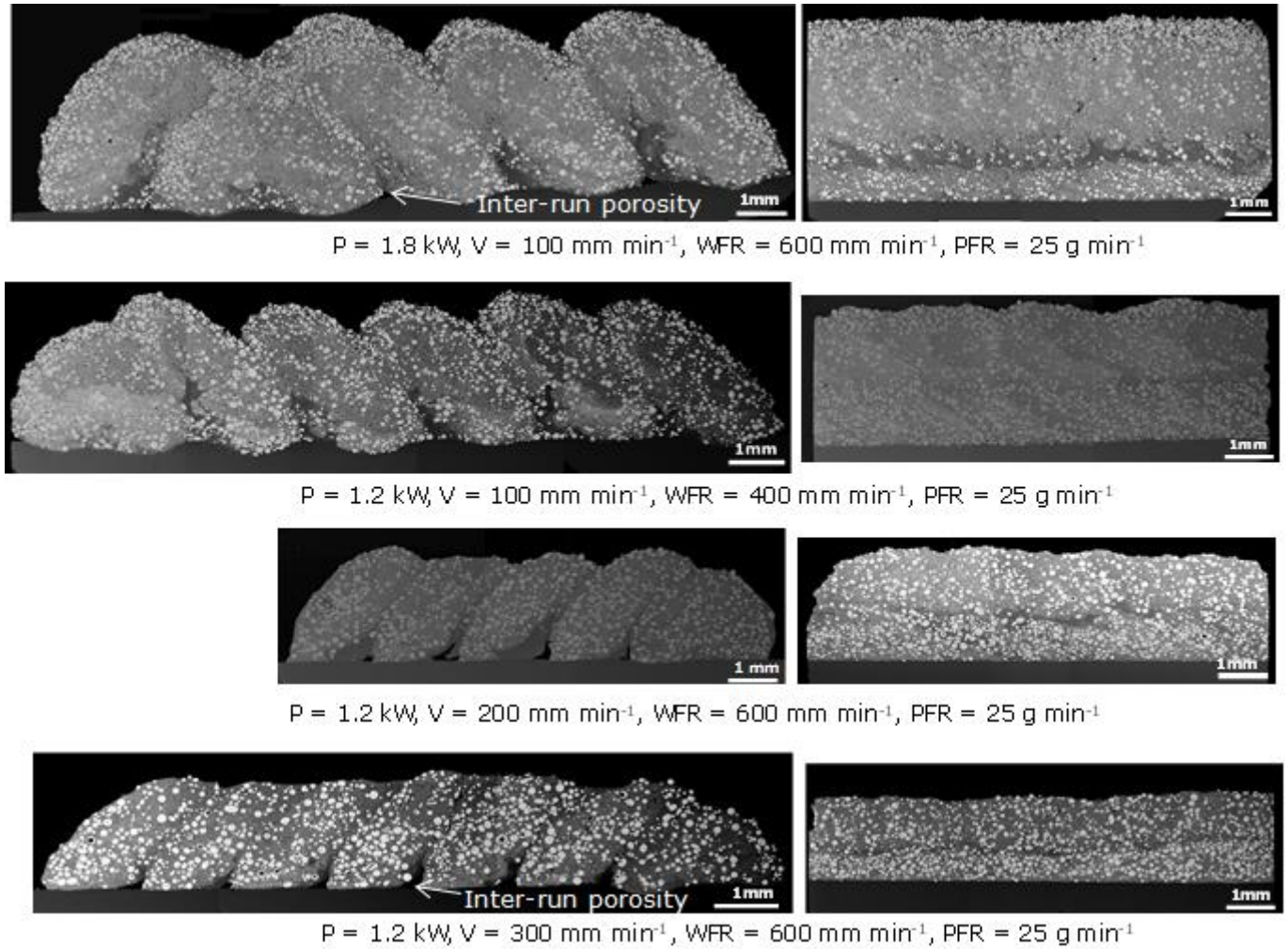

Figure 5.20: Transverse and longitudinal sections of overlapped-track composite coatings showing good fusion with the substrate and absence of cracks

Inter-run porosities were seen at the track-substrate region of some of the layers. There was a high concentration of the retained Spherotene particle at the top of the layer formed at 1.8 kW. However, even distribution of the retained was noticeable at 1.2 kW. The better distribution found at low energy input can be attributed to reduced Spherotene dissolution at the track-core.

Discussion

5.9 Concurrent laser cladding of Spherotene (WC/W2C) powder-Inconel 625 wire composite-Process characteristics

From the results presented in Figure 5.6, it was revealed that it is possible to deposit continuous single laser composite tracks via concurrent feeding of Spherotene powder and Inconel 625 wire. However, continuous tracks were not obtained at some cladding conditions because smooth wire deposition was not possible at those conditions. As explained previously in Chapter 4.2, wire dripping and wire stubbing occurred whenever the wire feed rate relative to the energy per unit of track is too low and excessively high, respectively.

Due to the injection of Spherotene powder, there was rightward shift in the process map shown in Figure 4.4 (Inconel 625 wire process characteristics) compared with the process map developed for the process characteristics of concurrently fed Spherotene powder-Inconel 625 wire laser cladding, as shown in Figure 5.6. The main effect of the Spherotene powder injection is that it reduced the amount of energy absorbed by the Inconel 625 wire outside the meltpool. This is because the powder covered some area fraction of the feed wire (due to powder spreading) outside the meltpool, therefore, interrupting the laser beam from reaching the feed wire.

For this reason, at wire feed rates at which wire dripping was found in the case of Inconel 625 wire laser cladding, there was higher tendency that smooth wire deposition may be found at the same condition during concurrent laser cladding of Spherotene powder-Inconel 625 wire composite. The combination of laser power and traverse speed remained the same. Also, the injection of Spherotene powder increased the propensity for wire stubbing occurring at some conditions where smooth wire deposition was observed for Inconel 625 wire laser cladding.

Consequently, there was rightward shift in the process map of Inconel 625 wire laser cladding with the concurrent injection of Spherotene powder.

5.10 Cracking phenomenon

The presence of residual stress has been identified as the main cause of cracking in metal matrix composite (MMC) coatings. Fracture occurs whenever the residual stress is more than the strength (toughness) of the matrix of the coating [72]. In this study, the total residual stress built up during meltpool solidification is considered as the sum of the effects of the thermal stress and compressive stress due to volume expansion. The volume expansion occurred because of the Spherotene dissolution leading to the formation of secondary carbides in the track. The increase in the amount of these carbides is believed to have resulted in the development of compressive stress during meltpool solidification. Also, thermal stress is an inherent characteristic of laser cladding since rapid solidification and high cooling rates are typical of the process. The thermal stress is thought to be higher during rapid solidification of composite meltpool of this type because of the formation of large volume fraction of different secondary carbides with entirely different coefficients of expansion [72, 114]. From this explanation, it can be established that the more the Spherotene dissolution, the higher the thermal stress and compressive stress built up during meltpool solidification. Now, the presence of cracks in the composite laser tracks formed at PFR of 35g min^{-1}, as shown in Figure 5.5 (a, b), shows that the total residual stress built up as a result of Spherotene dissolution was very high. It was higher than the toughness of the matrix therefore cracks were found in most of the tracks formed at this value of PFR. When the PFR was 25 g min^{-1}, there was a lower amount of Spherotene captured in the meltpool, for example, as seen in Figure 5.5 (c, d). The Spherotene dissolution was reduced and there was a decrease in the amount of secondary carbides formed. Consequently, the residual stress was

lower, even, lower than the toughness of the Inconel 625 matrix because cracks were not found in nearly all the tracks formed at this value of PFR (25 g min^{-1}).

5.11 Pore formation

Spherotene powder-Inconel 625 wire single laser tracks: The absence of pores in the continuous single laser tracks shows that, at every cladding condition, the combination of laser power and traverse speed are suitable for complete melting of the total volume of wire and powder deposited. Apart from wrong choice of the processing condition, porosity can result from the entrapment of gas within the meltpool. According to Zhou et al. [72], pores were found at the clad-substrate interface and near the surface region of the laser cladded WC/Ni alloy coatings. The presence of pores in the coatings was considered to be caused by the entrapment of gas bubbles in the track. The bubbles could not escape due to the larger WC particles sinking to the bottom of the pool. Also, the bubbles do not have enough time to flee from the molten pool because laser cladding is characterised with rapid solidification. However, in this work, gas entrapment effect is absent or not significant because no pores were found in the continuous composite tracks. In the work of Zhou et al. [72], gas bubbles may have been trapped in the powder during mixing of the WC and the Ni powders prior the laser deposition. In this present study, there was no pre-mixing of powder and even, the Spherotene powder captured in the meltpool was of lower volume fraction compared with the Inconel 625 wire. The possibility of gas being captured in the feed wire is low therefore the chances of gas bubble, hence, pores formation in the solidifying track is low. The fact that the laser processing was carried out in an argon filled transparent enclosure is another reason for the absence of gas bubble in the meltpool.

Spherotene powder-Inconel 625 wire overlapped-track layers: The overlapped layers of the composite are free of pores within the coating layers. This, as explained above, indicates

that the selected processing conditions for the depositions were right and there was no gas entrapped in the meltpool. However, the occurrence of inter-run porosities at the base of the overlapped region in some of the layers is due to poor geometrical qualities including low aspect ratio and high contact angle of the single tracks from which the layers were formed.

5.12 Spherotene powder deposition efficiency

The variation in the mass of Spherotene captured in the meltpool was clearly observed with the processing parameters. This variation can be attributed to the changes in the meltpool size as the parameters varied. In the past, it has been established that meltpool size is positively dependent on the laser power. This was confirmed by the increase in composite track width with increasing laser power, as shown in Figure 5.21. Due to wider meltpool obtained at higher laser powers, more Spherotene was captured resulting in higher deposition efficiency.

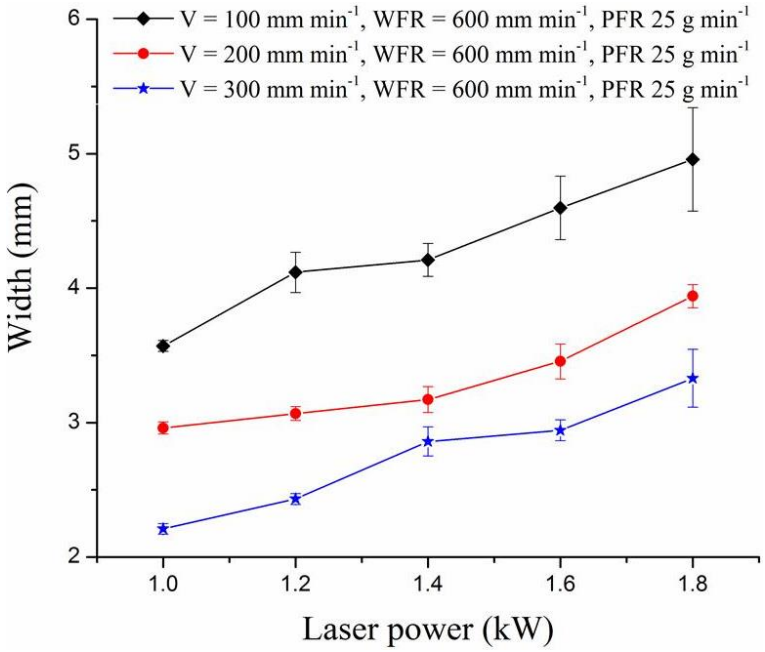

Figure 5.21: Variation of composite track width with the laser power

As presented in Figure 5.9, the nonlinearity between the powder deposition efficiency and the traverse speed can be attributed to the two competing factors (i.e. amount of Spherotene (1) delivered and (2) captured) that determine the powder deposition efficiency. From equation 3.8, powder deposition efficiency is effectively the mass ratio of the Spherotene captured to the mass of Spherotene delivered from the nozzle. Increasing the traverse speed lowers the material volume deposited (including the Spherotene captured in the meltpool) per unit length of track because the table moves faster with respect to the fixed position of the powder nozzle. Since the amount of Spherotene captured in the meltpool decreased and the amount of Spherotene blown from the nozzle is constant with the traverse speed, the powder deposition efficiency is expected to decrease. This observation is in agreement with the findings of Meacock and Villar [115] during the geometrical characterisation of CP2 titanium powder laser tracks.

With the increase in wire feed rate, the Spherotene deposition efficiency was found to increase, as seen in Figure 5.9. The change in the Spherotene deposition efficiency with the

WFR can be attributed to the powder stream attenuation by the feed wire. As shown schematically in Figure 5.22, the higher the wire feed rate, the thicker the meltpool and the lower the powder stream attenuation by the concurrently fed wire. The meltpool thickness is higher at increased wire feed rate because of the increase in material deposition rate. Due to thicker size of the meltpool, the feed wire travelled a relatively shorter distance to reach the meltpool whereas the distance covered will be longer if the meltpool thickness is lower, as shown in Figure 5.22.

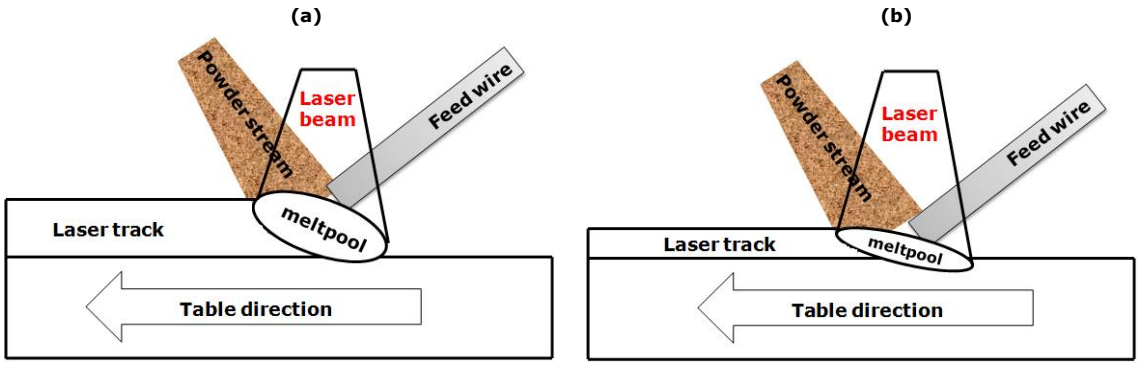

Figure 5.22: A diagram showing the amount of powder stream interruption by the feed wire at (a) high and (b) low wire feed rate

With this laser cladding arrangement involving the attenuation of the powder stream by the feed wire, shorter travel distance between the feed wire tip and the meltpool will be an advantage. The reason is that the attenuation is reduced with a decrease in the wire protrusion distance (i.e. the linear distance between the wire tip and the meltpool surface). When the attenuation is decreased, the amount of Spherotene captured in the meltpool increased resulting in increase in the Spherotene deposition efficiency.

Additionally, it is known that the wire deposition efficiency is ~ 100% whereas the Spherotene deposition efficiency ranged between 12 and 38% for the parameters utilised in

this study. The interpretation of this is that a greater volume of Inconel 625 wire than the Spherotene was captured in the meltpool.

5.13 Spherotene dissolution and volume fraction of the retained Spherotene

The variations of the volume fraction of Spherotene retained in the composite track with the processing parameters depend principally on two factors. Firstly, the amount of Spherotene dissolution and secondly, the amount of Spherotene particle captured in the composite track. As the particle dissolution increases due to increase in incident energy, the volume fraction of the Spherotene retained is bound to decrease. Also, any variation in processing parameter that brings about increase in the amount of Spherotene captured (or powder deposition efficiency) will tend to increase the amount, hence, volume fraction of the retained Spherotene.

Laser power: An increase in laser power will definitely lead to increase in energy per unit length of track. This produced higher energy meltpool causing more Spherotene dissolution, as shown in Figure 5.8. As explained previously, increase in laser power increases the amount of Spherotene captured (or powder deposition efficiency) in the meltpool. However, the decrease in the volume fraction of the retained Spherotene particle with increasing laser power indicates that there was a very high Spherotene dissolution such that the effect of the increase in the powder deposition efficiency was insignificant.

Traverse speed: In the past, an increase in the volume fraction of retained tungsten carbide (hard particulate) with increasing traverse speed during the laser cladding of pre-blended WC/Ni alloy composite powder has been reported [94]. This observation was attributed to low tungsten carbide dissolution at higher traverse speed. Similarly, low Spherotene dissolution at increased traverse speed was observed with this laser cladding arrangement

because energy per unit length track decreased. However, the Spherotene particle deposition efficiency which decreases with increasing traverse speed played a more significant role. The reason is because the volume fraction of retained Spherotene particle in the composite track decreased with an increase in traverse speed. This is a reverse of the previous findings as reported in the literature. Compared with the laser power, traverse speed has a lower influence on the energy per unit length of track. As a result, the gap in the amount Spherotene dissolution (dissolution ratio) is higher with changes in laser power than the traverse speed.

Wire feed rate: Previously, a positive relationship between the powder deposition efficiency and the wire feed rate has been explained in the Chapter 5.12 of this report. Nevertheless, compared with wire deposition efficiency (~100%), the deposition efficiency of the Spherotene powder (12-38%) is significantly smaller. Consequently, any increase in WFR will lead to greater increase in Inconel 625 wire volume than the volume of Spherotene in the composite track. This is the reason for the decrease in the volume fraction of Spherotene retained with the increase in WFR.

5.14 Spherotene distribution

The distribution of the Spherotene retained in the composite track is believed to be influenced mainly by the magnitude of the heat energy incident on the meltpool and partly by the distribution mode of the laser beam delivery. A significant feature of the composite track microstructure deposited at a very high energy per unit length of track (1080 J mm^{-1}), as shown in Figure 5.12, is the rare presence of relatively smaller Spherotene particles in the cladding core. This is not noticed at reduced energy per unit length of track (720 J mm^{-1}) as there was more even distribution of Spherotene throughout the track area. It is, therefore, assumed that high heat energy accumulation in the track (1080 J mm^{-1}), accompanied by an overall reduced thermal gradients in the track core and the slower solidification rates, gives

sufficient energy and time to the Spherotene particles to dissolve in the Inconel 625 matrix. Higher number density of Spherotene particles were retained at the track boundaries because of the higher thermal gradients due to increased heat transfer by convection and radiation modes to the surroundings. Also, at the track-substrate interface, heat energy was largely conducted to the substrate which acted as heat sink. As a result, some Spherotene particles were preserved near the substrate region of the composite track.

Usually, due to the Gaussian delivery mode of the fibre laser utilised in this work, more heat energy is concentrated at the core of the track. The intensity of the energy decreases from the centre towards the track boundary, as shown in Figure 5.23. This type of laser beam delivery mode is believed to have enhanced more Spherotene dissolution at the track core.

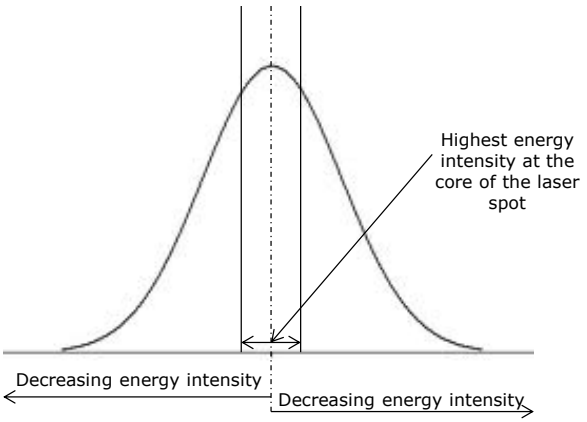

Figure 5.23: A diagrammatic representation of the Gaussian distribution mode of the fibre laser beam utilised in this study

In the case of the track deposited at 720J mm-1, cooling and solidification rates increased leading to a more uniform distribution of the retained Spherotene particles. Significantly high dissolution of Spherotene at the track core often enhanced by the fibre laser Gaussian delivery mode was not noticed. This is because of the reduction in the energy per unit length of track from 1080 to 720 J mm^{-1}.

5.15: Secondary phase (carbide) formation and Cr depletion in the matrix

The introduction of the tungsten carbide into a meltpool, during laser processing of metal alloy often results in microstructural modifications and large extent of compositional in-homogeneity. As suggested by Cooper et al. [11], these changes are usually a consequence of high melt temperature and the interaction between the tungsten carbide and the liquid metal. The interaction is in the form of carbide/melt mixing brought about by temperature gradient-driven fluid flow and results in dissolution of the carbide into the melt. The amount of tungsten carbide dissolution, as found in the literature, increases with increasing the amount of the carbide delivered into the meltpool [90], and increasing the processing energy input [18, 76].

In this study, more Spherotene dissolution occurred at higher energy per unit length of track because of the more intense heating from the higher energy meltpool. The dissolution started from the edges of the Spherotene particles resulting in the formation of W_2C phase predominantly around the retained (i.e. partially dissolved) particles. Apart from the formation of W_2C, W and C were also released into the molten Ni-matrix. As found in Table 5.7, the higher the energy per unit length of track, the more the Inconel 625 matrix is enriched in these elements. This confirms that the Spherotene dissolution increased with increase in energy per unit length of track.

As the molten track solidifies, the precipitation of a hard phase (Fe_3W_3C) termed as M_6C carbide first began to occur from the Ni-matrix. The M_6C, as shown in Figure 5.15, with other elements like Cr, Mo and Ni in solute precipitated randomly within the meltpool. Fe_3W_3C (dendritic carbide) around the retained Spherotene particle solidified around the smaller W_2C phase therefore, encapsulating them. The solidification continued with the formation of Ni-rich dendrites (dark Ni-matrix) and ended with the growth of eutectic

carbides ($M_{23}C_6$) in the interdendritic regions. During rapid solidification of molten Inconel 625 matrix, the interdendritic region becomes rich in Cr, Mo and Nb due to micro-segregation of these elements from the dendrite core. The relieved carbon from the Spherotene dissolution is believed to have combined with the Cr (due to strong Cr-C affinity) to form a eutectic carbide ($Cr_{23}C_6$) in-between the dendrite cores of the Ni-matrix. The more the amount of the relieved carbon due to Spherotene dissolution, the more the formation of $Cr_{23}C_6$ phase. This confirms the occurrence of more of the phase C ($Cr_{23}C_6$) in the cross-sectioned track shown in Figure 5.15c (higher (i.e. 1080 J mm^{-1}) incident energy) than in Figure 5.15f (lower (i.e. 720 J mm^{-1}) incident energy). This phenomenon explains the reason why there was increased depletion of Cr in the Ni-matrix whenever there was more Spherotene dissolution. From the EDX result presented in Table 5.7, the amount of Spherotene dissolution was a measure of the W content of the matrix region in-between the retained Spherotene particles. This is due to the fact that there was no trace of W element in the as-received Inconel 625 wire composition therefore, any presence of W in the composite matrix was considered to result from the Spherotene dissolution. Similar observation has been reported by Amado et al [93] during the deposition of crack free tungsten carbide (Spherotene) reinforced Ni(Cr) layers by laser cladding.

5.16 Micro-hardness and secondary phase contents of the composite tracks

Compared with the micro-hardness of the AISI 304L substrate (201$HV_{0.3}$) and Inconel 625 wire and powder laser tracks (224-248 $HV_{0.3}$), the micro-hardness of the matrix of Inconel 625 wire-Spherotene powder composite laser track (540-690 $HV_{0.3}$) showed a significant improvement. The high micro-hardness of the composite tracks can be attributed to the formation of the various secondary carbides resulting from the Spherotene dissolution in

Inconel 625 wire matrix. According to Liyanage et al. [91], Fe_3W_3C and W_2C had been identified as extremely hard but brittle phases. Also $Cr_{23}C_7$ is also known as a secondary strengthening phase [95].

The variation of the micro-hardness of the composite tracks as a function of the laser parameters can be attributed to the amount of these secondary carbides present in the tracks. When the laser power was high power or the traverse was low, the energy per unit length of track was relatively high. There was more Spherotene dissolution leading to increased formation of these hard phases (secondary carbides) in the composite tracks, as shown in Figure 5.15. As a result, higher micro-hardness was found at high laser power or low traverse speed. Spherotene dissolution decreased with increasing WFR. Relating this to the inverse relationship between the composite matrix micro-hardness and WFR (see Figure 5.17), it is believed that the volume fraction of the secondary carbides in the composite track matrix decreased with increasing the WFR. This implies that at higher WFR there was higher percentage volume composition of the relatively soft Ni matrix than the strengthening secondary carbides in the track microstructure.

5.17 Defects in overlapped-track layers of the composite

Poor bonding: Generally, poor fusion laser cladding is usually due to the fact that the total material delivery volume was too high for the supplied energy density. As shown in Figure 5.19, poor fusion/bonding between the overlapped-track layer and the substrate were found at laser powers of 1.0 kW and 1.2 kW with traverse speed of 100 mm min^{-1} and wire feed rate of 600 mm min^{-1}. This showed that the bond strength between the layers and the substrate is weak therefore rendering the layers unsuitable for intended application.

Cracking: As discussed earlier in section 5.11, cracking propensity increases with increasing the volume concentration of secondary carbides in the composite matrix. At the overlapped zones of the composite layers, it is expected that the volume concentration of the secondary carbides will be higher. This is due to the fact that the partially dissolved Spherotene in the overlapped region of the adjacent track will undergo additional heating during the overlapped cladding of another track. However, the absence of crack in the layers shows that the residual stress due to volume expansion in these regions is not greater than the strength of the matrix. This might be due to the high ductility of Inconel 625 wire and use of low incident energy.

5.18 Summary

- It was found possible to concurrently deposit Spherotene (WC/W_2C) powder-Inconel 625 wire composite using fibre laser cladding. Overlapped-track layers can be built which in this study were found to be minimally diluted, well bonded to the substrate and free of cracks and pores except for inter-run porosity.
- The process exhibited different characteristics including wire dripping, smooth wire deposition and wire stubbing. Continuous single tracks were formed only whenever there was smooth wire deposition.
- A process map predicting these characteristics at different processing conditions utilised in this study was developed. Compared with the process map developed for Inconel 625 wire laser cladding, the concurrent injection of Spherotene caused a rightward shift in the process map.
- The deposition efficiency of Spherotene particles ranging from 12 to 38% was found to vary with the processing parameters. It increased with increasing laser power and wire feed rate but decreased with increasing traverse speed. The wire deposition is believed to be nearly 100% because all the wire delivered entered the meltpool.
- The Spherotene dissolution ratio varied between 2 and 57% for the range of parameters used in this work. The higher the energy per unit length of track, the higher the dissolution ratio. The higher the wire feed rate, the lower the dissolution ratio.
- The volume fraction of Spherotene retained in the track ranged from 22 to 30 vol. % . Due to high Spherotene dissolution at high energy per unit length of track, the retained Spherotene volume fraction decreased with increasing the laser power. Although low Spherotene dissolution was observed at higher traverse speed, the volume fraction of the Spherotene retained decreased with increasing traverse speed

because of the greater impact of Spherotene deposition efficiency which decreased with the speed. Similarly, the 100% deposition efficiency of wire compared with the Spherotene deposition efficiency (max 38%) accounted for the decrease in the volume fraction of Spherotene retained with increasing wire feed rate.

- The distribution of the Spherotene retained was mainly influenced by the magnitude of the incident energy and partly by the Gaussian distribution mode of the fibre laser used in this work. At low energy per unit length of track, relatively uniform distribution of retained Spherotene was observed whereas at extremely high energy per unit length of track, a low number density of retained Spherotene was found in the track core.
- The microstructure of the composite coating formed with smooth wire deposition are pore and crack free consisting of dispersion of retained WC/W_2C powder (partially dissolved Spherotene), W_2C phase and precipitates (M_6C and $M_{23}C_6$) in continuous γ Ni-matrix. The phases were confirmed by XRD and SEM/EDAX techniques.
- The amount of Cr depletion from the Ni-matrix was found to increase with increasing the extent of Spherotene dissolution. The released C from Spherotene dissolution tied up the Cr in the interdendritic region to form $Cr_{23}C_6$ carbide.
- The average micro-hardness of the composite matrix was significantly improved (540-690 $HV_{0.3}$) as compared to the substrate (201 $HV_{0.3}$) and Inconel 625 wire and powder laser tracks (224-248 $HV_{0.3}$). It increased with increasing laser power but decreased with increasing traverse speed and wire feed rate. This was accounted for by the amount of the secondary carbides (W_2C, M_6C and $M_{23}C_6$) formed which has direct relationship with the micro-hardness.

6.0 Corrosion behaviours of laser deposited Inconel 625 powder, Inconel 625 wire and Spherotene-Inconel 625 wire composite coatings

6.1 Introduction

This chapter investigates and compares the corrosion behaviours of the substrate (AISI 304L), the typical laser track layers of wire- and powder-fed Inconel 625 in de-aerated 3.5% NaCl solution. Also, the corrosion performances of the concurrently fed Spherotene powder-Inconel 625 wire composite laser coatings at low and high energy per unit length of track are investigated. Their corrosion properties were obtained by carrying out open circuit potential and potentiodynamic polarisation tests as well as microstructural characterisation of the samples before and after the tests. The differences in the corrosion performances of the deposited coatings are identified and the effects of the microstructural changes and Fe dilution (from the substrate) with respect to the differences are discussed. The chapter is divided into two sections, i.e. results and discussions, followed by a summary of the important findings.

6.2 Corrosion behaviour of 304L stainless steel substrate

As detailed in Chapter 3.13, the open circuit potential (E_{oc}) and potentiodynamic scan tests were performed based on the guidelines provided in ASTM standards G5-94 and G61-86 at room temperature. All surfaces were ground and polished before the tests. Similar tests were performed for the substrate and all the coatings with the potentiodynamic scan starting from 1-hour E_{oc} position.

It was known from the literature [32] that there are some degrees of variations in the corrosion tests results (both immersion and potentiodynamic tests). Therefore, the tests were performed at least thrice for the substrate (and for each of the coatings). The average of the results including E_{oc} on immersion and after an hour, corrosion potential (E_{corr}), breakdown potential (E_b) and passive current density (I_p) were determined and tabulated. These corrosion parameters have been defined in Chapter 3.13.2 (see Figure 3.9).

6.2.1 Open circuit potential vs time

In this study, the E_{oc} measurement of the 304L stainless steel substrate was measured over a period of an hour. Figure 6.1 shows the plots of change in E_{oc} with the time.

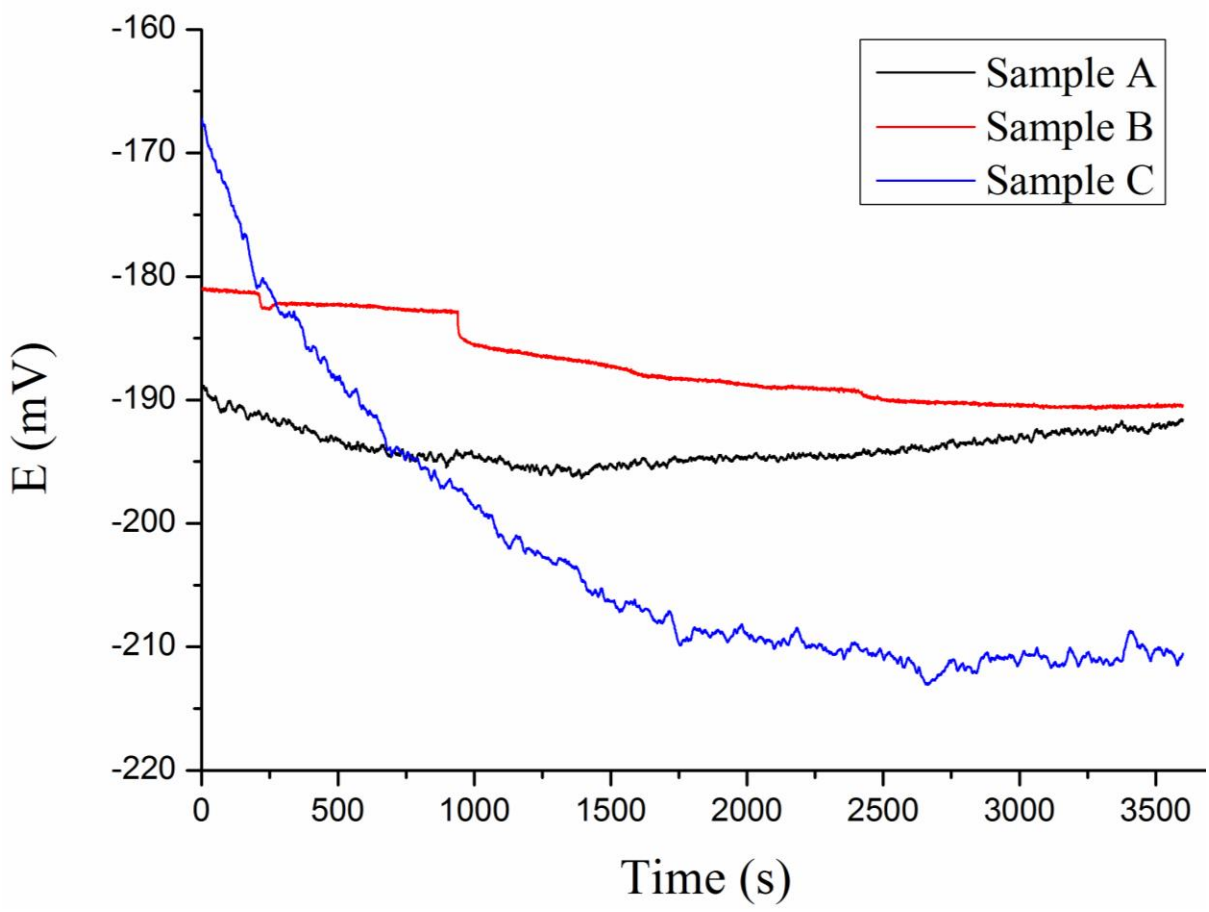

Figure 6.1: Open circuit potential vs time for the 304L stainless steel substrate

As presented in Figure 6.1, there are some variations in the E_{oc} of the substrate. This is believed to be caused by the surface nature of the samples before the tests. The E_{oc} behaviour is hugely sensitive to sample surface details. However, in all cases, the E_{oc} initially decreased. Towards the end of 1hr-immersion in 3.5% NaCl solution, the potential became relatively constant with time. At this point, the E_{oc} was assumed to have reached a steady state.

Table 6.1: Summary of the results of the corrosion test for 304L stainless steel substrate

Sample	E_{oc} on immersion (mV)	E_{oc} after 1 hour (mV)	E_{corr} (mV)	E_b (mV)	I_p (mA cm^{-2})
304L Stainless steel	-179 ± 11	-196 ± 12	-235 ± 16	340 ± 10	1.9×10^{-3}

The average values, as presented in Table 6.1, of E_{oc} on immersion in the electrolyte and after an hour was found to be -179 ± 11 and -196 ± 12 respectively (all values are with respect to Ag/AgCl reference electrode).

6.2.2 Potentiodynamic polarisation scan

This test was basically used to determine the passivation behaviour of the substrate and the coatings. All precautions were observed during sample preparation in order to avoid any crevice effects on the sample surface. Especially, the boundary between the sample and the resin was properly coated with stop-off lacquer. It is well known that this region is a potential site for crevice corrosion which often alters the passivation behaviour of the samples. Figure 6.2 presents the potentiodynamic polarisation scans of the 304L stainless steel substrate in de-aerated 3.5% NaCl solution at room temperature.

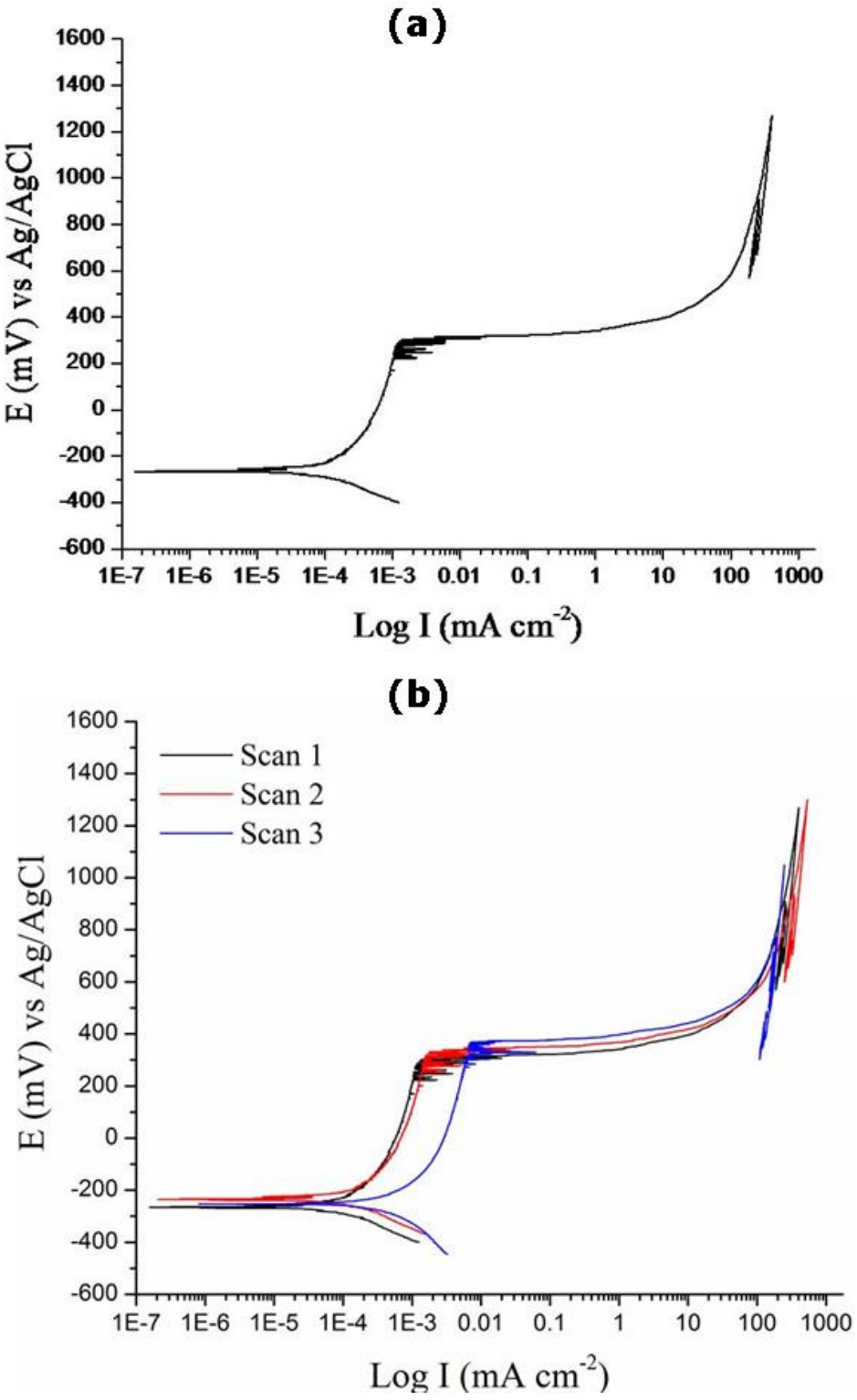

Figure 6.2: Cyclic polarisation curves of 304L stainless steel substrate in de-aerated 3.5% NaCl solution at room temperature, (a) the selected polarisation curve (b) the amount of scatter in the repeated scans

The average value of the E_{corr} measured from the polarisation curve was -235 ± 16. This shows a difference of 39 mV from the E_{oc} value obtained after 1 hour immersion in the electrolyte. Other deductions from the curves including the average passive current density and breakdown potential are summarised in Table 6.1. As expected, variations were observed in the polarisation scans of the substrate (see Figure 6.2b). However, the variation is believed to be moderate.

The average passive current density was 1.9×10^{-3} mA cm^{-2}. A rapid increase in current density was observed in the curve after a narrow passive region, precisely at 340 ± 10 mV (wrt Ag/AgCl electrode) which is the breakdown potential (E_b). The rapid increase in current density after passivation usually suggests pitting or crevice corrosion on the surface of the test metal. Also, the positive hysteresis observed in the polarisation curves (of the substrate samples) and corrosion pits visually detected on the stainless steel samples, after the test, confirmed the occurrence of localised (pitting) corrosion on the metal surface.

6.2.3 Characterisation of the 304L stainless steel substrate after polarisation

Figure 6.3 shows the SEM/BSE images, at different magnifications, of a 304L stainless steel sample after the potentiodynamic polarisation scan. Clearly, there was evidence of pitting corrosion occurring on the surface of the substrate. This shows that the corrosion was not uniform on the surface. As a result, the corrosion was very rapid at small areas and more intense than uniform corrosion [99]. The images in Figures 6.3c and 6.3d clearly show the corrosion pits and other corrosion products on the corroded surface of the substrate.

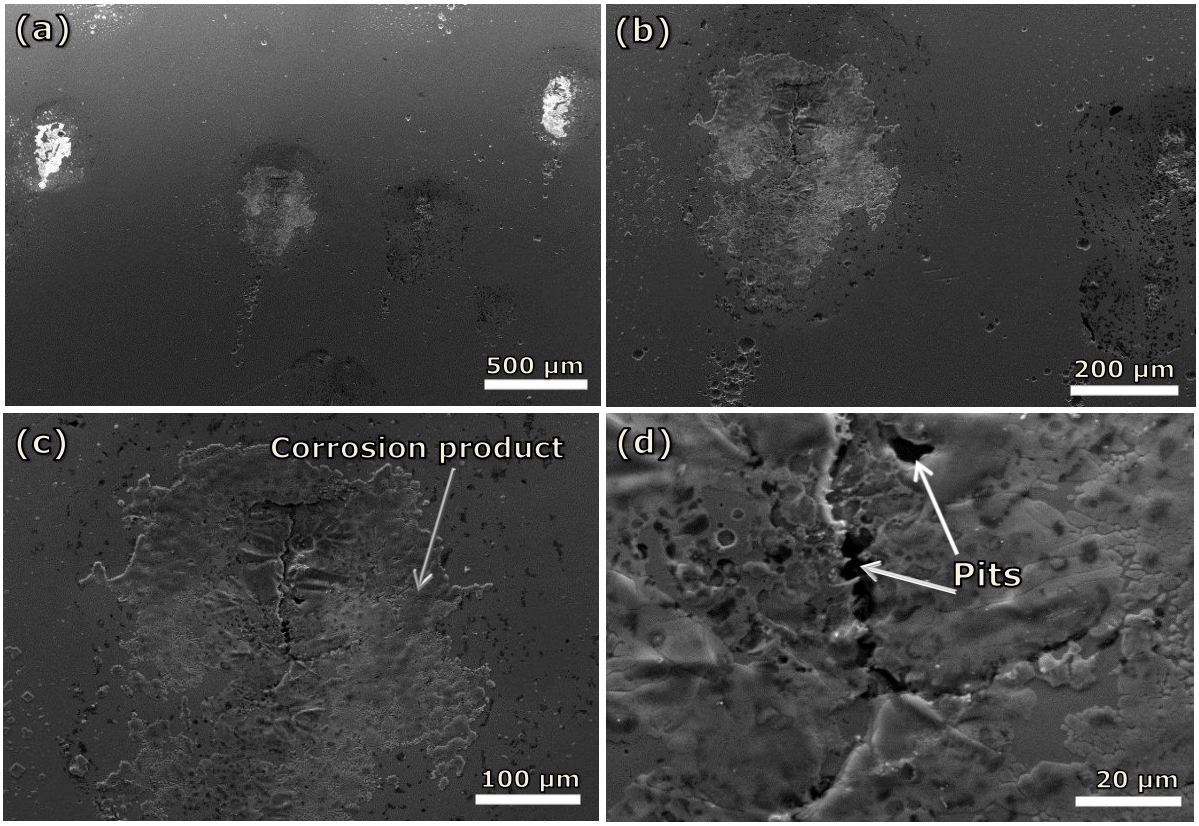

Figure 6.3: SEM/BSE images of the corroded surface of the 304L stainless steel substrate in 3.5% NaCl solution showing pits formation.

6.3 Corrosion behaviour of the typical Inconel 625 coatings formed via wire and powder lateral feeding systems

The results of the corrosion (one-hour immersion and potentiodynamic scan) tests on the typical Inconel 625 laser coatings formed via wire and powder feeding are presented in this section. All tests were conducted in a similar way as performed for the substrate.

6.3.1 Open circuit potential vs time

Figure 6.4 shows the comparison of the change in E_{oc} with time of Inconel 625 wire and Inconel 625 powder laser coatings in de-aerated 3.5% NaCl solution at room temperature. Relatively, the E_{oc} of the wire coating remained constant with time throughout the test. In the

case of the powder coating, the E_{oc} was inclined towards the negative potential. The slope of inclination reduced significantly towards the end of the 1hr-immersion. The decrease in E_{oc} with respect to time usually implies that there is dissolution of pre-formed oxide film on the surface of the sample on immersion in the electrolyte. However, a slight decrease of about 8 mV in an hour was observed. This suggests that the pre-formed oxide film dissolved at a very slow rate.

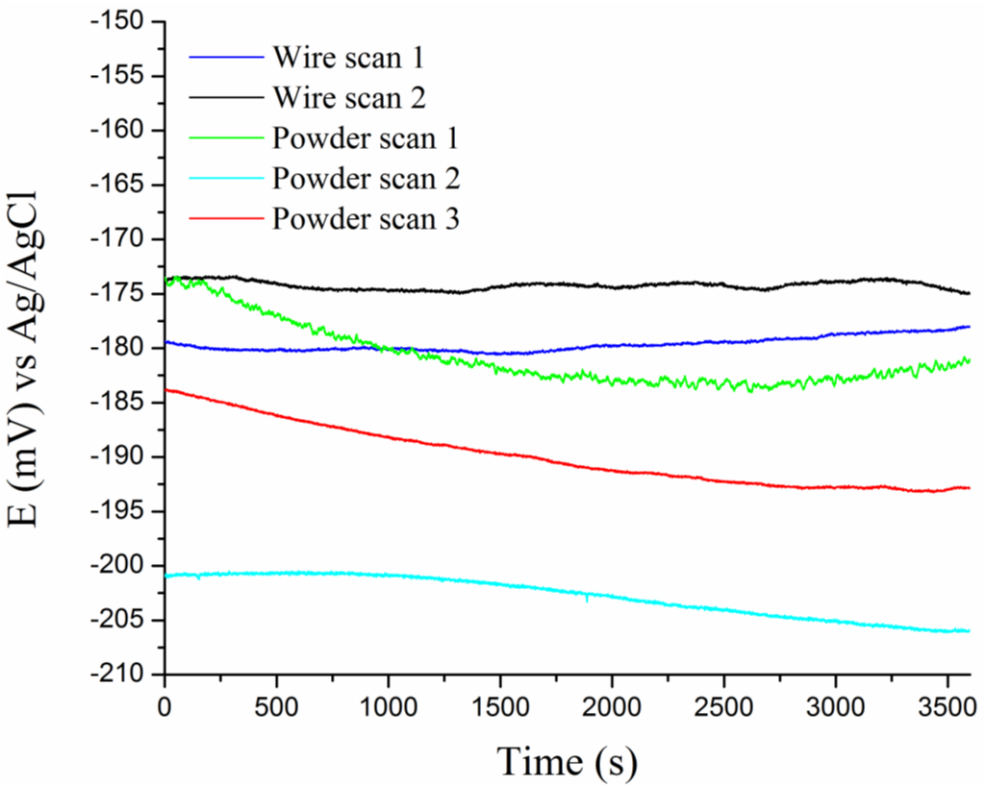

Figure 6.4: Change in E_{oc} with time of Inconel 625 wire and Inconel 625 powder coatings in de-aerated 3.5% NaCl solution at room temperature (a) comparison between the wire and powder coatings and (b) variations in the iterations.

Table 6.2: Summary of the results of the corrosion test for Inconel 625 wire and Inconel 625 powder laser coatings

Sample	E_{oc} on immersion (mV)	E_{oc} after 1 hour (mV)	E_{corr} (mV)	E_b (mV)	I_p (mA cm^{-2})
Inconel 625 wire	-176 ± 4	-176 ± 2	222 ± 8	585 ± 5	3.0×10^{-4}
Inconel 625 powder	-186 ± 14	-194 ± 12	253 ± 56	584 ± 8	1.1×10^{-3}

As shown in Figure 6.4, large scatter was seen in the E_{oc} vs time curves of the powder coating samples. Perhaps, the scatter may be caused by variations in the surface microstructure at different regions of the typical powder coating. The average E_{oc} on immersion and after 1-hour E_{oc} for the Inconel 625 wire coating, as presented in Table 6.2, were -176 ± 4 mV and -176 ± 2 mV respectively. The averages for the powder coating were -186 ± 14 mV and -194 ± 12 mV on immersion and after 1-hour E_{oc} respectively.

6.3.2 Potentiodynamic polarisation scan

The cyclic polarisation curves for the typical Inconel 625 coatings formed by wire and powder feeding as compared with the substrate are revealed in Figure 6.5. Generally, the two coatings exhibited better corrosion resistance in the 3.5% NaCl solution than the stainless steel substrate. Inconel 625 wire coating passivated at the lowest current density (3.0×10^{-4} mA cm^{-2}) followed by the corresponding powder coating (1.1×10^{-3} mA cm^{-2}). Since the formation of passive layer at low current density hinders the severe loss of material at higher current density, lower passive current density therefore connotes improved corrosion resistance. In the past, the passive current density (I_p) obtained for wrought Inconel 625 in de-aerated 3.5% NaCl solution at room temperature is (4.6×10^{-4} mA cm^{-2}) [116]. The I_p obtained for Inconel 625 wire coating is very close to this value.

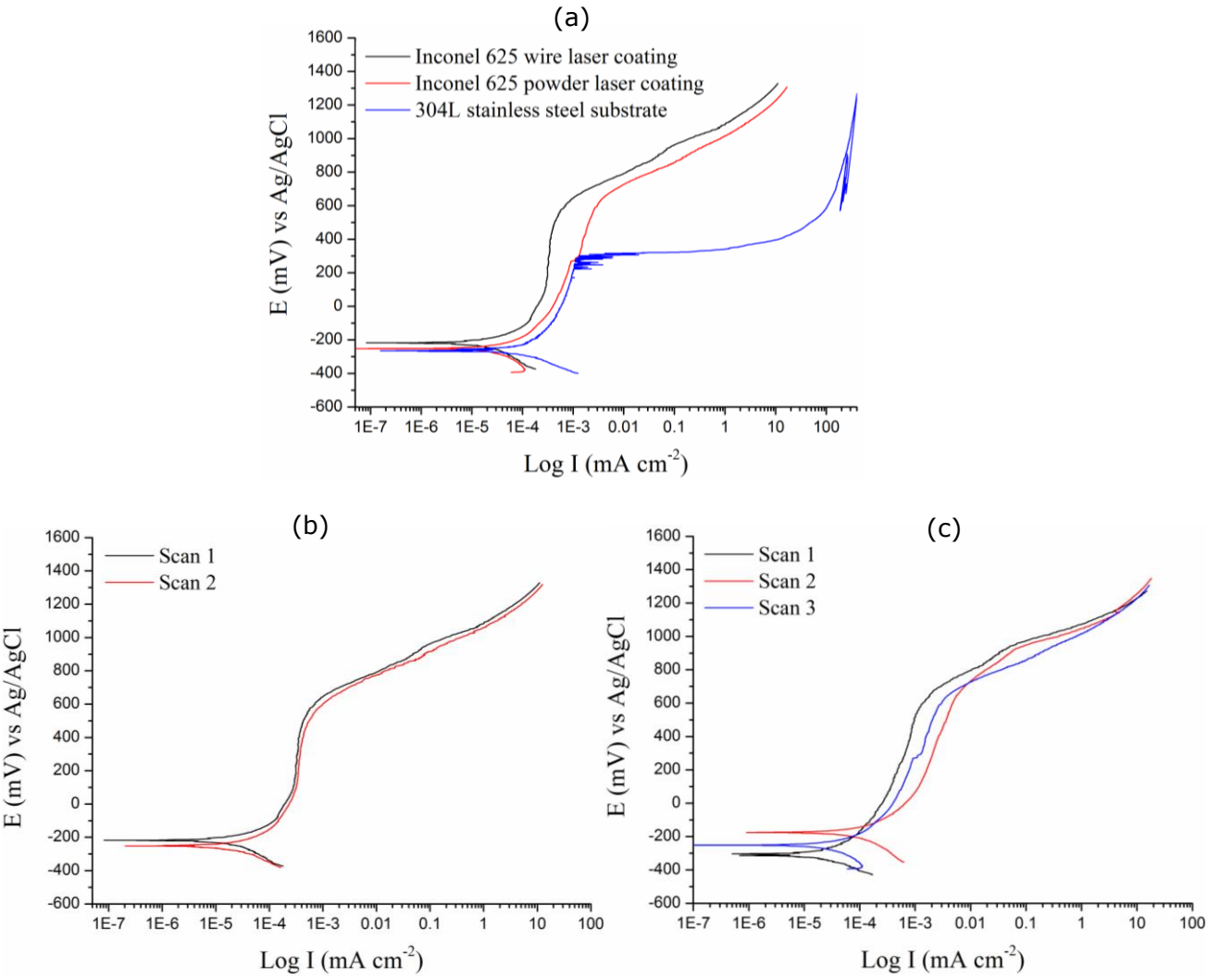

Figure 6.5: Cyclic polarisation curves showing (a) comparison among Inconel 625 laser coatings by wire and powder feeding, and 304L stainless steel substrate (b) amount of scatter in wire coating (c) amount of scatter in powder coating

As listed in Table 6.2, nearly equal breakdown potential (E_b) value of ~585 mV was found for the two coatings. This value is very close to a value quoted for wrought Inconel 625 (600 mV using Ag/AgCl as reference electrode) but greater than E_b values (max = 487 mV wrt Ag/AgCl electrode) found for laser remelted HVOF Inconel 625 coatings in de-aerated 3.5% NaCl solution at room temperature [116]. As reported earlier in section 6.2, the E_b value (340 mV wrt Ag/AgCl electrode) found for the stainless steel is lower than the two coatings.

Compared with the Inconel 625 wire coating and the substrate, Inconel 625 powder coating has the lowest E_{corr} (-255 ± 56 mV). The deviations from the average E_{corr} of the typical powder coating was very wide, as seen in Figure 6.6c. From the values presented in Table 6.2, Inconel 625 wire coating appeared to be nobler than both the substrate and the Inconel 625 powder coating because its E_{corr} value (-220 ±8 mV) was the highest.

In addition, the increase in current density after the passive region in the polarisation curves of the two typical coatings was not as rapid as that of the substrate. As explained previously, the sudden and rapid increase in current density after passive region suggests the possibility of corrosion pits in the test sample. Instead of pitting effect as observed in the corroded substrate surface, there was uniform corrosion of the Inconel 625 coatings in the transpassive region. This was confirmed by the absence of pits in the corroded surfaces of the two coatings, for example, as shown in Figure 6.7.

The average values of all corrosion results obtained for the two coatings are summarised in Table 6.2. As found in the literature [32, 116], all values deduced from the polarisation curves are close to the results found for the corrosion behaviour of wrought Inconel 625 under nearly similar conditions.

6.3.3 Characterisation of the wire- and powder-fed Inconel 625 laser coatings after polarisation

The SEM/BSE images showing the top views of the typical Inconel 625 powder- and wire-fed laser coatings before and after potentiodynamic polarisation scan are presented in Figures 6.6 and 6.7 respectively. Interdendritic light phase precipitate and continuous dark dendritic phase were observed in the images presented in Figure 6.6. This is similar to the microstructure (longitudinal section) of Inconel 625 wire and powder previously reported in chapter 4.4.3 and 4.7.3 respectively.

As seen in Figures 6.6a and 6.6b, Inconel 625 wire laser coating comprised mainly long columnar dendrites growing in a particular direction. The light phase which is considered as Nb- and Mo-rich precipitate existed at the interdendritic regions.

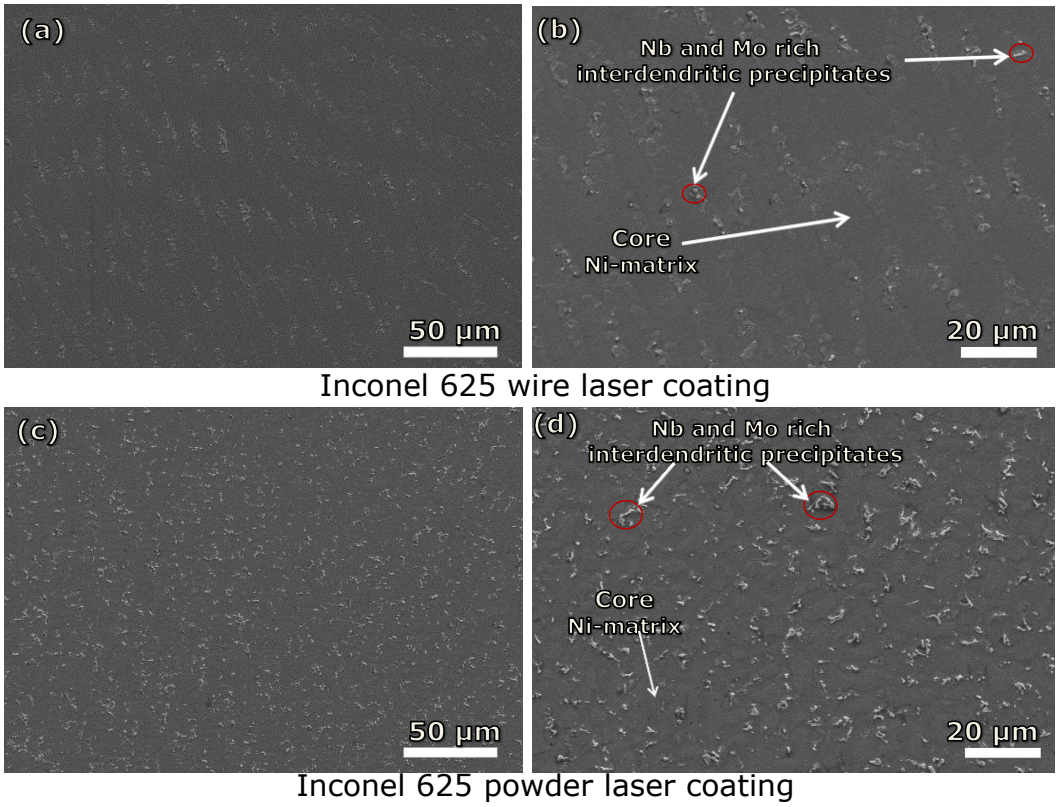

Figure 6.6: SEM/BSE images showing the plan views of the (a-b) Inconel 625 wire, and (c-d) Inconel 625 powder laser coatings before polarisation test.

In the case of the Inconel 625 powder laser coating shown in Figures 6.6c and 6.6d, the microstructure was relatively finer consisting of cellular/equiaxed dendrites solidification mode. Accordingly, more interdendritic spaces existed at the boundaries between the core dendrites. Additionally, a higher number of Nb-and Mo-rich interdendritic precipitate was noticed in the powder coating. This is believed to have constituted to increased microstructural in-homogeneity in the powder coating, for example, as evidenced in Figures 6.6 (c & d) and 6.7 (c & d).

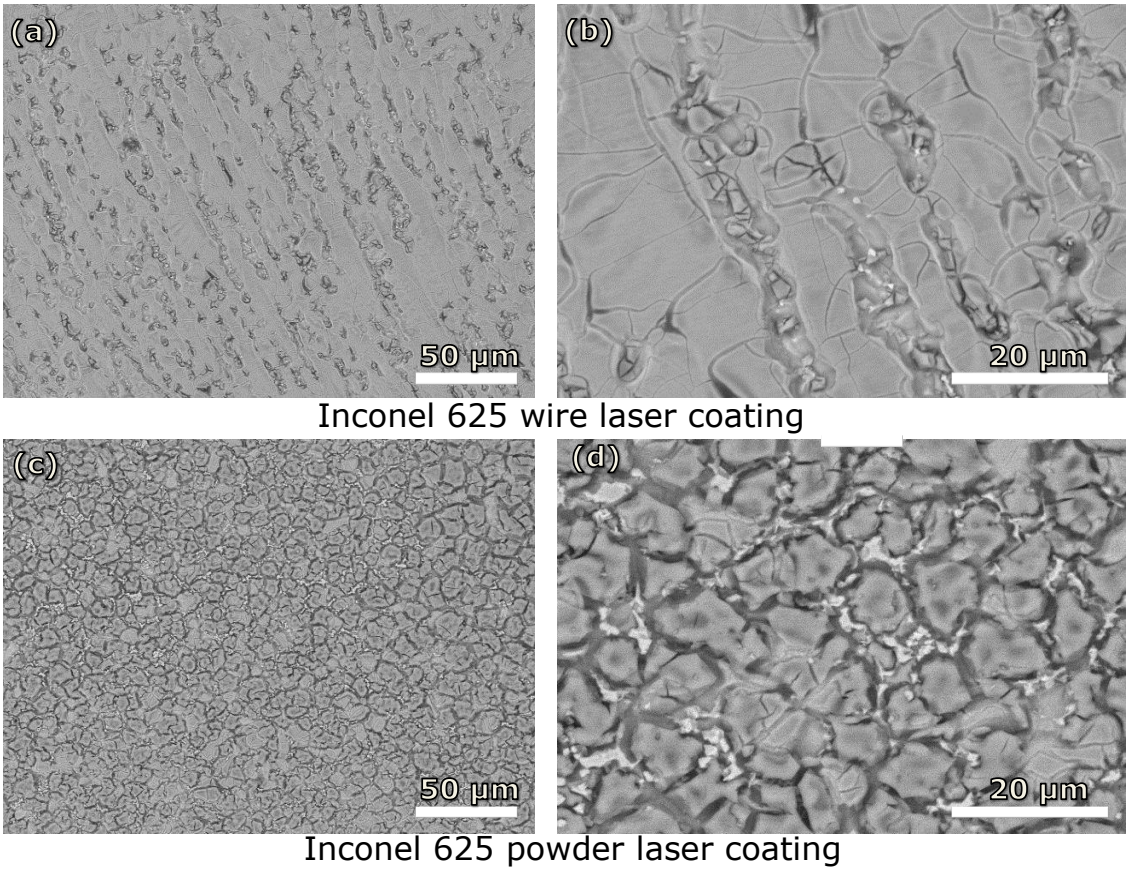

Figure 6.7: SEM/BSE images showing the uniformly corroded surfaces of the (a-b) Inconel 625 wire, and (c-d) Inconel 625 powder laser coatings after polarisation test.

Figures 6.7a and 6.7b shows the magnified SEM images of the surface of Inconel 625 wire coating after the potentiodynamic polarisation test. It is shown that the surface corroded uniformly since there is no evidence of pits on the surface. Likewise, uniform corrosion was observed on the surface of the Inconel 625 powder coating after the polarisation scan, for example, as shown in Figures 6.7c and 6.7d. The light phase (precipitate) in-between the grey-like matrix remained unaffected in the two typical coatings after the tests.

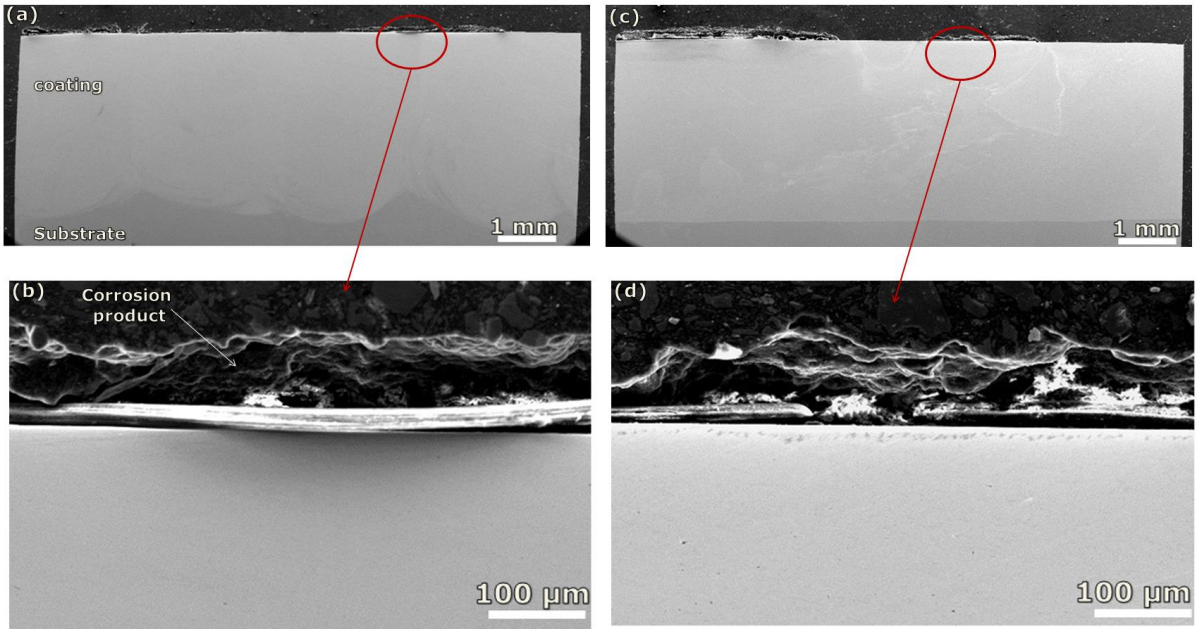

Figure 6.8: Cross-sectional view of (a, b) Inconel 625 powder, (c, d) Inconel 625 wire laser coatings after polarisation in 3.5% NaCl

The corroded samples were sectioned transversely so as to show the thickness of the corrosion products formed on the top surface of the coatings. As shown in Figure 6.8, the total thickness of the corrosion products in the two coatings is a maximum of 0.1 mm probably indicating slow corrosion rates. Also, there was no ingress of the electrolyte or the existence of corrosion products within the coatings. This indicates that the substrate is fully protected by the two typical Inconel 625 laser coatings.

After the tests, the SEM/EDX mapping of the top surface of the Inconel 625 powder coating was carried out, as shown in Figure 6.9. It was found that the grey region marked ‘A’ covering the core dendrite is very rich in Mo (34.5 wt.%) and O (36.3 wt. %). The significant presence of O indicates that the core dendrites suffered from oxidation leading to formation of probably oxides or compounds of molybdenum. The light contrast (precipitate) marked ‘B’ at the boundaries in-between the dendrite core contains negligible amount of O (0.9 wt. %) but still contain high proportion of Mo (12.8 wt. %) and Nb (14.0 wt. %). The negligible O

content and no noticeable change in contrast show that the phase ‘B’ suffered insignificantly from the corrosion attack.

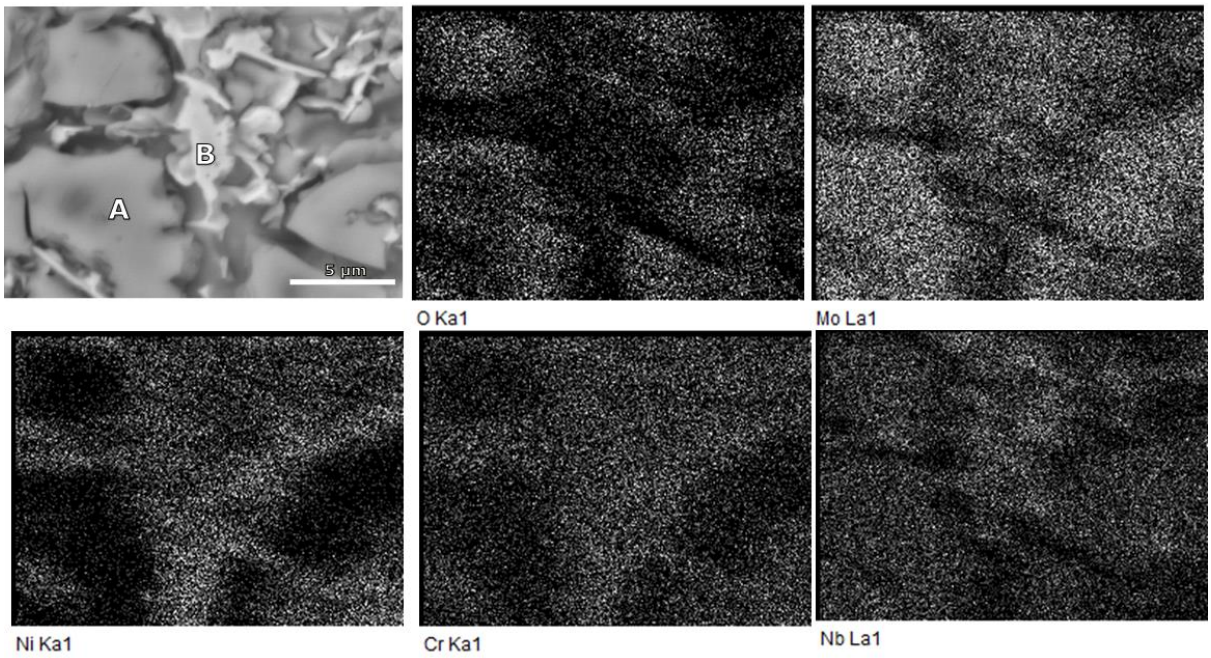

Figure 6.9: SEM/EDX mapping of the top surface of Inconel 625 powder laser coating after potentiodynamic polarisation scan in 3.5% NaCl solution

The results of the detailed composition (EDX) analysis undertaken at the regions A and B are presented in Table 6.3. The line scan analysis across the phases present on the surface of the corroded sample of Inconel 625 powder laser coating is shown in Figure 6.10.

Table 6.3: Summary of the composition analysis (wt. %) of the different regions of the SEM image in Figure 6.9

Symbol	O	Cr	Fe	Ni	Nb	Mo
A	36.3	6.2	3.3	4.0	15.5	34.5
B	0.9	20.1	1.0	51.4	14.0	12.8

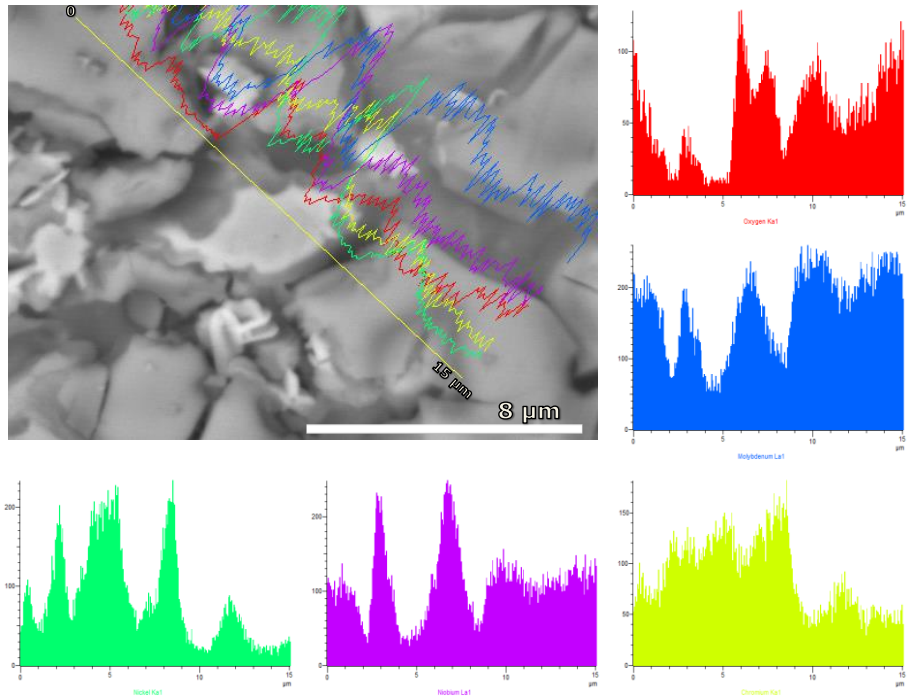

Figure 6.10: Elements distribution profiles of O, Mo, Cr, Nb and Ni across the phases present in the SEM image shown in Figure 6.10

EDX elemental compositional analysis was repeated for the corroded surface of Inconel 625 wire laser coating sample. Similar to the results obtained for Inconel 625 powder coating, the core dendrites were attacked while the light precipitate in the interdendritic was not affected as indicated by the EDAX results presented in Table 6.4. However, compared to the results in Table 6.3, there was noticeable decrease in O, Mo and Fe contents and increase Ni and Cr contents in the composition of the region A (i.e. corroded region) of the wire coatings. The low O (19.5 wt. %) and high Cr (15.7 wt. %) and Ni (37.2 wt. %) suggest that there was reduced oxidation.

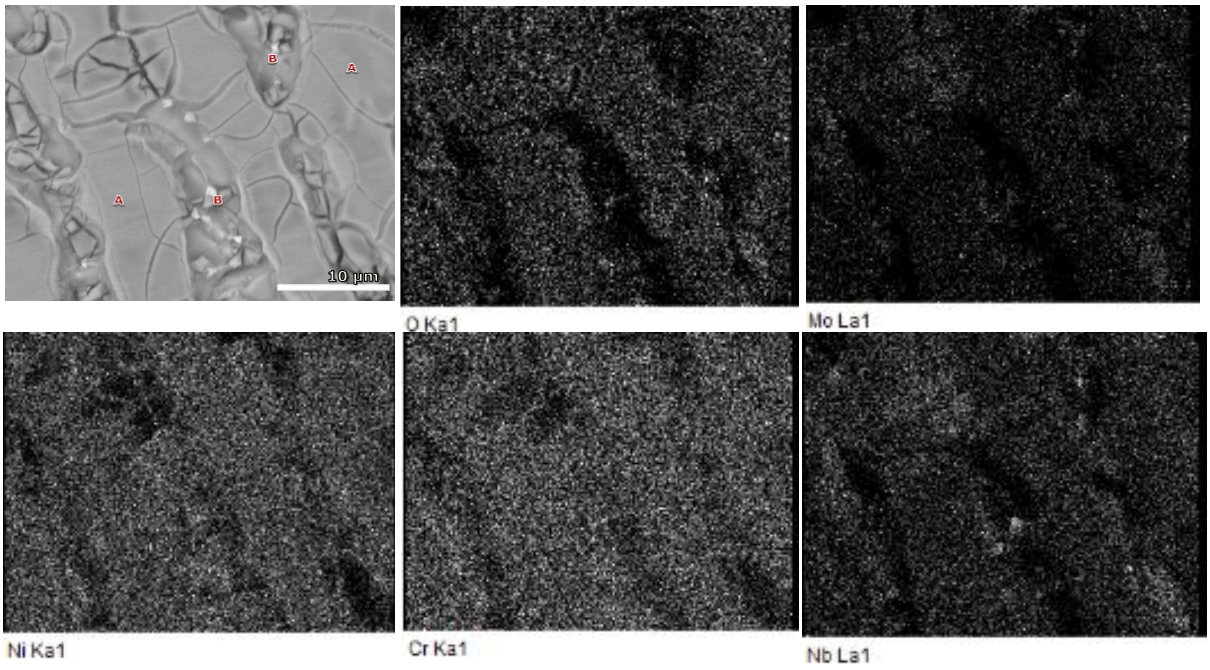

Figure 6.11: X-ray mapping of the top surface of Inconel 625 wire laser coating after potentiodynamic polarisation scan in 3.5% NaCl solution

Table 6.4: Summary of the composition analysis (wt. %) of the different regions of the SEM image in Figure 6.11

Symbol	O	Cr	Fe	Ni	Nb	Mo
A	19.5	15.7	1.2	37.2	9.0	17.5
B	2.6	21.6	0.9	58.8	5.3	10.8

6.4 Corrosion behaviours of the concurrently fed Spherotene (WC/W_2C) powder-Inconel 625 wire composite coatings

The corrosion study of Spherotene (WC/W_2C) powder-Inconel 625 wire laser coatings formed at two energy (J mm^{-1}) levels was investigated. The selected layers were deposited at 240 J mm^{-1} and 1080 J mm^{-1}. The reason is that the dissolution ratio of the injected Spherotene particle varied significantly with the energy input. As shown in Figure 5.20 of

Chapter 5.8, the microstructures of the two coatings are somewhat different because of the varying amount of Spherotene dissolution in them. As a result, the effects of the Spherotene powder dissolution on the corrosion resistance of the composite coatings will be determined by comparing their corrosion performances at low (240 J mm^{-1}) and high (1080 J mm^{-1}) energy per unit length of track.

6.4.1 Open circuit potential (Eoc) vs time

Figure 6.12 presents the E_{oc} vs time curves of the Spherotene powder-Inconel 625 wire composite coatings formed at low and high energy per unit length of track.

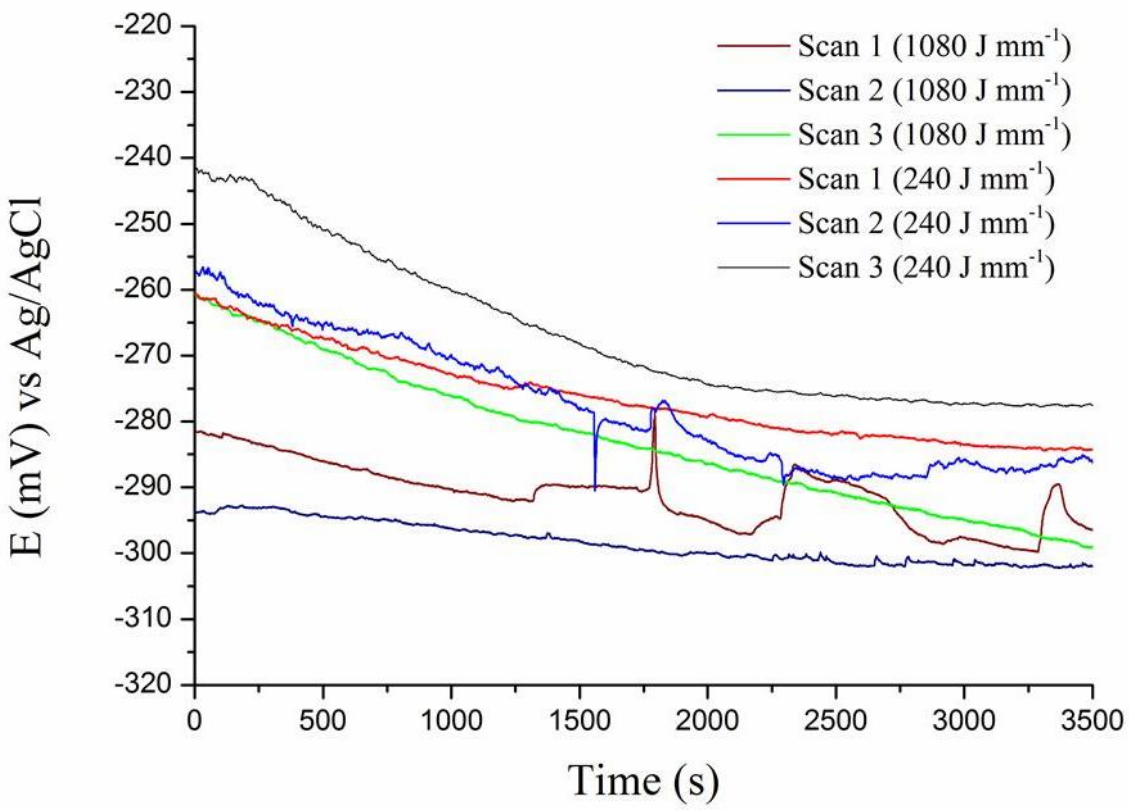

Figure 6.12: E_{oc} vs time curves of concurrently fed WC/W_2C powder-Inconel 625 wire composite laser coatings formed at low (240 J mm^{-1}, P = 1.2 kW, V = 300 mm min^{-1}) and high (1080 J mm^{-1}, P = 1.8 kW, V = 100 mm min^{-1}) energy per unit length of track

For all the samples, the E_{oc} (wrt to Ag/AgCl electrode) started to decrease in the negative direction on immersion into the de-aerated 3.5% NaCl solution. As explained previously in

section 6.3.1, this indicates the dissolution of pre-oxide film into the electrolyte. Towards the end of 1 hour, the E_{oc} became nearly constant with the time. This shows that the open circuit potential has stabilised. The average values of E_{oc} on immersion and after 1-hr immersion in the electrolyte for the two coatings are summarised in Table 6.5.

Table 6.5: Summary of the results of the corrosion test for the concurrently fed WC/W_2C powder-Inconel 625 wire composite coatings

Energy input (J mm^{-1})	E_{oc} on immersion (mV)	E_{oc} after 1 hour (mV)	E_{corr} (mV)
1080	-278 ± 19	-297 ± 3	-309 ± 4
240	-253 ± 10	-282 ± 5	-295 ± 5

6.4.2 Potentiodynamic polarisation scan

Figure 6.13 shows the corrosion performance of the Spherotene powder-Inconel 625 wire composite coatings in de-aerated 3.5% NaCl solution at room temperature. Compared to the cyclic polarisation curves obtained for Inconel 625 coatings (wire- and powder-fed), there was no evidence for passivation in the curves obtained for the composite coatings. This shows that the composite coatings demonstrated poor corrosion resistance compared with the Inconel 625 coatings. A transition from the active to transpassive region is noticed for the composite coatings. At 1080 J mm^{-1}, a significant increase in current density with a little change in potential is observed. This indicates a possibility of pitting form of corrosion occurring. In the case of the composite coating formed at 240 J mm^{-1}, the gradient of the current density against potential reduced in the transpassive region. Generally, the absence of passivation demonstrated by the composite coatings is possibly due to Spherotene dissolution resulting to increased microstructural in-homogeneity.

The corrosion potential (E_{corr}) value of the composite coating deposited at 240 J mm^{-1} is higher than the value obtained when the incident energy was 1080 J mm^{-1}. This indicates that

the former is nobler than the latter. Table 6.5 presents the summary of the of the corrosion performances of the two composite coatings.

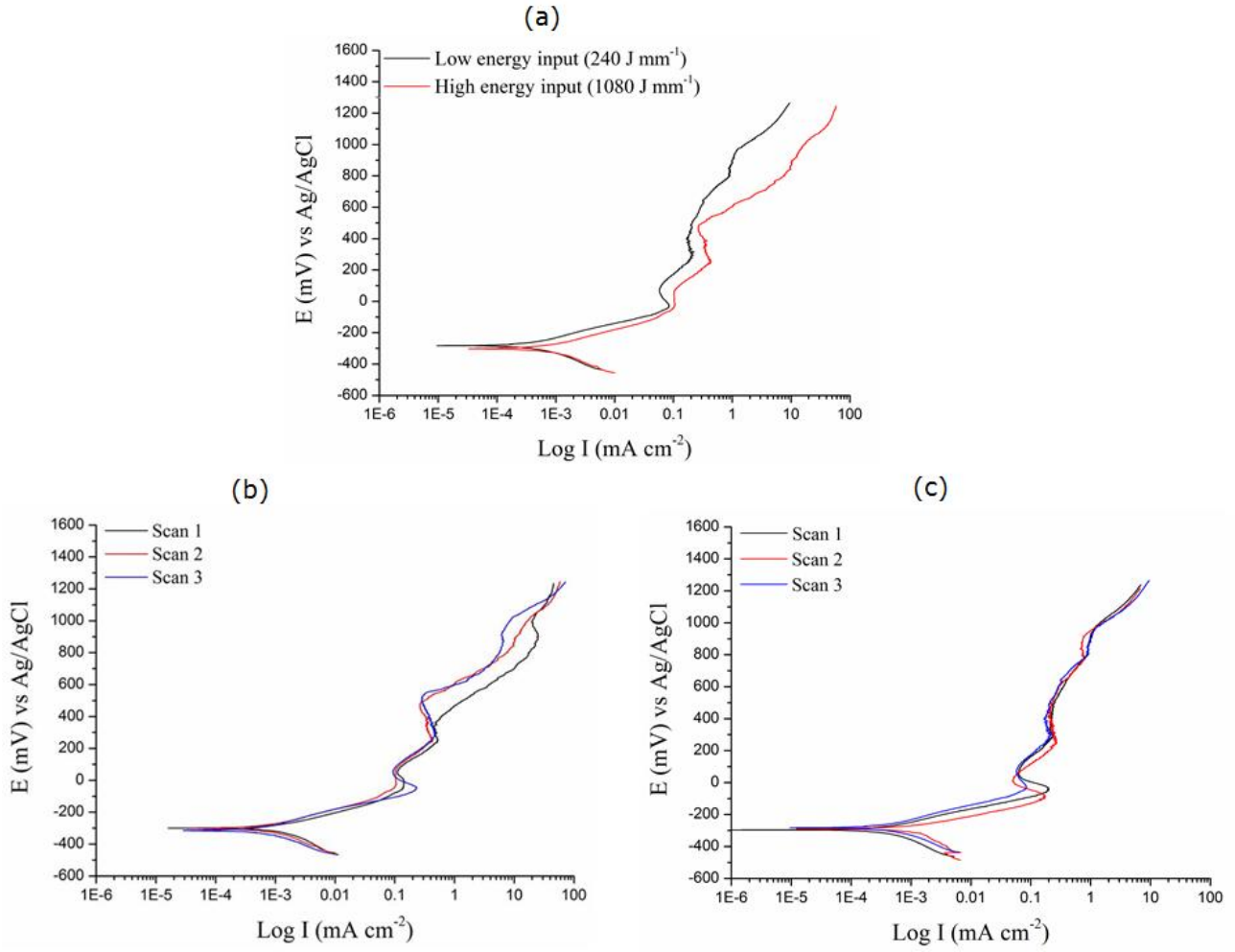

Figure 6.13: Cyclic polarisation curves of concurrently fed WC/W_2C powder-Inconel 625 wire composite laser coatings. (a) Comparison of the coatings formed at low (240 J mm^{-1}, P = 1.2 kW, V = 300 mm min^{-1}) and high (1080 J mm^{-1}, P = 1.8 kW, V = 100 mm min^{-1}) energy per unit length of track, (b) amount of scatter at 1080 J mm^{-1}, (c) amount of scatter at 240 J mm^{-1}.

6.4.3 Microstructural characterisation of the Spherotene-Inconel 625 wire coatings before and after corrosion

The cross-section of the corroded samples of the composite coatings deposited at 240 J mm^{-1} and 1080 J mm^{-1} are shown in Figures 6.14 and 6.15 respectively. The Figures reveal the microstructure of the two coatings and the depth of the corroded region on the top of the

coatings. Their microstructures are very different. At 1080 J mm^{-1}, there is large amount of Spherotene dissolution. Consequently, the coating is predominantly characterised by the formation of intermetallic compounds (mainly M_6C, $M_{23}C_6$ and W_2C carbides) and unevenly distributed few retained Spherotene particles. At 240 J mm^{-1}, more Spherotene were retained and evenly distributed throughout the coating. This is because the Spherotene dissolution is reduced at low energy level. The formation of intermetallic compounds is not as predominant as found at 1080 Jmm^{-1}.

The corrosion damage in the two coatings is limited to the topmost region and there was not any damage to the substrate. The substrate, as shown in Figures 6.14 and 6.15, is well protected from the corrosion attack because there was no ingress of electrolyte, hence, a formation of corrosion products at the coating-substrate interface. However, in the case of the composite laser coating formed at 1080 J mm^{-1}, the damage at the top region is relatively more severe because there is evidence of pit formation at the surface, as clearly shown in Figure 6.15c.

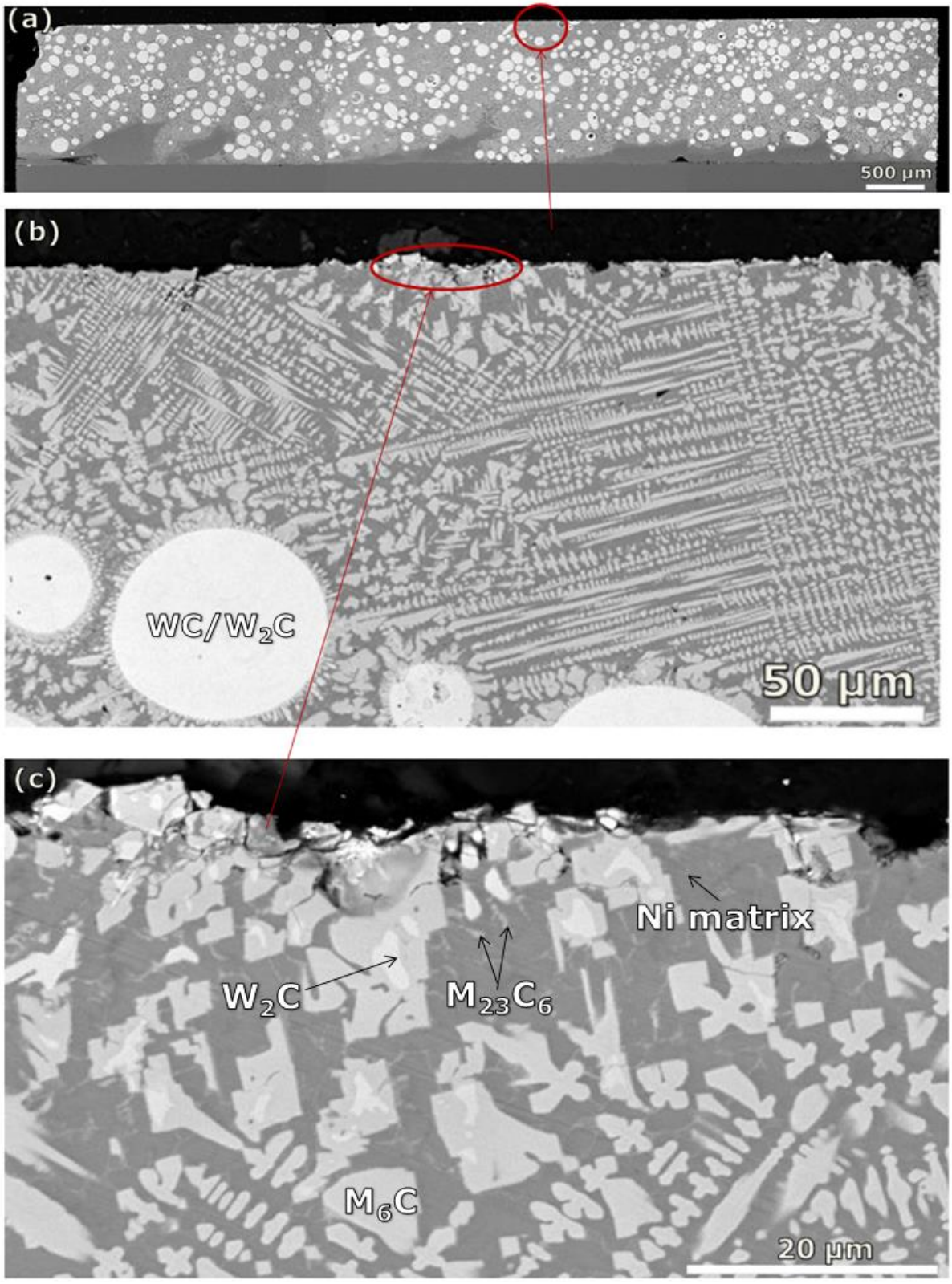

Figure 6.14: BSE/SEM images of the cross-section of the concurrently fed Spherotene-Inconel 625 wire composite laser coating formed at 240 J mm^{-1} after the corrosion tests

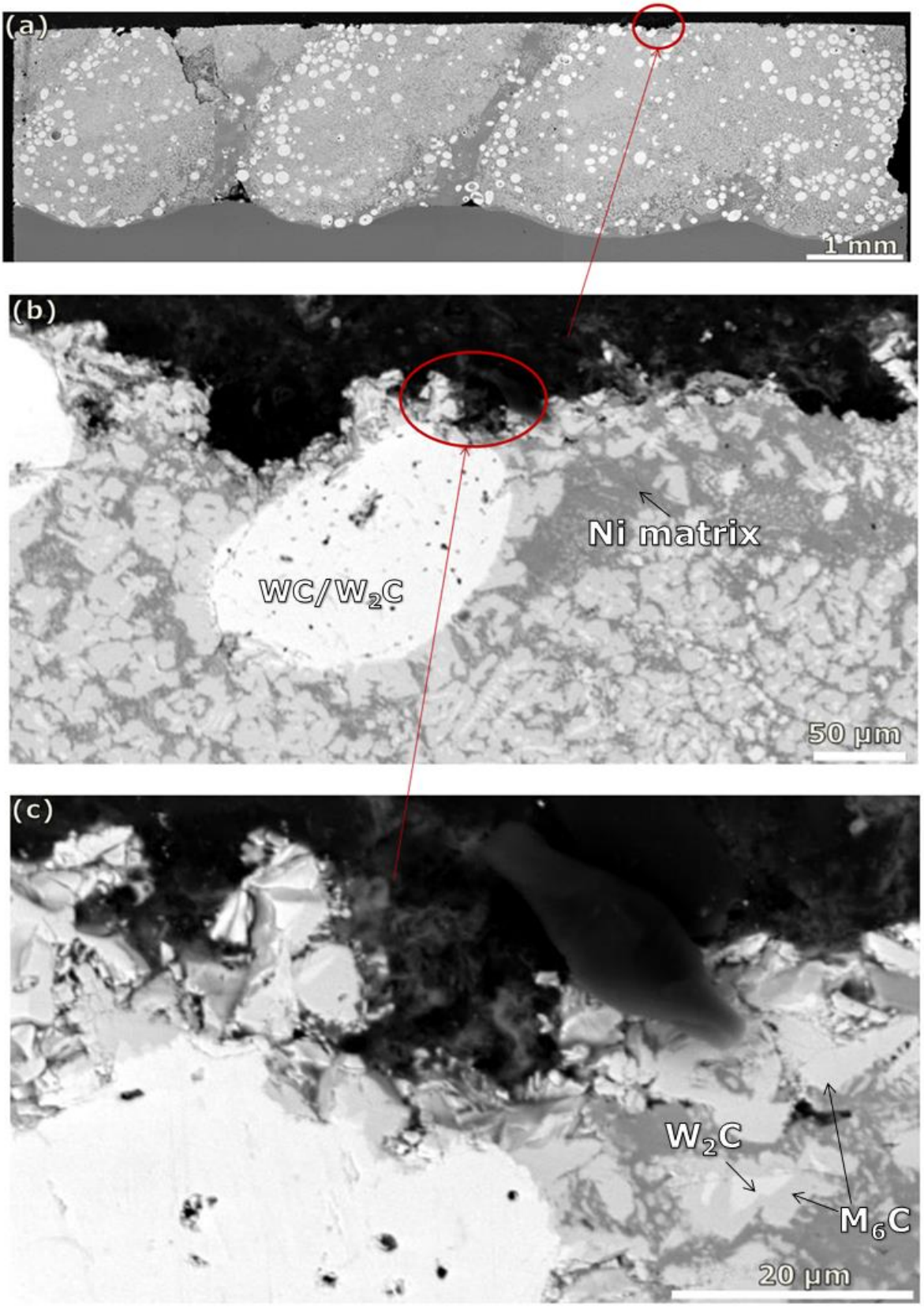

Figure 6.15: BSE/SEM images of the cross-section of the concurrently fed Spherotene-Inconel 625 wire composite laser coating formed at 1080 J mm^{-1} after the corrosion tests

The corroded surface of the samples were also characterised so as to know the corrosion mechanism that occurred in the coatings. BSE/SEM images of the top surface of the two samples, at low and high energy levels, before and after the potentiodynamic polarisation scan are presented in Figure 6.16 and 6.17.

As seen in Figure 6.16, the composite coating formed at 240 J mm^{-1} appears to be uniformly attacked in the corrosive environment (de-aerated 3.5% NaCl solution) because there is no evidence of pit formation within the corroded region. Compared to its initial microstructure before the tests, a faceted structure appeared clearly within the Spherotene particles in the

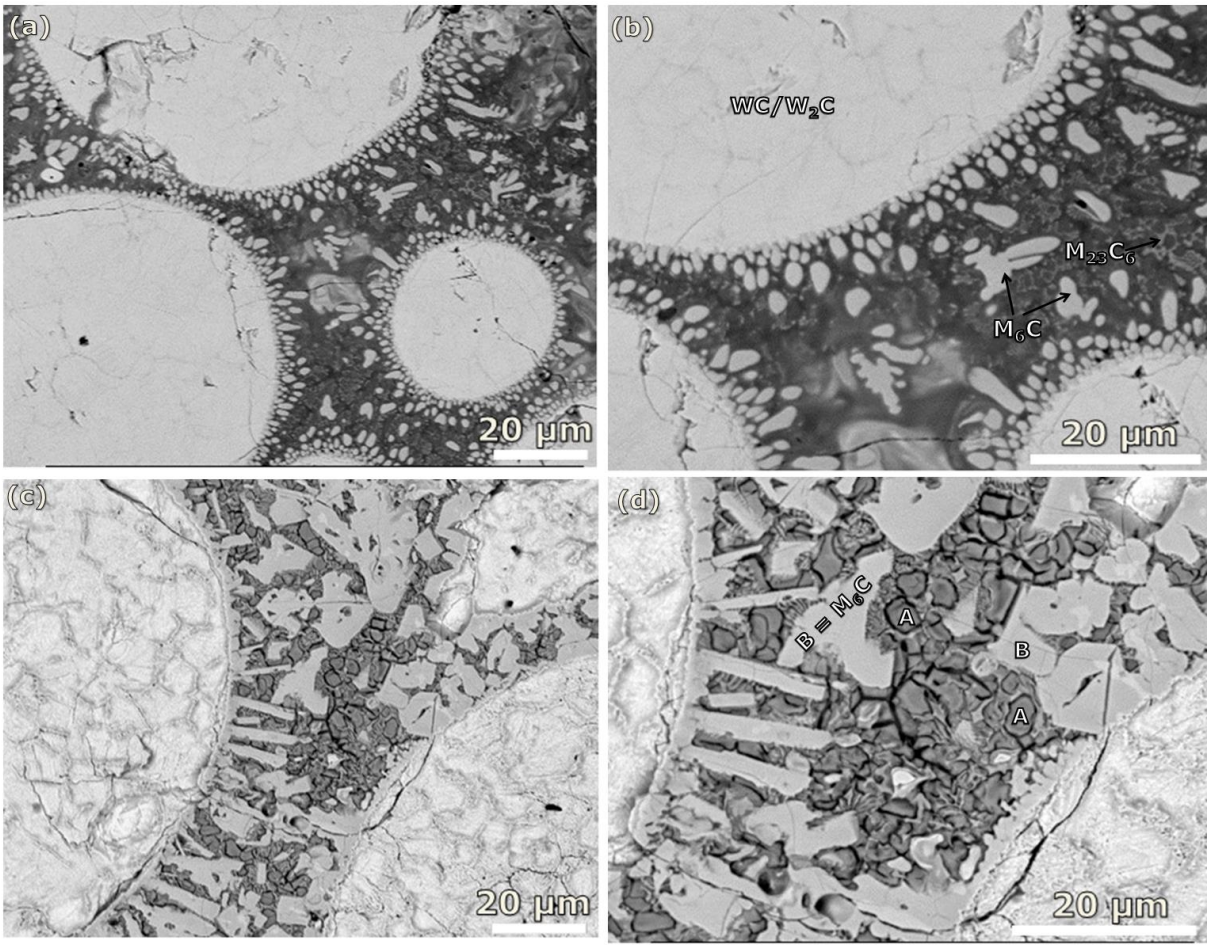

Figure 6.16: SEM/BSE images showing the microstructure of the top surface of Spherotene powder-Inconel 625 wire composite laser coatings formed at 240 J mm^{-1} (a, b) before and (c, d) after the potentiodynamic polarisation scan test in de-aerated 3.5% NaCl solution.

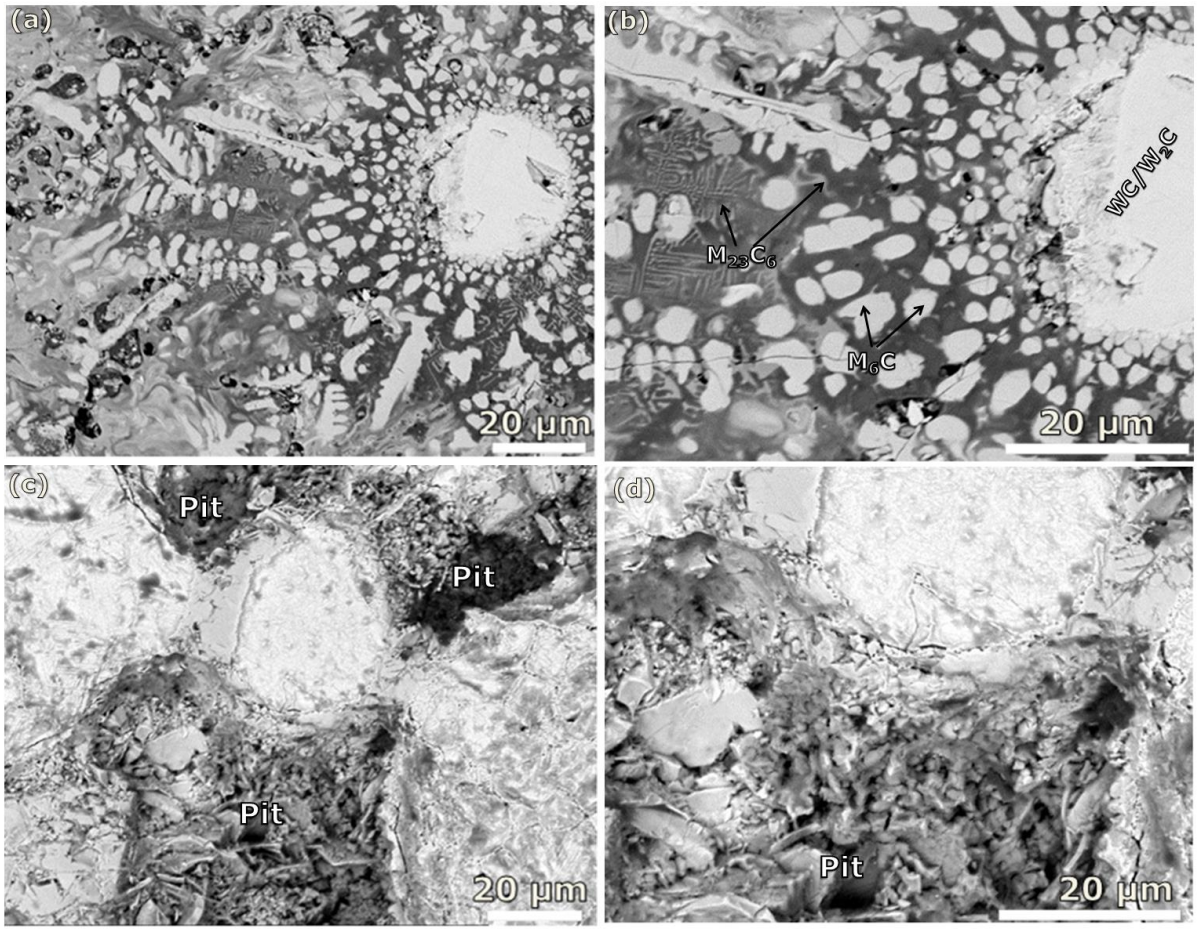

Figure 6.17: SEM/BSE images showing the microstructure of the top surface of Spherotene powder-Inconel 625 wire composite laser coatings formed at 1080 J mm^{-1} (a-c) before and (d-f) after the potentiodynamic polarisation scan test in de-aerated 3.5% NaCl solution.

coating. The difference is believed to be a result of chemical attack on the Spherotene particles. Therefore, it is considered that the Spherotene particles showed moderate corrosion damage the severity of which is clearly shown in Figure 6.16c. Within the composite matrix in-between the retained Spherotene particles, some microstructural changes due to the corrosion attack was observed. A new phase (marked as 'A') is seen to form on the dark Ni-matrix phase. There is no significant change in the colour and shape of the blocky carbide previously identified as M_6C (marked as 'B'). The EDX analysis was conducted on the two phases identified as A and B respectively, as seen in Figure 6.16d. The results which are averages of 5 measurements are presented in Table 6.6.

Table 6.6: Chemical composition (wt. %) of the phases A and B identified in Figure 6.16

Phase	O	Cr	Fe	Ni	Nb	Mo	W
A	22 ± 4	11± 2	1 ± 0.3	9 ± 2	4 ± 1	4 ± 1	50 ± 5
B	1 ± 0.1	8 ± 1	0.1 ± 0.1	19 ± 2	2 ± 0.1	6 ± 1	65 ± 4

It was found that the phase marked 'A' is richer in O indicating that it is a product of oxidation (corrosion). The other phase marked 'B' is composed of negligible amount of O (1 wt. %) after polarisation test in de-aerated 3.5% NaCl. Also, there is no significant change in the composition of M_6C (marked as 'B') after the test when compared with its composition before the test, as presented in Table 5.6. The SEM/EDX mapping in Figure 6.18 also reveals that there is more of oxygen and less of nickel in the phase marked A (i.e. corrosion product) whereas the blocky carbide 'B' contains more nickel and tungsten.

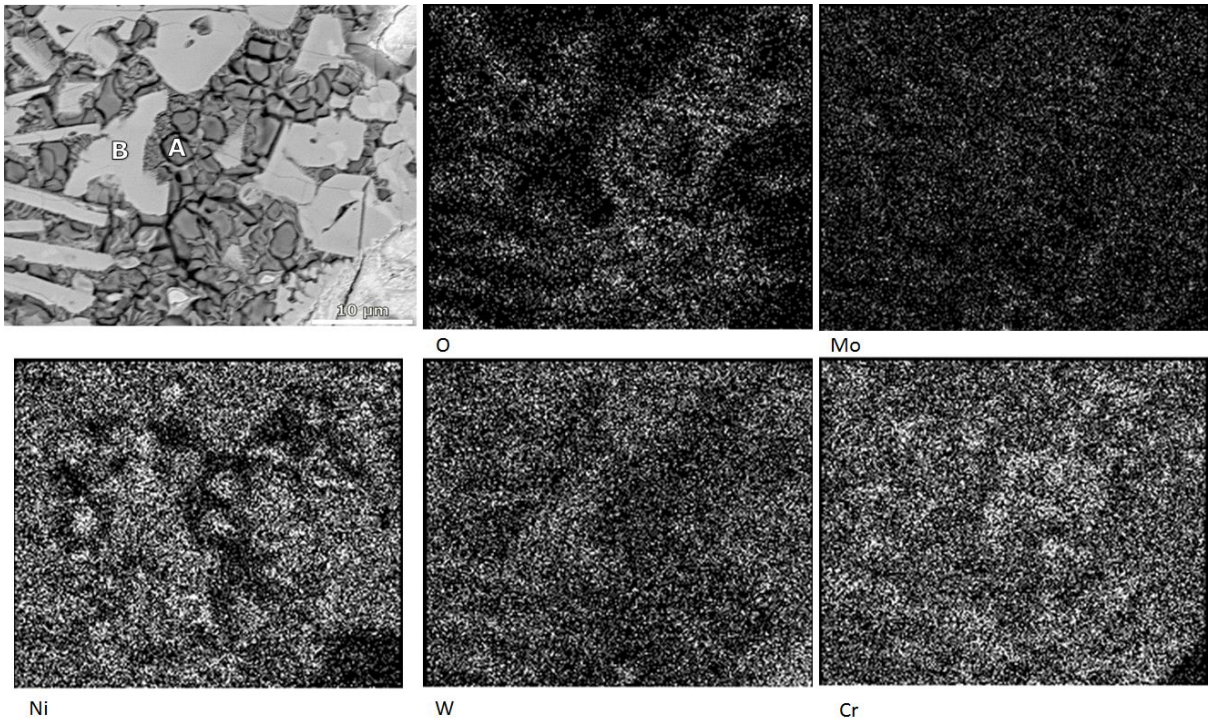

Figure 6.18: SEM/EDX mapping of the top surface of WC/W_2C powder-Inconel 625 wire laser coating formed at 240 J mm^{-1} after potentiodynamic polarisation scan in de-aerated 3.5% NaCl solution

The type of corrosion observed in the composite coating formed at 1080 J mm^{-1} is different. As shown in the Figure 6.17, pits were formed around the edges of the retained Spherotene powder. This indicates the occurrence of localised corrosion after the potentiodynamic polarisation scan test. Corrosion damage on the retained Spherotene was also observed.

Discussion

6.5 Open circuit potential (E_{oc})

Prior to potentiodynamic polarisation test, the E_{oc} values were determined by immersing the coating samples in the 3.5% NaCl solution for 1 hour at open circuit condition. This was done in order to allow the electrochemical reaction to reach a steady state before continuing with the polarisation scan test. As illustrated in Figure 6.19, there are different reactions taking place at the metal-electrolyte interface on immersion in an electrolyte. These reactions are responsible for the changing E_{oc} value with the time.

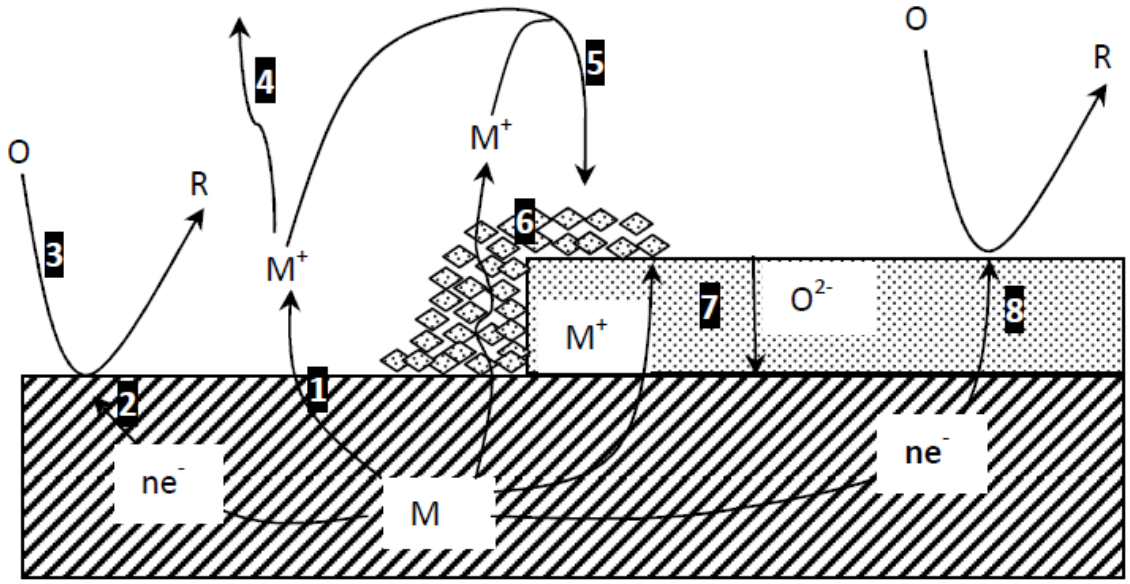

Figure 6.19: A diagram showing different processes taking place during surface corrosion (1) metal dissolution forming ions, (2) oxygen or proton reduction at metal surface, (3) transport of oxygen or ions to the surface, (4) metal ion transport from surface to the solution, (5) precipitation of corrosion product (6) metal ion transport through the product, (7) oxygen diffusion through solid corrosion product (8) oxygen/proton reduction at solid product layer [109]

An oxide film usually termed as native oxide is rapidly formed whenever a freshly prepared metal surface (sample) is exposed to the atmosphere. Upon immersion of the samples in the electrolyte, the native oxide tends to dissolve. If the initial dissolution of the native oxide is predominant, the E_{oc} will shift to a more negative value. On the other hand, the dissolving native oxide may be suppressed by the formation of passive film (corrosion product) which protects the metal surface from further oxidation. In this case, the E_{oc} starts to shift to a more positive value. Therefore, it can be concluded that the direction of the potential (E_{oc}) change with time is related to the initial dissolution of the native oxide and formation of the protective oxide (passive film) while inside the electrolyte.

According to Niaz [109] and Ahmed [117], the native oxide dissolution depends on the thickness of the oxide before immersion. For this reason, similar duration was kept between the sample preparation and the start of the E_{oc} in all tests conducted. However, the variation in the negative dip in the samples of the same coating shows that oxide film formation on the metal surface cannot be precisely controlled. In all the tested samples except the Inconel 625 wire coatings, the negative dip in the E_{oc} vs time curves indicates that native oxide dissolution was very dominant in the first 1hr before a steady state can be reached. The nearly parallel curve obtained for the Inconel 625 wire coatings probably suggests that the native oxide dissolution is minimal. This might be due to presence of thicker native oxide and/or rapid formation of passive film on immersion to electrolyte. The scatter in the average values of E_{oc} before and after immersion for each coating can be attributed to variations in the coating microstructure from one region to another. Different regions of the coating surface have different potential. This is due to different oxygen concentration, compositions of material and concentration of active species in solution from one part of the corroding surface to another [100, 109].

6.6 Potentiodynamic polarisation scan tests

Corrosion parameters including passive current density, breakdown potential and corrosion potential are often used for evaluating the corrosion resistance of materials using electrochemical analysis. All these parameters can be extracted from the polarisation curve (plot of E (mV) against Log I (mA cm^{-2})) generated during the polarisation scan test. The differences in the curves obtained for the substrate and all other coatings including composite coatings can be attributed to the ability of each material (or coating) to form a protective oxide film (otherwise termed passive film) over its surface. Usually, a passive film was formed on samples' surfaces prior to the polarisation scan test. This is confirmed by the E_{oc} behaviour as shown in Figures 6.1, 6.4 and 6.12. At the start of the polarisation scan, there is reduction of metal ions in the oxide film leading to alteration of the surface. After the completion of the reduction process, the metal ion began re-oxidising resulting in the re-nucleation of the oxide film (passive film). The formation of passive film (i.e. passivation) on the corroding metal surface slows down or prevents further corrosion damage by the electrolyte. If the passivation is achieved at relatively lower current density, it can be interpreted as a positive characteristic in uniform corrosion resistance. The reason is that mass of material loss is related to the amount of current flowing through the anode in a corrosion cell (Faraday's laws of electrolysis) [99, 100].

On the other hand, any damage to the passive film can drastically reduce the corrosion resistance and initiate localised corrosion damage such as pitting [82]. The breakdown potential is the ability of the material to resist the formation of the localised attack on the passive film. A high E_b shows that the damage nuclei cannot readily initiate on the passive film at a relatively lower applied voltage. Also, any damage nuclei initiated at voltages under the repassivation potential can be healed therefore, not ending in local defects. Accordingly, a higher breakdown potential implies a better resistance against non-uniform (localised)

corrosion. In terms of corrosion potential, a sample with higher corrosion potential is believed to be nobler than a sample with relatively lower corrosion potential.

6.6.1 304L stainless steel substrate

The corrosion resistance of the stainless steels has been related to its composition in the past [118, 119]. Due to its high Cr content, a chromium enriched passive film (Cr_2O_3) formed on the surface gives the steel good resistance to corrosion. This was confirmed by the ability of the steel sample to passivate at low current density (1.9×10^{-3} mA cm^{-2}), as presented in Table 6.1. However, the formation of pits randomly on the surface of the substrate, after the polarisation scan test, indicates that the film can easily be damaged at a reasonably high potential. In this study, the breakdown potential obtained for 304L stainless (340 mV wrt Ag/AgCl electrode) is somewhat low compared with the wrought Inconel 625 alloy (600 mV wrt Ag/AgCl electrode) [116] and Inconel 625 coatings (585 mV wrt Ag/AgCl electrode). This was expected because stainless steels (especially type 316 and 304L) demonstrate localised corrosion in specific environments, particularly in chloride ion rich solutions [120, 121]. This is particularly due to the absence or significantly low amount of Mo (<1%) in the stainless steels [100, 122].

6.6.2 Inconel 625 wire and Inconel 625 powder laser coatings

As shown in Figure 6.5, the polarisation curves for both the Inconel 625 wire and Inconel 625 powder laser coatings shows better corrosion properties than the stainless steel substrate. The absent of pitting in the two coatings can be related to the high Mo and Cr contents of the Inconel 625 alloy [9]. The formation of passive film (probably Cr_2O_3), by the two coatings, at relatively lower current densities compared to the substrate implies the material loss due to corrosion effect is reduced. The higher breakdown potential demonstrated by the two coatings implies that damage nuclei could not be easily initiated on the film. Even, at

transpassive region, the gradient of the current density against potential is significantly low indicating that there was not permanent damage on the passive film.

The slight difference in the polarisation curves hence, corrosion behaviours of Inconel 625 powder and Inconel 625 wire laser coatings can be traced to the difference in their microstructures. The type of grain structures and the grain size can influence the corrosion behaviours of metals [99, 121]. As shown in Figure 6.6, the microstructure of the top (exposed) surface of Inconel 625 powder is fully characterised with cellular/equiaxed dendrites of relatively finer grain sizes. This shows that the grain boundaries which are narrow regions of mismatch between the grains are more in number in the powder laser coating. On the other hand, the corresponding wire coating was characterised with coarser microstructure containing long growth of columnar dendrites. Relatively, the grain boundaries take up smaller fraction of the wire coating surface. According to Bradford [99], the grain boundaries act as collecting site for impurity atoms that do not fit well inside the metal crystals. Also, at moderate temperature, diffusion is much more rapid along the boundaries than within the grains. Therefore, atoms collect more rapidly and form precipitate at the boundaries otherwise called interdendritic regions. The combined effects of these result in increased inhomogeneity in the powder coating.

Additionally, it has been previously established in Chapter 4.15 that the Fe composition in the meltpool relates directly with the amount of interdendritic precipitates (most likely Laves) formed during the solidification of liquid Inconel 625 alloy. This precipitate with different electrochemical potentials is expected to form galvanic couple with the surrounding Ni-matrix dendrites therefore, initiating a galvanic form of corrosion around the interdendritic region. The Fe dilution was found to be 3.4 and 15.8% and the volume fraction of the interdendritic precipitates was estimated to be 0.7 and 2.3% in the typical Inconel 625 wire and powder laser coatings, respectively (see Table 4.9). Due to larger amount of

microstructural in-homogeneity in powder coating, more galvanic couple is believed to have formed in the coating than the corresponding Inconel 625 wire coating. Probably, this is the reason for higher passive current density and lower corrosion potential found for Inconel 625 powder coating when compared with the corresponding wire coating.

For comparison, the results of the corrosion tests of wrought Inconel 625 alloy, as found in the literature, and Inconel 625 laser clads using wire and powder feedstock are presented together in Table 6.7. Generally, the corrosion performance of both Inconel 625 wire and Inconel 625 powder coatings are close to the wrought Inconel 625 alloy.

Table 6.7: Corrosion properties of wrought Inconel 625 and laser clad Inconel 625 coatings in de-aerated 3.5% NaCl solution

Material	Environmental condition			Corrosion properties			Reference
	Temperature	Reference electrode	Electrolyte	E_{corr} (mV)	I_p (mA cm^{-2})	E_b (mV)	
Wrought Inconel 625 alloy	Room temperature	Ag/AgCl	de-aerated 3.5% NaCl solution	-264	4.7×10^{-4}	600	[116]
Wrought Inconel 625 alloy	30°C	SCE	de-aerated 3.5% NaCl solution	-310 ± 6	1.5×10^{-3}	650	[32]
Inconel 625 wire laser coating	Room temperature	Ag/AgCl	de-aerated 3.5% NaCl solution	-222 ± 8	3.0×10^{-4}	585 ± 5	
Inconel 625 powder laser coating	Room temperature	Ag/AgCl	de-aerated 3.5% NaCl solution	-253 ± 56	1.1×10^{-3}	584 ± 8	

6.6.3: Spherotene-Inconel 625 wire composite laser coating

The corrosion behaviour observed in the composite coating is complex and more severe compared to the Inconel 625 alloy laser coatings. In the composite coating formed at 240 J mm^{-1}, corrosion damage was observed within the partially dissolved Spherotene particles and within the Ni-matrix phase in-between the secondary carbides. As discussed earlier in Chapter 5.15, Spherotene injection into molten Inconel 625 alloy, during laser processing,

resulted in microstructural modifications and large extent of compositional in-homogeneity. For example, precipitation of the secondary carbides such as Fe_3W_3C (M_6C) and $Cr_{23}C_6$ ($M_{23}C_6$) results in the depletion of useful alloy element such as Cr and Mo from the Ni-matrix. Chromium, the main alloying elements in Inconel 625 alloy, is added to promote resistance to corrosion. Its role is to passivate the external surface of the alloy by forming a thin oxide film (Cr_2O_3) over it. Now, the Ni-matrix phase, especially those regions adjacent to the secondary carbides, is more vulnerable to corrosion damage because of the Cr depletion in this region.

Accordingly, the Ni matrix phase was severely attacked. This is believed to be caused by two things. First, the Cr depletion from Ni matrix phase reduces the corrosion resistance of the matrix phase. Secondly, due to the differences in their electrochemical potentials, galvanic couples are believed to have been formed between the secondary carbides and the Cr depleted regions of the matrix adjacent to the carbides. Although there is no data stating the positions of the carbides including the Spherotene in the electrochemical series, the Ni matrix is believed to be the sacrificial anode in the galvanic cell mechanism because it was preferentially attacked whereas the blocky carbide showed no corrosion damage.

Similarly, the corrosion damage within the partially dissolved Spherotene (i.e. retained) may be as a result the galvanic couple formed between the partially dissolved Spherotene and the secondary carbides phase at its interphase. In the past, corrosion of tungsten carbide particulate has been observed by Cooper et al. [11] after six month exposure of laser melted WC-Inconel 625 powder composite laser coating to seawater. This type of corrosion was considered as unusual.

The formation of pits around the retained Spherotene particles in the composite coating formed at high energy per unit length of track (1080 J mm^{-1}) is a result of massive depletion

of Cr and Mo from these regions of the coating. In the microstructure of this coating detailed in Chapter 5.6, there was increased depletion of Cr in the Ni-matrix due to increased Spherotene dissolution. More C released into the matrix increased the formation of $Cr_{23}C_6$ due to Cr-C affinity. Also, there was more amount of M_6C which is enriched with Mo and Cr depending on the composition of the matrix region. All these collectively result in depletion of the matrix in Cr and Mo. Since the Spherotene dissolution is a surface phenomenon, it is expected that there will be more of these phases hence, higher Cr- and Mo- depletion around the edges of the retained Spherotene. It is known that Mo and Cr are the primary alloying elements resisting the alloy 625 against localised corrosion. The presence of localised corrosion around the Spherotene is therefore believed to be a result of extensive depletion of these elements around the partially dissolved Spherotene. In general, the corrosion in the two composite coatings is limited to the top surface of the coating and there were no corrosion products within the composite later and at the layer-substrate interface. This indicates that the substrate is well protected from corrosion by the laser clad layers of Spherotene-Inconel 625 wire composite.

6.7 Summary

- The corrosion behaviours of Inconel 625 powder, Inconel 625 wire and Spherotene-Inconel 625 wire composite laser coatings as well as 304L stainless steel substrate were successfully examined and compared using 1hour open circuit potential immersion tests and potentiodynamic polarisation scan tests in de-aerated 3.5% NaCl solution.
- The 304L stainless steel passivated at low current density (1.9×10^{-3} mA cm^{-2}) but demonstrated high degree of localised (pitting) corrosion at a low potential (340 mV wrt Ag/AgCl electrode).
- Compared to the stainless steel substrate, both the Inconel 625 wire and powder laser coatings exhibited improved corrosion resistance. They passivated at relatively lower current densities with wider passivation region and suffered from no localised corrosion attack as evidenced on their surfaces after the tests.
- The Inconel 625 wire laser coating demonstrated better corrosion properties in terms of passive current density and corrosion potential than the corresponding Inconel 625 powder laser coating. This was attributed to reduced microstructural inhomogeneity which is probably caused by low Fe dilution experienced by the Inconel 625 wire laser coating.
- The corrosion performance of Inconel 625 wire laser coating is very close to that of wrought Inconel 625 alloy.
- The corrosion mechanism is complex in the Spherotene-Inconel 625 wire composite laser coatings. This is a result of large amount of microstructural modification and compositional in-homogeneity caused by the Spherotene dissolution in the composite coating.

- The Ni-matrix regions adjacent to the secondary carbides (M_6C, W_2C and $M_{23}C_6$) are deficient in Cr therefore, causing them to be selectively corroded whenever galvanic couple is formed between these regions and the adjacent carbides.
- Corrosion attack was observed within the retained Spherotene particles. This was due to the galvanic type of corrosion between the Spherotene and the secondary carbides at its interface of which the Spherotene is believed to act as anode.
- Localised corrosion attack, evidenced by pits formation around the Spherotene edges, was observed in the composite laser coating formed at extremely high energy per unit length of track (1080 J mm^{-1}). This is due to massive depletion of Cr and Mo around the edges of the retained Spherotene caused by large extent of Spherotene dissolution experienced at high energy input.

7.0 Conclusions and future work

7.1 Conclusions

The first aim of this work is to study the fibre laser cladding of Inconel 625 using wire and powder as the feedstock material. Secondly, the effect of the concurrent injection of Spherotene in the fibre laser cladding of Spherotene powder-Inconel 625 wire composite was investigated. The process characterisation, microstructural evolution, micro-hardness and corrosion properties variations related to the processing parameters, nature of the feedstock (Inconel 625) used and Spherotene dissolution arising from the composite cladding were analysed. The following sections conclude the results and discussion of this work.

7.2 Laser cladding of wire and powder based Inconel 625 coatings

7.2.1 Laser deposition

This study has found that pore- and crack-free, minimally diluted and well bonded Inconel 625 tracks deposited by laser cladding using wire and powder as the feedstock material are possible. Overlapped-track layers with similar qualities as the single tracks were built.

7.2.2 Process characterisation

The fibre laser deposition of Inconel 625 wire, at different processing parameters, are characterised with wire dripping, smooth wire transfer and wire stubbing. Within the range of parameters utilised in this research work, a map predicting the deposition process characteristics at varying processing parameters has been developed. Energy per unit length of track and wire feed rate influence the process characteristics. Smooth wire deposition (smooth wire transfer) was achieved at the processing conditions where the selected wire feed

rate is appropriate for the available energy per unit length of track. Continuous tracks of Inconel 625 wire were deposited whenever there was smooth transfer of wire. At energy per unit length of track below 200 J mm^{-1}, it is impracticable, for the set up employed in this study, to successfully deposit continuous tracks.

7.2.3 Substrate dilution

Within the range of parameters used in this study, powder based tracks showed higher dilution ratio, ranging between 10-41%, than wire based tracks (<1% to 24%). For the two cladding processes, the dilution ratio showed positive dependency on laser power and traverse speed but varied inversely with the material feed rates (WFR and PFR). The significance level of the effect of each of the parameters on the dilution was carried out using ANOVA. The material feed rate (WFR or PFR) has the most significant effect.

7.2.4 Microstructural characterisation of wire and powder based Inconel 625 coatings

The powder and wire based Inconel 625 coatings deposited in this work comprised dendritic γ-Ni (FCC) phase and interdendritic Mo- and Nb- rich precipitates. The volume fraction of interdendritic precipitates in the coatings increased with increasing the Fe dilution. A typical powder based coating exhibited fine cellular/equiaxed dendritic solidification mode whereas the corresponding wire track comprised relatively coarse columnar grain structure.

When the effects of traverse speed, laser power and wire feed rate on the coating microstructure were investigated, it was found that relatively finer microstructure is obtainable at higher traverse speed, lower laser power and lower wire feed rate. Also, this study revealed that the clad micro-hardness increases as the microstructure becomes finer.

7.2.5 Corrosion performance of wire and powder based Inconel 625 coatings

The corrosion behaviour of a typical Inconel 625 wire and corresponding Inconel 625 powder coatings were investigated. The wire based coating showed slightly improved corrosion

performance in terms of passive current density and corrosion potential. However, the two coatings have nearly equal breakdown potential and were uniformly attacked. The Inconel 625 powder coating showed a large degree of scatter in the corrosion behaviour indicating some degree of in-homogeneity in its microstructure. The corrosion property of the laser clad Inconel 625 wire coating is close to that of the wrought Inconel 625 alloy. Compared with substrate which demonstrated localised corrosion attack, the two coatings showed improved corrosion resistance.

7.3 Laser cladding of Spherotene powder/Inconel 625 wire composite coatings

7.3.1 Laser deposition

This study has established that well bonded, minimally diluted and pore- and crack-free composite coatings can be successfully deposited by using concurrent fibre laser cladding of Spherotene and Inconel 625 wire. Overlapped-track layers free of cracks and having good metallurgical bonding were also deposited.

7.3.2 Effect of Spherotene injection on the process characterisation of Inconel 625 wire laser cladding

When the Spherotene particles were introduced, a rightward shift was found in the process map developed for Inconel 625 wire laser cladding. Continuous laser tracks of Spherotene/Inconel 625 wire composite are possible only when there is smooth transfer of wire.

7.3.3 Macro-constituent of Spherotene powder/Inconel 625 wire composite laser coatings

In this study, it was revealed that the volume fraction of the Spherotene retained in the composite track (ranging between 16 and 30%) depends mainly on (1) the amount of Spherotene dissolution and (2) amount of Spherotene captured in the meltpool. It was found that the volume fraction of the Spherotene retained decreased with increasing laser power, traverse speed and wire feed rate.

The Spherotene deposition efficiency ranged between 12 and 38%. It varied directly with the laser power and wire feed rate but inversely with the traverse speed. The variation of Spherotene dissolution ratio (ranging between 2 and 57%) with the processing parameters indicates that the amount of Spherotene dissolution increases with increasing laser power but decreases with increasing traverse speed and wire feed rate.

7.3.4 Micro-constituent of Spherotene powder/Inconel 625 wire composite laser coatings

The microstructural examination of the Spherotene powder/Inconel 625 wire composite coatings revealed the presence of WC/W_2C powder (partially dissolved Spherotene), W_2C phase and precipitates (Fe_3W_3C and $Cr_{23}C_6$) in continuous γ Ni-matrix. The γ-Ni matrix was increasingly enriched in W and C as the Spherotene dissolution increased. The more the Spherotene dissolution the more the amount of precipitates formed in the coatings. The precipitation of $Cr_{23}C_6$ and Fe_3W_3C resulted in the depletion of useful alloy contents such as Cr and Mo in the interdendritic regions and in the dendritic γ-Ni matrix around the carbides. The amount of the secondary carbides and Cr depletion was found to increase at higher energy per unit length of track.

7.3.5 Micro-hardness of the laser coatings of Spherotene powder/Inconel 625 wire composites

The high micro-hardness of the matrix region of the composite coatings (more than 200% harder than Inconel 625 laser coatings) is due to the formation of the secondary carbides such as W_2C, Fe_3W_3C and $Cr_{23}C_6$ in the matrix. The micro-hardness of the composite matrix increased with the laser power but decreased with increasing traverse speed and wire feed rate.

7.3.6 Corrosion performance of Spherotene powder/Inconel 625 wire composite laser coatings

The composite coatings deposited at two different energy levels demonstrated different corrosion performance in de-aerated 3.5% NaCl solution because of varying amount of Spherotene particle dissolution. Generally, the corrosion damage in the composite coating is complex and largely results from galvanic couples existing between the different phases present. The coating formed at higher energy level (1080 J mm^{-1}) suffered more corrosion damage as there was evidence of pitting around the retained Spherotene particles. At lower energy level (240 J mm^{-1}), the corrosion attack was rather uniform throughout the exposed surface of the coating.

Compared with the Inconel 625 laser coatings, there was no evidence of passivation in the polarisation scan curves obtained for the Spherotene powder/Inconel 625 wire composite laser coatings deposited. The corrosion potentials were also of more negative values. The composite therefore showed lower resistance to corrosion as compared to Inconel 625 laser coatings.

7.3.7 Significance of the results

It is shown in this work that the life span of stainless steel components can be extended in chloride ion rich corrosive environment (e.g. oil and gas environments) by coating them with Inconel 625 laser coatings. However, using Inconel 625 wire coatings is more advantageous because of better process economy and improved corrosion resistance. In industrial applications where a combination of wear and corrosion damage is the major problem, this work also demonstrates that Spherotene powder-Inconel 625 wire laser coating provides adequate protection against such damage. Significantly higher surface hardness shown by the MMC coatings is a potential evidence for a reduced wear rate. Better protection of stainless steel components against high wear and corrosive damage is obtained by reducing the Spherotene dissolution and the degree of Fe dilution from the substrate which is possible through process control.

7.4 Future work

The basic questions relating to the objectives of this work have been answered in this thesis. Nevertheless, in the course carrying out this work, further questions arose. These questions can be studied for future research.

1. The corrosion performance of the coatings was assessed mainly by potentiodynamic tests in this work. However, further tests can still be done to completely understand the corrosion behaviour of the coatings. These include salt spray test and long term immersion test.
2. The type of corrosion oxide layer formed can be identified. The influence of the oxide layer on the corrosion behaviour of the coatings might qualify to be a topic for future research.

3. An increase in Spherotene dissolution was found to increase corrosion damage of the composite coatings in this work. It is considered that encapsulating the Spherotene with pure nickel alloy before laser deposition may further reduce its dissolution hence improves the corrosion performance of the coatings.
4. Investigating the abrasive wear performance of the Spherotene (WC/W_2C) powder/Inconel 625 wire composite laser coatings is another area of research.
5. The feed rate of the Spherotene was fixed at 25 g min^{-1} for all the composite coatings deposited in this study. Further research can be done at lower feed rates such as 20, 15, 10 and 5 g min^{-1}.

Appendices

APPENDIX A. PROCESSING PARAMETERS

Table A1: Processing parameters and visual observations for Inconel 625 wire single track deposition

S/N	Laser power (kW)	Transverse speed (mm min^{-1})	Wire feed rate (mm min^{-1})	Energy/ unit length (J mm^{-1})	Deposition volume/unit length (mm^3 mm^{-1})	Visual observation of the process
1	1.8	100	400	1080	4.5	Dripping
2	1.8	100	600	1080	6.8	Smooth flow of wire
3	1.8	100	800	1080	9.1	Smooth flow of wire
4	1.8	100	1000	1080	11.3	Smooth flow of wire
5	1.8	100	1200	1080	13.6	Smooth flow of wire
6	1.8	100	1400	1080	15.8	Stubbing
7	1.8	200	400	540	2.3	Dripping
8	1.8	200	600	540	3.4	Smooth flow of wire
9	1.8	200	800	540	4.5	Smooth flow of wire
10	1.8	200	1000	540	5.7	Smooth flow of wire
11	1.8	200	1200	540	6.8	Stubbing may occur
12	1.8	200	1400	540	7.9	Stubbing
13	1.8	300	400	360	1.5	Dripping
14	1.8	300	600	360	2.3	Dripping may occur
15	1.8	300	800	360	3.0	Smooth flow of wire
16	1.8	300	1000	360	3.8	Smooth flow of wire
17	1.8	300	1200	360	4.5	Stubbing may occur
18	1.8	300	1400	360	5.3	Stubbing
19	1.6	100	400	960	4.5	Dripping
20	1.6	100	600	960	6.8	Smooth flow of wire
21	1.6	100	800	960	9.1	Smooth flow of wire
22	1.6	100	1000	960	11.3	Smooth flow of wire
23	1.6	100	1200	960	13.6	Stubbing
24	1.6	100	1400	960	15.8	Stubbing
25	1.6	200	400	480	2.3	Dripping
26	1.6	200	600	480	3.4	Smooth flow of wire
27	1.6	200	800	480	4.5	Smooth flow of wire
28	1.6	200	1000	480	5.7	Stubbing may occur
29	1.6	200	1200	480	6.8	Stubbing
30	1.6	200	1400	480	7.9	Stubbing
31	1.6	300	400	320	1.5	Dripping
32	1.6	300	600	320	2.3	Smooth flow of wire
33	1.6	300	800	320	3.0	Smooth flow of wire
34	1.6	300	1000	320	3.8	Stubbing may occur

S/N	Laser power (kW)	Transverse speed (mm min^{-1})	Wire feed rate (mm min^{-1})	Energy/ unit length (J mm^{-1})	Deposition volume/unit length (mm^3 mm^{-1})	Visual observation of the process
35	1.6	300	1200	320	4.5	Stubbing
36	1.6	300	1400	320	5.3	Stubbing
37	1.4	100	400	840	4.5	Dripping may occur
38	1.4	100	600	840	6.8	Smooth flow of wire
39	1.4	100	800	840	9.1	Smooth flow of wire
40	1.4	100	1000	840	11.3	Stubbing may occur
41	1.4	100	1200	840	13.6	Stubbing
42	1.4	100	1400	840	15.8	Stubbing
43	1.4	200	400	420	2.3	Dripping may occur
44	1.4	200	600	420	3.4	Smooth flow of wire
45	1.4	200	800	420	4.5	Smooth flow of wire
46	1.4	200	1000	420	5.7	Stubbing may occur
47	1.4	200	1200	420	6.8	Stubbing
48	1.4	200	1400	420	7.9	stubbing
49	1.4	300	400	280	1.5	Dripping may occur
50	1.4	300	600	280	2.3	Smooth flow of wire
51	1.4	300	800	280	3.0	Stubbing may occur
52	1.4	300	1000	280	3.8	Stubbing
53	1.4	300	1200	280	4.5	Stubbing
54	1.4	300	1400	280	5.3	Stubbing
55	1.2	100	400	720	4.5	Smooth flow of wire
56	1.2	100	600	720	6.8	Smooth flow of wire
57	1.2	100	800	720	9.1	Stubbing may occur
58	1.2	100	1000	720	11.3	Stubbing
59	1.2	100	1200	720	13.6	Stubbing
60	1.2	200	400	360	2.3	Dripping may occur
61	1.2	200	600	360	3.4	Smooth flow of wire
62	1.2	200	800	360	4.5	Stubbing may occur
63	1.2	200	1000	360	5.7	Stubbing
64	1.2	200	1200	360	6.8	Stubbing
65	1.2	300	400	240	1.5	Dripping may occur
66	1.2	300	600	240	2.3	Smooth flow of wire
67	1.2	300	800	240	3.0	Stubbing may occur
68	1.2	300	1000	240	3.8	Stubbing
69	1.2	300	1200	240	4.5	Stubbing
70	1.0	100	400	600	4.5	Smooth flow of wire
71	1.0	100	600	600	6.8	Smooth flow of wire
72	1.0	100	800	600	9.1	Stubbing
73	1.0	100	1000	600	11.3	Stubbing
74	1.0	100	1200	600	13.6	Stubbing

S/N	Laser power (kW)	Transverse speed (mm min^{-1})	Wire feed rate (mm min^{-1})	Energy/ unit length (J mm^{-1})	Deposition volume/unit length (mm^3 mm^{-1})	Visual observation of the process
75	1.0	200	400	300	2.3	Smooth flow of wire
76	1.0	200	600	300	3.4	Stubbing may occur
77	1.0	200	800	300	4.5	Stubbing
78	1.0	200	1000	300	5.7	Stubbing
79	1.0	200	1200	300	6.8	Stubbing
80	1.0	300	400	200	1.5	Dripping may occur
81	1.0	300	600	200	2.3	Stubbing may occur
82	1.0	300	800	200	3.0	Stubbing
83	1.0	300	1000	200	3.8	Stubbing
84	1.0	300	1200	200	4.5	Stubbing

Table A2: Results of geometrical characterisation for Inconel 625 wire single track deposition

S/N	Laser power (KW)	Scanning speed (mm min^{-1})	Wire feed rate (mm min^{-1})	Average Height (mm)	Average Width (mm)	Average Cross-sectional area (mm^2)	Aspect ratio	contact angle (degrees)
1	1.8	100	400	n/a	n/a	n/a	n/a	n/a
2	1.8	100	600	1.9	4.8	6.6	2.6	75
3	1.8	100	800	2.4	4.6	8.6	1.9	92
4	1.8	100	1000	2.7	4.7	10.7	1.7	99
5	1.8	100	1200	3.1	4.8	12.6	1.5	105
6	1.8	100	1400	n/a	n/a	n/a	n/a	n/a
7	1.8	200	400	n/a	n/a	n/a	n/a	n/a
8	1.8	200	600	1.1	4.5	3.3	4.2	50
9	1.8	200	800	1.5	4.1	4.3	2.8	71
10	1.8	200	1000	1.8	3.6	5.1	2.1	89
11	1.8	200	1200	2.1	3.6	6.1	1.8	97
12	1.8	200	1400	n/a	n/a	n/a	n/a	n/a
13	1.8	300	400	n/a	n/a	n/a	n/a	n/a
14	1.8	300	600	0.9	3.3	2.6	3.7	57
15	1.8	300	800	1.1	3.5	2.9	3.1	66
16	1.8	300	1000	1.4	3.3	3.5	2.4	79
17	1.8	300	1200	1.6	3.1	4.1	1.9	93
18	1.8	300	1400	n/a	n/a	n/a	n/a	n/a
19	1.6	100	400	n/a	n/a	n/a	n/a	n/a
20	1.6	100	600	1.9	4.2	6.5	2.2	86
21	1.6	100	800	2.5	3.8	8.2	1.5	106
22	1.6	100	1000	2.9	4.2	10.3	1.4	108
23	1.6	100	1200	n/a	n/a	n/a	n/a	n/a
24	1.6	100	1400	n/a	n/a	n/a	n/a	n/a
25	1.6	200	400	n/a	n/a	n/a	n/a	n/a
26	1.6	200	600	1.2	3.6	3.3	2.9	69
27	1.6	200	800	1.5	3.5	4.2	2.2	83
28	1.6	200	1000	1.9	3.3	5.1	1.7	99
29	1.6	200	1200	n/a	n/a	n/a	n/a	n/a
30	1.6	200	1400	n/a	n/a	n/a	n/a	n/a
31	1.6	300	400	n/a	n/a	n/a	n/a	n/a
32	1.6	300	600	0.9	3.4	2.2	3.7	57

S/N	Laser power (KW)	Scanning speed (mm min^{-1})	Wire feed rate (mm min^{-1})	Average Height (mm)	Average Width (mm)	Average Cross-sectional area (mm^2)	Aspect ratio	contact angle (degrees)
33	1.6	300	800	1.2	3.0	2.8	2.5	77
34	1.6	300	1000	1.4	3.4	3.5	2.4	79
35	1.6	300	1200	n/a	n/a	n/a	n/a	n/a
36	1.6	300	1400	n/a	n/a	n/a	n/a	n/a
37	1.4	100	400	1.6	3.7	4.4	2.3	82
38	1.4	100	600	2.0	3.8	6.2	1.9	94
39	1.4	100	800	2.5	3.8	8.2	1.5	106
40	1.4	100	1000	2.9	4.0	10.0	1.4	111
41	1.4	100	1200	3.4	4.3	12.6	1.3	116
42	1.4	100	1400	n/a	n/a	n/a	n/a	n/a
43	1.4	200	400	1.1	3.0	2.5	2.7	73
44	1.4	200	600	1.3	3.1	3.1	2.5	78
45	1.4	200	800	1.6	3.0	4.0	1.8	95
46	1.4	200	1000	2.0	2.8	4.9	1.4	110
47	1.4	200	1200	n/a	n/a	n/a	n/a	n/a
48	1.4	200	1400	n/a	n/a	n/a	n/a	n/a
49	1.4	300	400	0.8	2.8	1.7	3.5	59
50	1.4	300	600	1.0	2.9	2.1	3.0	68
51	1.4	300	800	1.3	2.7	2.7	2.2	85
52	1.4	300	1000	n/a	n/a	n/a	n/a	n/a
53	1.4	300	1200	n/a	n/a	n/a	n/a	n/a
54	1.4	300	1400	n/a	n/a	n/a	n/a	n/a
55	1.2	100	400	1.5	3.2	3.9	2.1	86
56	1.2	100	600	2.2	3.3	6.1	1.5	107
57	1.2	100	800	2.7	3.5	8.1	1.3	113
58	1.2	100	1000	n/a	n/a	n/a	n/a	n/a
59	1.2	100	1200	n/a	n/a	n/a	n/a	n/a
60	1.2	200	400	1.0	2.8	2.1	2.7	73
61	1.2	200	600	1.4	2.8	3.0	2.0	90
62	1.2	200	800	1.7	2.7	3.8	1.6	103
63	1.2	200	1000	n/a	n/a	n/a	n/a	n/a
64	1.2	200	1200	n/a	n/a	n/a	n/a	n/a
65	1.2	300	400	0.9	2.6	1.8	2.9	69
66	1.2	300	600	1.1	2.7	2.1	2.5	77
67	1.2	300	800	1.4	2.5	2.7	1.8	96
68	1.2	300	1000	n/a	n/a	n/a	n/a	n/a
69	1.2	300	1200	n/a	n/a	n/a	n/a	n/a
70	1	100	400	1.6	3.3	4.2	2.1	88

S/N	Laser power (KW)	Scanning speed (mm min^{-1})	Wire feed rate (mm min^{-1})	Average Height (mm)	Average Width (mm)	Average Cross-sectional area (mm^2)	Aspect ratio	contact angle (degrees)
71	1	100	600	2.3	3.1	6.2	1.3	113
72	1	100	800	n/a	n/a	n/a	n/a	n/a
73	1	100	1000	n/a	n/a	n/a	n/a	n/a
74	1	100	1200	n/a	n/a	n/a	n/a	n/a
75	1	200	400	n/a	n/a	n/a	n/a	n/a
76	1	200	600	1.5	2.5	3.0	1.7	98
77	1	200	800	n/a	n/a	n/a	n/a	n/a
78	1	200	1000	n/a	n/a	n/a	n/a	n/a
79	1	200	1200	n/a	n/a	n/a	n/a	n/a
80	1	300	400	1.0	2.1	1.9	2.1	87
81	1	300	600	1.1	2.1	1.9	1.9	94
82	1	300	800	n/a	n/a	n/a	n/a	n/a
83	1	300	1000	n/a	n/a	n/a	n/a	n/a
84	1	300	1200	n/a	n/a	n/a	n/a	n/a

Table A3: Processing parameters and results of geometrical characterisation for Inconel 625 powder single track deposition

S/N	Laser power (kW)	Traverse speed (mm min^{-1})	Powder feed rate (mm min^{-1})	Energy/ per unit length of track (J mm^{-1})	Height (mm)	Width (mm)	Cross-sectional area (mm^2)	Aspect ratio	Contact angle (degrees)
1	1.8	100	10	1080	2.0	3.9	5.4	1.9	92
2	1.8	100	20	1080	3.2	4.3	10.9	1.3	113
3	1.8	100	30	1080	3.3	4.7	12.7	1.4	116
4	1.8	200	10	540	1.1	3.7	2.6	3.4	60
5	1.8	200	20	540	1.6	3.5	4.4	2.2	85
6	1.8	200	30	540	2.2	3.8	6.3	1.7	98
7	1.8	300	10	360	0.7	3.4	1.7	4.5	47
8	1.8	300	20	360	1.1	3.5	2.5	3.2	63
9	1.8	300	30	360	1.5	3.6	3.8	2.4	79
10	1.6	100	10	960	1.9	3.9	5.2	2.1	88
11	1.6	100	20	960	2.6	4	7.9	1.5	106
12	1.6	100	30	960	3.2	4.2	9.8	1.3	113
13	1.6	200	10	480	1.0	3.5	2.3	3.5	59
14	1.6	200	20	480	1.5	3.6	3.8	2.4	80
15	1.6	200	30	480	1.9	3.4	4.9	1.8	95
16	1.6	300	10	320	0.7	3.6	1.5	5.2	42
17	1.6	300	20	320	1.0	3.4	2.3	3.2	63
18	1.6	300	30	320	1.3	3.3	3.2	2.5	78
19	1.4	100	10	840	1.8	3.6	4.7	2.1	88
20	1.4	100	20	840	2.4	3.7	6.8	1.5	106
21	1.4	100	30	840	2.9	4.2	8.3	1.5	107
22	1.4	200	10	420	1.0	3.5	2.2	3.6	58
23	1.4	200	20	420	1.5	3.4	3.5	2.2	83
24	1.4	200	30	420	1.7	3.4	4.4	2.0	92
25	1.4	300	10	280	0.7	3.3	1.5	5.0	44
26	1.4	300	20	280	1.0	3.3	2.2	3.2	64
27	1.4	300	30	280	1.3	3.3	2.9	2.6	76
28	1.2	100	10	720	1.6	3.4	3.9	2.2	85
29	1.2	100	20	720	2.2	3.4	5.5	1.5	105
30	1.2	100	30	720	2.8	3.8	7.5	1.4	110
31	1.2	200	10	360	0.9	3.1	1.9	3.5	59
32	1.2	200	20	360	1.3	3.2	2.9	2.4	79
33	1.2	200	30	360	1.7	3.2	4.0	1.8	95
34	1.2	300	10	240	0.6	3.0	1.2	5.1	43
35	1.2	300	20	240	0.9	3.1	1.8	3.4	61

S/N	Laser power (kW)	Traverse speed (mm min^{-1})	Powder feed rate (mm min^{-1})	Energy/ per unit length of track (J mm^{-1})	Height (mm)	Width (mm)	Cross-sectional area (mm^2)	Aspect ratio	Contact angle (degrees)
36	1.2	300	30	240	1.2	2.9	2.6	2.4	80
37	1	100	10	600	1.4	3.3	3.3	2.3	83
38	1	100	20	600	2.1	3.4	5.2	1.6	102
39	1	100	30	600	2.6	3.6	6.8	1.4	111
40	1	200	10	300	0.8	3.1	1.6	3.8	56
41	1	200	20	300	1.3	3.0	2.6	2.4	81
42	1	200	30	300	1.6	3.0	3.4	1.9	93
43	1	300	10	200	0.5	2.8	1.0	5.3	41
44	1	300	20	200	0.9	2.9	1.6	3.3	63
45	1	300	30	200	1.1	2.9	2.2	2.6	76

Table A4: Processing parameters and visual observation for Spherotene (WC/W_2C) powder-Inconel 625 wire composite single track deposition

S/N	Laser power (kW)	Transverse speed (mm min^{-1})	Wire feed rate (mm min^{-1})	Powder feed rate (g min^{-1})	Energy/ unit length (J mm^{-1})	Visual observation of the process
1	1.8	100	400	25	1080	Smooth wire flow
2	1.8	100	600	25	1080	Smooth wire flow
3	1.8	100	800	25	1080	Smooth wire flow
4	1.8	100	1000	25	1080	Stubbing may occur
5	1.8	100	1200	25	1080	Stubbing
6	1.8	200	400	25	540	Dripping may occur
7	1.8	200	600	25	540	Smooth wire flow
8	1.8	200	800	25	540	Smooth wire flow
9	1.8	200	1000	25	540	Stubbing may occur
10	1.8	200	1200	25	540	Stubbing
11	1.8	300	400	25	360	Dripping may occur
12	1.8	300	600	25	360	Smooth wire flow
13	1.8	300	800	25	360	Smooth wire flow
14	1.6	100	400	25	960	Smooth wire flow
15	1.6	100	600	25	960	Smooth wire flow
16	1.6	100	800	25	960	Smooth wire flow
17	1.6	100	1000	25	960	Stubbing
18	1.6	200	400	25	480	Dripping may occur
19	1.6	200	600	25	480	Smooth wire flow
20	1.6	200	800	25	480	Stubbing may occur
21	1.6	200	1000	25	480	Stubbing
22	1.6	300	400	25	320	Dripping may occur
23	1.6	300	600	25	320	Smooth wire flow
24	1.6	300	800	25	320	Stubbing may occur
25	1.4	100	400	25	840	Smooth wire flow
26	1.4	100	600	25	840	Smooth wire flow
27	1.4	100	800	25	840	Stubbing may occur
28	1.4	100	1000	25	840	Stubbing
29	1.4	200	400	25	420	Smooth wire flow
30	1.4	200	600	25	420	Smooth wire flow
31	1.4	200	800	25	420	Stubbing may occur
32	1.4	200	1000	25	420	Stubbing

S/N	Laser power (kW)	Transverse speed (mm min^{-1})	Wire feed rate (mm min^{-1})	Powder feed rate (g min^{-1})	Energy/ unit length (J mm^{-1})	Visual observation of the process
33	1.4	300	400	25	280	Dripping may occur
34	1.4	300	600	25	280	Smooth wire flow
35	1.4	300	800	25	280	Stubbing may occur
36	1.2	100	400	25	720	Smooth wire flow
37	1.2	100	600	25	720	Smooth wire flow
38	1.2	100	800	25	720	Stubbing
39	1.2	200	400	25	360	Smooth wire flow
40	1.2	200	600	25	360	Smooth wire flow
41	1.2	200	800	25	360	Stubbing
42	1.2	300	400	25	240	Smooth wire flow
43	1.2	300	600	25	240	Stubbing may occur
44	1.2	300	800	25	240	Stubbing
45	1.0	100	400	25	600	Smooth wire flow
46	1.0	100	600	25	600	Smooth wire flow
47	1.0	100	800	25	800	Stubbing
48	1.0	200	400	25	300	Smooth wire flow
49	1.0	200	600	25	300	Stubbing may occur
50	1.0	200	800	25	300	Stubbing
51	1.0	300	400	25	200	Smooth wire flow
52	1.0	300	600	25	200	Stubbing may occur
53	1.0	300	800	25	200	Stubbing

Table A5: Results of geometrical characterisation for Spherotene (WC/W_2C) powder-Inconel 625 wire composite single track deposition

S/N	Power (kW)	Traverse speed (mm min^{-1})	Wire feed rate (mm min^{-1})	Powder feed rate (g min^{-1})	Average height (mm)	Average width (mm)	Average cross-sectional area (mm^2)	Aspect ratio	Contact angle (degrees)
1	1.8	100	400	25	2.0	4.8	9.5	2.4	80
2	1.8	100	600	25	3.3	5.0	12.2	1.5	106
3	1.8	100	800	25	4.0	4.8	14.6	1.2	118
4	1.8	100	1000	25	4.4	4.9	16.7	1.1	122
5	1.8	100	1200	25	n/a	n/a	n/a	n/a	n/a
6	1.8	200	400	25	1.8	4.0	4.8	2.2	84
7	1.8	200	600	25	2.1	3.9	6.0	1.9	94
8	1.8	200	800	25	2.4	3.7	7.0	1.6	104
9	1.8	200	1000	25	2.8	3.6	8.0	1.3	115
10	1.8	200	1200	25	n/a	n/a	n/a	n/a	n/a
11	1.8	300	400	25	1.2	3.6	3.2	3.0	67
12	1.8	300	600	25	1.6	3.3	3.6	2.1	86
13	1.8	300	800	25	1.8	3.5	4.5	2.0	91
14	1.6	100	400	25	2.8	4.4	9.4	1.6	104
15	1.6	100	600	25	3.3	4.6	12.0	1.4	110
16	1.6	100	800	25	4.0	4.5	14.5	1.1	120
17	1.6	100	1000	25	n/a	n/a	n/a	n/a	n/a
18	1.6	200	400	25	1.8	3.8	4.7	2.1	87
19	1.6	200	600	25	2.1	3.5	6.0	1.7	100
20	1.6	200	800	25	2.4	3.6	6.9	1.5	106
21	1.6	200	1000	25	n/a	n/a	n/a	n/a	n/a
22	1.6	300	400	25	1.3	3.4	3.1	2.6	75
23	1.6	300	600	25	1.5	2.9	3.6	2.0	91
24	1.6	300	800	25	1.7	3.0	4.2	1.7	99
25	1.8	100	400	25	3.0	4.1	9.5	1.4	111
26	1.4	100	600	25	3.4	4.2	12.0	1.2	116
27	1.4	100	800	25	3.9	4.2	14.0	1.1	123
28	1.4	100	1000	25	n/a	n/a	n/a	n/a	n/a
29	1.4	200	400	25	1.8	3.5	4.5	1.9	92
30	1.4	200	600	25	2.1	3.2	5.8	1.5	107
31	1.4	200	800	25	2.4	3.2	6.8	1.3	113
32	1.4	200	1000	25	n/a	n/a	n/a	n/a	n/a
33	1.4	300	400	25	1.3	3.2	2.9	2.5	78
34	1.4	300	600	25	1.5	2.9	3.4	1.9	93
35	1.4	300	800	25	1.9	2.6	4.0	1.4	110

S/N	Power (kW)	Traverse speed (mm min^{-1})	Wire feed rate (mm min^{-1})	Powder feed rate (g min^{-1})	Average height (mm)	Average width (mm)	Average cross-sectional area (mm^2)	Aspect ratio	Contact angle (degrees)
36	1.2	100	400	25	2.7	3.9	9.0	1.5	107
37	1.2	100	600	25	3.2	4.1	11.6	1.3	115
38	1.2	100	800	25	n/a	n/a	n/a	n/a	n/a
39	1.2	200	400	25	1.6	3.2	4.2	1.9	92
40	1.2	200	600	25	2.1	3.1	5.7	1.5	107
41	1.2	200	800	25	n/a	n/a	n/a	n/a	n/a
42	1.2	300	400	25	1.3	2.9	2.7	2.2	85
43	1.2	300	600	25	1.6	2.4	3.2	1.5	104
44	1.2	300	800	25	n/a	n/a	n/a	n/a	n/a
45	1.0	100	400	25	2.7	3.5	8.5	1.3	114
46	1.0	100	600	25	3.3	3.6	10.7	1.1	123
47	1.0	100	800	25	n/a	n/a	n/a	n/a	n/a
48	1.0	200	400	25	1.7	2.7	4.0	1.7	101
49	1.0	200	600	25	2.4	2.8	4.8	1.2	119
50	1.0	200	800	25	n/a	n/a	n/a	n/a	n/a
51	1.0	300	400	25	1.4	2.2	2.6	1.6	102
52	1.0	300	600	25	2.1	2.2	3.0	1.0	125
53	1.0	300	800	25	n/a	n/a	n/a	n/a	n/a

APPENDIX B. ANOVA ANALYSIS OF DILUTION RATIO RESULTS

Table B1: Mean dilution ratio for the Inconel 625 wire tracks

S/N	Laser power (kW)	Traverse speed (mm min^{-1})	Wire feed rate (mm min^{-1})	Mean Fe content (wt. %)	Mean dilution ratio (%)	Square of dilution ratio
1	1.8	100	600	9	12	142
2	1.8	100	800	6	7	55
3	1.8	100	1000	3	5	21
4	1.8	200	600	18	21	438
5	1.8	200	800	8	10	102
6	1.8	200	1000	3	5	22
7	1.8	300	600	22	24	592
8	1.8	300	800	9	11	122
9	1.8	300	1000	5	6	40
10	1.6	100	600	7	9	76
11	1.6	100	800	2	3	10
12	1.6	100	1000	2	2	5
13	1.6	200	600	9	12	134
14	1.6	200	800	4	5	27
15	1.6	200	1000	2	3	10
16	1.6	300	600	13	16	244
17	1.6	300	800	5	6	41
18	1.6	300	1000	4	5	23
19	1.4	100	600	3	5	22
20	1.4	100	800	2	2	4
21	1.4	100	1000	1	1	2
22	1.4	200	600	4	6	36
23	1.4	200	800	2	3	8
24	1.4	200	1000	2	2	5
25	1.4	300	600	6	8	65
26	1.4	300	800	3	4	13
27	1.4	300	1000	2	2	6
Total					**195**	**2263**

4.1: Degrees of freedom (DOF)

$$\text{Total DOF}\left(D_T\right): = \text{Total number of trial conditions} - 1 = 27 - 1 = 26$$

$$\text{DOF for laser power } (D_P) := \text{Number of levels of } P - 1 = 3 - 1 = 2$$

$$\text{DOF for traverse speed } (D_V) = \text{Number of levels of } V - 1 = 3 - 1 = 2$$

$$\text{DOF for wire feed rate } (D_{WFR}) = \text{Number of levels of } WFR - 1 = 3 - 1 = 2$$

$$\text{DOF for error term } (D_{error}) = D_T - (D_P + D_V + D_{WFR}) = 26 - (2 + 2 + 2) = 20$$

4.2 Sum of squares total (SS)

Sum of squares total is a measure of the deviations of the experimental data from the overall mean value of the data.

$$\text{Sum of squares total } (S_T) = \sum_{i=1}^{n} \left(Y_i - \bar{Y} \right) = \sum_{i=1}^{n} Y_i^2 - \frac{T^2}{n} = 2263 - \frac{195^2}{27} = 855$$

$$\text{Sum of squares for laser power } (SS_P) = \frac{P_1^2}{N_{P_1}} + \frac{P_2^2}{N_{P_2}} + \frac{P_3^2}{N_{P_3}} - \frac{T^2}{n}$$

$$= \frac{(12+7+5+21+10+5+24+11+6)^2}{9} + \frac{(9+3+2+12+5+3+16+6+5)^2}{9} +$$

$$\frac{\left(5+2+1+6+3+2+8+4+2\right)^2}{9} - \frac{195^2}{27} = 260$$

$$\text{Sum of squares total for traverse speed } (SS_V) = \frac{V_1^2}{N_{V_1}} + \frac{V_2^2}{N_{V_2}} + \frac{V_3^2}{N_{V_3}} - \frac{T^2}{n} = 73$$

$$\text{Sum of squares total for wire feed rate } (SS_{WFR}) = \frac{WFR_1^2}{N_{WFR_1}} + \frac{WFR_2^2}{N_{WFR_2}} + \frac{WFR_3^2}{N_{WFR_3}} - \frac{T^2}{n} = 393$$

$$\text{Sum of squares total for error terms } (SS_{error}) = SS_T - (SS_P + SS_V + SS_{WFR}) = 855 - (260 + 73 + 393) = 129$$

4.3 Mean square (MS)

The mean square (i.e. variance) was determined by dividing the sum of squares total of each factor by the degrees of freedom of the factor.

$$\text{Mean square for laser power}\,(MS_P) = \frac{SS_P}{D_P} = \frac{260}{2} = 130$$

$$\text{Mean square for traverse speed}\,(MS_V) = \frac{SS_V}{D_V} = \frac{73}{2} = 37$$

$$\text{Mean square for wire feed rate}\,(MS_{WFR}) = \frac{SS_{WFR}}{D_{WFR}} = \frac{393}{2} = 197$$

$$\text{Mean square for error terms}\,(MS_{error}) = \frac{SS_{error}}{D_{error}} = \frac{129}{20} = 6.5$$

4.4 F value (Variance ratio)

It is the ratio of the mean square for a factor to the mean square corresponding to the error term.

$$\text{F value for laser power}\,(F_P) = \frac{MS_P}{MS_{error}} = \frac{130}{6.5} = 20$$

$$\text{F value for traverse speed}\,(F_V) = \frac{MS_V}{MS_{error}} = \frac{37}{6.5} = 5.7$$

$$\text{F value for wire feed rate}\,(F_{WFR}) = \frac{MS_{WFR}}{MS_{error}} = \frac{197}{6.5} = 30.3$$

Table B2: F-table $F_{0.05}(F_1, F_2)$, 95% confidence [105]

f_1 = number of degrees of freedom of numerator f_2 = number of degrees of freedom of denominator									
f_2 \ f_1	1	2	3	4	5	6	7	8	9
1	161.45	199.50	215.71	224.58	230.16	233.99	236.77	238.88	240.54
2	18.513	19.000	19.614	19.247	19.296	19.330	19.353	19.371	19.385
3	10.128	9.5521	9.2766	9.1172	9.0135	8.9406	8.8868	8.8452	8.8123
4	7.7086	6.9443	6.5914	6.3883	6.2560	6.1631	6.0942	6.0410	5.9988
5	6.6079	5.7861	5.4095	5.1922	5.0503	4.9503	4.8759	4.8183	4.7725
6	5.9874	5.1433	4.7571	4.5337	4.3874	4.2830	4.2066	4.1468	4.0990
7	5.5914	4.7374	4.3468	4.1203	3.9715	3.8660	3.7870	3.7257	3.6767
8	5.3177	4.4590	4.0662	3.8378	3.6875	3.5806	3.5005	3.4381	3.3881
9	5.1174	4.2565	3.8626	3.6331	3.4817	3.3738	3.2927	3.2296	3.1789
10	4.9646	4.1028	3.7083	3.4780	3.3258	3.2172	3.1355	3.0717	3.0204
11	4.8443	3.9823	3.5874	3.3567	3.2039	3.0946	3.0123	2.9480	2.8962
12	4.7472	3.8853	3.4903	3.2592	3.1059	2.9961	2.9134	2.8486	2.7964
13	4.6672	3.8056	3.4105	3.1791	3.0254	2.9153	2.8321	2.7669	2.7144
14	4.6001	3.7389	3.3439	3.1122	2.9582	2.8477	2.7642	2.6987	2.6458
15	4.5431	3.6823	3.2874	3.0556	2.9013	2.7905	2.7066	2.6408	2.5876
16	4.4940	3.6337	3.2389	3.0069	2.8524	2.7413	2.6572	2.5911	2.5377
17	4.4513	3.5915	3.1968	2.9647	2.8100	2.6987	2.6143	2.5480	2.4943
18	4.4139	3.5546	3.1599	2.9277	2.7729	2.6613	2.5767	2.5102	2.4563
19	4.3808	3.5219	3.1274	2.8951	2.7401	2.6283	2.5435	2.4768	2.4227
20	4.3513	3.4928	3.0984	2.8661	2.7109	2.5990	2.5140	2.4471	2.3928
21	4.3248	3.4668	3.0725	2.8401	2.6848	2.5727	2.4876	2.4205	2.3661
22	4.3009	3.4434	3.0491	2.8167	2.6613	2.5491	2.4638	2.3965	2.3419
23	4.2793	3.4221	3.0280	2.7955	2.6400	2.5277	2.4422	2.3748	2.3201
24	4.2597	3.4026	3.0088	2.7763	2.6207	2.5082	2.4226	2.3551	2.3002
25	4.2417	3.3852	2.9912	2.7587	2.6030	2.4904	2.4047	2.3371	2.2821

Table B3: Mean dilution ratio for the Inconel 625 powder tracks

S/N	Laser power (kW)	Traverse speed (mm min^{-1})	Powder feed rate (g min^{-1})	Mean Fe content (wt. %)	Mean dilution ratio (%)
1	1.8	100	10	35	34
2	1.8	100	20	20	23
3	1.8	100	30	13	16
4	1.8	200	10	41	38
5	1.8	200	20	31	31
6	1.8	200	30	21	23
7	1.8	300	10	48	41
8	1.8	300	20	36	35
9	1.8	300	30	26	28
10	1.6	100	10	31	31
11	1.6	100	20	18	21
12	1.6	100	30	12	15
13	1.6	200	10	40	37
14	1.6	200	20	29	30
15	1.6	200	30	19	22
16	1.6	300	10	44	40
17	1.6	300	20	31	32
18	1.6	300	30	25	27
19	1.4	100	10	29	30
20	1.4	100	20	17	20
21	1.4	100	30	11	14
22	1.4	200	10	38	36

S/N	Laser power (kW)	Traverse speed (mm min^{-1})	Powder feed rate (g min^{-1})	Mean Fe content (wt. %)	Mean dilution ratio (%)
23	1.4	200	20	26	28
24	1.4	200	30	17	20
25	1.4	300	10	41	38
26	1.4	300	20	28	29
27	1.4	300	30	24	26
28	1.2	100	10	25	27
29	1.2	100	20	16	19
30	1.2	100	30	10	13
31	1.2	200	10	33	33
32	1.2	200	20	25	27
33	1.2	200	30	14	17
34	1.2	300	10	39	37
35	1.2	300	20	27	29
36	1.2	300	30	21	15
37	1	100	10	21	24
38	1	100	20	12	15
39	1	100	30	8	10
40	1	200	10	27	29
41	1	200	20	20	22
42	1	200	30	10	13
43	1	300	10	33	33
44	1	300	20	22	25
45	1	300	30	17	20

APPENDIX C. RAW XRD SPECTRA INCLUDING THE JCPDS FILE NUMBER OF THE PHASES PRESENT

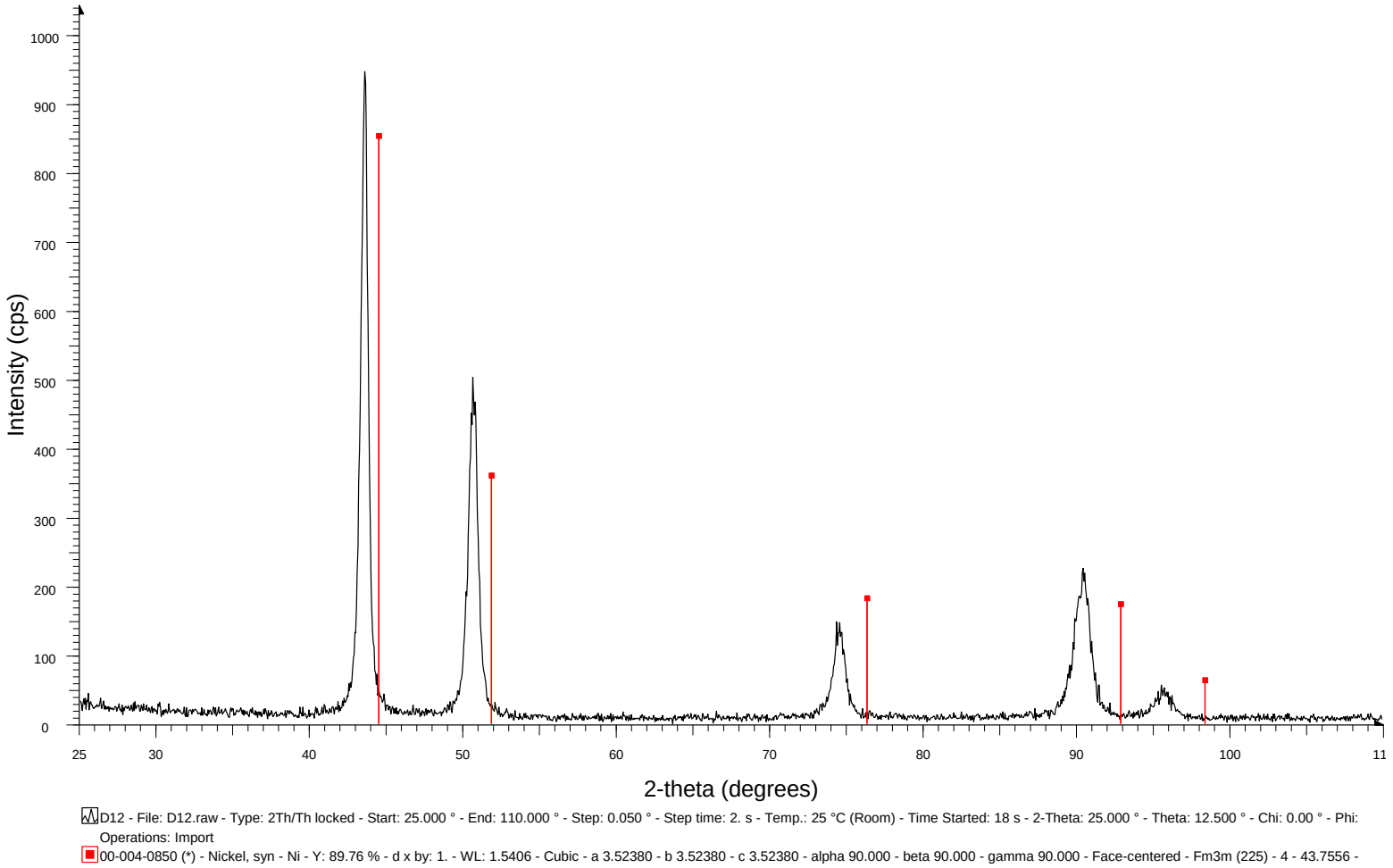

Figure 1: XRD Spectrum for Inconel 625 wire laser coating

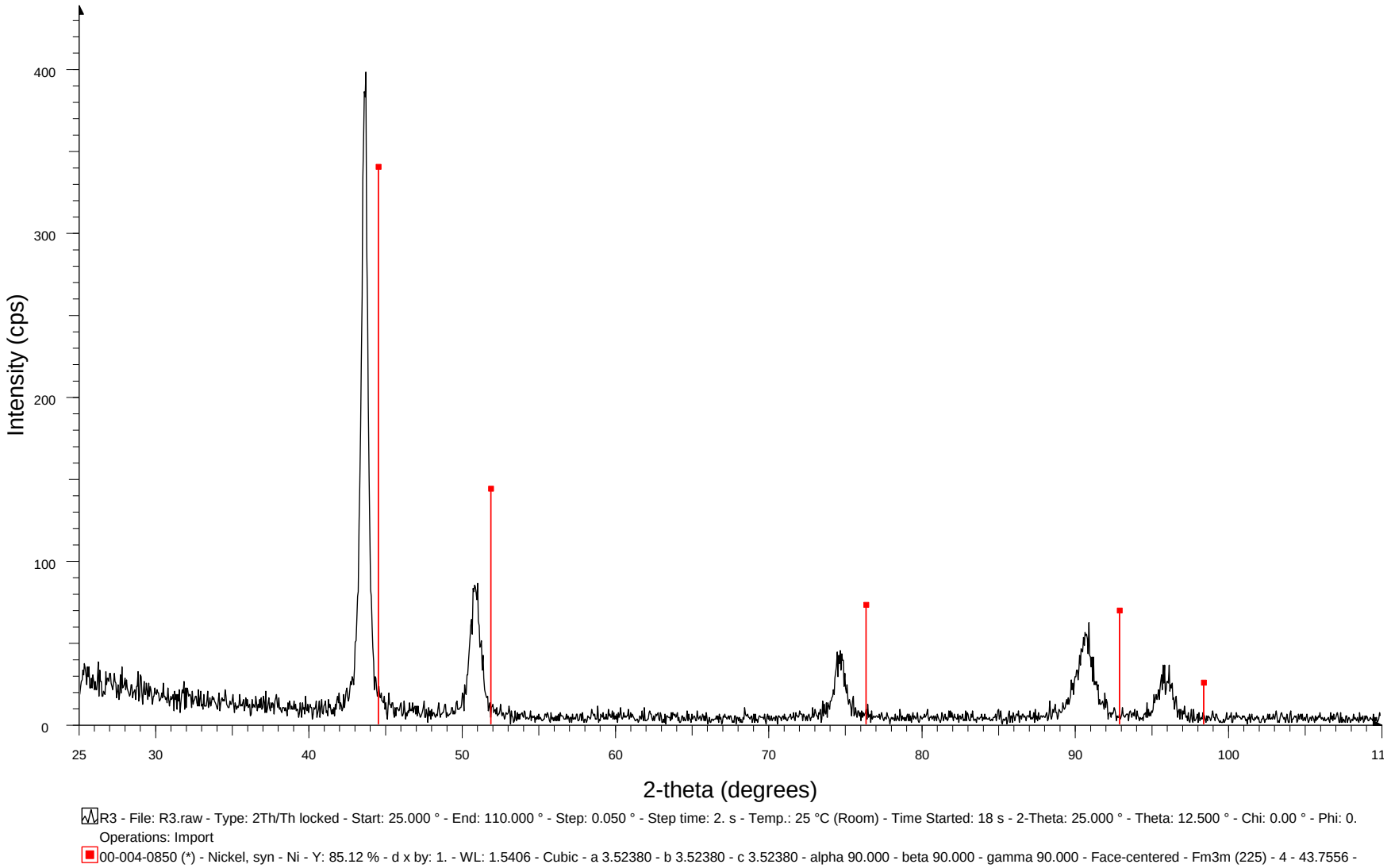

Figure 2: XRD Spectrum for Inconel 625 powder laser coating

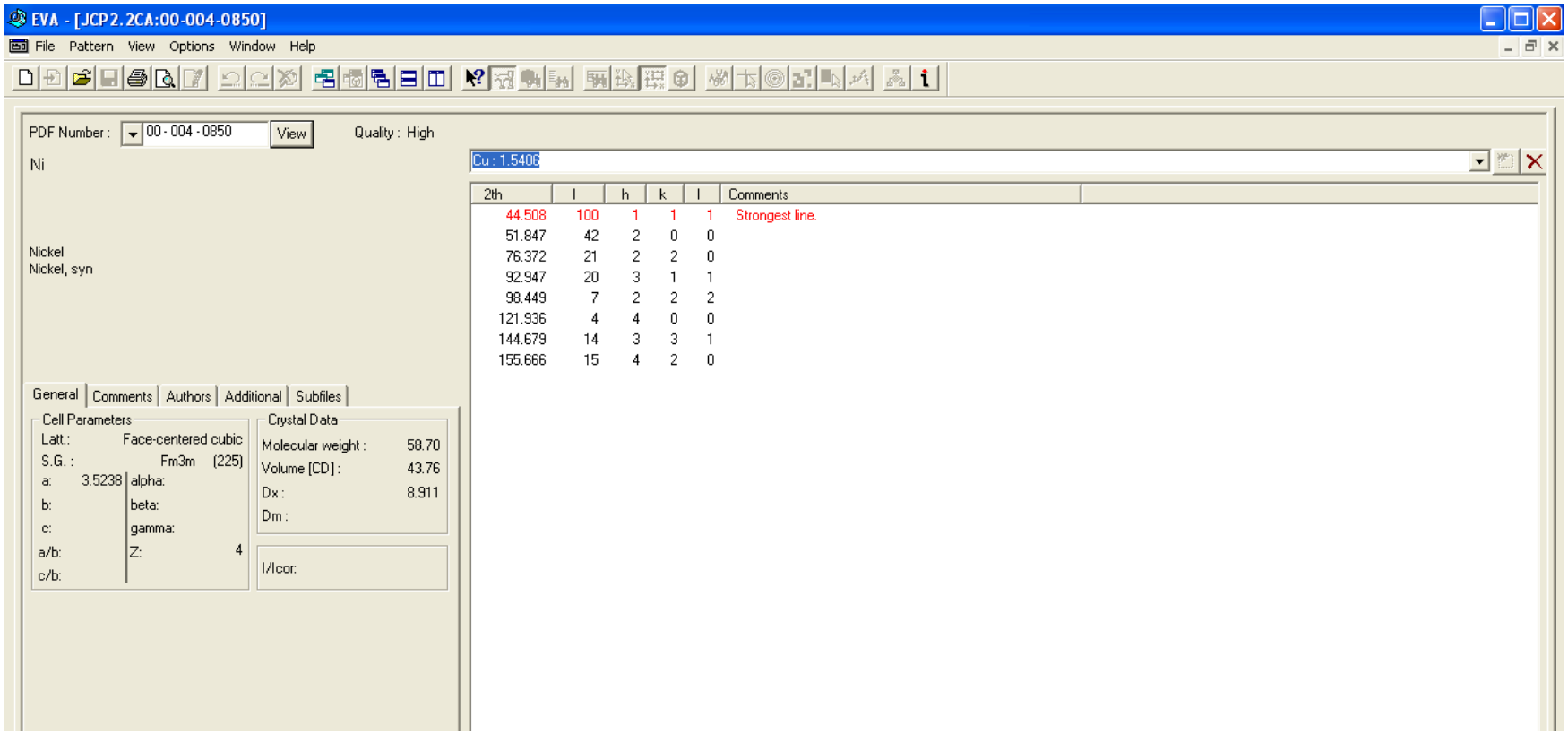

Figure 3: JCPDS data for pure Ni-phase

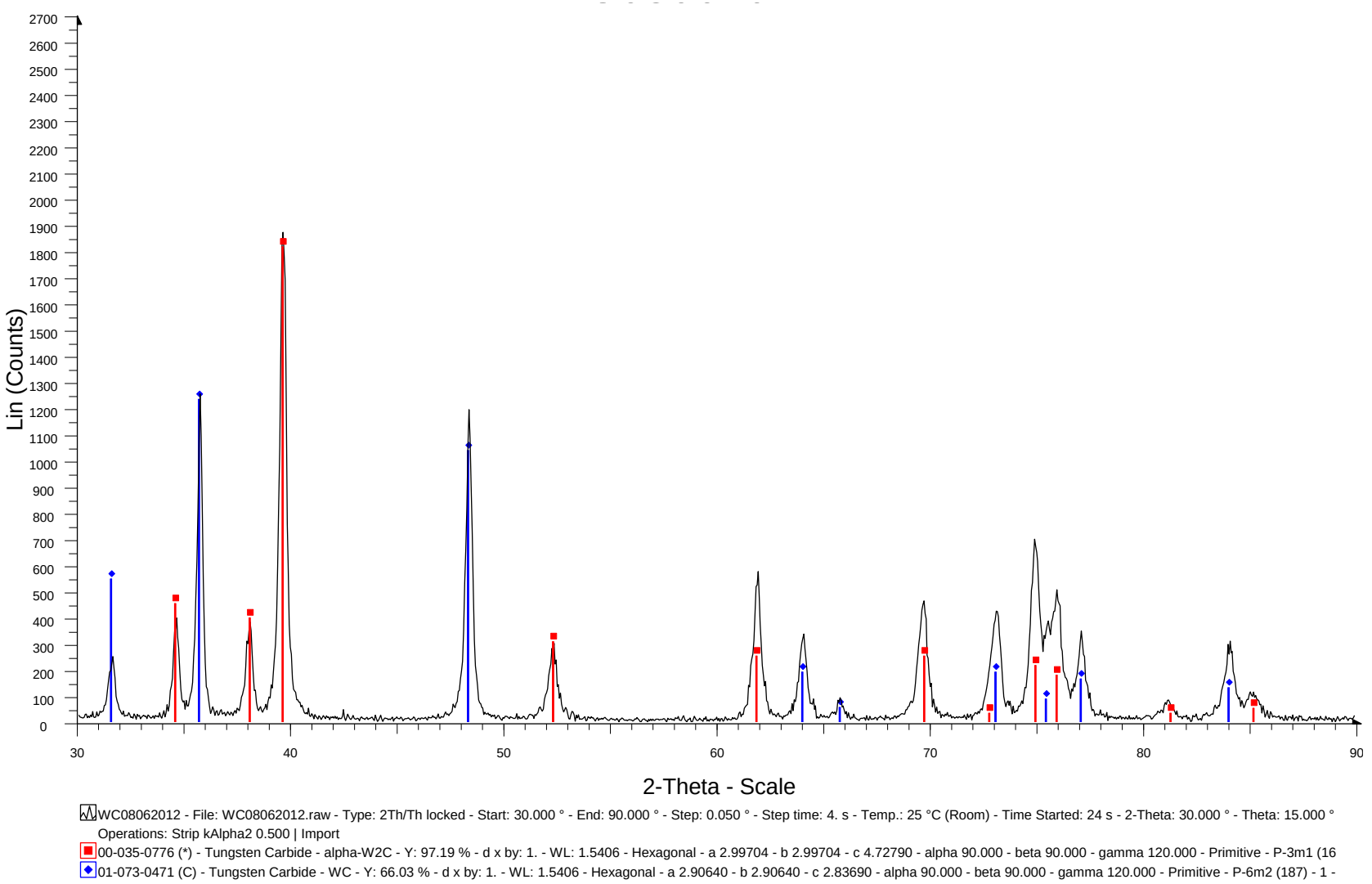

Figure 4: XRD spectrum for Spherotene (WC/W_2C) powder

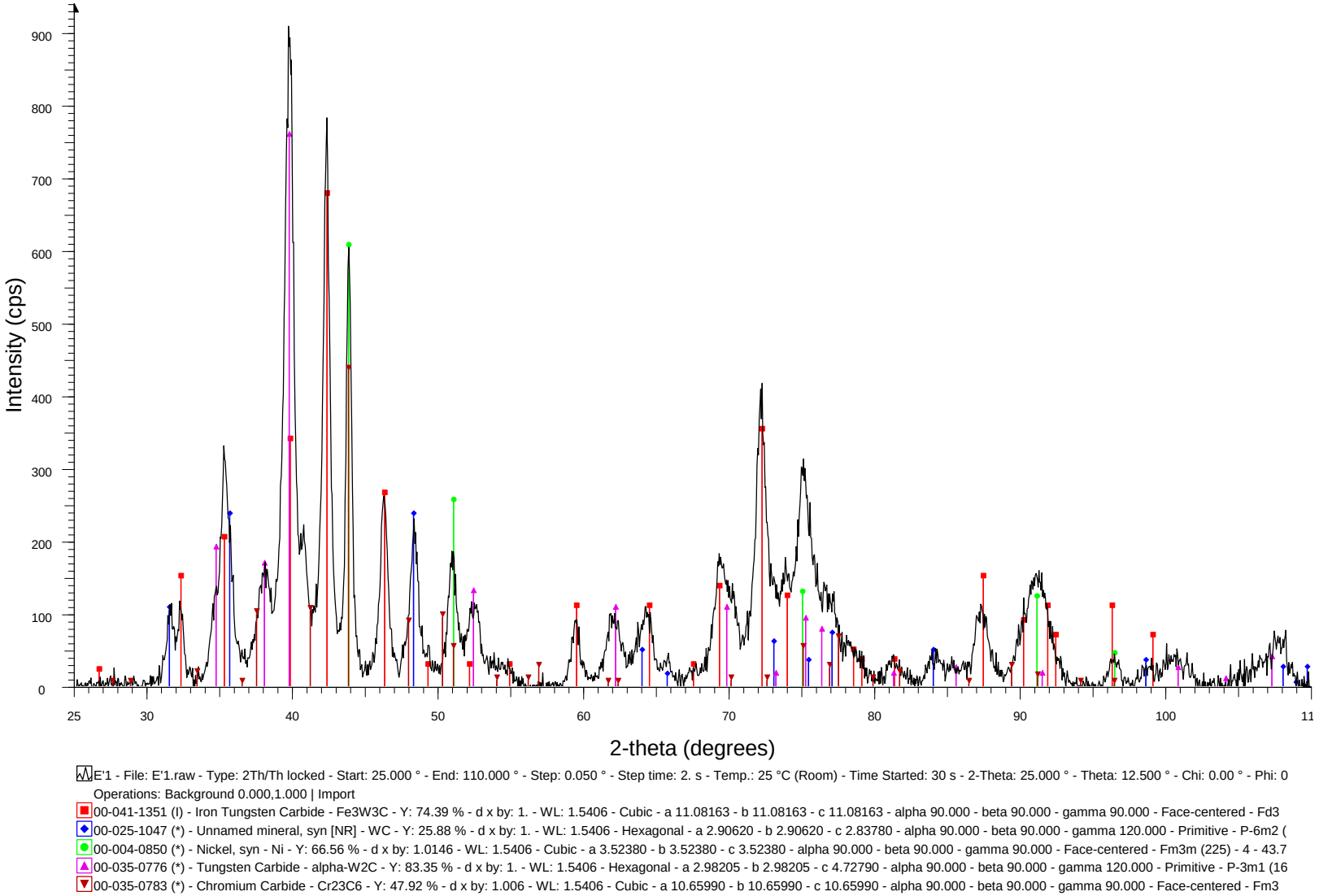

Figure 5: XRD Spectrum for Spherotene-Inconel 625 wire laser coating formed at 1080 J mm^{-1}. (This corresponds to W in Figure 5.14)

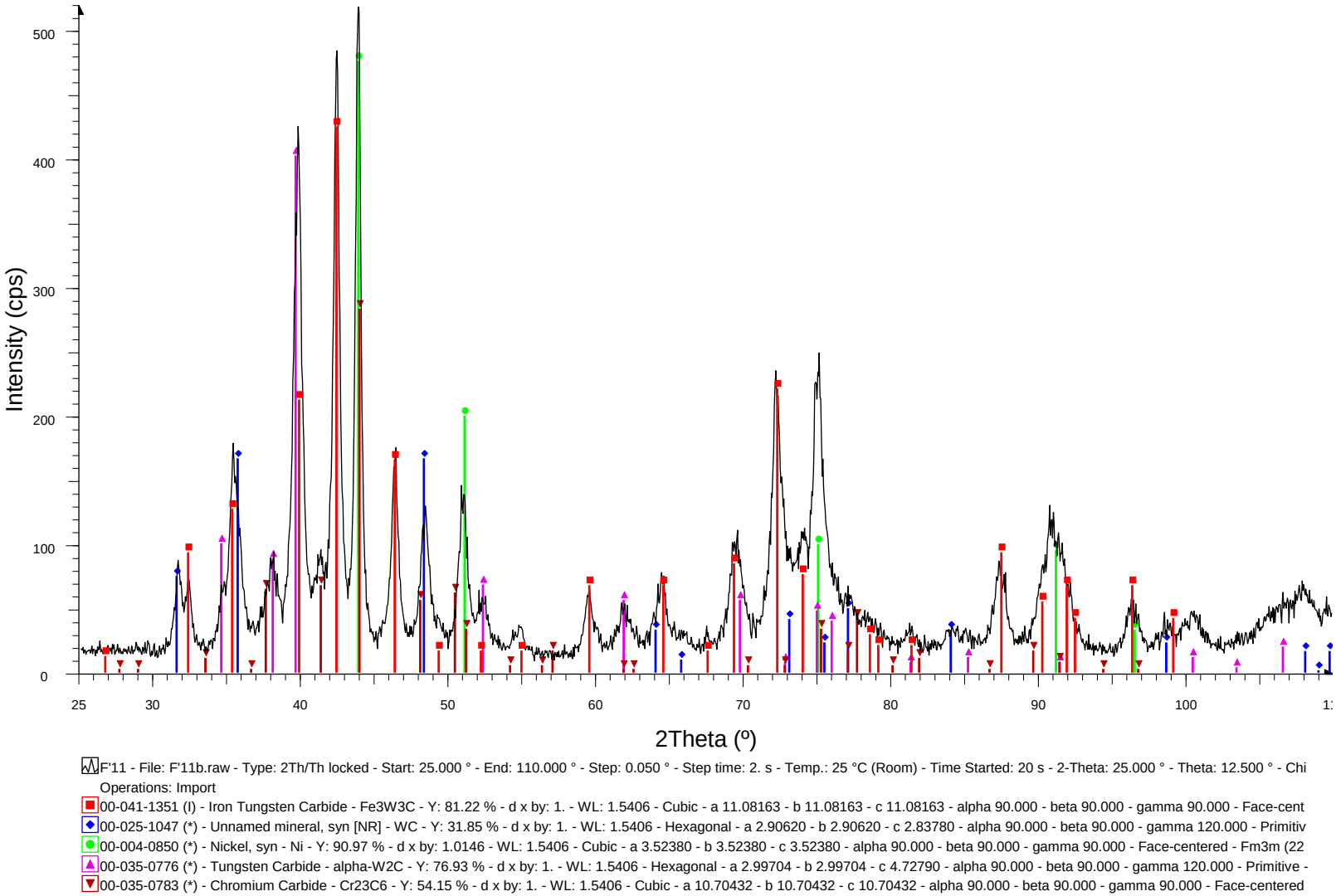

Figure 6: XRD Spectrum for Spherotene-Inconel 625 wire laser coating formed at 960 J mm^{-1}. (This corresponds to X in Figure 5.14)

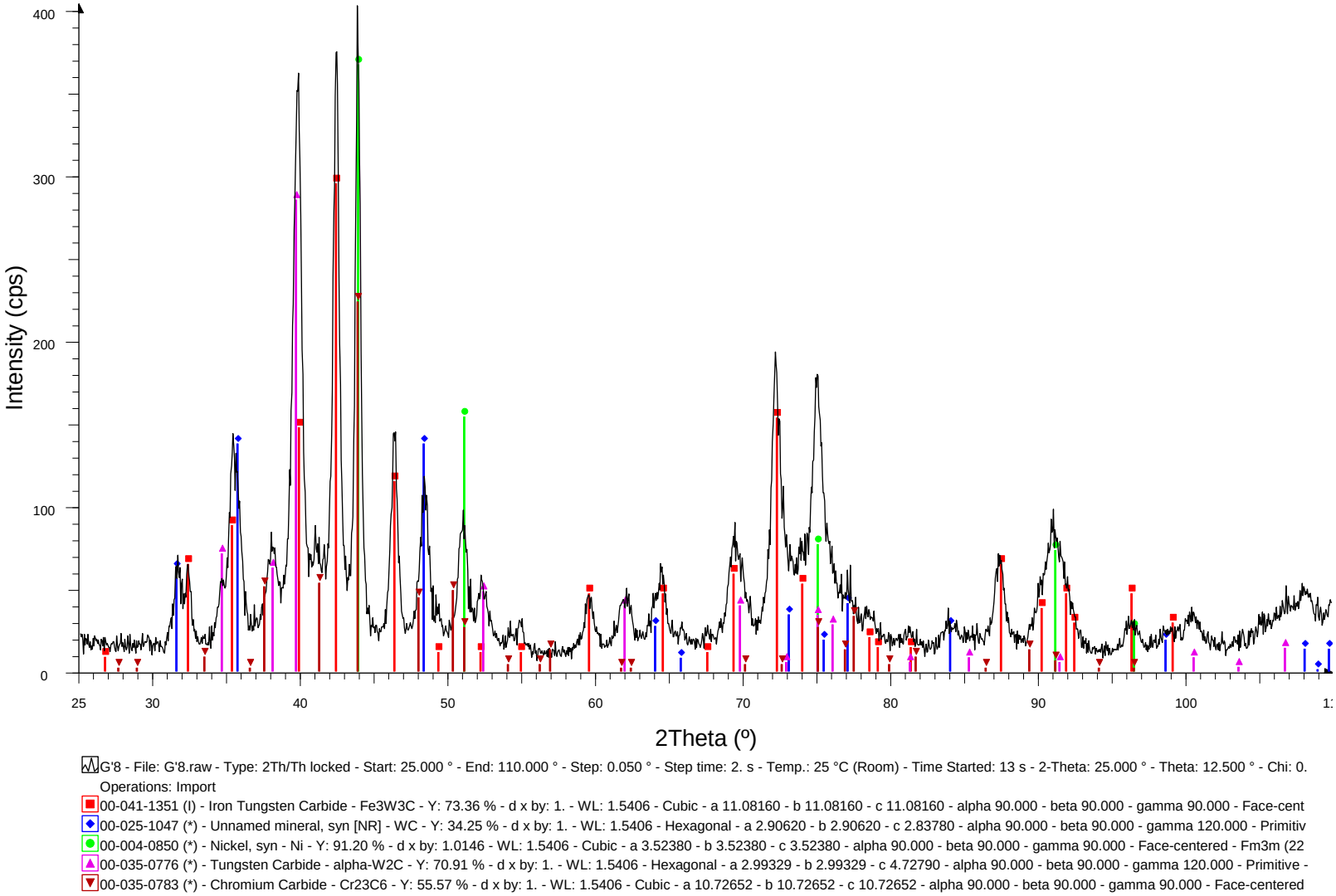

Figure 7: XRD Spectrum for Spherotene-Inconel 625 wire laser coating formed at 840 J mm^{-1}. (This corresponds to Y in Figure 5.14)

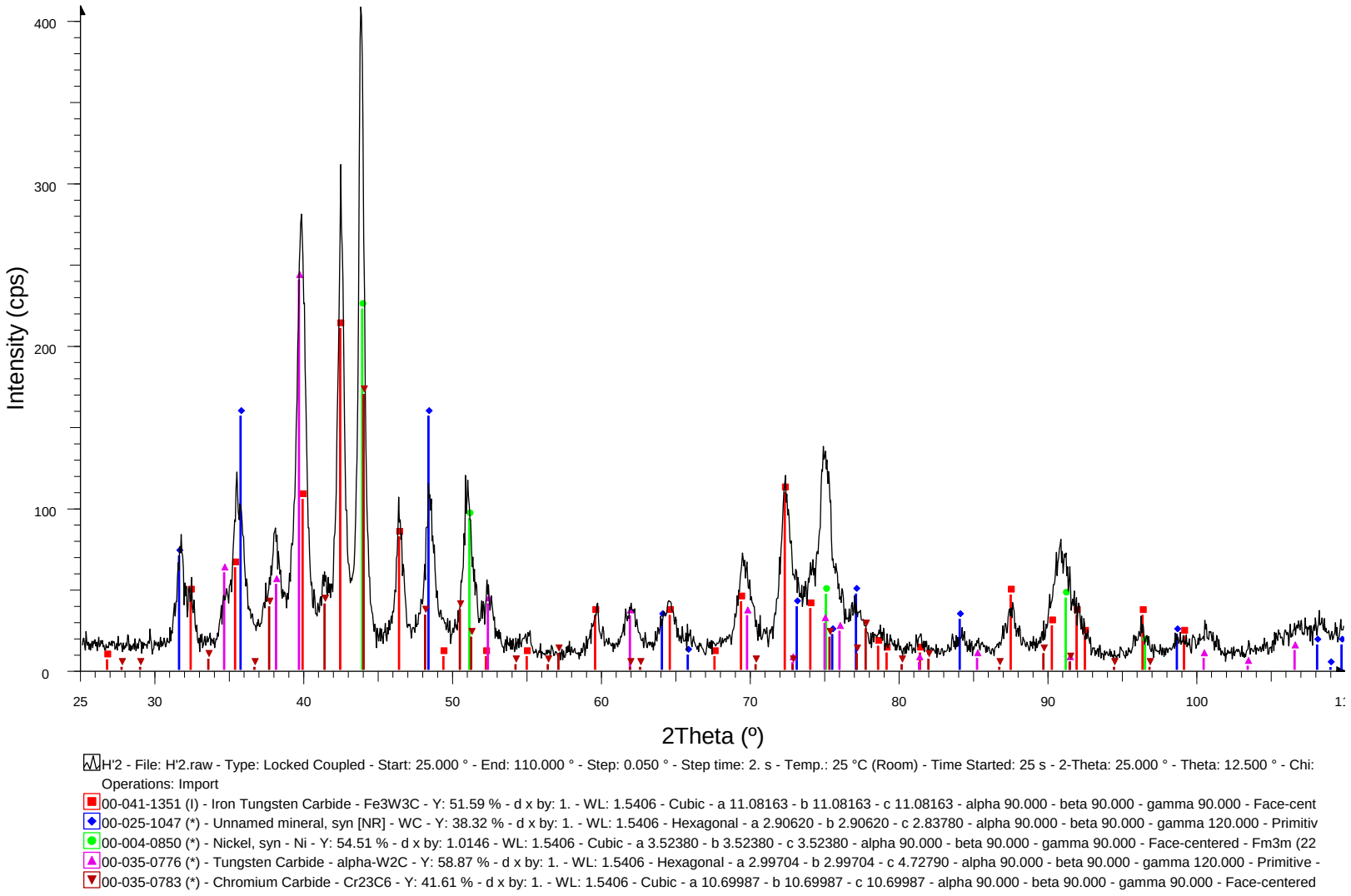

Figure 8: XRD Spectrum for Spherotene-Inconel 625 wire laser coating formed at 720 J mm^{-1}. (This corresponds to Z in Figure 5.14)

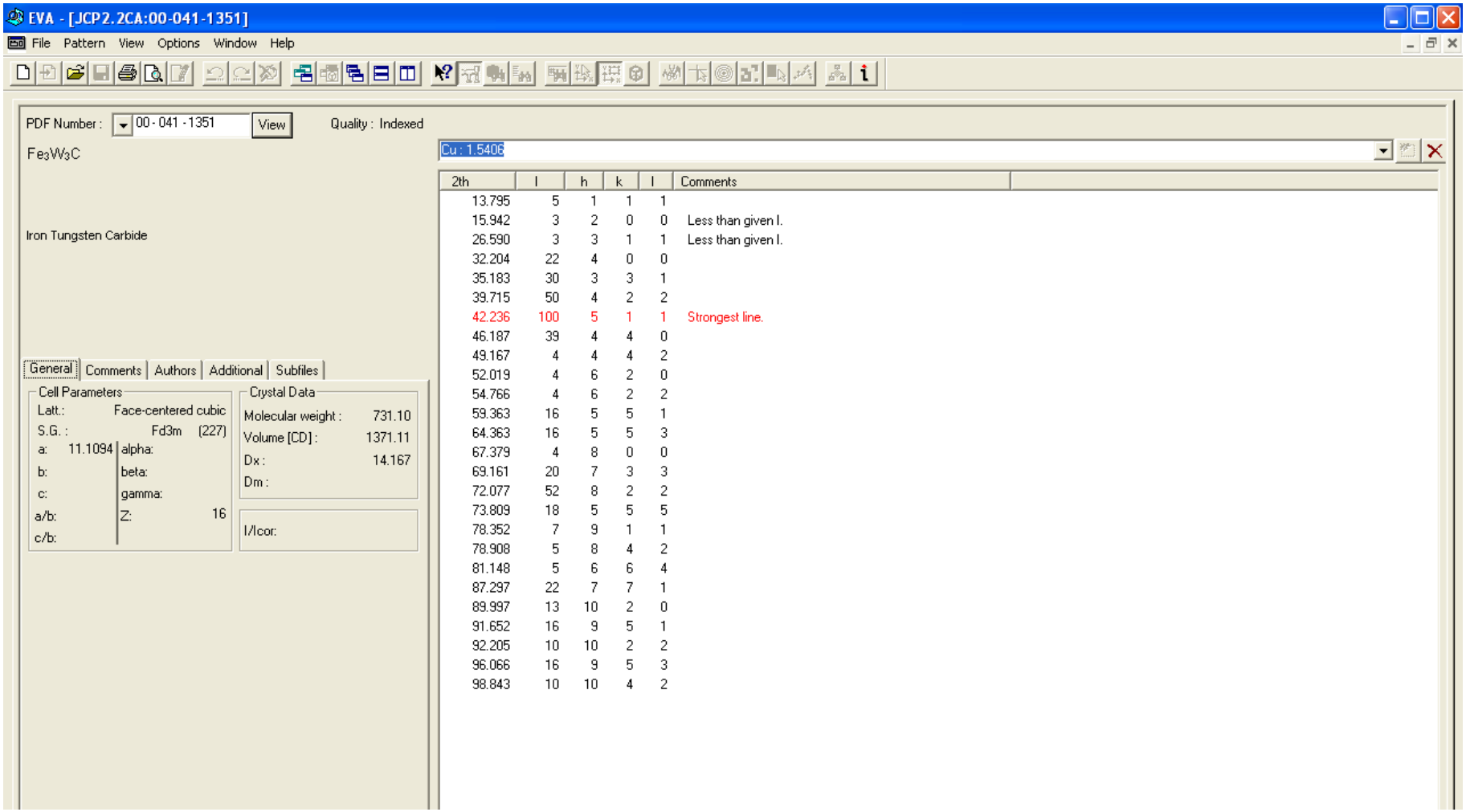

Figure 9: JCPDS data for Fe_3W_3C-phase

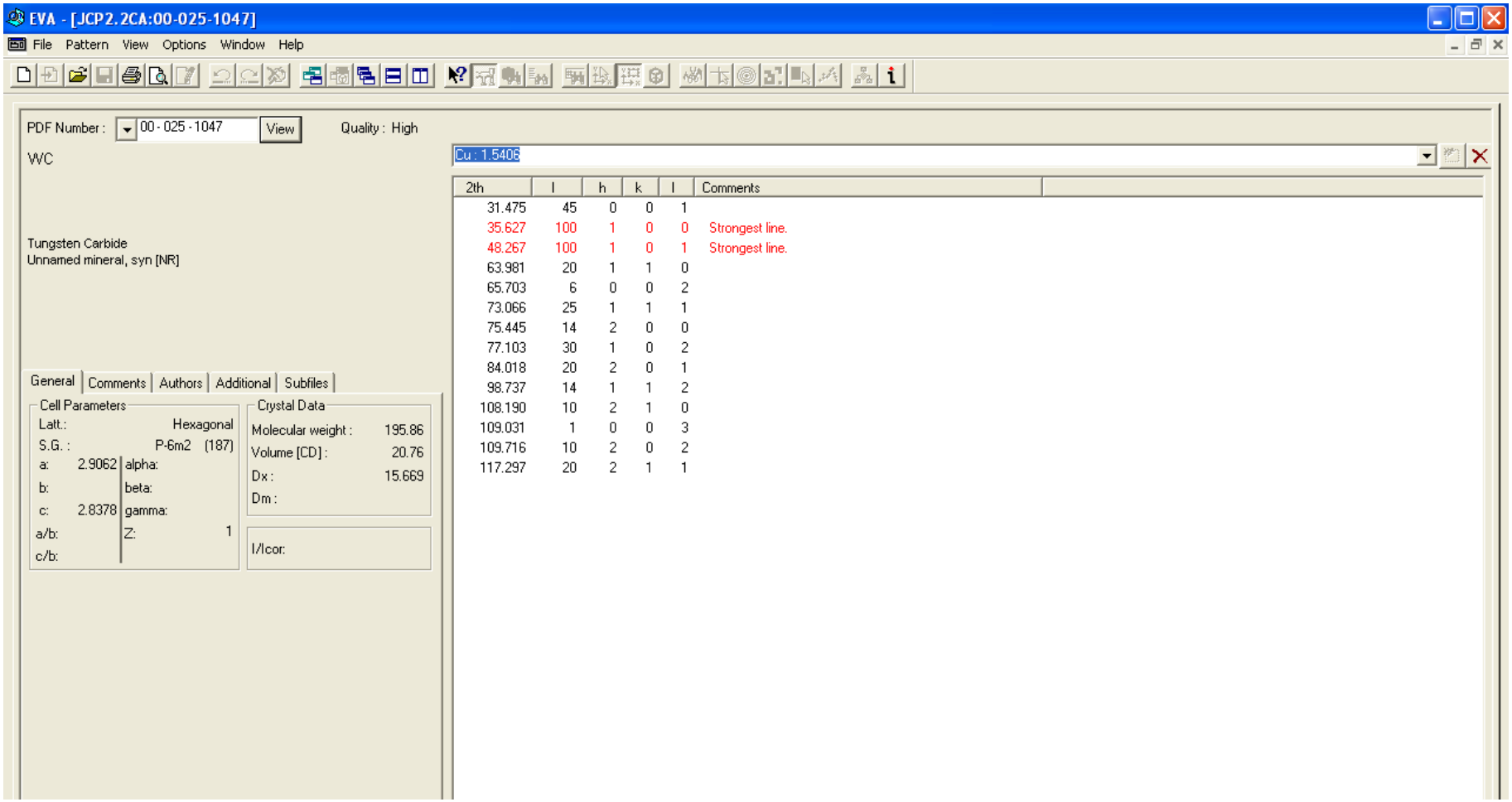

Figure 10: JCPDS data for WC-phase

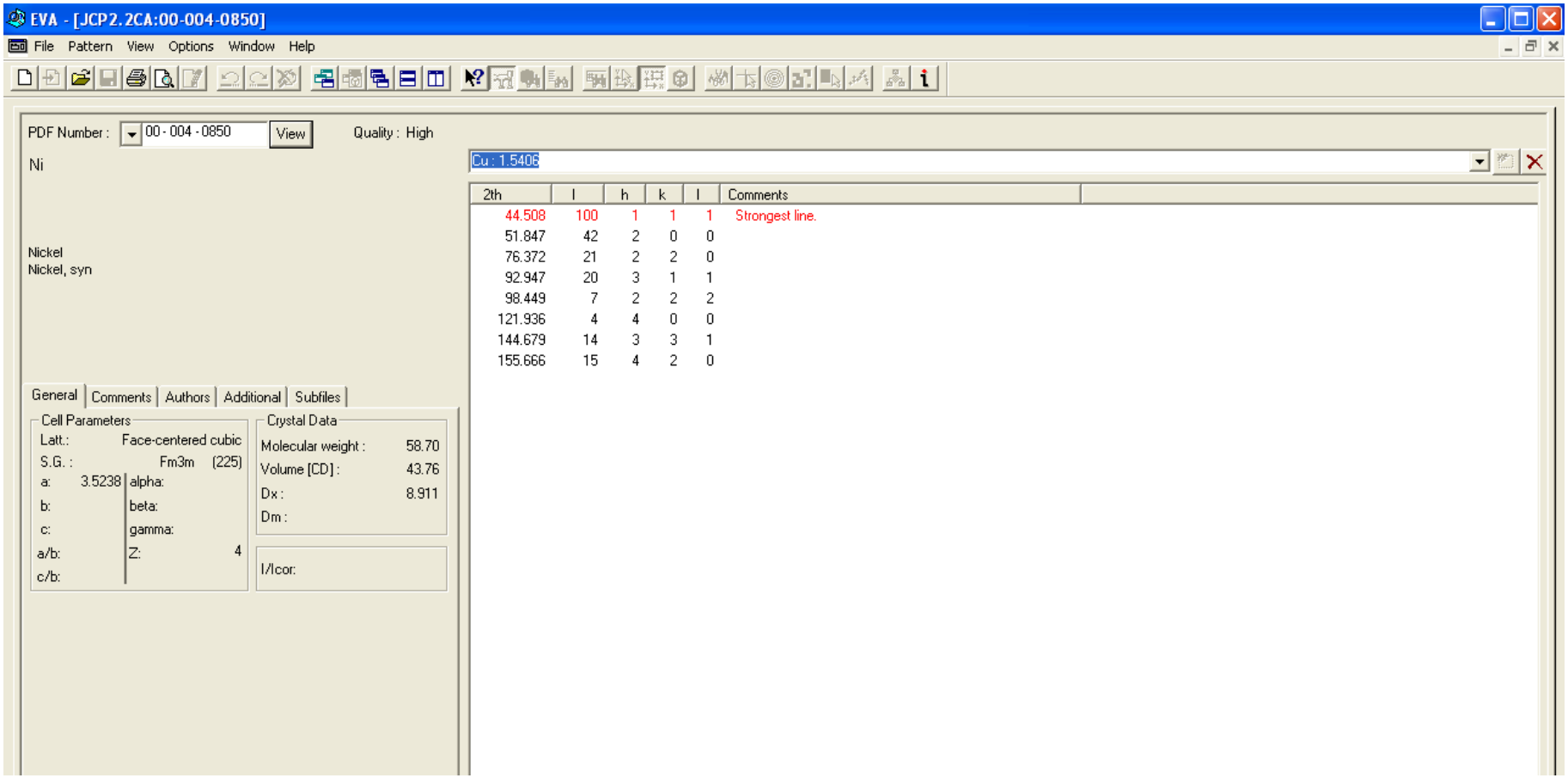

Figure 11: JCPDS data for FCC Ni-matrix-phase

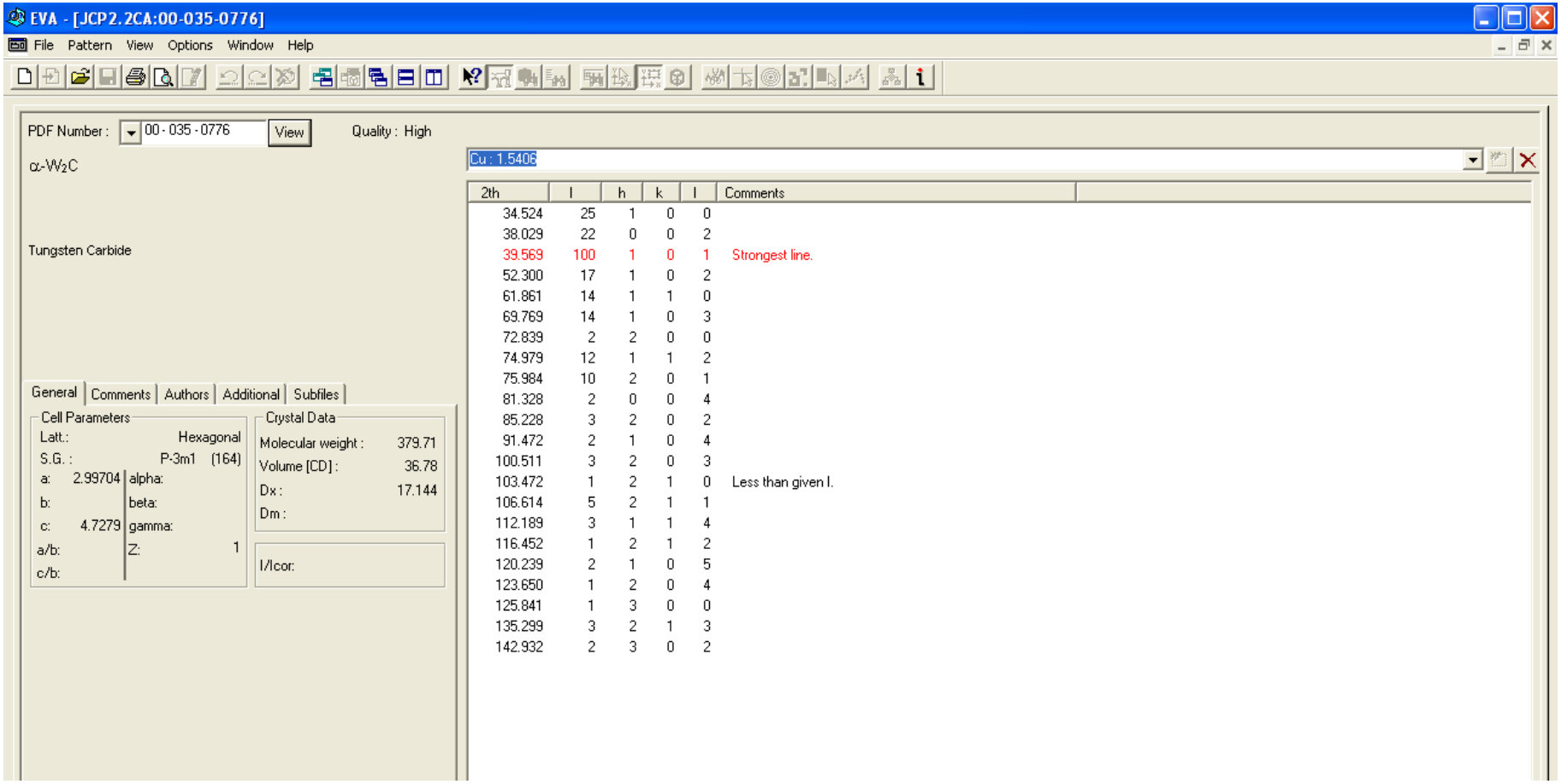

Figure 12: JCPDS data for W_2C-phase

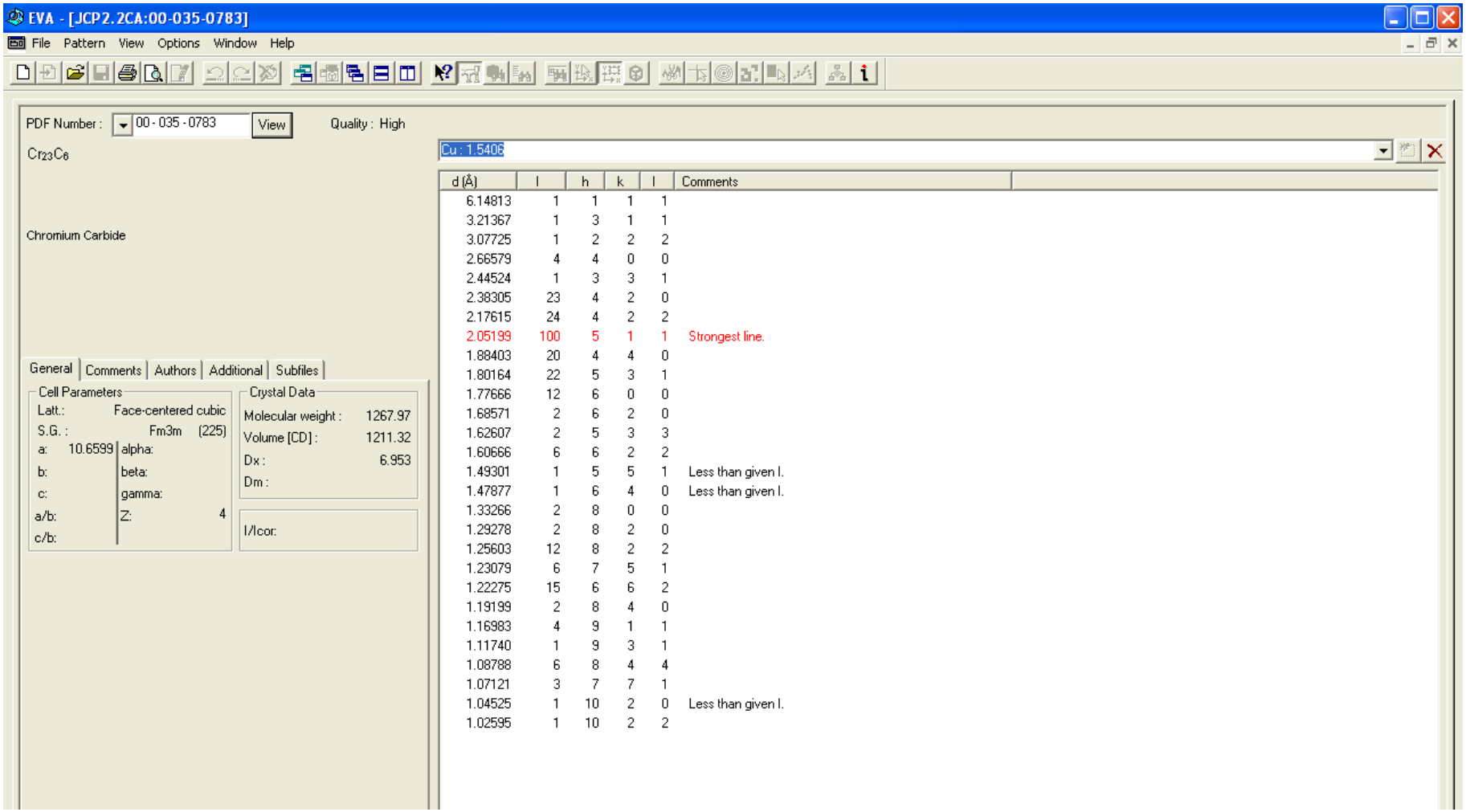

Figure 13: JCPDS data for $Cr_{23}C_6$-phase

APPENDIX D. TEST CERTIFICATE OF THE CHEMICAL ANALYSIS CONDUCTED FOR SPHEROTENE POWDER

LONDON & SCANDINAVIAN METALLURGICAL CO LIMITED
Fullerton Road, Rotherham, South Yorkshire S60 1DL, England

Sustainable Technology

ANALYTICAL SERVICES

Tel. 01709-833763
Fax. 01709-830391

UKAS TESTING 1091

CERTIFICATE OF ANALYSIS

Page No. 1 of 1

Material analysed has been supplied to LSM Analytical Services for3rd party analysis

To				
University of Nottingham **Department of Materials** **Engineering & Materials Design** **University Park** **University Park** **Nottingham** **NG7 2RD**	Certificate Date	**03/05/2012**	Certificate No. **3202376**	Lab Request No. **3203728**
	Date of Receipt	**19/04/2012**		
	Analysis Start Date	**26/04/2012**	Your Ref. / Order No. **ENG3907663**	
	Analysis End Date	**26/04/2012**		

Sample Details

No. of Samples Submitted : 1

FAO
Katy Voisey

This Certificate replaces any test report with Request Number **3203728** previously issued

Analysis Results

3209856
WC/W2C

W	92.24	%
TC	3.96	%

END OF REPORT

Analysis on 'As Received' Basis

Material: Non-Metallic

Comments / Remarks

Analysed using in - house documented procedures for technique(s) :

Leco XRF

Leco Nitrogen - Thermal Conductivity Leco Carbon, Sulphur, Oxygen - Infra-Red

Certificate Signed by

- ☐ **C. Jowitt** Laboratory Manager
- ☐ **P. W. Hurditch** Chief Chemist
- ☐ **B. Morales** Sales Development Manager
- ☐ **H Whitham** Sales Support Chemist

Signed

Please refer to www.lsmanalytical.com for our Conditions of Assay

Registered Office as above Registered in England No 345279 V.A.T. No. GB 789 6326 65

APPENDIX E. DETERMINATION OF THE WEIGHT FRACTIONS OF WC AND W_2C IN THE SPHEROTENE POWDER

First, the sum of the W (92.2 wt. %) and C (4.0 wt. %) composition in the Spherotene, as obtained via chemical analysis, is not equal to 100%. Therefore, the Spherotene composition was normalised as follows:

$$W = \frac{92.2}{96.2} \times 100 = 95.8 wt.\%$$

$$C = \frac{4.0}{96.2} \times 100 = 4.2 wt.\%$$

Note that the sum of the weight fractions of WC (F_{WC}) and W_2C (F_{W2C}) will be equal to 1

$$F_{WC} + F_{W_2C} = 1$$

Let x (g) be the amount of WC in 100g of Spherotene

Let y (g) be the amount of W_2C in 100g of Spherotene

Therefore by weight fraction,

$$x + y = 1$$

Recall that,

(1) The weight fraction of C in Spherotene is 4.2 wt. %

(2) The weight fraction of W in Spherotene is 95.8 wt.%

(3) The atomic mass of C is 12 and that of W is 184

Therefore, the weight fraction of C in x (g) of WC and y (g) of W_2C should be equal to 4.2 wt. %. Also, the weight fraction of W in x (g) of WC and y (g) of W_2C should be equal to 95.8 wt. %. This gives the simultaneous equations shown below:

$$x\left(\frac{12}{196}\right)+y\left(\frac{12}{380}\right)=4.2$$

$$x\left(\frac{184}{196}\right)+y\left(\frac{368}{380}\right)=95.8$$

Solving the simultaneous equation, we have x = 35.3g and y = 64.7g.

Therefore, we have 35.3g of WC and 64.7g of W_2C in 100g of Spherotene.

By weight fraction, there is 35% of WC and 65% of W_2C in the supplied Spherotene powder.

References

1. Chen, Z., Lim, L.C., Qian, M., *Laser cladding of WC-Ni composite.* Journal of Materials Processing Technology, 1996. **62**(4): p. 321-323.

2. Xu, P., Lin, C., Zhou, C., Yi, X., *Wear and corrosion resistance of laser cladding AISI 304 stainless steel/Al2O3 composite coatings.* Surface and Coatings Technology, 2014. **238**: p. 9-14.

3. Desale, G.R., Paul, C. P., Gandhi, B. K., Jain, S. C., *Erosion wear behavior of laser clad surfaces of low carbon austenitic steel.* Wear, 2009. **266**(9-10): p. 975-987.

4. Huang, Y., *Characterization of dilution action in laser-induction hybrid cladding.* Optics & Laser Technology, 2011. **43**(5): p. 965-973.

5. Sexton, L., Lavin, S., Byrne, G., Kennedy, A., *Laser cladding of aerospace materials.* Journal of Materials Processing Technology, 2002. **122**(1): p. 63-68.

6. Ion, J.C., *Laser Processing of Engineering Materials. Principles, Procedure and Industrial Applications*. 2005, Biddles Limited, King's Lynn: Oxford.

7. Canning, J., *Fibre lasers and related technologies.* Optics and Lasers in Engineering, 2006. **44**(7): p. 647-676.

8. Dominic, V., MacCormack, S., Waarts, R., Sanders, S., Bicknese, S., Dohle, R., Wolak, E., Yeh, P.S., Zucker, E., *110 W fibre laser.* Journal of Electronics Letters, 1999. **35**(14): p. 1158-1160.

9. Dowden, J. M., *The theory of laser materials processing*. 2009, Netherlands: Springer.

10. Liu, F., Lin, X., Leng H., Cao, J., Liu, Q., Huang, C., Huang., W, *Microstructural changes in a laser solid forming Inconel 718 superalloy thin wall in the deposition direction.* Optics & Laser Technology, 2013. **45**: p. 330-335.

11. Cooper, K.P., Slebodnick, P., Thomas, E. D., *Seawater corrosion behavior of laser surface modified Inconel 625 alloy.* Materials Science and Engineering A, 1996. **206**(1): p. 138-149.

12. Sims, C.T., Stollof, N. S., Hagel, W.C., *The Superalloys*. First ed. 1987, New York: A Wiley-Interscience Publication. 27-131.

13. Al-fadhli, H.Y., Stokes, J., Hashmi, M. S. J., Yilbas, B. S., *The erosion-corrosion behaviour of high velocity oxy-fuel (HVOF) thermally sprayed Inconel-625 coatings on different metallic surfaces.* Surface and Coatings Technology, 2006. **200**(20-21): p. 5782-5788.

14. Pflueger, S. *Laser cladding with direct diode lasers* 2009 8th December, 2013 [cited 2013 08-12-2013]; Available from: http://www.optoiq.com/index/lasers-for-manufacturing/display/ils-article-display/articles/optoiq2/lasers-for_manufacturing/laser-surface_treatment/laser-cladding_/2010/3/laser-cladding-with-direct-diode-lasers.html.

15. Xu, J.S., Zhang, X.C., Xuan, F.Z., Wang, Z.D., Tu, S.T. , *Microstructure and sliding wear resistance of laser cladded WC/Ni composite coatings with different contents of WC carticle.* Journal of Materials Engineering and Performance, 2011.

16. Tobar, M.J., Álvarez, C., Amado, J. M., Rodríguez, G., Yáñez, A., *Morphology and characterization of laser clad composite NiCrBSi–WC coatings on stainless steel.* Surface and Coatings Technology, 2006. **200**(22–23): p. 6313-6317.

17. Liu, Z., Cabrero, J., Niang, S., Al-Taha, Z. Y., *Improving corrosion and wear performance of HVOF-sprayed Inconel 625 and WC-Inconel 625 coatings by high power diode laser treatments.* Surface and Coatings Technology, 2007. **201**(16-17): p. 7149-7158.

18. Zhou, S., Dai, X., Zeng, X., *Effects of processing parameters on structure of Ni-based WC composite coatings during laser induction hybrid rapid cladding.* Applied Surface Science, 2009. **255**(20): p. 8494-8500.

19. Zhou, S., Huang, Y., Zeng, X., Hu, Q., *Microstructure characteristics of Ni-based WC composite coatings by laser induction hybrid rapid cladding.* Materials Science and Engineering: A, 2008. **480**(1-2): p. 564-572.

20. Zeng, X., Zhu, B., Tao, Z., Cui, K., *Analysis of energy conditions for laser cladding ceramic-metal composite coatings.* Surface and Coatings Technology, 1996. **79**(1–3): p. 162-169.

21. Amado, J. M., Tobar, M. J., Alvarez, J. C., Lamas, J., Yáñez, A., *Laser cladding of tungsten carbides (Spherotene®) hardfacing alloys for the mining and mineral industry.* Applied Surface Science, 2009. **255**(10): p. 5553-5556.

22. Rüdiger, P. *Encyclopedia of Laser Physics and Technology*. 2008 [cited 2011 14th January, 2011]; Available from: http://www.rp-photonics.com/lasers.html.

23. *Optoelectronics Research Centre*. [cited 2011 14th January, 2011]; Available from: http://www.orc.soton.ac.uk/61.html#.

24. Westchler, M. *How laser works*. How stuffs work [cited 2011 15th January, 2011]; Available from: http://www.howstuffworks.com/laser.htm/printable.

25. Santos, E.C., Shiomi, M., Osakada, K., Laoui, T., *Rapid manufacturing of metal components by laser forming.* International Journal of Machine Tools and Manufacture, 2006. **46**(12-13): p. 1459-1468.

26. Tellez, A.M., *Fibre Laser Metal Deposition with Wire: Parameters Study and Temperature Control*, PhD Thesis, *Department of Mechanical, Materials and Manufacturing Engineering*, University of Nottingham: Nottingham. 2010 p.1-222.

27. *Metals Handbook*. 10th ed. Vol. 1 & 2. ASM Inetrnational.

28. Reed, R.C., *The superalloys Fundamentals and Apllications*. 2006, Cambridge, UK: Cambridge University Press.

29. Donachie, M., Donachie, J., *Superalloys. A Technical Guide*. 2002, ASM international: USA.

30. Sims, T., Stoloff, N. S., Hagel, W.C., *Superalloys II: High-temperature materials for aerospace and industrial power*. 1987, New York, USA: Wiley.

31. Durand-Charre, M., *The Microstructure of Superalloys*. 1997: CRC Press.

32. Ahmed, N., *Characterisation of different forms of Inconel 625 for determining the effects of microstructural modifications on electrochemical behaviour*, PhD thesis, *Department of Mechanical, Materials and Manufacturing Engineering*, University of Nottingham. 2008: p. 156-192

33. *Inconel 625* Specification*. 2011 [cited 2011 15th January, 2011]; Available from: http://www.alloywire.com/inconel_alloy_625.html.

34. Dinda, G.P., Dasgupta, A.K., Mazumder, J., *Laser aided direct metal deposition of Inconel 625 superalloy: Microstructural evolution and thermal stability*. Materials Science and Engineering: A, 2009. **509**(1-2): p. 98-104.

35. Paul, C.P., Ganesh, P., Mishra, S. K., Bhargava, P., Negi, J., Nath, A. K., *Investigating laser rapid manufacturing for Inconel-625 components.* Optics & Laser Technology, 2007. **39**(4): p. 800-805.

36. *Inconel 625 – Composition, Properties and Applications of Inconel 625 Nickel-Chromium-Molybdenum Alloy by Alloy Wire International*. [cited 2011 15th January, 2011]; Available from: http://www.azom.com/Details.asp?ArticleID=4196.

37. Kim, H.I., Park, H.S., Koo, J.M., Yang, S.H., kim, M.Y., Seok, C.S., *Welding Characteristics Evaluation of GMAW and laser Cladding for the Gas Turbine 1st Blade*. Key Engineering Materials, 2007. **353-358**(2007): p. 519-522.

38. Floreen, S., Fuchs, G. E., Yang, W. J., *The metallurgy of Alloy 615.* The Minerals, Metals and Materials Society, 1994: p. 13-37.

39. Cieslak, M.J., *The welding and solidification metallurgy of Alloy 625*, in *68th annual AWS meeting*. 1991, Welding Research Supplement: Chicago. p. 49s-56s.

40. Parimia, L.L., Ravi, G. A., Clark, D., Attallah, M. M. , *Microstructural and texture development in direct laser fabricated IN718.* Journal of Materials Characterization, 2014. **89**: p. 102-111.

41. DuPont, J. N., *Solidification of an Alloy 625 weld overlay.* Metallurgical and Materials Transactions A, 1996. **27A**: p. 3612-3620.

42. Rombouts, M., Maes, G., Mertens, M., Hendrix, W., *Laser metal deposition of Inconel 625: Microstructure and Mechanical properties.* Journal of Laser Applications, 2012. **24**(5).

43. Lippold, J. C., *Recent developments in weldability testing for advanced materials.* ASM International. Joining of Advanced and Specialty Materials VII, 2005.

44. Lin, W., Lippold, J.C., Baeslack III, W., A., *An evaluation of heat-affected zone liquation cracking susceptibility, part I: Development of a method for quantification.* Welding Journal, 1993: p. 135-153.

45. Young, G. A., Capobianco, T. E., Penik, M. A. , Morris, B. W., Mcgee, J. J. , *The mechanism of ductility dip cracking in nickel-chromium alloys.* Welding Journal, 2008. **87**: p. 31-43.

46. Rowe, M. D., *Ranking the resistance of wrought superalloys to strain-age cracking.* Welding Journal, 2006: p. 27-34.

47. Lehockey, E. M., Palumbo, G., Lin, P., *Improving the Weldability and Service Performance of Nickel- and Iron-Based Superalloys by Grain Boundary Engineering.* Journal of Metallurgical and Materials Transactions A, 1998. **29A**(1998): p. 3069-3079.

48. Burakowski, T., Wierzchon, T., *Surface engineering of metals: Principles, equipment, technologies*. 1999, USA: CRC press.

49. Costa, L., Vilar R., , *Laser powder deposition.* Rapid Prototypying, 2009. **15**(4): p. 264-279.

50. Alimardani, M., Fallah, V., Khajepour, A., Toyserkani, E., *The effect of localized dynamic surface preheating in laser cladding of Stellite 1.* Surface and Coatings Technology, 2010. **204**(23): p. 3911-3919.

51. Costa L., Villar, R., Reti T., Deus, A. M., A *Rapid Tooling by Laser Powder Deposition: Process Simulation Using Finite Element Analysis*. 2004.

52. Van Acker, K., Vanhoyweghen, D., Persoons, R., Vangrunderbeek, J., *Influence of tungsten carbide particle size and distribution on the wear resistance of laser clad WC/Ni coatings.* Wear, 2005. **258**(1-4): p. 194-202.

53. Chryssolourius G., Zannis, S., Tsirbas, K., Lalas C., *An Experimental Investigation of Laser Cladding.* . Cirp annals Manufacturing Technology, 2002. **5**(1): p. 145 -148.

54. Li, X., Liu, Z., Li, H., Wang, Y., Li, B., *Investigations on the behavior of laser cladding Ni–Cr–Mo alloy coating on TP347H stainless steel tube in HCl rich environment.* Surface and Coatings Technology, 2013. **232**(0): p. 627-639.

55. Shepeleva, L., Medres, B., Kaplan, W. D., Bamberger, M., Weisheit, A., *Laser cladding of turbine blades.* Surface and Coatings Technology, 2000. **125**(1-3): p. 45-48.

56. Huang, S.W., Samandi, M., Brandt, M., *Abrasive wear performance and microstructure of laser clad WC/Ni layers.* Wear, 2004. **256**(11-12): p. 1095-1105.

57. Cao, X., Xiao, M. , Jahazi, M. , Fournier, J., Alain, M., *Optimization of Processing Parameters During Laser Cladding of ZE41A-T5 Magnesium Alloy Castings Using Taguchi Method.* Materials and Manufacturing Processes, 2008. **23**(2008): p. 413–418.

58. Zhu, Y.Y., Li, Z. G., Li, R. F., Li, M., Feng, K., Wu, Y. X., Wada, T., Kato, H., *High power diode laser cladding of Fe–Co–B–Si–C–Nb amorphous coating: Layered microstructure and properties.* Surface and Coatings Technology, 2013. **235**(0): p. 699-705.

59. Ocelík, V., Eekma, M., Hemmati, I., De Hosson, J. Th M., *Elimination of Start/Stop defects in laser cladding.* Surface and Coatings Technology, 2012. **206**(8–9): p. 2403-2409.

60. de Oliveira, U., Ocelík, V., De Hosson, J.Th.M., *Analysis of coaxial laser cladding processing conditions.* Surface and Coatings Technology, 2005. **197**(2-3): p. 127-136.

61. Syed, W.U.H., Pinkerton, A.J., Li, L., *A comparative study of wire feeding and powder feeding in direct diode laser deposition for rapid prototyping.* Applied Surface Science, 2005. **247**(1-4): p. 268-276.

62. Bi, G., Schurmann, B., Gasser, A., Wissenbach, K., Poprawe, R., *Development and Qualification of a Novel Laser-Cladding Head with Integrated Sensors.* International Journal of Machine Tools and Manufacture, 2007. **47**(2007): p. 555-561

63. Medrano, A., Janet, F., Segal, J., Pashby, I., , *Fibre laser metal deposition with wire: parameters study and temperature monitoring system.*, in *SPIE 7131, XVII International symposium on Gas Flow, Chemical Lasers and High-Power Lasers*. 2008: Lisboa, Portugal.

64. Kim, J.-D., Peng, Y., *Plunging method for Nd : YAG laser cladding with wire feeding.* Optics and Lasers in Engineering, 2000. **33**(4): p. 299-309.

65. Heralic, A., Christiansson, A. K., Ottosson, M., Lennartson, B., *Increased stability in laser metal wire deposition through feedback from optical measurements.* Optics and Lasers in Engineering, 2010. **48**(4): p. 478-485.

66. Heralic, A., *Towards full Automation of Robotized laser Metal-wire Deposition*, PhD Thesis, *Department of Signals and Systems*, CHALMERS University of Technology, Goteborg: Goteborg, Sweden. 2009.

67. Syed, W.U.H., Li, L., *Effects of wire feeding direction and location in multiple layer diode laser direct metal deposition.* Applied Surface Science, 2005. **248**(1-4): p. 518-524.

68. Mok, S.H., Bi, G., Folkes, J., Pashby, I., *Deposition of Ti-6Al-4V using a high power diode laser and wire, Part I: Investigation on the process characteristics.* Surface and Coatings Technology, 2008. **202**(16): p. 3933-3939.

69. Sue, A., S.H., Qiu B. H., *Improving Hardfacing for Drill Bits and Drilling Tools.* Journal of Therma Spray Technology, 2010.

70. Deuis, R.L., Yellup, J.M., Subramanian, C., *Metal-matrix composite coatings by PTA surfacing.* Composites Science and Technology, 1998. **58**(2): p. 299-309.

71. Nurminen, J., Näkki, J., Vuoristo, P., *Microstructure and properties of hard and wear resistant MMC coatings deposited by laser cladding.* International Journal of Refractory Metals and Hard Materials, 2009. **27**(2): p. 472-478.

72. Zhou, S., Zeng, X., Hu, Q., Huang, Y., *Analysis of crack behavior for Ni-based WC composite coatings by laser cladding and crack-free realization.* Applied Surface Science, 2008. **255**(5, Part 1): p. 1646-1653.

73. Fallah, V., Alimardani, M., Corbin, S.F., Khajepour, A., *Impact of localized surface preheating on the microstructure and crack formation in laser direct deposition of Stellite 1 on AISI 4340 steel.* Applied Surface Science, 2010. **257**(5): p. 1716-1723.

74. Carotenuto, G., Gallo, A., Nicolais L., *Degradation of SiC particles in aluminium-based composites* Materials Science 1994. **29**(19): p. 4967-4974.

75. Farayibi, P.K., Folkes, J., Clare, A., Oyelola, O., *Cladding of pre-blended Ti–6Al–4V and WC powder for wear resistant applications.* Surface and Coatings Technology, 2011. **206**(2-3): p. 372-377.

76. Wu, P., Zhou, C. Z., Tang, X. N., *Microstructural characterization and wear behavior of laser cladded nickel-based and tungsten carbide composite coatings.* Surface and Coatings Technology, 2003. **166**(1): p. 84-88.

77. St-Georges, L., *Development and characterization of composite Ni–Cr+WC laser cladding.* Wear, 2007. **263**(1-6): p. 562-566.

78. Wang, F., Mei, J., Wu, X., *Microstructure study of direct laser fabricated Ti alloys using powder and wire.* Applied Surface Science, 2006. **253**(3): p. 1424-1430.

79. Syed, W.U.H., Pinkerton, A. J., Liu, Z., Li, L., *Coincident wire and powder deposition by laser to form compositionally graded material.* Surface and Coatings Technology, 2007. **201**(16-17): p. 7083-7091.

80. Borges, B., Quintino, L., Miranda, R. M., Carr, P., *Imperfections in laser cladding with powder and wire fillers.* International Journal of Advanced Manufacturing Technology, 2010. **50**(2010): p. 175-183.

81. Qian, M., Lim, L. C., Chen, Z. D., Chen, W. I., *Parametric studies of laser cladding processes.* Journal of Materials Processing Technology, 1997. **63**(1-3): p. 590-593.

82. Zareie Rajani, H.R., Akbari Mousavi, S.A.A., Madani Sani, F., *Comparison of corrosion behavior between fusion cladded and explosive cladded Inconel 625/plain carbon steel bimetal plates.* Materials & Design, 2013. **43**(0): p. 467-474.

83. Kobryn, P.A., Moore, E.H., Semiatin, S.L., *The effect of laser power and traverse speed on microstructure, porosity, and build height in laser-deposited Ti-6Al-4V.* Scripta Materialia, 2000. **43**(4): p. 299-305.

84. Pinkerton A. J., Wang, W., Li L., *Component repair using laser direct metal deposition.* Journal of Engineering Manufacture, 2008. **222**(Part B): p. 827-836.

85. Kou, S., *Welding Metallurgy*. 2nd edition. 2003, John Wiley & Sons, Inc.: New Jersey, USA.

86. Toyserkani, E., Khajepour, A., Corbin, S., *Laser Cladding*. 2005, CRC Press.

87. Quan, Y.J., Chen, Z. H., Gong, X. S., Yu, Z.H., *Effects of heat input on microstructure and tensile properties of laser welded magnesium alloy AZ31.* Materials Characterization, 2008. **59**(10): p. 1491-1497.

88. Hofmeister W., Griffith, M., Ensz, M., Smugeresky, J., *Solidification in direct metal deposition by LENS processing.* JOM, 2001. **53**(9): p. 30-34.

89. Dey, G.K., Albert, S., Srivastava, D., Sundararaman, M., Mukhopapahyay, P., *Microstructural studies on rapidly solidified Inconel 625.* Materials Science and Engineering A 1989. **119**: p. 175-184.

90. Guo, C., Chen, J., Zhou, J., Zhao, J., Wang, L., Yu, Y., Zhou, H., *Effects of WC–Ni content on microstructure and wear resistance of laser cladding Ni-based alloys coating.* Surface and Coatings Technology, 2012. **206**(8–9): p. 2064-2071.

91. Liyanage, T., Fisher, G., Gerlich, A. P., *Microstructures and abrasive wear performance of PTAW deposited Ni–WC overlays using different Ni-alloy chemistries.* Wear, 2012. **274–275**(0): p. 345-354.

92. Kamdi Z., Shipway, P.H., Voisey K.T., Sturgeon A.J., *Abrasive wear behaviour of conventional and large-particle tungsten carbide-based cermet coatings as a function of abrasive size and type.* Wear 2011: 271(0) p. 1264-1272.

93. Amado, J.M., Tobar, M. J., Yáñez, A., Amigó, V., Candel, J. J., *Crack Free Tungsten Carbide Reinforced Ni(Cr) Layers obtained by Laser Cladding.* Physics Procedia, 2011. **12, Part A**(0): p. 338-344.

94. Anandan, S., Pityana, S., Dutta Majumdar, J., *Structure–property-correlation in laser surface alloyed AISI 304 stainless steel with WC+Ni+NiCr.* Materials Science and Engineering: A, 2012. **536**(0): p. 159-169.

95. SI, S. H., Yuan, X. M., Liu, Y. L., HE, Y. Z., Keesam, S., *Effect of laser power on microstructure and wear resistance of WC/Ni cermet coating.* Journal of Iron and Steel Research, 2006. **13**(2): p. 74-78.

96. Kurlov, A.S., Gusev, A. I., *Tungsten carbides and W-C phase diagram.* Journal of Inorganic Materials, 2006. **42**(2): p. 121-127.

97. Balla, V.K., Bose, S., Bandyopadhyay, A., *Microstructure and wear properties of laser deposited WC-12%Co composites.* Materials Science and Engineering: A, 2010. **527**(24-25): p. 6677-6682.

98. Thethewey, K. R., Chamberlain, J., *Corrosion for science and engineering*. 2nd edition ed. 1995: Longman Group Limited.

99. Bradford, S.A., *Corrosion Control*, ed. J.E. Bringas. Vol. 1. 2001`, Alberta, Canada: CASTI Publishing Inc. 1-497.

100. Fontana, M.G., *Corrosion Engineering*. 3rd edition edition. 1986, McGraw-Hill book company: New York. 1-218.

101. Rashidi, N., Alavi-Soltani, S., Asmatulu, R., *Crevice Corrosion Theory, Mechanisms and Prevention Methods* in *3rd Annual GRASP Symposium, Wichita State University*. 2007: Wichita State Universityp. 215-216.

102. Yang, Y. Z., Jiang, Y. M., Li, J., *In situ investigation of crevice corrosion on UNSS32101 duplex stainless steel in sodium chloride solution.* Corrosion Science, 2013. **76**: p. 163-169.

103. Cao, C., Cheung, M. M. S., *Non-uniform rust expansion for chloride-induced pitting corrosion in RC structures.* Construction and Building Materials, 2014. **51**: p. 75-81.

104. Lee, W. J., Pyun, S. I., Yeon, J. W., Chun, K. S., Choi, I. K., *A study of pitting corrosion of sensitised 316 stainless steel in aqeous 0.01 M NaCl solution using abrading electrode technique and AC-impedance spectroscopy.* Materials Science Forum, 1998. **289**: p. 915-924.

105. Majumdar, J. D., Manna, I., *Laser surface alloying of AISI 304-stainless steel with molybdenum for improvement in pitting and erosion-corrosion resistance.* Materials Science and Engineering: A, 1999. **267**(1): p. 50-59.

106. Tuominen J., Vouristo, P., Mantyla T., Latokartano J., Vihinen, J., Andersson P.H, *Microstructure and corrosion behaviour of high power diode laser deposited Inconel 625 coatings.* Journal of Laser Applications, 2003. **15**(1).

107. Ahmed, N., Bakare, M. S., McCartney, D. G., Voisey, K. T., *The effects of microstructural features on the performance gap in corrosion resistance between bulk and HVOF sprayed Inconel 625.* Surface and Coatings Technology, 2010. **204**(14): p. 2294-2301.

108. Shrestha, S., Sturgeon, A. J., *The use of advanced thermal spray processes for corrosion protection in marine environments.* Surface engineering, 2004. **20**(4): p. 237-243.

109. Niaz, A., *Complementary use of electrochemical testing techniques to study corrosion processes of HVOF Inconel 625, CoNiCrAlY and WCCoCr coatings*, PhD thesis, *Department of Mechanical, Materials and manufacturing Engineering*, University of Nottingham, Nottingham. 2013: p. 1-314.

110. Roy, R. K., *A Primer on Taguchi method*, V.N. Reinhold, Editor. 1990: New York.

111. Gao, S., Zhou, Y., Xi, M. , *Investigation on Inconel 625 Alloy Thin-Walled Parts by Direct Laser Fabrication*, in *Advanced Material Research*. 2011, Trans Tech Publications, Switzerland. p. 3687-3691.

112. Hussein, N.I.S., Segal, J., McCartney, D. G., Pashby, I. R., *Microstructure formation in Waspaloy multilayer builds following direct metal deposition with laser and wire.* Materials Science and Engineering: A, 2008. **497**(1-2): p. 260-269.

113. *Spherotene*. [cited 2013 22/04/2013]; Available from: http://www.lasercladding.co.uk/spherotene.aspx.

114. Zhang, W., Liu, S., *Cracking behavior of ceramic particles reinforced Ni-base alloys composite coating by laser cladding.*Surface Review and Letters, 2005. **12**(1).

115. Meacock, C., Vilar, R., *Laser powder microdeposition of CP2 Titanium.* Materials & Design, 2008. **29**(2): p. 353-361.

116. Tuominen, J., Vuoristo, P., Mäntylä, T., Kylmälahti, M., Vihinen, J., Andersson, P.H., *Improving Corrosion Properties of High-Velocity Oxy-Fuel Sprayed Inconel 625 by Using a HighPower Continuous Wave Neodymium-Doped Yttrium Aluminum Garnet Laser*. Journal of Thermal Spray Technology, 2000. **9**(4): p. 513-519.

117. Ahmed, N., *Characterisation of different forms of Inconel 625 for determining the effects of microstructural modifications on electrochemical behaviour*, PhD thesis, *Department of Mechanical, Materials and Manufacturing Engineering*, University of Nottingham, Nottingham. 2008.

118. Lothongkum, G., Wongpanya, P., Morito, S., Furuhara, T., Maki, T., *Effect of nitrogen on corrosion behavior of 28Cr–7Ni duplex and microduplex stainless steels in air-saturated 3.5 wt% NaCl solution.* Corrosion Science, 2006. **48**(1): p. 137-153.

119. Merello, R., Botana, F. J., Botella, J., Matres, M. V., Marcos, M., *Influence of chemical composition on the pitting corrosion resistance of non-standard low-Ni high-Mn–N duplex stainless steels.* Corrosion Science, 2003. **45**(5): p. 909-921.

120. Abioye, T.E., Folkes, J., Clare, A.T., *A parametric study of Inconel 625 wire laser deposition.* Journal of Materials Processing Technology, 2013. **213**(12): p. 2145-2151.

121. Mahmood K., Stevens, N., Pinkerton, A.J., *Laser clad corrosion protection for mild and harsh environments.* Journal of Surface Engineering, 2012.

122. Wika, S.F. *Pitting and Crevice Corrosion of Stainless Steel under Offshore Conditions*. 2012 18/10/2013 [cited 2013 18/10/2013]; Available from: http://www.diva-portal.org/smash/get/diva2:566900/FULLTEXT01.pdf.